UTPP–37

The measurement of crosssection of Drell-Yan process in Proton-Antiproton Collisions at $\sqrt{s}$=1800 GeV

September 1990

TOSHIHIRO MIMASHI

Submitted in partial fulfillment of the requitements for
the Degree of Doctor of Science
in the Doctoral program in University of Tsukuba

AAB2560

Abstract

The production cross section and the QCD higher order contribution, K factor of Drell-Yan process have been measured in dielectron mode in proton-antiproton collisions at the center of mass energies of 1800 GeV. The experiment has been performed at Fermi National Accelerator Laboratory in the United States using Tevatron accelerator during the period of 1988 though 1989. A number of physics quantities are measured using the CDF (Collider Detector at Fermilab) detector in the pseudorapidity range -2.4 $< \eta <$ 2.4. Total integrated luminosity used for this analysis is 4.76 pb^{-1}. The cross section has been measured down to $\sqrt{\tau} = 0.0066$ which is much lower than measured before. Both the cross section and the K factor are compared with theoretical predictions calculated with a number of different parton distribution functions. Since the production cross section depends both on the K factor and parton distribution functions, the discussion will be done from two points of view. The discussion starts from K factor measurement. The K factor has been measured in Z^0 mass region at first, then assuming that the K factor is constant over the invariant mass region 12 GeV/c^2 $<$ M $<$ 105 GeV/c^2 , the behavior of parton distribution function in a low mass region (12 GeV/c^2 $<$ M $<$ 30 GeV/c^2) is discussed. According to the theoretical prediction of K factor, this assumption is good approximation in the measured mass region independently of parton distribution functions. The Z^0 production cross section times branching ratio of ($Z^0 \rightarrow e^+e^-$) was 205.5 $\pm$ 13.82 (sta) $\pm$ 16.0 (sys)$\pm$ 15.4 (lum) (pb). The K factor, assuming HMRSB parton distribution function, is measured to be 1.53 $\pm$ 0.4. The parton distributions function HMRSE and HMRSB reproduces the shape of the differential cross section at Y=0 well.

The production properties of the Drell-Yan process are also studied. The rapidity distribution and Pt spectrum of the parent virtual photon or Z^0 are presented, as well as the decay electron angular distribution, the Pt spectrum in the center-of-mass system. All these quantities are consistent with Monte Carlo simulation data using EHLQ 1 parton distribution function within the error. Finally a comparison is made between dielectrons from the Drell- Yan process and heavy flavor productions.

Acknowledgements

I would like to express my deep thanks to my thesis advisor Prof. K.Kondo for his guidance and encouragement throughout my graduate career, and giving me an oppotunity to work on the CDF experiment. I could learn many things from his positive attitude toward physics research.

I wish to express my deepest appreciation to Drs. M.Binkley and M.Sekiguchi who have been my co-worker. During my stay at Fermilab, I could learn a lot of things from them, hardware, software and how to solve many physics problems from global point of view.
Dr. M.Atac gave me a deep impression. He taught me many of hardware skills by showing it by himself.

I am deeply indebted to Prof. H.J.Frisch who gave me valuable pieces of advice for my thesis work. When I faced with difficulties in my analysis, he always gave me hearty encouragements and useful suggestions.

Prof. S.Errede, and Dr. C.Newman-Holmes also gave me a lot of help as the electroweak analysis group convener, they gave me chances to present my analysis result at the meeting, and useful suggestions. And they sometimes educated me by themselves.

Prof. K.Takikawa, Drs. M.Mishina, S.Mikamo, T.Yamanouchi, F.Abe and Prof. S.Mori are appreciated for their kindly encouragements.
I also appreciate Prof. S.Miyashita, Drs. S.Kim, K.Yasuoka and Prof. C.Blocker for their useful discussion about electron analysis. Especially Dr. S.Kim gave me several suggestions and discussions during my stay at Univ. of Tsukuba.

I was happy to work with Prof. A.Clark, Drs. M.Gold, and A.Yagil. They taught me how to analyze the hadron collider data. Many of techniques used in my

analysis come from their suggestions.

I also thank to Drs. J.Stirling, T.Matsuura, K.Ellis and H.Iso for their support to calculate QCD higher order contribution in Drell-Yan process. I wish to express my special appreciation to Dr. A.Tellestrup (CDF co-leader), Prof. M.Shochet(CDF co-leader), Drs. R.Kephart, K.Stanfield (Previous head of research division) and L.Lederman (Previous director) for their effort of CDF organizations.

It was pleasure to me to work with other coworkers, R.Markeloff,
Drs. R Snider, J.C.Yun , R.Wagner, J.Marriner, J.Bellinger,
Mr. J.Welch, Mrs. S.Gonzales, L.Desjardines, Dr. M.H.Schub, and M.Yokoyama for VTPC and FTC operation and Dr. H.Kuterian, E.Kearns, V.Scarpine for discussion of electroweak analysis. I appreciate Dr. P.Tipton, F.Ukegawa and Dr. P.Kesten for their useful suggestions about heavy flavor physics.

I would like to thank Drs. G.P.Yeh and G.W.Foster for impressive event display which is very important for my analysis.

A deep thanks go to Drs. P.Berge, A.Para, A.W.Byon and A.Mukherjee for their suggestions about tracking code.

Dr. J.Patrick has developed micro codes for Flash ADC readout. Without his help, we could not readout the data from our Flash ADC system.

I wish to thank Prof. M.Shapiro for suggestions about PAPAGENO Monte Carlo.

Drs. Y.Fukui, M.Shibata, Y.Morita, Messrs. S.Ogawa and M.Ninomiya gave me useful information for the end plug calorimeter.

Dr. E.E.Schmidt, R.Krull are appreciated for their lots of effort of 'Data summary tape production' which were used in my analysis.

I also appreciated Dr. D.Amidei who spent his variable time for me to prepare

a filter code to make my private data summary tape.

I wish to express my appreciation to Drs. I.Nakano, T.Kamon, A.Yamashita, K.Hara, Y.Funayama, M.Franklin, Messrs. M.Kurisu, M.Takano, L.Demortier, Y.Seiya, T.Ino, R.Oishi, Y.Hagura, and Mr. T.Chikamatsu, T.Kaneko,

N.Mitsushio, who gave me a lot of useful cooperation and guidance throughout the data taking and analysis.

C.Picciolo, D.Hahn, F.Shelter are our nice secretaries working for our experiment. I could enjoy their friendly atmosphere during my stay at Fermilab.

I thank Japanese secretary K.Kunori who has always been giving us kindly support at Fermilab.

I thank K.Kumashiro, M.Uenishi working for their secretary work at Univ. of Tsukuba.

Finally, I would like to thank my parents and grandmother for their continuous support.

This work was supported by the U.S. Department of Energy; U.S. National Science Foundation; A.P.Sloan Foundation; Istituto Nazionale di Fisica Nuclear; Ministry of Education, Science and Culture of Japan.

Contents

Chapter 1

Introduction

1.1 Introduction

This article describes an analysis of electron pairs in the proton-antiproton collisions at a center of mass energy of 1800 GeV. This is the highest energy $p\bar{p}$ collider experiment over the world. The experiment has been done at Fermi National Accelerator Laboratory in U.S.A. using the CDF (Collider Detector at Fermilab) detector.

The CDF is the general purpose detector built to study proton-antiproton collisions at $\sqrt{s} = 1.8$TeV. The experiment carried out from 1988 September to 1989 April. The analysis based on total 4.76 pb $^{-1}$ data taken at that period. The measured physics quantities are basically

- Differential production cross section of Drell-Yan process
- Transverse momentum distribution of decay electrons and parents virtual photons

And the main subjects of this article are

- The study of parton distribution function
- The test of QCD using massive lepton pairs

In general, the predictions and tests of the basic parton model show good agreement with experiment data. The anomalous features are the overall cross section level (high by a factor of 1.4-2.0 : K factor) and unexpectedly large mean transverse momenta.

QCD offers the explanation of these anomalies and the measurements of dilepton production provide important quantitative test of QCD.

The organization of the paper is as follows. Chapter 1 is this introduction and reviews of experimental and theoretical progresses of lepton pair production analysis. Chapter 2 describes the CDF detector, trigger and data aquisition system, Chapter 3 describes the event selection, data reduction and the trigger requirements are described. Then it presents the efficiency and backgrounds for finding electrons. The results are presented and discussed in Chapter 4. There is a discussion of Drell-Yan and Z0 production results. The background to the Drell-Yan process from B meson decay is described also. Finally, some events of special interest, either for very high mass or Pt, are presented. Chapter 5 presents the conclusions.

1.2 Drell-Yan Model

This section reviews experimental and theoretical progress in studies of the production of the massive lepton pair production in hadronic collisions. Massive lepton pair production is one of the best methods for investigating the behavior of the parton distribution function at small x and quantum chromodynamics concept and computations.

1.2.1 The parton model and structure of hadron

The parton model

Present evidence indicates that matter is built from two types of fundamental fermions called quarks and leptons which are structureless and point-like on a scale of 10^{-7} m known as partons [37][15]. The quarks are point-like, spin 1/2 fermions. They behave like leptons, but they differ from leptons in that they interact strongly via gluon exchange, while leptons fell only the electroweak force. The evidence of the internal structure of hadrons has been shown by deep inelastic lepton scattering of nucleons [16] and hadron spectrum [21].

The structure function

The structure functions are the covariant scalar quantities used to describe the deep inelastic lepton scattering from nucleons [17][18]. They have been determined for the reactions,

$l^- +$ nucleon $\rightarrow l^- +$ hadron

$\nu +$ nucleon $\rightarrow l^- +$ hadron

Under the assumption that a single vector boson exchange dominates, the dynamics of the reaction is described by the three structure function F_1, F_2, F_3 which are in turn functions of just two covariant kinematic quantities.

$x=-q^2/2p\cdot q,\ -q^2$

where q is the four momentum transfer between the lepton and target nucleon and p is the incident nucleon four momentum. In the parton model, x is interpreted as the fraction of longitudinal momentum of the parent hadron (Bjorken x) [19]. Taking

into account the isospin invariance, the deep inelastic lepton scattering measurement provide the following equations, for charged leptons

$$F_2^l(x) = \sum Q_i^2 x n_i(x)$$

and for neutrinos,

$$F_2^\nu(x) = \sum x \cdot n_i(x)$$

where n(x)dx is the number of quarks carrying longitudinal momentum fraction x. If we write down above equation in the explicit form,

$$F_2^{en}(x) = \frac{4}{9}x[d(x) + \bar{d}(x)] + \frac{1}{9}x[u(x) + \bar{u}(x)] + \frac{1}{9}x[s(x) + \bar{s}(x)]$$

$$F_2^{\nu p}(x) = 2x[d(x) + \bar{u}(x)]$$

$$F_2^{\bar{\nu} p}(x) = 2x[u(x) + \bar{d}(x)]$$

$$F_3^{\nu p}(x) = 2x[\bar{u}(x) - d(x)]$$

$$F_3^{\bar{\nu} p}(x) = 2x[\bar{d}(x) + u(x)]$$

In principle, it is possible to extract the individual quark distributions from these measurement.

The difference between charged leptons and neutrino scattering arises from the difference between the weak and electromagnetic forces, so that the electromagnetic coupling requires the appearance of the quark charge. In addition, the model requires exact relationship to hold between the structure functions,

$$F_2^l = 2xF_1^l$$

$$F_2^\nu = \pm xF_3^\nu = 2xF_1^\nu$$

where the sign is positive for neutrino-quark and antineutrino-antiquark scattering and negative for other choices.

Hence the proton is composed of uud valence quarks and neutron is composed of udd valence quarks respectively [21][22], these u(x), d(x) must satisfy the relation,

$$\int_0^1[u_p(x)-\bar{u}_p(x)]dx = 2$$
$$\int_0^1[d_p(x)-\bar{d}_p(x)]dx = 1$$
$$\int_0^1[s_p(x)-\bar{s}_p(x)]dx = 0$$

$$u(x) = u_p(x) = d_n(x), \quad u(x) = u_v(x) + u_s(x)$$
$$d(x) = d_p(x) = u_n(x), \quad d(x) = d_v(x) + d_s(x)$$

where $u_p(x)dx$, $u_n(x)dx$ mean the number of u quarks carrying longitudinal momentum fraction x in proton and neutron respectively and $u_v(x)$, $u_s(x)$ mean valence and sea quark contributions [20].

Theoretical arguments have been presented about the behavior of the quark distribution function in the two extrema region, $x \to 1$ and $x \to 0$. The behavior of the F_2 for $x \to 1$ limit was shown by Drell and Yan [1] and by West [23]. The results can be obtained by using counting rule arguments [25][38]. For a system which is composed of n point-like constituents, the form factor at large q^2 is expected to be $\sim q^{-(2n-1)}$ and

$$F_2(x) \sim (1-x)^{2n-3}$$

(For proton, n is 3) [25][24]. Experimental data on the ratio of the F_2 structure function of the neutron to that of proton indicate that the d and u quark distribution differences. When $x \to 1$, data are consistent with $d_p(x)/u_p(x) \to 0$ which led to [39]

$$d_p(x) \to (1-x)u_p(x)$$

as $x \to 1$. For the sea quark distribution, the configuration which contains at least one sea quark has to be considered. The proton is the n=5 system ($qqqq\bar{q}$), so that $x \to 1$ limit, $s_p(x) \sim (1-x)^7$.

In the limit as $x \to 0$, the nucleon plus virtual photon sub-energy becomes large and Regge forms [38][37] can be obtained for the structure function, $F_2 \sim a + b\sqrt{x} \Rightarrow A + B \cdot x^{(1-\alpha(0))}$. The first term comes from Pomeron and second term represent isospin exchange. $\alpha(0)$ is the intercept at of leading Regge trajectory. Pomeron exchange describes the quark and antiquark distribution in the sea, $q_s \sim 1/x$ as $x \to 0$. The second term comes from the contribution of the valence quarks. For the valence quarks, the leading trajectories have $\alpha(0) \sim \frac{1}{2}$ so that $q_v \sim 1/\sqrt{x}$. Totally we can write down the number of valence and sea quarks carrying longitudinal momentum fraction x as follows,

$$\begin{aligned} q_v(x) &= A_v(1-x)^3/\sqrt{x} \\ q_s(x) &= A_s(1-x)^7/x \end{aligned} \tag{1.1}$$

Next, we have to think about Q^2 dependence of these quantities. The scaling violation [26] have been observed in deep inelastic scattering phenomena. As a consequence, the quark distributions obtained by using the quark-parton model depend on the value of the four-momentum transfer squared Q^2 of the lepton. As Q^2 increases, the quark distributions change in shape. The large x region is depressed, while the low x region becomes enhanced [28][27]. This effect is well explained by the QCD theory. As Q^2 increases, the probability for a quark to radiate a gluon also increases so that the quark is left with smaller momentum. An analytic parametrization of the quark distribution functions, including Q^2 dependence are discussed in Ref [49].

$$x \cdot q(x,z) = A(z)x^{\alpha(z)}(1-x)^{\beta(z)}$$

The Q^2 dependence is absorbed in the parameter z defined as $z = \ln\frac{\ln(Q^2/\Lambda^2)}{\ln(Q_0^2/\Lambda^2)}$. The parameter Λ which characterizes the strength of scaling violation. Once the quark distributions are delivered from the data at some low value of Q_0^2, the expression written above allows to follow the evolution of such distribution for all $Q^2 > Q_0^2$.

1.2.2 Differential cross section

In May 1970, Sidney D. Drell and Tung-Mow Yan proposed the electromagnetic process to account for the continuum of lepton pairs from hadron-hadron collisions. In the parton model proposed by them, the massive virtual photon in the reaction,

$$(HadronA) + (HadronB) \rightarrow \gamma^* + X \rightarrow l^+l^- + anything$$

is produced by point-like annihilation of a quark from one initial hadron with an antiquark from other. The measurements have been made in many experiment in pp, $p\bar{p}$, K $^{\pm}$p, $\pi^{\pm}$p. In these case, both initial partons are "on" or "near" the mass shell. Integrating over whole transverse momentum region of the massive lepton pair and over whole decay angles in the lepton pair rest frame, the theoretical prediction in the classical model gives the differential cross section as the following formula

$$\frac{d\sigma^2}{dx_1 dx_2} = (\frac{4\pi\alpha^2}{9m^2}) \sum_i Q_i^2 [q_{p_i}(x1)\bar{q}_{\bar{p}_i}(x2) + \bar{q}_{p_i}(x1) q_{\bar{p}_i}(x2)] \qquad (1.2)$$

where α is the usual electroweak coupling $\alpha \cong 1/137$.

$q_{p_i}(x1)$ is the quark parton distribution function of the proton. And Q_i is the fractional charge of quark. The "i" is summed over all flavor. For example the quark distribution factor at proton-proton scattering at y = 0, where $x1 = x2 = \sqrt{\tau}$ can be expressed (ignoring c,b,t quarks) as

$$\frac{8}{9}u(\sqrt{\tau})\bar{u}(\sqrt{\tau}) + \frac{2}{9}d(\sqrt{\tau})\bar{d}(\sqrt{\tau}) + \frac{2}{9}s(\sqrt{\tau})\bar{s}(\sqrt{\tau})$$

and for proton-antiproton collisions it can be written

$$\frac{4}{9}[u(\sqrt{\tau})u(\sqrt{\tau}) + \bar{u}(\sqrt{\tau})\bar{u}(\sqrt{\tau})] + \frac{1}{9}[d(\sqrt{\tau})d(\sqrt{\tau}) + \bar{d}(\sqrt{\tau})\bar{d}(\sqrt{\tau})] + \frac{1}{9}[s(\sqrt{\tau})s(\sqrt{\tau}) + \bar{s}(\sqrt{\tau})\bar{s}(\sqrt{\tau})] \qquad (1.3)$$

where u(x) means $u(x) = u_{p_i}(x) = \bar{u}_{\bar{p}_i}(x)$. This assumes the strong factorization. Re-expressing this in terms of the measurable dilepton parameters 'the invariant mass of lepton pairs M' and 'the rapidity of virtual gamma Y',

$$\frac{d\sigma^2}{dmdy} = (\frac{8\pi\alpha^2}{9m^2 s}) \sum_i Q_i^2 [q_{p_i}(x1)\bar{q}_{\bar{p}_i}(x2) + \bar{q}_{p_i}(x1) q_{\bar{p}_i}(x2)]$$

The kinematics of the process yields the following relations. The energy of the virtual photon can be written

$$E_\gamma = (x1 + x2)\sqrt{s}/2$$

And a longitudinal momentum along the beam direction is

$$P_l = (x1 - x2)\sqrt{s}/2$$

$$x_f = x1 - x2 = 2P_l/\sqrt{s}$$

$$M_\gamma^2 = sx1x2 = E_\gamma^2 - P_l^2$$

$$\tau = M^2/s = x1x2$$

These quark distribution factor as the function of τ depends on critically the anti-quark distribution in proton-proton collisions and the cross falls off at the large τ, on the other hand, in proton-antiproton collisions the cross section is less suppressed than pp case especially the valence components dominate region such as $\sqrt{\tau} > 0.1$. A direct consequence of equation (1.2) is the prediction of scaling

$$\frac{M^4 d\sigma}{dM^2 dx_f} = f(\tau, x_f)$$

The parton model with scaling distribution predicts that both $m^3\frac{d\sigma}{dm}, m^3\frac{d\sigma^2}{dmdy}$ at y=0 depends on $\sqrt{\tau}$ alone for given incident hadrons. Since in our experiment, the measured $\sqrt{\tau}$ region is $\sqrt{\tau} \simeq 0.0066 - 0.016$ where sea quark dominated region, we can treat $u(\sqrt{\tau}) \simeq \bar{u}(\sqrt{\tau})$ so that it is reasonable to compare pp and p $\bar{p}$ data in same level for the discussion of scaling of the cross section. The comparison will be made at Chapter 4.

1.2.3 The QCD corrections of Drell-Yan model

Anomalous K factor can be explained by QCD perturbative approach, assuming, so call 'strong factorization', ie that the Drell-Yan cross section can be predicted

to arbitrary order in perturbative theory, once the relevant structure functions are known from deep inelastic scattering. In this section, the QCD correction for the calculation of several physics quantities related Drell-Yan processes are described.

The QCD corrections of Drell-Yan model

The QCD has a peculiar property following from its renormalization group properties that the effective coupling constant becomes small at the momentum scale Q^2 as $(Q^2) \rightarrow \infty$, $\alpha_s(Q^2) \rightarrow 0$. This property is called as an asymptotic freedom. The quark-gluon coupling constant can be expressed as

$$\alpha_s(Q^2) = \frac{12\pi}{(33-2N_f)ln(Q^2/\Lambda^2)}[1 - O(\frac{1}{ln(Q^2)})]$$

where N_f is the number of flavor and Λ is a scale constant. For five quark flavors (N_f=5), it becomes

$$\alpha_s(Q^2) \sim \frac{12\pi}{(23)ln(Q^2/\Lambda^2)}$$

With our Q^2 range, the value of α_s is small so that a perturbation expansion is not unreasonable.

A single quark with energy E can be replaced by a quark plus collinear gluon with total energy E and there are infinite number of such replacements. The cross section diverges when all equivalent collinear final states are summed over. The problem is circumvented in practical calculations by the procedure proposed by Politzer [28] and Sachrajda [29] who found the solution in the leading log Q^2 approximation, these divergencies can be factored out and absorbed into the incoming particle wave function, this procedure, called the factorization theorem, has been later generated to all logs in perturbation theory, called LLA (Leading Log Approximation) by Sachrajda [29]. As the result, the structure function of the parent particles become Q^2 dependent. But at the same time, it indicate that it is expected that the same pattern of scaling violation as those measurement in deep inelastic lepton scattering

should be seen in Drell-Yan cross section measurement [48]. The gluon emission will generate scaling violation as in deep inelastic scattering. The analysis of scaling violations in deep inelastic scattering indicates that the parameter Λ which reflects the fundamental momentum scale of the strong interaction. The scaling violation also should be seen in Drell-Yan lepton pair production. They are more distinctive when sufficiently accurate dilepton data distributed over a wide range of M and $\sqrt{s}$. Although it was impossible to get a wide range of $\sqrt{s}$ in the previous pp data, now CDF can get that $\sqrt{s}$ =1800 GeV collisions which are much bigger than that of ISR $\sqrt{s} = 27 \sim 63$. This will be discussed Chapter 4.

K factor (Experimental review)

Early experiments obtained the Drell-Yan process showed that measured cross section was a factor of two larger than the expected cross section. This discrepancy result in the inclusive of the anomalous K factor in the differential cross section. The scale factor K_{exp} defines as

$$[\frac{d\sigma}{dM}]_{measure} = K_{exp}[\frac{d\sigma}{dM}]_{naive}$$

are measured at many experiments. The results are summarized in Table 1.1. Since K_{exp} is a function of $\sqrt{s}, \sqrt{\tau}, X_F$, different $\sqrt{s}, \sqrt{\tau}, X_F$ are spanned by the different experiments. [1]

K factor (Theoretical review)

When certain perturbative QCD corrections are included in Drell-Yan cross section calculation, the results are modified in two ways.

- The emission of collinear gluons [29] from the incoming quark lines give rise to large mass singularity logarithm. This problem was solved as discussed in

[1] The different sets of parton distributions are employed by the different experiment listed in the Table 1.1

the previous section.

- The emission of hard and soft gluon give rise to finite perturbative corrections which are different for the two processes, ie Drell-Yan lepton pair production and deep inelastic scattering [202].

K factor can be explained by the second item, so that mainly the second item is discussed in this section.

The radiative correction is of comparable size to the contribution of the lowest order diagrams mainly due to the $\alpha\pi^2$ term originating from the continuation from the space-like (deep inelastic scattering) to time-like (Drell-Yan lepton pair production) Q^2. Some progress has been made in understanding a certain class of constant corrections. One of the example is that one gluon correction to the Born diagram shown in Fig 1.1. The contributions of these diagrams are, to leading power in $1/\epsilon$ which are used in dimensional regularization with N=4+2ϵ.

$$C_F \cdot \frac{\alpha_s}{2\pi} \cdot \pi^2 \cdot \frac{1}{\epsilon^2} \cdot \delta(1-\tau) \cdot (Q^2)^\epsilon$$

$$C_F \cdot \frac{\alpha_s}{2\pi} \cdot \pi^2 \cdot \frac{1}{\epsilon^2} \cdot \delta(1-\tau) \cdot (-Q^2)^\epsilon$$

where $Q^2 > 0$ in both case. The contribution to the K-factor is therefore

$$2R_e(DY - DIS) = C_F \cdot \frac{\alpha_s}{2\pi} \cdot \pi^2 \cdot \delta(1-\tau)$$

in the limit of $\epsilon \to 0$.

The lowest order diagram of Drell-Yan process is the annihilation of a quark-antiquark pair to a virtual photon with $q^2 = m^2$. To first order α_s, there are several additional terms in which either q or $\bar{q}$ has been radiated from a quark or parent gluon [40][41][42] [43][44][45] [46][47]. These contributions make Drell-Yan cross section large. The corresponding diagrams are shown in Fig 1.2. In the diagram of Fig 1.2B, a gluon is exchanged between the quark and antiquark. In the diagram of Fig 1.2C-D, a gluon is emitted in addition to the virtual photon, they are called

as 'annihilation diagram'. The diagram of Fig 1.2E-F shows one of the quark in the two colliding hadrons interacts with a gluon of the other hadron, and emit a virtual photon. These are called as 'Compton diagrams'. These vertex corrections and soft gluon emission analogous introduce the large multiplication factor K

$$K = 1 + \frac{\alpha_s}{2\pi} \cdot \frac{4}{3}(1 + \frac{4\pi^2}{3})$$

and

$$\sigma \approx K \cdot \sigma_{naive}$$

The detail QCD calculation result of these processes will be presented at Chapter 4.

Transverse momentum distribution of lepton pairs

In the lowest order Drell-Yan mechanism, the transverse momentum of the virtual photon is related to the transverse momentum of the annihilating quarks. In the parton model, such a momentum is related through the uncertainty principle to the size of the parent hadron and is expected to be of the order of 300 MeV/C independent of $\sqrt{s}$. However the mean Pt value $< Pt >$ exhibits linear size well described by the form at fixed $\sqrt{\tau}$ value [31][40].

$$< Pt >= a + b\sqrt{s}$$

Typical size of a, b are a=0.44 and b=0.026 at $\sqrt{\tau} = 0.22$. The constant term comes from intrinsic transverse momentum of quark-antiquark pair. The second term is related with QCD higher order processes; ie. Compton and Annihilation diagrams. To calculate these mean Pt distribution within the QCD frame, the simple perturbative expansion can be applied only when both Pt and the dilepton mass M are large compared with QCD energy scale Λ [31]. The cross section for Annihilation and Compton diagrams at low Pt behave like

$$\frac{d\sigma}{dPt^2} \sim \frac{1}{Pt^2}$$

[33] And it gives

$$< Pt^2 >= \alpha_s(M^2) \cdot f(\tau, lnM^2)$$

where f depends on the parton densities. At these calculations, the problem is that the cross section diverge as Pt tends to 0. This is compounded by not knowing the initial transverse momentum distribution of quarks in hadrons. Adding to this effect, the equation becomes

$$< Pt^2 >= \alpha_s(M^2) \cdot f(\tau, lnM^2) + < Kt^2 >$$

where $< K_t^2 >$ means RMS of the intrinsic transverse momentum.

Angular distribution in the lepton pair rest frame

In the low mass region, we have to treat only virtual photon contribution. The Drell-Yan model leads to the prediction of a simple decay angular distribution of the leptons in the center of mass frame of the lepton pair. At the collinear collision, the quark-antiquark annihilation produces a photon with its spin aligned along the beam axis. The amplitude for the decay of the photon into a lepton pair is

$$A(\hat{\theta}, \phi) = \uparrow\uparrow Y_0^1(\hat{\theta}, \phi) + \downarrow\uparrow Y_1^1(\hat{\theta}, \phi)$$

where the arrows indicate the spin alignments of lepton and Y are the spherical harmonic functions. After integrated over azimuth angle, the angular distribution becomes,

$$\frac{dN}{d(cos\hat{\theta})} = 1 + cos^2\hat{\theta}$$

Several groups have measured the decay angular distribution for dileptons and fitted by

$$\frac{dN}{d(cos\hat{\theta})} = 1 + \alpha \cdot cos^2\hat{\theta}$$

[34][2][35]

Around Z^0 mass region, the contribution from weak neutral interaction gives rise to a parity violating term proportional to cos $\hat{\theta}$, so that the angular distribution of decay lepton in the rest frame becomes slightly asymmetric.

$$\frac{d\sigma}{d(cos\hat{\theta})} = A \cdot (1 + cos^2\hat{\theta}) + B \cdot cos\hat{\theta}$$

The cross section can be written exactly,

$$\begin{aligned}\frac{d\sigma}{d(cos\hat{\theta})} = & \sum_i \frac{3\pi\alpha^2 Q_i^2}{2\hat{s}}(1 + cos^2\hat{\theta}) \\ & - \frac{3\alpha Q_i G_f M_Z^2(\hat{s} - M_Z^2)}{8\sqrt{2}[(\hat{s} - M_Z^2)^2 + M_Z^2\Gamma_Z^2]} \\ & \times[(R_e + L_e)(R_q + L_q)(1 + cos^2\hat{\theta}) + 2(R_e - L_e)(R_q - L_q)cos\hat{\theta}] \\ & + \frac{3G_f^2 M_Z^4 \hat{s}}{64\pi[(\hat{s} - M_Z^2)^2 + M_Z^2\Gamma_Z^2]} \\ & \times[(R_e^2 + L_e^2)(R_q^2 + L_q^2)(1 + cos^2\hat{\theta}) + 2(R_e^2 - L_e^2)(R_q^2 - L_q^2)cos\hat{\theta}]\end{aligned}$$

where R_f, L_f means the left- and right- handed fermion coupling

$$L_f = 2T_3 - 2Q_f \cdot sin^2\theta_w, R_f = -2Q_f \cdot sin^2\theta_w$$

where T_3 is the third component of weak isospin [36]. The first term comes from pure electromagnetic process and the third term comes from pure weak interaction and the second term comes from the interference of those two processes.

Chapter 2

Apparatus

2.1 Tevatron beam

The Tevatron accelerator produced the world highest energy proton-antiproton collisions at a center of mass energy of 1.8 TeV. Protons and antiprotons are corrected into 6 bunches, so that a beam crossing occurred every 3.5 μsec. The schematic drawing is shown in Fig 2.1. Protons are accelerated up to 200 MeV by a linear accelerator at the first stage and injected into a booster. Then they are accelerated up to 8 GeV and injected into the main ring whose diameter is around 2 Km. After accelerated up to 150 GeV, protons are injected into the Tevatron ring which are implemented in the same tunnel of the main ring and the final acceleration is done up to 900 GeV.

On the other hand, antiprotons are produced from bunches of 2000 billion protons accelerated up to 120 GeV at the main ring and a tungsten target. The produced antiprotons are corrected through a lithium lense and sent to the antiprotons debuncher-accumulator complex. Since the antiprotons are produced with a broad momentum spread, the momentum spread and the size of the antiproton beam are reduced by a process known as stochastic cooling at the accumulator ring and transfer into the main ring. As same as protons, antiprotons are accelerated up

to 150 GeV at the main ring and transferred into the Tevatron ring to get further acceleration up to 900 GeV. The peak luminosity has been improved from 3×10^{29} Cm $^{-1}$ s $^{-1}$ to over 2×10^{30} Cm $^{-1}$ s $^{-1}$

2.2 The CDF detector

2.2.1 Overview

Collider Detector at Fermilab (CDF) is a 5000 t detector built for proton - antiproton collider experiment at a center of mass energy of 1.8 TeV. Fig 2.2 shows a perspective view of the CDF detector [52]. The detector is composed of the charged particle tracking systems, the electromagnetic and the hadron calorimeters, the central solenoid magnet which provide 1.4116 Tesla magnetic field parallel to the beam direction, and the muon detectors. The detector is separated into three parts in the polar angle space, the central detector , ($30° < \theta < 150°$), the end plug detector ($10° < \theta < 30°, 150° < \theta < 170°$), and identical the forward-backward detectors ($2° < \theta < 10°, 170° < \theta < 178°$). A cut through on half of the detector is shown in Fig 2.3

2.2.2 Beam-Beam counter

The lowest level trigger uses the Beam-Beam counter located between the central detector and the forward detectors, at Z = $\pm$ 581.6 cm from the nominal collision point [85][86]. It is used not only for a minimum bias trigger in level 0, but also used as primary luminosity monitor [87]. The counter is made from single layer, 2.5 cm thick SCSN23 scintillator and arranged in rectangle surrounding the beam pile. (Fig 2.4) It covers $0.317 < \theta < 4.47$ ($3.24 < \eta < 5.89$). The total number of counters are sixteen in each forward and backward region. The counter has excellent timing properties. ($\sigma < 200$ps)

2.2.3 Tracking

The following five types of tracking chambers are used in the CDF detector.

The vertex time projection chamber (VTPC) The Vertex Time Projection Chamber (VTPC) [53] consists of eight double time projection chambers surrounding the beam pipe and mounted end to end along the beam direction. Fig 2.5 shows the VTPC location in the central detector. The whole VTPC system is 2.9 m long in beam direction and the active volume is 6.5 cm to 21 cm in radius [60], and covers $5° < \theta < 175°$. Fig 2.6 shows two VTPC modules. One module is divided into two drift regions by a high voltage center grid, each has 15.25 cm long drift regions. Maximum drift time was set to 3.5 μ sec [59]. Each end plane is divided into octants with 24 sense wires and 24 cathode pads. As shown in Fig 2.6, adjacent modules have a relative rotation angle of $\phi = \arctan(0.2)$ around beam axis, so that it provide ϕ information from small angle stereo and eliminate the clack caused by octant boundaries.

A track Z position and R (radial direction) position is measured by TDC data from sense wire signal and track ϕ informations are measured with both FADC data from cathode pad and small angle stereo of rotated modules. (Appendix C) The VTPC pad readout are implemented only on the 8 planes. Fig 2.5 shows the module position where pads data are read out. Pad readout are instrumented to cover the end plug region.

The clock speed of TDC is set to 8nsec and that of FADC is set to 94.3 nsec.

The VTPC provide,

- Measurement of primary Z vertex position
- Identify multiple interactions in the same beam crossing
- Measurement of Charged multiplicity, $dN_{ch}/d\eta$

(charged multiplicity η dependence) for Minimum bias physics [84]

- Provide event topologies and reject beam gas events
- Provide the end plug ($10° < \theta < 30°$), and forward($3.5° < \theta < 10°$) region tracking. This is essential for e/π^0 separation and the forward muon identification.
- Identification of gamma conversion caused at outside of the VTPC

Since the VTPC is implemented most inner part of the detector, it is extremely important to minimize the material of the VTPC as same as beam pipe. The beam pipe is made by 5.08 cm diameter, 500 μm wall thickness beryllium tube. The VTPC consists of light-nuclei material such as Rohacell foam, Kapton film and epoxy glass or graphite fibers. The minimization of materials also prevailed in the choice of chamber mounted electronics and cables. The surfacemount technology on thin (0.625 mm) G10 board are used as preamplifier board [62]. The output of preamplifier are sent through copper coaxial cable optimized for low mass. Fig 2.7 shows the average amount of material in radiation lengths.

The central tracking chamber (CTC) The central tracking chamber is 1.3 m radius and 3.2 m long large cylindrical drift chamber [63]. Under the 1.4116 Tesla magnetic field supplied by the large central solenoidal coil, the CTC can measure charged particle transverse momentum with the accuracy of $\delta Pt/Pt^2 < 0.002$ (GeV/c) $^{-1}$ in the angle region $40° < \theta < 140°$ and using vertex constraint fit on beam position, the rms momentum resolution is improved up to $\delta Pt/Pt^2 < 0.0011$ (GeV/c) $^{-1}$.

The CTC has 84 layers of wires and they are grouped into nine "superlayers" as shown in Fig 2.8. Five of them have 12 sense wires parallel to the beam direction and they are called axial wire. Other four layers have 6 wire tilted by 3 degree to

provide the θ information of each track and called as stereo wire cell. All superlayers have a 45 degree tilt respect to the radial direction to compensate for the Lorentz angle of drift electron in the magnetic field. The maximum drift time is set to 800 n sec and one TDC bin is set to 8 nsec.

The forward tracking chamber(FTC) The forward tracking chamber [64] is a radial drift chamber which covers in the angle region $2 < \theta < 10, 170 < \theta < 178$. (Fig 2.9) The FTC is composed of 72 wedge shape cells and each cell contains planes of radial anode and field shaping wires and planes of cathode strip. The planes are slanted by 2 degree relative to the beam axis, so that left-right ambiguities can be resolved by requiring that a track points out vertex. Each anode plane has twenty four sense wires and twenty six field shaping wires. Four of twenty four sense wires are used for charge division. The tracks were reconstructed in ϕ -Z plane measuring the drift time using LRS 1879 multi hits TDC's. The maximum drift time is set to 800 n sec and one time bin width was set to 8 n sec. Then tracks are reconstructed in R-Z plane using charge division sense wires. The charge division sense wires of every other cells were joined in the inner cylinder compartment and currents are measured from outer end of wires and read out using 26.5 MHz Flash ADC's.

The central drift tube (CDT) The central drift tube is implemented surrounding the CTC [65] [66]. The CDT is composed of three layers of 3 m long, 1.27 cm diameter stainless steel tubes.(Fig 2.10) Tracks in R-ϕ plane are measured by drift time and charge division has been used to measure Z position of each track. Typical resolution of these measurements are 2.5 mm in axial direction and 200 μm in azimuthal direction.

The small angle chamber (SAC) The small angle chambers are implemented between the FTC and forward calorimeter for special use of very forward silicon

calorimeter.

The central region tracking has been done with three of these tracking devices, the CTC, CDT and VTPC. The event Z vertices are measured by the VTPC. The VTPC can perform good R-Z track measurement but weak in R-ϕ reconstruction. On the other hand, the CTC has a good measurement in R-ϕ plane, but relatively weak in R-Z measurements, so that it refers the vertex position measured by the VTPC. The CDT has been installed to add more track R-Z information. In addition to the normal track reconstruction, the VTPC and CDT takes very important role in electron and photon identification. For an electron identification, the VTPC is used to reject the gamma conversion occurred outside of the VTPC. For each electron candidate who has a good CTC track, the VTPC activities between event vertex and EM shower centroid has been investigated.

The CDT has been used as preradiator for central photon identification.

In the end plug region, charged particle tracks are measured with the VTPC and CTC. Although the CTC still has good ϕ measurement in this region, the quality of R-Z reconstruction becomes worse, so that the VTPC-CTC track linking are much more important in this region. [1] The VTPC pad read out are implemented to cover the plug region so that it can perform track ϕ measurement more precisely. The CTC-VTPC track matching are much improved by this measurement and it is also useful to identify the electron in $1.7 < \eta$ where CTC tracks don't have enough information anymore. In addition to the normal track reconstruction, the VTPC pad data are used calculating dE/dx of charged track in order to identify gamma conversion occurred at beam pipe. The forward region tracking has been performed with the VTPC and FTC. The FTC has good measurement in ϕ direction, but weak in R direction so that the VTPC R-Z track informations are combined to perform good 3 dimensional track reconstruction. These are out line of all tracking system.

[1] The detail description will be in the next chapter.

Since each tracking device has strong and weak point in the measurement direction, the tracking system was designed to help weak points of other detectors.

Readout electronics The basic outline of readout electronics are common in all tracking systems except for the CDT. There are two kinds of readout path in the tracking system. One is TDC readout and the other is Flash ADC readout. Flash ADC readout are used in the VTPC pad system and the FTC charge division system.

The chamber signals are amplified at pre-amplifiers mounted on each chamber and sent to the Amp-Shaper-Discriminator board (ASD board) located on the end wall of the central detector [61] [63]. An ASD board contains 48 channels of the main amplifier, signal shaper and discriminator. The signals are digitized by those discriminators, then timing informations are sent to the counting room through 200 feet flat cable as differential ECL signal. Finally signals are digitized by LRS 1879 multi hits TDC's. In the Flash ADC system, the signals are amplified by preamplifiers which are mounted on the chamber. The amplified signals are carried to the Pulse Amplifier Shaper(PAS) board [58] located on the end wall through minicoax cables. After processing on the PAS board , they are sent to the counting room with 200 feet twisted pair cables and received by line receiver that has base line restorer on the FASTBUS [54][54] FADC module [109]. FADC modules digitize the analog signal and send them to the SLAC scanner processors.

2.2.4 Calorimeter

The CDF calorimeter system is composed of three electromagnetic calorimeters, (The central EM calorimeter, the end plug EM calorimeter and the forward EM calorimeter) and four hadron calorimeters(the central hadron calorimeter, The end wall hadron calorimeter, the end plug hadron calorimeter and the forward hadron

calorimeter). All calorimeters are sampling type calorimeters and the whole system covers $-4 < \eta < 4$ in pseudorapidity range and 2 π azimuthal angle. The central and wall calorimeter ($30^\circ < \theta < 150^\circ$) use scintillators and the plug, forward ($2^\circ < \theta < 30^\circ, 150^\circ < \theta < 178^\circ$) calorimeter use gas chambers as sampling media. Electromagnetic calorimeters are composed of lead plates absorber and sampling media and steals are used as absorber in hadron calorimeters. The electromagnetic and hadron calorimeters have approximately uniform granularity in rapidity-azimuthal angle space and constructed in the tower geometry pointing at the interaction region. Fig 2.11 shows tower size of the calorimeter in $\eta - \phi$ space. Typical tower size is set to 0.1 in $\delta\eta$ and 15° in $\delta\phi$ for the central scintillator calorimeter and 5° in the plug and forward gas calorimeters.

The central electromagnetic calorimeter The central electromagnetic calorimeter is used to measure the energy of electrons and photons. It is implemented surrounding the central solenoidal magnet, and covers $-1.1 < \eta < 1.1$ pseudorapidity region [70][76][77][78]. The calorimeter is broken up into 15° wedge style tower geometry. Fig 2.12 shows one of the 15° calorimeter segments. It is composed of 31 layers of polystyrene scintillator and 30 layers of lead absorber. The total radiation length is 19 X_0.

Light from scintillator is readout from Y7 wave shift sheets on both side of wedges and converted to electronic signals and amplified by phototubes located outside of the central hadron calorimeter. Around the electromagnetic shower maximum position, (around 6 radiation length in depth), a proportional chamber with fine grained strip (1.5 cm spacing) and wires are implemented to measure the electron shower position accurately. The position resolution is 5 mm in azimuthal direction and 3 mm in η direction. Energy resolution of the calorimeter is $\delta Et/Et = [(0.135/\sqrt{Et})^2 + (0.020)^2]^{1/2}$.

The central and end wall hadron calorimeter The central hadron calorimeter is implemented outside of the central electromagnetic calorimeter. It is composed of 32 layers of acrylic scintillator and steel absorber and it covers $45° < \theta < 135°$. Total absorption length is $4.7/sin\theta$ [73].

The end wall hadron calorimeter are mounted on the steel end wall of the magnet york. The same sampling media and absorber are used as the central hadron calorimeter. It has 15 layer in depth and $4.5/cos\theta$ absorption length. [2]

The end plug electromagnetic calorimeter The end plug electromagnetic calorimeter [50][51][108] covers polar angle $10° < \theta < 30°, 150° < \theta < 170°(1.1 <| \eta |< 2.4)$ with segmentation $\delta\eta = 0.09$ at $1.41 <| \eta |< 2.4$, $\delta\eta = 0.045$ at $1.1 <| \eta |< 1.41$ and $\delta\phi = 5°$ (Fig 2.13). The detector consists of 34 layers of proportional counters and 2.7 mm lead plate absorber as shown in Fig 2.14. Total thickness is 18 radiation length [71]. The pad signals are ganged in a longitudinal direction and readout as three depth segments. The first segment consists of 5 layers, the second segment consists of 24 layers and the third segments consists of last 5 layers.

Two kinds of strip patterns are implemented around the shower maximum of the calorimeter. These are orthogonal with each other. Fig 2.15 and Fig 2.16 shows each strip pattern. The η position and ϕ position are measured respectively, then they are merged. The η strip width is set to be $\delta\eta = 0.02$ and ϕ strip width is set to be $\delta\phi = 1°$. The coverage of these strip chambers are limited in $1.2 <| \eta |< 1.8$ region. The energy resolution of this chamber is approximately $\sigma/\mathrm{E}\ (\%) = 28/\sqrt{E}(\%)$.

The end plug hadron calorimeter The end plug hadron calorimeter is composed of 2 inches of steel and 0.75 inches of proportional tube chamber with cathode pad readout. It covers $10° < \theta < 30°, 150° < \theta < 170°$ region, and operated around

[2]The central hadron calorimeter uses 2.5 cm steel absorber and the end wall hadron calorimeter uses 5.1 cm thick steel.

2.1 KV under argon-ethen 50%-50%. It has 6 X_0 absorption length and steels work as flux return of the central solenoidal magnet.

The forward electromagnetic calorimeter The forward electromagnetic calorimeters are implemented at 6.5 m far from interaction region to cover $2° < \theta < 10°, 170° < \theta < 178°$ polar angle range [72]. It was operated around 1.9 KV which is middle of proportional region. There are 30 layer in depth and each 15 layers are ganged and readout as two depth segment. The energy resolution is $25\%/\sqrt{E} + 0.5$ The position resolution is between $1 \sim 4$ mm, depends on location in the chamber. The calorimeter offers typical the pion misidentification probability less than 0.5 % with electron identification efficiency greater than 90%.

The forward hadron calorimeter The forward hadron calorimeters are located outside of the forward electromagnetic calorimeters. They are composed of 27 pairs of proportional tube chamber and steel absorber and cover the pseudorapidity range of $2.2 <| \eta |< 4.2$ [75]. It is operated around 1.7-2.4 KV under argon-ethen 50%-50%.

Readout electronics The basic readout electronics are common in all calorimeter. The output signals of photo tubes or gas chambers are sent to a special crate-based analog front-end system, RABBIT system, [56] (Redundant Analog Bus Based Information Transfer) that are implemented at the end wall of the central, forward detector. Since the calorimeter needs a very large dynamic range, ie. from a few tens of MeV for minimum ionizing particle to several hundreds of GeV jet, 16 bit ADC's are used in the system. In the RABBIT system, the output voltage of the detector has been read out as follows.

For each event, the sampling of two voltage levels are performed. The first sampling has been done just before the interaction time, it is taken as reference.

The second sampling has been performed after the interaction. The difference of these two sampling voltages should be proportional to the integrated signal. After digitizing these voltage difference, the values are sent from RABBIT system to the fast intelligent scanner, called MXs, [57] located in the counting room. The scanner subtract the pedestal and multiply gain factor, then gives these information to the FASTBUS data acquisition system.

2.2.5 Muon chamber

There are two kinds of muon chamber in CDF. One is the central muon chamber [67][68]. It is implemented surrounding the central hadron calorimeter. The central muon chamber consists of three layers of drift chamber and measures azimuthal position using drift time and z coordinate from the charge division sense wires Fig 2.17). The momentum of muons are measured by the CTC and it covers $-0.65 < \eta < 0.65$ in pseudorapidity region. The other is the forward muon chamber [69] implemented at outside of the forward hadron calorimeter with toroid magnet (Fig 2.18). The forward muon chamber covers $3° < \theta < 16°, 164° < \theta < 177°$.

2.2.6 Super conducting magnet

The Superconducting solenoidal magnet is implemented to supply magnetic field parallel to the beam direction in the central detector, so that the CTC is able to measure the transverse momentum of charged particles. The superconducting solenoidal magnet [81] [82] is 3 m in diameter and 5m long and produces 1.4116 Tesla magnetic field. The coil is made by 1164 turns of an aluminum stabilized NbTi/Cu superconductor, fabricated by EFT method [83]. The overall radiation length is 0.85. The return path of magnetic flux is formed by the iron of return york and the absorber of the end plug/end wall calorimeter.

2.2.7 Trigger

Overview

The four level triggers [140], level 0, 1, 2, 3, are used to reduce the rate from the interaction rate of 50 KHz to the rate at which events can be written on tape of 1 Hz. The level 0 trigger is the lowest level of the trigger system. It requires the time of flight counters settled in both forward and backward of the central detector to be hit. The trigger decision has been made within 100 n sec after the beam crossing and inhibit data taking during the next beam crossing if the event satisfied the trigger. The level 1 trigger is made in the 7 μsec. This trigger refers only the global feature of the event. The information of energy flow in the detector is used in level 2 trigger. The level 1 trigger reduces a rate of event to a few KHz. At the level 2 trigger, the decision time is almost 10 μ sec, so that the dead time according to the level 2 trigger decision is 5-10 %. In this level, the topological features of the transverse energy deposition such as clustering of energy in calorimeter are referred. Since the data acquisition system needs order 1 msec to readout whole detector components. The data aquisition system starts to read out detector data after a level 2 trigger is satisfied. To perform these, the level 2 trigger reduced the trigger rate down to 100 Hz. The final level trigger, level 3, consist of a software processor farm. Sixty Motorola 68020 processor were used for level 3 trigger. Finally the output rate of whole trigger system was set to 1 Hz. The CDF trigger has capable of parton identification, such as e, μ, τ, ν and jet. And it prepares trigger table for each parton in each trigger level, and the final decision has been made 'or' of those. This overlapping trigger makes trigger efficiency estimation possible. These trigger informations are kept in the raw data tape. They are also used for fast event selection of fast event reconstruction path. In order to calculate Drell-Yan cross section, electron trigger has been used. The central muon trigger also used for electron trigger study. The detail of central electron and muon trigger is discussed

later.

2.2.8 Luminosity measurement

The luminosity has been measured using both the CDF beam beam counter (BBC's) [85] [86] [87] and accelerator information. For luminosity measurement, [88] [89] [90] [91] [92], the Tevatron accelerator was run at two different energies, ie $\sqrt{s}$ = 546 GeV and 1800 GeV. In order to get an absolute luminosity value at $\sqrt{s}$ = 546 GeV, we started to estimate non-diffractive and diffractive inelastic cross section at $\sqrt{s}$ = 546 GeV, then tried to extrapolate it to $\sqrt{s}$ = 1800 GeV. To get an absolute normalization of the BBC cross section (σ_{BBC}) at $\sqrt{s}$ = 546, the luminosity measured with beam parameter and the rate in the BBC are used. The total luminosity can be expressed by the beam parameters as follows,

$$L = \frac{N_p \cdot N_{\bar{p}}}{4\pi\sigma_x\sigma_y} \cdot f$$

where

- N_p : The number of protons per bunch
- $N_{\bar{p}}$: The number of antiprotons per bunch
- σ_x : Horizontal size of a bunch
- σ_y : Vertical size of a bunch
- f : Revolution frequency of the beams

The transverse profile of the beam is measured by flying wires and a wall current monitor measures beam intensities and longitudinal profile for each bunch.

Finally we obtained $\sigma^{eff}_{BBC} = 32.8 \pm 3.6$mb. The σ^{eff}_{BBC} has been estimated also from other respect. The second method used values reported by UA4 collaboration [93][94]. Using MBR Monte Carlo, acceptance correction for the CDF BBC system

has been applied to translate σ^{eff}_{BBC} of UA4 measurement to σ^{eff}_{BBC} in CDF. The correction of inefficiencies of the BBC's due to radiation damages also was applied. From this method, we can get $\sigma^{eff}_{BBC} = 36.6 \pm 1.7$ mb. To calculate the final value of σ^{546}_{BBC}, we took an average of those two measurements and finally the value $\sigma^{eff}_{BBC} = 35.8 \pm 1.7$ mb. has been gotten.

In order to extrapolate the value into $\sqrt{s}$ = 1800 GeV, the ratio R,

$$R = \frac{\sigma^{1800}_{BBC}}{\sigma^{546}_{BBC}}$$

is calculated using beam parameters to be R= 1.30. Using this ratio R and σ^{546}_{BBC}, σ^{1800}_{BBC} are estimated to be

$$\sigma^{546}_{BBC} = 47.0 \pm 2.21 \pm 2.15mb$$

where the first error comes from the contribution of σ^{546}_{BBC} and second term comes from R. At the end, an uncertainty from Luminosity becomes ±6%

Chapter 3

Offline analysis

3.1 Event reconstruction

3.1.1 Electromagnetic cluster

An electron identification starts from the clustering of energy depositions in the electromagnetic calorimeters [96]. At first, two kinds of tower lists are made. One is a seed tower list. All towers with Et above the seed tower Et threshold 5 GeV are put on it. Et is calculated with energy deposits in the electromagnetic calorimetry and a Z vertex position measured by the VTPC. The other is a list of hit towers which had Et more than 0.1 GeV. These towers are used to calculate cluster energy. Then the highest Et seed is taken from the seed tower list and next the hit tower list is referred. A tower is merged into the cluster if it is a neighbor of the current tower. (Only towers adjacent in η are merged in the central region and any of 9 towers surrounding the current tower are merged in the plug and forward region.) Maximum number of tower is set as follows,

- 3 $\times$1 (η $\times\phi$) - The central calorimeter
- 5 $\times$5 (η $\times\phi$) - The plug calorimeter
- 7 $\times$7 (η $\times\phi$) - The forward calorimeter

The ratio of the Et of the new tower to the Et of the current tower is limited to be less than 1 in order to prevent clusters from having valleys. Each tower cannot

belong to more than one cluster. After clustering these electromagnetic towers, the cluster is accepted as EM cluster if total Et is greater than 5 GeV and the ratio of the hadronic energy to the electromagnetic energy is less than 0.125.

3.1.2 Vertex finding

The event Z vertices are calculated with the VTPC wire information. Using this event vertex, transverse energy and pseudorapidity are calculated [121]. In the 1988-1989 Run, the multiple interaction event rate went up to 20 % at 2 $\times 10^{30}\ cm^2 sec^{-1}$. The Z vertex distribution peaked at Z=0 with σ_z = 30 cm [121].

3.1.3 Track reconstruction

The tracks are reconstructed from digitized TDC and ADC counts. TDC is used in the VTPC, CTC and FTC. And flash ADC data is used for in the VTPC pad and the FTC charge division system. The raw data are stored in Data bank (D bank) as digitized TDC and ADC counts. In the case of tracking bank, element bank (E bank) is almost identical to D bank. E bank also stores TDC and ADC counts of each detector. From these E banks, tracks are reconstructed detector by detector, except for the CTC track reconstruction in the end plug region and the detector oriented segment banks such as the CTCS, VTCS, FTCS are produced. One segment bank contains all information on a corresponding track. A track is parametrized by 5 parameters,

- Cot θ : cotangent of track polar angle
- ϕ : track azimuthal angle
- D0 : impact parameter
- Z : intercept on the Z axis in R-Z plane
- Cur : curvature of track

The error matrix information is also written in the segment bank.

In the end plug region, CTC tracks are reconstructed using the VTPC information, because the CTC dose not have sufficient information in this region. The CTC and VTPC linking assumes both detectors to be over efficient, and tries to find the set of links which gives the best over all χ^2.

Finally these detector oriented tracks are merged to form a final tracking segment bank TRKS.

3.1.4 Clustering the energy deposits in the calorimeters

Raw data are stored in the detector oriented data bank (D bank). There are mainly 7 kinds of D bank corresponding to 7 calorimeters

CEM, CHAD, WHAD, PEM, PHAD, FEM and FHAD [122] [123]

The raw data are stored as corrected ADC count. [1] These ADC counts are converted into the energy deposition in each channel and stored in detector oriented E bank. The several kinds of offline noise filters, such as PEM spike noise [129] [130] [131], noise from slow neutrons [127] [128], the forward hadron and plug hadron calorimeter cable noise [124] [125] [126] have been applied during the conversion of D bank to E bank. Then the detector oriented E banks are merged into a calorimeter tower bank TOWE. The energy clustering (The electron clustering and the jet clustering) are done using TOWE bank and make a segment bank called CALS. A CALS bank corresponds to a physics object such as an electron, a photon, and a jet (a parton). It contains all informations on the cluster such as corrected transverse energy, η and ϕ location.

3.1.5 Others

A precise measurement of an electromagnetic cluster centroid was done using the strip chamber implemented in the central and plug EM calorimeters. At the first

[1] Gas gain correction and Amplifier correction has been applied

stage, η and ϕ positions are calculated respectively, then they are combined. The strip chamber segment bank, CASS, is made for each strip chamber cluster.

A missing transverse energy was measured using all calorimeter informations and a segment bank, METS [132] [133] was made event by event.

In addition to these informations, trigger information, luminosity information and several parameters used to produce the data summary tapes (DST's) are also kept in the DST.

3.1.6 Parton reconstruction

The parton reconstruction was done using these calorimeter and tracking informations. The higher level segment banks were made for each reconstructed parton. For example, an ELES bank is made for an electron and a photon, and a CMUO bank is made for a central muon. These segment banks contain not only kinematical variables of the parton, but also the variables for the parton identification.

3.2 Electron identification

In this section, the parameters used to identify electrons are described. First, the parameters common in the central and plug electron identification are described, then the parameters special to either the central or plug electron identification are described respectively.

3.2.1 Parameters common over all regions

Had/Em The ratio of the energy deposit in the hadronic calorimeter to that of electromagnetic calorimeter.

The VTPC hit occupancy [98] In order to reject gamma conversion electrons produced outside of the VTPC, a high VTPC hit occupancy has been required. The VTPC hit occupancy is defined as follows: The road is assumed between the primary

vertex and the centroid of EM cluster with the width of $\delta\ \eta$ = 5 mm and $\delta\ \phi$ = 5 mm in the shower maximum depth, R=184.5 cm for the central electromagnetic calorimeter and Z = 190 cm for the end plug electromagnetic calorimeter. The number of expected hits in the road is calculated. Since the VTPC has 24 sense wires in radial direction, the maximum number of expected hits is 24. If a track passed close to radial board (within 0.035 radian from octant boundaries) or module boundaries, we don't expect the hits. Then the number of active hits in the road are counted from wire TDC information. Hits are counted as active if there is an overlap between road and a translated R-Z position of each hit. Finally the VTPC hit occupancy is defined as,

$$\epsilon \equiv \frac{N_{active}}{N_{expect}} \tag{3.1}$$

Fiducial cut For the central and plug electron, the fiducial volume is defined as the region excluding the following regions:[99]

- In the central calorimeter
  1. Tower 9
  2. Tower 7 of chimney module
  3. Local wedge $\mid X \mid\ > 2.1$ cm from the tower center
- In the end plug calorimeter
  1. Outer 2 η annul
  2. Inner 2 η annul
  3. 5 degrees in ϕ from each quadrant boundary
  4. Dead channels
  5. Runs with more than 30 dead channels.
- In the VTPC

  1. Less than 10 expected hit : If the distance between a road and an octant boundary is closer than 0.035 radian, the wire hits are subtracted from expected hits.)

3.2.2 Electron identification in the central calorimeter

In order to identify electrons in the central calorimeter, the following variables are used:

Lshr The Lshr variable [100] is a χ^2 like lateral shower profile. A central calorimeter tower covers 0.1 in pseudorapidity and 15 degree in azimuthal angle [101]. The lateral shower profile, Lshr, is calculated from energy deposition in three tower segments of a seed tower and the two adjacent towers in η . The definition of Lshr is

$$Lshr \equiv 0.14 \times \sum_k \frac{M_k \times P_k}{\sqrt{0.14^2 \times E + \delta P_k^2}} \tag{3.2}$$

where the sum is over the towers adjacent to the seed tower, P_k is the expected energy in the adjacent tower k, M_k is the measured energy in adjacent tower k, E is electromagnetic energy in the 3 tower segments and δP_k is the error in P which is derived from 1 cm variation in the impact points. P_k has been calculated with the central strip chamber and the event Z vertex.

Good 3 dimensional track At least one 3 dimensional track reconstructed by the central tracking chamber is required. The track must be fitted with curvature to be able to calculate transverse momentum of the particle.

E/P The energy of a central electromagnetic calorimeter and the momentum of a 3 dimensional track pointing to the cluster are compared. The variable E/P is defined as

$$E/P \equiv \frac{E_{EM}}{P_{CTC}} \tag{3.3}$$

where E_{EM} is an energy deposition in the electromagnetic calorimeter and P_{CTC} is the highest track momentum in the cluster. The ratio is calculated from corrected energy and vertex constrained momentum [102].

Lateral shower shape χ^2 with the central strip chamber The χ^2 is calculated as a deviation of a transverse shower profile of the strip chamber signal from an electron shower shape expected from the test beam data [103].

A match between the shower center position and the extrapolated the CTC track position In the central calorimeter, a shower centroid is calculated using the central strip chamber and the CTC track is extrapolated to strip chamber position assuming track momentum measured by the CTC [104].

3.2.3 Electron identification in plug calorimeter

A match between the shower center position and the extrapolated the CTC track position In the plug region, a shower position is calculated with the strip [106] if available. The shower center calculated by the pad information is used if $\eta > 1.5$ (avoid the strip chamber boundary) or $\delta\ \eta > 0.04$ (avoid the dead strip and mislinking η and ϕ strip informations) or $\delta\ \phi > 0.04$ (avoid the dead strip and mislinking η and ϕ strip informations) where $\delta\ \eta$ and $\delta\ \phi$ are the difference between the shower centroid calculated with pad information and that with strip information. CTC tracks are extrapolated to the shower maximum position in the end plug electromagnetic calorimeter (Z = 190 cm). The distance between the shower centroid and the extrapolated the CTC track position is calculated in the unit of cm [105].

A match between the shower center position and the extrapolated the VTPC track position A match between the VTPC track and the shower centroid in the end plug calorimeter is evaluated in the units of $\delta\ \eta$ and $\delta\ \phi$ (radian),

instead of δ R (cm) and $\delta\ \phi$ (cm), because the error of the polar angle measurement with the VTPC is more constant in $\delta\ \eta$ unit than the error in terms of δ R (cm). The momentum resolution in the VTPC pad is almost 30 % for a 1 GeV/c Pt track [109] and the momentum information is not useful in our interested momentum region so that $\delta\ \phi$ has been calculated as a difference in ϕ between the shower center and the VTPC track azimuthal angle at vertex position. The detail matching algorithm are described in appendix C.

Lateral χ^2 3 ×3 The χ^2 is calculated as the deviation of measured lateral shower profile from the expected shower profile of the test beam data. The energy deposition of 3 rows in η and 3 rows in ϕ around shower center are used to calculated this χ^2 [107] [108].

dE/dx of track In order to identify gamma conversions at beam pipe, dE/dx of electron candidates are calculated using the VTPC pad information [110].

3.2.4 Isolation distribution

The isolation variable of electromagnetic clusters are defined as follows.

$$Isol \equiv \frac{Econe(0.4) - Et}{Et} \tag{3.4}$$

where Econe(0.4) means the sum of Et in a cone with a radius of R = $\sqrt{\delta\phi^2 + \delta\eta^2}$ = 0.4 around the electron and Et means the Et of the EM cluster. Here we normalize the isolation value by Et of the electron. In the heavy flavor semileptonic decay, the jet activities around the electron depend on the Pt of the parent b or c quarks, so that we have to normalize these activities by the Pt of parent quarks. Instead of the Pt of the parent quark, the Pt of the decay electron is used to normalize the isolation variable assuming that the Pt of the electron is approximately linear to the Pt of the parent quark. As a result, the isolation variable doesn't depend of electron Pt for

heavy flavor semileptonic decay. This is very important for backgrounds estimation. The details are described at section 3.6.1. On the other hand, for electrons coming from Drell-Yan process, if we assume the underlying events contribution "Econe(0.4) - Et" is common in all mass region, the variable $Isol$ depends on the electron Pt: it tends to be big in low Pt electron, and tends to be small for large Pt electrons. It means the isolation cut efficiency depends on invariant mass value. The estimation of this dependence will be discussed later, but it is small when we set the cut value at 0.1. Then I_{max} is defined as,

$$I_{max} \equiv Max(Isol_1, Isol_2) \tag{3.5}$$

$Isol_1$ and $Isol_2$ are the isolation of the 1st and 2nd electrons.

3.3 Data reduction

In this section, the data samples used for physics analysis are described. In the section 3.3.1, the CDF data summary tape production and its output streams [111] are described. Then in the section 3.3.2, the data set stripped out of the CDF common data summary tapes for this analysis is shown.

3.3.1 The CDF data summary tape production

During the 1988-89 run, the raw data were written on total 5500 reels of nine track tape and they were processed through the version 5.1 CDF offline event reconstruction programs [112]. The data summary tape (DST) production has been done using a Vax 3100 farm and ACP system [113] [114]. About 150 MIPS of processing power was available in these systems.

Overview

The event reconstruction codes were written by more than one hundred collaborators to be able to do physics analysis with fully corrected data. All data flow

between these programs are controlled by YBOS bank [115]. The bank format is determined in "Data Analysis Structure (DAIS)" [116]. At the first stage, the detector oriented analysis has been done, such as reconstructing tracks, converting calorimeter ADC counts into corrected energy value and suppressing several kinds of noise. Then 'the parton reconstruction analysis', such as the reconstruction of an electron, a jet and a muon, has been done using the reconstructed tracks and the cluster of the calorimeter energy deposit (a jet clustering for a jet reconstruction and an electromagnetic energy clustering for an electron-photon identification). Finally the physics oriented DSTs are produced. There are a number of physics oriented output streams such as the electron-photon output stream, the QCD jet output stream, the muon output stream [117], the electroweak output stream [118] [119], the heavy flavor (top and bottom) output stream and the missing Et (Neutrino) output stream [120].

Total 8100 DST's were produced in Version 5.1 production [111]. Full reconstruction needs 240 sec in VAX 780 CPU time per event.

Physics oriented output stream

After reconstructing events, they are separated into several physics oriented output streams. For our study, 'the electron and photon output stream' is used to make a dielectron sample and 'a central muon + a central or plug electron sample in the electroweak output stream' are used to make 'an electron + a muon' sample, so that only these two streams are described here.

The inclusive electron data summary tape production The inclusive electron-photon DST has been produced applying cuts described below. Since the only central and plug electrons are used in this analysis, only the cuts related to the central or plug electrons are described.

The offline Et threshold depend on the trigger. They are

- Calorimeter Et > 5 GeV for the 5GeV-5GeV dielectron trigger (Central)
- Calorimeter Et > 10 GeV for the 12 GeV central electron trigger
- Calorimeter Et > 23 GeV for the 25 GeV end plug photon trigger
- Calorimeter Et > 8 GeV for the 10 GeV-10 GeV diphoton trigger

Then the electron-photon qualities are examined. If they satisfy the following criteria, they are kept in DST as candidates of electron or photon events.

For the central electron,

- The track Pt > 4 (GeV/c) or the track Pt > [(offline calorimeter Et threshold)-1] (GeV/c)
- Number of track > 0
- Had/Em < .125
- χ^2_{strip} < 15
- Lshr < 0.3
- Track-Strip chamber position matching δZ < 5 (Cm)

For the central photon,

- Number of track = 0, if the number of associated track is greater or equal to 1, the track Pt < 4 (GeV/c) and the track Pt < (the offline calorimeter Et threshold)-1) (GeV/c) are required.
- Had/Em < .125
- χ^2_{strip} < 20

- Isolation [2]

$$\sum E_t(R = 0.7) < 15\,(GeV)$$

or

$$\sum E_t(R = 0.4) < 15\,(GeV) \quad \text{and} \quad \text{Lshr} < 0.2$$

And for the plug electron and photon,

- Had/Em < 0.1
- χ^2_{3x3} < 25
- E1/E2 < 0.5

where E1 and E2 are energy deposition in the 1st and 2nd depth segment of the end plug EM calorimeter.

In addition to these single electron/photon cuts, another path is prepared for isolated two EM clusters. If more than one EM cluster satisfied the following cuts, the events are kept in DST.

- An isolated EM cluster: Isol (R=0.7) < 0.25 [3]
- Had/Em < 0.125 for the central calorimeter,
  and Had/Em < 0.1 for the plug calorimeter
- The Et of EM cluster is greater than Et threshold defined as above.

Total 1500 reels of 9 track tapes and 75 reels of 8 mm tapes are produced for an inclusive electron sample. [4]

[2] The sum of the calorimeter Et in each tower with a centroid within a distance of 0.7 in η - ϕ space of the centroid of the EM cluster

[3] Definition of 'Isol' is described at Equation 3.4

[4] One 8mm tape can contain ten 9 track tapes data.

electron + muon data summary tape production In the electroweak output stream, there are three kinds of substream for "The central muon + the central or plug electron". The substreams select the events passing one of the following cut parameter sets [118] [119].

Substream 1 : (The central electron + the central muon)

For the central electron,

- Calorimeter Et > 7 GeV
- Had/Em $< .055 + .00045 \times$ Energy (GeV)
- Lshr < 0.2 or Isol < 0.1
- E/P < 2 or Track Pt > 5 GeV/c
- Strip $\chi^2 < 15$
- Track-Strip chamber position matching $\delta Z < 5$ cm and $\delta\phi < 3$ cm

For the central muon,

- Muon chamber stub
- Track Pt > 5 GeV/c

or the track with minimum ionization in the central calorimeter

- Track Pt > 5 GeV/c
- Calorimeter Et (in the corresponding tower) < 6 GeV
- δR to electron > 0.1 ($\delta R = \sqrt{\delta\eta^2_{e-\mu} + \delta\phi^2_{e-\mu}}$)

Substream 2 :(The plug electron + the central muon)

For the plug electron,

- Calorimeter Et > 10 GeV

- Had/Em $< .055 + .00045 \times$ Energy (GeV)
- Isol < 0.2
- VTPC hit occupancy > 0.5
- $\chi^2_{3\times3} < 15$

For the central muon,

- Muon chamber stub
- Track Pt > 5 GeV/c

Substream 3 :(Central muon) + (Central, Plug or electron)

For the central muon,

- Track Pt > 7 GeV/c
- Track-Muon chamber hit position matching $\delta\phi < 10$ cm

For the central or plug electron,

- Calorimeter Et > 10 GeV
- Had/Em $< .055 + .00045 \times$ Energy (GeV)
- Lshr < 0.2 for CEM and Lateral $\chi^2_{3\times3} < 15$ for PEM

3.3.2 Data sample

From the CDF data summary tapes, dielectron events and electron + muon events are stripped out for our analysis. In this section, the data sample used for our measurements are described.

Dielectron samples (Mini DST)

The dielectron events are stripped out of the CDF electron data summary tapes. A total integrated luminosity of 4.76 pb^{-1} is used for this analysis. In order to make dielectron DST's, the tight cuts are applied to one central electron. The other leg of the pair is required to be either the central electromagnetic cluster associated with a track or an end plug electromagnetic cluster. There are total of 12350 central - central electron pairs (3 nb) and 7280 central - plug electron pairs (1.73 nb). The tight cut efficiency for the central electrons is 75±2 %. In order to reject gamma conversions, a pair invariant mass > 0.5 GeV/c^2 is required, then the 9880 central-central pairs are retained (2.4 nb). When loose cuts are applied to the 2nd electron, the 2900 the central-central pairs and 1320 the central-plug pairs(0.3 nb) are survived. The electron identification efficiency of the second electrons are 94±3 % for central electrons and 92 ± 3 % for the plug electrons. The set of tight and loose cut parameter values are written on Table 3.1. Although electron Et cut is applied at the CDF electron DST production, no additional Et cut is applied for this stage. From this dielectron sample, three kinds of data samples are made: sample 0 (Sample for efficiency studies), sample 1 (Drell Yan sample) and sample 2 (Heavy flavor sample).

Sample 0 (Sample for efficiency studies) This sample was made for studies of the trigger efficiency and the offline electron identification efficiency. No additional cut except for the CDF fiducial volume cuts were applied to the dielectron DST data. Total 10700 central-central electron pairs and 4400 central-plug electron pairs are kept in this sample.

Sample 1 (Drell Yan sample) A sample is made for Z^0 and Drell-Yan measurements. Since the trigger Et threshold is different in the central and plug electromagnetic calorimeters, only the central calorimeter is used for the low mass Drell-Yan

study (Mass < 40 GeV/c^2) and both the plug and central calorimeters are used for the high mass Drell-Yan studies (Mass > 40 GeV/c^2). In order to reduce the backgrounds, at least one good electron is required in the central region and another loose cut electron is required in either the plug or central calorimeters. For the central - central electron pairs, the 5GeV-5GeV dielectron trigger is required. The central 12 GeV single electron trigger is required for the central - plug electron pairs. But the end plug photon trigger is not used for this study. Kinematical and geometrical cuts are defined as follows.

For the central -central pairs,

- Within the CDF Fiducial volume
- Lshr should be calculated
- Strip Chamber (both strip and wire) should have a signal
- VTPC expected hits > 4
- Calorimeter Et of each electron > 6 GeV

For the central- plug electrons, the central electrons should satisfy,

- With in the CDF Fiducial volume
- Lshr should be calculated
- Strip Chamber (both strip and wire) should have a signal
- VTPC expected hits > 4
- Calorimeter Et of electron > 15 GeV

The plug electron are required to be

- Within the CDF Fiducial volume

- VTPC expected hits > 4
- Calorimeter Et of each electron > 6 GeV

Total 2247 central-central electron pairs are kept in this sample and 985 events have its invariant mass greater than 12 GeV/c^2 and 220 events out of 985 are kept after requiring isolation against both electrons. For the central-plug electron pairs, 230 events are kept and 170 events are found in the mass region of 40 GeV/c^2 $< M$ and 130 out of 170 events satisfied isolation cuts.

Sample 2 (Heavy flavor sample) A sample is made for dielectron Pt distribution measurement in the pseudorapidity range $| \eta_e | < 1.0$. Since nonisolated electrons have to be treated, tight cuts are applied to both electrons to reduce the background contamination. For this analysis, only the central calorimeter is used. Kinematical and geometrical cuts are defined as well as the central-central electron pairs of Sample 1, and the 5 GeV - 5 GeV dielectron trigger is required. Since the Pt of electrons from the heavy flavor semileptonic decays are small, track Pt rather than calorimeter Et was used. In addition to these cuts, the invariant mass is required to be larger than 0.5 GeV/c^2 to reject the gamma conversion. After requiring mass > 0.5 GeV/c^2, 1076 events are obtained from total 1354 central-central electron pairs.

The electron + muon sample (Mini DST)

The 'central muon + central or plug electron' events are stripped out of the CDF electroweak data summary tapes adding to the following cuts:

For the central electron

- Good 3 dimensional track
- Had/Em $<$ .055 + .00045 $\times$ Energy (GeV)

- Lshr < 0.2
- The CDF fiducial cut

For the plug electron

- Had/Em $<$ .055 + .00045 $\times$ Energy (GeV)
- Lateral $\chi^2_{3\times3} < 15$

A total integrated luminosity of 3.0 pb^{-1} is used for this analysis. Although Et cut is applied in the CDF electroweak DST production, no additional Et cut is applied at this stage. From this electron + muon sample, the following two data samples are made: sample 3 (Sample for efficiency studies) and sample 4 (Heavy flavor sample)

Sample 3 (Sample for efficiency studies) This sample is made for studies of the trigger efficiency. No additional cut are applied to the electron + muon mini DST data.

Sample 4 (Heavy flavor sample) This sample is made for the study of heavy flavor leptonic decay property. Since electrons do not have isolation requirements, fairly tight cuts are applied to both electron and muon to reduce background contaminations. Only central electron + central muon pairs are kept in this sample.

- Calorimeter Et > 6 GeV
- Had/Em $<$ .055 + .00045 $\times$ Energy (GeV)
- Lshr < 0.2
- 0.6 $<$ E/P $<$ 1.5 or Track Pt > 5 GeV/c
- VTPC hit occupancy > 0.6

For the central muon,

- Track Pt > 6 GeV/c
- Track position matching δ x < 10 cm
- Track slope matching δ dx < 0.1
- Hadron Calorimeter tower energy < 6 GeV
- EM Calorimeter tower energy < 2 GeV

Total 334 electron + muon pairs are kept in this sample.

3.4 Trigger efficiency

The trigger study described here concentrates on two of the electron triggers which are used for Drell-Yan cross section measurement. They are the 12 GeV central electron trigger and the 5 GeV- 5 GeV dielectron trigger [134] [135]. In addition to the level 0 BBC trigger, the 12 GeV central electron trigger is composed of three trigger stages, level 1, level 2 [140] [141] and level 3 triggers [144] [145]. The 5 GeV - 5 GeV dielectron trigger is composed of two stages of hardware triggers, level 1 and level 2, but no level 3 is used. The trigger study has been done using 'the dielectron sample 0' and 'the electron + muon sample 3'.

3.4.1 Level 1 and Level 2 electron triggers

In this section, the product of level 1 and 2 trigger efficiencies are described [136] [137]. For this study, the two of level 2 triggers are used. They are

- A Single electron trigger requiring an energy deposition of Et > 12 GeV in the central electromagnetic calorimeter with a "trigger tower" ($\delta\ \eta = 0.2$, $\delta\ \phi$=15°) and a track of Pt > 6 GeV/c found by the online track processor.

- A dielectron trigger requiring two or more EM clusters each with 5 GeV and a track Pt > 4.8 GeV/c found by the online track processor [138] [139].

And an electron related level 1 triggers are,

- The central tower threshold is set to 6 GeV and total electromagnetic Et is required to be greater than 6 GeV. For this level 1 trigger, the calorimeter summer table 3 is used (for the 12 GeV central single electron trigger).
- The central tower threshold is set to 3 GeV and total electromagnetic Et is required to be greater than 3 GeV. For this level 1 trigger, the calorimeter summer table 0 is used (for the 5 GeV - 5 GeV central dielectron trigger).

The 12 GeV central single electron trigger The 12 GeV central electron trigger was studied using ' an electron + a muon sample 3' and 'the plug electron + central electron sample'. In order to study the efficiency of the central 12 GeV electron trigger, the events triggered by the central muon were selected from this sample and the tight offline electron cuts are applied to the electron candidates, then the electron trigger efficiency is calculated as a function of electron Pt.

The electron trigger efficiency depends on the isolation of electrons. This is partially because the level 2 electron trigger has a Had/Em cut in it and partially because level 2 track momentum measurement also depends on track isolation. The trigger efficiency ϵ is defined as follows,

$$\epsilon \equiv \frac{N_{trigg}}{N_{total}}, \tag{3.6}$$

where N_{trigg} and N_{total} are

- N_{total} : The number of events triggered by the central muon trigger and has an electron candidate which passed offline tight electron identification cut.
- N_{trigg} : The number of events triggered by the central electron trigger in the N_{total} events.

Fig 3.1 shows the central 12 GeV single electron trigger efficiency as a function of electron Pt for nonisolated electrons. Since these events are triggered without calorimeter informations at the level 1 trigger, the measured efficiency is the product of level 1 and level 2 trigger efficiency. These electrons mainly come from heavy flavor leptonic decay, so that this trigger efficiency is used for heavy flavor electron Pt distribution measurement. As shown in Fig 3.1, the trigger is full efficient at the calorimeter Et $>$ 15 GeV. The trigger efficiency of isolated electron [5] with Et $>$ 15 GeV is measured to be 95.0 $\pm$ 4.5 %. The trigger efficiency for the nonisolated electrons (Isolation $>$ 0.1) becomes 92.0 $\pm$ 3.8 % with Et $>$ 15 GeV. The same kinds of analysis has been done using the plug electron + central electron event sample. We selected events triggered by the plug electron in the sample and estimated the central electron trigger efficiency to be 96.2 $\pm$ 0.8 % with Et $>$ 15 GeV for isolated electrons. [6]

The 5GeV-5GeV central dielectron trigger The dielectron trigger efficiency was estimated using the dielectron event sample which is triggered by the 12 GeV central single electron trigger. The efficiencies are calculated separately for the isolated, nonisolated electrons and the electrons coming from J/Ψ decay. When we calculate the nonisolated electron trigger efficiency, the following cuts are applied to dielectron sample 0:

- Both electrons should satisfy offline tight electron cuts
- Dielectron invariant mass $>$ 7 GeV/c^2 (For J/Ψ sample, 2.8 (GeV/c^2) $<$ M $<$ 3.2 (GeV/c^2) is required)
- Triggered by 12 GeV central single electron trigger

On the other hand, for isolated electron trigger efficiency measurement, we demand

[5] I_{max} $<$ 0.1 is required. The definition of I_{max} is equation 3.4 and equation 3.5
[6] I_{max} $>$ 0.1 is required. The definition of I_{max} is equation 3.4 and equation 3.5

- one tight cut electron and one loose cut electron
- Invariant mass $>$ 7 GeV
- Triggered by 12 GeV central electron trigger
- Both electron isolation should be less than 0.1 [7]

This is because an isolation requirement reduces the non-electron backgrounds significantly, so that the loose electron cuts instead of tight electron cuts are applied for the trigger study of isolated electrons. Fig 3.2 shows the Et dependence of the 5 GeV electron trigger efficiency for isolated and nonisolated electrons and J/Ψ decay electrons. [8] For isolated electron, the efficiency was measured to be 93.3 $\pm$ 2.1 % at Et $>$ 6 GeV.

The 5 GeV electron trigger efficiency is also studied with "a central electron + a central muon" sample. The method is the same as that of the 12 GeV electron trigger study. First, the events triggered by the central muon are selected. Then the number of events which satisfied "5 GeV central electron + 3 GeV central muon trigger (ELECTRON_EMC_5_CMU_3)" are counted. Fig 3.3 shows the trigger efficiency as a function of the electron Pt. For this plot, no isolation cut is applied. When an isolation cut is applied, the efficiency becomes 97.5 $\pm$ 2.5 % for electrons with Et above 6 GeV. The 5 GeV electron trigger efficiency measured with the electron + muon sample is the product of level 1 and level 2 trigger efficiency. On the other hand, the 5 GeV electron trigger efficiency measured with the dielectron sample includes the efficiency of level 2 trigger only. Because we demand level 2 central 12 GeV electron trigger which should satisfy level 1 electron trigger. But these efficiency is consistent within the error, so that we assumed the level 1 trigger efficiency is 100 % and combined the results from "an electron + a muon data" and

[7] The definition of isolation variable is written in Section 3.6.1
[8] Since the electron trigger tower size is $\delta\eta = .2$, $\delta\phi$=15°, high Pt J/Ψ 's are not always recognized as two separate EM clusters.

"dielectron data" trigger efficiency study to calculate final 5 GeV trigger efficiency. The efficiency is defined as follows,

$$\epsilon \equiv \frac{(N1_{trigg} + N2_{trigg})}{(N1_{total} + N2_{total})} \tag{3.7}$$

where $N1_{trigg}, N1_{total}, N2_{trigg}$ and $N2_{total}$ are

- $N1_{total}$:The number of events which were triggered by the central muon trigger and had an electron candidate satisfying the offline tight electron identification cuts (the electron + muon sample 3).
- $N1_{trigg}$:The number of events triggered by the 5 GeV central electron + 3 GeV central muon trigger in the $N1_{total}$ events (the electron + muon sample 3).
- $N2_{total}$:The number of events which were triggered by the central 12 GeV electron trigger and had another electron candidate. (The loose cut is applied for the isolated electron study and the tight cut is applied for the nonisolated electron trigger efficiency study.) (the dielectron sample 0)
- $N2_{trigg}$:The number of events triggered by the central dielectron trigger in the $N2_{total}$ events (the dielectron sample 0).

Finally the combined efficiency is measured to be 94.3 ± 1.7 %. This is the efficiency of the 5 GeV electron trigger, so that the efficiency of the dielectron trigger is square of this efficiency.

Next the opening angle dependence of the trigger efficiency is studied. Because of the size of the trigger tower, level 2 trigger is inefficient for electron pairs with a small opening angle. The study has been done using the following sample:

- Both electrons should pass the tight cut
- The dielectron invariant mass > 0.5 GeV/c^2

- The central 12 GeV trigger should be satisfied
- Electron Et (calorimeter) > 6 GeV

The Level 2 dielectron trigger efficiency is plotted as a function of opening angle in Fig 3.4. The inefficiencies of level 2 trigger are seen in the small opening angle pairs. These inefficiencies will be corrected to measure the electron Pt distribution from heavy flavor cascade decay.

3.4.2 Level 3 electron triggers

There are also several types of level 3 trigger [135]. For our study, " Single electron 12 GeV trigger in the central plastic scintillator " has been used [142] [143]. The level 3 electron trigger performs the following items:

- Clean up serval kinds of calorimeter noise [129] [130] [131], [127] [128] [124] [125] [126]
- Recalculates Had/Em and makes a cut Had/Em < 0.125
- Calculates Lshr and makes a cut of Lshr < 0.5 (This Lshr variable is level 3 version Lshr which is different from that of the offline analysis.)
- Calculates the CTC track transverse momentum with level 3 code and requires Pt > 6 GeV/c

The efficiency of level 3 electron trigger has been measured from electron + muon sample 3. For this sample, we demand the following additional requirements.

- Level 2 central electron 12 GeV trigger is satisfied
- Level 2 central muon trigger is satisfied for electron + muon sample.
- Offline tight electron cuts are applied.

All events in this sample satisfy level 1 and level 2 electron trigger so that the only level 3 trigger efficiency can be extracted. And by requiring muon trigger, these events can be kept independent of level 3 electron trigger. In order to reject fake electrons, tight electron cuts are applied.

When we measure physics quantities, the electron efficiencies are calculated as

$$\epsilon \equiv \epsilon_{L2} \times \epsilon_{L3} \times \epsilon_{of} \tag{3.8}$$

- ϵ_{L2} : Level 2 trigger efficiency × Level 1 trigger efficiency
- ϵ_{L3} : Level 3 trigger efficiency
- ϵ_{Of} : Offline electron tight cut efficiency

Since both offline electron identification and Level 3 trigger require that Lshr cut [9], in the case that a real electron has Lshr greater than 0.2 in the offline calculation, and greater than 0.5 in level 3, that is treated as offline electron identification inefficiency, but is not taken as that of level 3. The inefficiency of level 3 is taken, if offline Lshr cut is satisfied, but it is not satisfied at level 3. The trigger efficiency has been measured for only isolated electrons. The efficiency is 98 ± 2 % for the central isolated electrons with Et larger than 15 GeV. [10]

3.5 Electron identification efficiency

The electron identification efficiencies for low and high momentum electrons have been studied with two kinds of methods. One method (Method 1) calculates the efficiency from second electron of J/Ψ and Z^0 and the other method (Method 2) calculates it by counting the difference between the number of opposite and same sign pairs. The studies have been done using the dielectron sample 0.

[9]Level 3 required that level 3 version Lshr < 0.5, and offline electron identification demands that offline version Lshr < 0.2.

[10]For the nonisolated electron study, only the dielectron trigger is used.

3.5.1 Electron cut value optimization

The applied cut values are determined by looking at the distribution of each cut parameter of the pure electron sample. Fig 3.5 shows the distribution of each cut parameter of the 2nd electron for four different electron samples, Z^0, J/Ψ , isolated J/Ψ and nonisolated J/Ψ. In order to get pure electron samples, all other cuts which seem to be independent of the studied cut are applied. Table 3.2 shows which cuts are applied to investigate the distribution of each cut parameter of pure electrons. As same as the central electron, the plug electron identification cut values are determined by electrons of the central-plug Z^0 events in the Sample 0. Fig 3.6 shows distribution of each parameter.

3.5.2 Electron cut efficiency study (Method 1)

The electron cut efficiencies of low and high momentum electrons have been studied with decay electrons from J/Ψ and Z^0. Since each cut efficiency depends on the isolation, it has been studied with and without the isolation cut. To make the J/Ψ sample, a set of tight electron cuts is required on a central electron, then another EM cluster is required in the central region. For the Z^0 sample, one tight cut central electron and another EM cluster in the central or plug calorimeters have been required. The events whose electron pair invariant mass is between 2.8 and 3.2 GeV are defined as J/Ψ candidates and between 75 and 105 GeV are defined as Z^0 candidates. J/Ψ mass is calculated using track momentum measured by the CTC and the Z^0 mass is calculated using energy deposit in the calorimeter. The efficiency of each cut has been calculated from the distribution of the second electron of these J/Ψ and Z^0 candidates. Fig 3.7 shows the dielectron mass distribution around the J/Ψ peak after applying each cut to the 2nd electrons. The numbers of signal events and background events in the J/Ψ mass region are estimated by interpolating the continuum. A tight and a loose cut are used to measure Drell-Yan cross section.

For the central electrons, we define the tight cut parameter set as

- $Had/Em < 0.055 + 0.00045 \times Energy(GeV)$
- Lateral shower shape (Lshr) < 0.2
- VTPC hit occupancy > 0.2
- CTC track - cluster matching
  $\delta Z < 3\ cm$
  $\delta X < 1.5\ cm$
- $\chi^2_{strip} < 10$
- $E/P < 1.5$
- The CDF fiducial volume cut
- CTC track

and loose parameter set as

- Had/Em $Had/Em < 0.055 + 0.00045 \times Energy(GeV)$
- Lateral shower shape (Lshr) < 0.2
- VTPC hit occupancy > 0.2
- The CDF fiducial volume cut
- CTC track

The efficiency of each cut is also investigated. Table 3.3 shows cut efficiencies of each cut parameter. Figs 3.7 and 3.8 show invariant mass distributions around J/Ψ mass satisfying and not satisfying the cut described below. The detail of cut efficiency calculation is written in the appendix B. The tight cut efficiency is measured at first, then the efficiency of each cut parameter is measured using it. Since the decay electrons of Z^0 are isolated well, the nonisolated electron efficiency has been measured only using J/Ψ decay electrons.

The tight cut efficiency is 85.7 ± 6.0 %, and the loose cut efficiency is 96.3 ± 3.0 % for the central isolated electrons in the J/Ψ sample. For the central electrons in Z^0 sample, the tight cut efficiency is 77.0 ± 4.6 %, and the loose cut efficiency is 91.6 ± 3.0 %.

For the plug electrons, only one cut parameter set is defined:

- Had/Em
  $Had/Em < 0.055 + 0.00045 \times Energy(GeV)$
- VTPC track matching
  $\delta\eta < 0.06$
- Lateral shower shape
  $\chi^2_{3\times3} < 10$
- The CDF fiducial volume cut

The efficiency of the isolated electron is estimated to be 91.2 ± 3.0 % from Z^0 sample. In order to obtain the lateral shower $\chi^2_{3\times3}$ cut efficiency and Had/Em cut efficiency, a good VTPC track is required. On the other hand, to get the

VTPC track reconstruction efficiency, the Had/Em and $\chi^2_{3\times3}$ cuts are applied. The efficiency of each cut parameter is listed in Table 3.4.

3.5.3 Electron cut efficiency study (Method 2)

The Pt dependence and the isolation dependence of electron cut efficiency are studied more.

The cut efficiency Pt dependence In order to obtain the cut efficiency Pt dependence, the study started from these assumptions.

- The number of fake electron backgrounds in same sign pairs are the same as in opposite sign pairs, so that the difference between opposite sign pairs and same sign pairs come from real electron pairs.

The cut efficiency has been calculated counting N_{diff} before and after applying a cut.

$$N_{diff} \equiv N_{opp} - N_{same} \tag{3.9}$$

where N_{opp} is the number of opposite sign pairs and $N_{same}$is the number of same sign pairs.

Fig 3.9 shows the isolated electron pair cut efficiency as a function of dielectron invariant mass. This method works well only when the number of real electron pairs are dominated against backgrounds, so that the Pt dependence are calculated with isolated electron pairs first and isolation dependence are estimated at J/Ψ mass region. The cut efficiencies do not depend on the electron Pt so much. Only E/P cut efficiency becomes worse in the Z^0 mass region because of the effect of radiative photon from decay electrons.

The cut efficiency isolation dependence The isolation dependence of cut efficiency is calculated using J/Ψ sample. The same method is applied to the

dielectron pairs with the invariant mass between 2.8 and 3.2 GeV. Fig 3.10 shows the isolation dependence of several electron cuts.

3.6 Backgrounds estimation

3.6.1 Backgrounds for Drell-Yan electron pairs

In this section, the background contaminations from the heavy flavor semileptonic decay and fake electrons from QCD jet in the isolated electron pairs are described. Then the backgrounds from $Z \rightarrow \tau\tau \rightarrow ee$ process will be discussed.

Overview

There are mainly two kinds of backgrounds for our study. One comes from QCD jets. They are fake electrons or electrons coming from nonprimary vertex, i.e. the charged $\pi^{\pm}$ and π^0 overlapping, the interacting π and the gamma conversion. In order to reject charged $\pi^{\pm}$ and π^0 overlapping, E/P, Lshr, χ^2_{strip} and a match between track and electromagnetic cluster centroid cuts are required for the central electrons. The $\chi^2_{3\times3}$ and the VTPC track matching cuts are required for the plug electron identification. For rejection of interacting π, the Had/Em and χ^2_{strip} cuts are used for the central electron identification and only the Had/Em cut are used for that of the plug electrons. In order to reject gamma conversions outside of the VTPC, the VTPC hit occupancy cut is applied.

Other backgrounds come from the following physics processes:

- semi-leptonic decay of heavy flavor quarks (b, c quark)
- $Z \rightarrow \tau\tau \rightarrow ee$.

Except for $Z \rightarrow \tau\tau \rightarrow ee$ [147], these backgrounds are produced in jets [148], so that the isolation of electron candidates in the background events must be worse than that of Drell-Yan electrons. The background contamination is estimated from

the isolation distribution. The dielectron data sample 1 is used to obtain Drell-Yan production cross section. Since we are going to demand two isolated electrons ($I_{max} < 0.1$) to calculate Drell-Yan cross section, the next section describes the background estimation in the sample of two isolated electrons.

Backgrounds estimation for the central-central electron pairs

The background estimation has been done for the central-central Drell-Yan electron pair measurements. It was estimated from I_{max} distribution. Especially, the background estimation is important in the invariant mass below 30 GeV/c^2 region, because backgrounds from QCD jets and heavy flavor semileptonic decays become large. Main systematic error comes from the uncertainty of this background estimation. Fig 3.11 shows the I_{max} distribution of opposite sign pairs. A tight cut central electron and another loose cut central electron are required for these pairs. [11]

The number of background events is estimated assuming "the shape of the isolation distribution of backgrounds in the opposite sign pairs is equal to that of same sign pairs". In order to check whether this assumption is correct, the isolation distribution of electron + muon events whose lepton candidates coming from heavy flavor semileptonic decay or QCD jet, has been looked at. Let's discuss these backgrounds separately. It must be a reasonable assumption that the number of the fake electron backgrounds is the same in the opposite pairs as in the same sign pairs. The question is:

[11] Fig 3.12A shows the I_{max} distribution for electron pairs with one tight and one loose cut electron. Fig 3.12B shows the I_{max} distribution for two tight cut electron pairs. And Fig 3.12C shows [(Fig 3.12A) - (Fig 3.12B)]. According to the UA1 paper [193], the ratio of opposite sign pairs and same sign pairs from heavy flavor decay is 5.5:1, so that Fig 3.12A still contains a lot of background in $I_{max} > .3$, because the number of opposite/same sign pairs are same in this region, however the number of same sign pairs drops rapidly for isolated electrons relative to opposite sign pairs. Fig 3.12C means, even though tight cuts are applied to both electrons, the background rejection does not change a lot, but a lot of the signal is lost. The 'Tight cut + loose cut' combination is thus used for the isolated electron study (Drell-Yan study) and 'Two tight cuts' are applied for the nonisolated electron study (heavy flavor study).

whether the isolation distribution of the heavy flavor decay electrons is the same in the opposite as in the same charge pairs ? Because the physics process is different, the same sign pairs come from cascade decay, while the opposite sign pairs come from direct semileptonic decay from $b\bar{b}$, $c\bar{c}$.

In order to look at the isolation distribution of leptons from heavy flavor decay only, tight cuts are applied to the both leptons. Fig 3.13 shows the isolation distribution of leptons in the electron + muon sample compared with the tight cut electron pair sample. Fig 3.14 also shows the distribution from the $b\bar{b}$ ISAJET Monte Carlo generator [146] [149].

The big differences can not be seen in the isolation distribution between the opposite and same sign pairs so that it indicates that our assumption is reasonable. The number of backgrounds in Drell-Yan sample is estimated as follows,

$$N_{o1} = DY1 + BK1 \tag{3.10}$$

$$N_{o2} = DY2 + BK2 \tag{3.11}$$

$$R1 = \frac{BK2}{BK1} \leftarrow \frac{N_{s2}}{N_{s1}} \tag{3.12}$$

$$R2 = \frac{DY2}{DY1} \tag{3.13}$$

where

- N_{s1}: The number of the same sign pairs in $I_{max} < 0.1$
- N_{s2}: The number of the same sign pairs in $0.1 < I_{max} < 0.5$
- N_{o1}: The number of the opposite sign pairs in $I_{max} < 0.1$
- N_{o2}: The number of the opposite sign pairs in $0.1 < I_{max} < 0.5$
- $DY1$: The number of the Drell-Yan pairs in $I_{max} < 0.1$

- $DY2$: The number of the Drell-Yan pairs in $0.1 < I_{max} < 0.5$
- $BK1$: The number of the background pairs in $I_{max} < 0.1$
- $BK2$: The number of the background pairs in $0.1 < I_{max} < 0.5$

The $N_{o1} and N_{o2}$ can be measured from real data directly, so that DY1, DY2, BK1, BK2 can be calculated easily, if we know the value R1 and R2.

$$DY1 = \frac{1}{R1 - R2} \times (R1 \cdot N_{o1} - N_{o2}) \tag{3.14}$$

$$BK1 = \frac{1}{R1 - R2} \times (-R2 \cdot N_{o1} + N_{o2}) \tag{3.15}$$

$$DY2 = \frac{R2}{R1 - R2} \times (R1 \cdot N_{o1} - N_{o2}) \tag{3.16}$$

$$BK1 = \frac{R1}{R1 - R2} \times (-R2 \cdot N_{o1} + N_{o2}) \tag{3.17}$$

As discussed at section 3.2.4, for electrons from heavy flavor semileptonic decay, the isolation variable dose not depend on the electron Et, because we normalized it by the electron Et. In order to measure parameter R1, the same sign pairs whose invariant mass is greater than 12 GeV are used. Fig 3.15 shows I_{max} distribution of same sign pairs. R1 has been measured to be 32.25 ± 16.7.

Basically R2 is measured using both "real data" and

" Drell-Yan Monte Carlo (ISAJET) + The CDF detector simulation". We assume that underlying event activities are same in Z^0 events and low mass Drell-Yan events (12 GeV/c^2 $< M <$ 75 GeV/c^2). The R1 has been measured at Z^0 mass region (75 GeV/c^2 $< M <$ 105 GeV/c^2) using data, then it has been extrapolated into below Z^0 mass region with Monte Carlo simulation. The R1 is roughly 100 times bigger than the R2. Table 3.5 shows the background estimation of each mass region for $\frac{d\sigma}{dm}$ measurement and Table 3.7 shows that of $\frac{d^2\sigma}{dmdy}|_{Y=0}$ measurement. Fig 3.16 shows the isolation distribution of Drell-Yan electrons in the simulated data for each mass region.

In order to reject backgrounds, the isolation cut (Isolation < 0.1) is applied on both electrons for Drell-Yan measurements. The invariant mass dependence of isolation cut efficiency is estimated from this simulation data (Fig 3.17B). Fig 3.17A shows the invariant mass dependence of the backgrounds contamination.

Backgrounds estimation for central-plug electron pairs

The central-plug electron pairs are used to measure Drell-Yan process whose invariant mass is greater than 40 GeV/c^2 where the backgrounds are much smaller than that of below 30 GeV/c^2. The background estimation for the central-plug pairs has been done using I_{max} distribution as well as the central-central electron pairs. Since I_{max} is defined as the maximum isolation value of two electrons, the isolation variable should be defined as the plug and central electrons have similar isolation distribution. At first, the plug electron isolation is compared with that of central electrons. We demands one good electron in the central region and another loose cut electron in the central or plug electromagnetic calorimeter. Fig 3.18 shows the isolation distribution of the 2nd electron in the central or plug calorimeter in Z^0 mass region (75 GeV/c^2 $< M <$ 105 GeV/c^2). Since we can not measure the charge of plug electrons, these distribution contain both same and opposite sign pairs. From the isolation distribution of the 1st central electron, the number of background events in the central-plug electron sample are estimated. After subtracting these backgrounds, ϵ is defined as,

$$\epsilon \equiv \frac{N_{0.1 < Isol < 0.5}}{N_{Isol < 0.1}}$$

The ϵ of the plug electron is compared with that of the central electron. For the central electron, the ϵ is determined to be $\epsilon = 0.044 \pm 0.019$ and for the plug electron $\epsilon = 0.061 \pm 0.022$. These are consistent within an error so that we concluded the isolation distribution shows the same behavior in the plug as in the central region.

The I_{max} variable in the central-plug pair is defined as same as the central-central

pair. Figs 3.19 show the I_{max} distribution at 40 GeV/c^2 < M < 75 GeV/c^2 and 75 GeV/c^2 < M < 105 GeV/c^2. The expected number of backgrounds is tabulated in Table 3.6. In order to calculate the backgrounds, the shape of the isolation distribution of the backgrounds are assumed to be the same as that of the central-central same sign pairs, so that same R1 and R2 values are used.

Backgrounds from $Z^0 \rightarrow \tau\tau \rightarrow ee$

In order to estimate the $Z \rightarrow \tau\tau \rightarrow ee$ background contamination, the ISAJET Monte Carlo and the CDF detector simulation have been used. A total of 28.3 pb^{-1} is simulated and the expected number of backgrounds are subtracted from the data. Table 3.8 shows the number of estimated $Z \rightarrow \tau\tau \rightarrow ee$ events in each mass bin.

Backgrounds from J/Ψ and Υ

The measurements of isolated electron pairs have been done for the pairs whose invariant mass is greater than 12 GeV/c^2, so that J/Ψ and Υ are not the background anymore.

3.6.2 Backgrounds for heavy flavor semileptonic decay electron pairs

Overview

The backgrounds for the heavy flavor semileptonic decay are discussed in this section. The backgrounds come from

- Fake electrons
- Dielectron production in Drell-Yan process
- J/Ψ , Υ
- $Z \rightarrow \tau\tau \rightarrow ee$.

Since both fake electron backgrounds and heavy flavor decay electron are not isolated, the isolation distribution can not be used to distinguish them, so that the non-electron backgrounds are estimated using other methods. The dielectron data sample 2 is used to measure dielectron transverse momentum distribution. In order to measure the Pt distribution of heavy flavor decay electrons, we demand that both electrons should have bad isolation, i.e. Iso_{max} > 0.1 to reject Drell-Yan dielectron production. The backgrounds estimation in this final sample is described below.

non-electron backgrounds

The background contamination has been studied with the E/P distribution of electrons. The E/P distribution is divided into 2 part; REGION1 : (0.8 < E/P < 1.2) and REGION2 : (E/P < 0.8 or 1.2 < E/P < 1.5). REGION 1 is the signal dominated region and REGION 2 is the background dominated region. The following parameters are defined:

- S1: The number of real electrons in REGION 1.
- S2: The number of real electrons in REGION 2.
- B1: The number of fake electrons in REGION 1.
- B2: The number of fake electrons in REGION 2.
- O1: The number of observed electrons in REGION 1.
- O2: The number of observed electrons in REGION 2.

$$O1 = S1 + B1 \tag{3.18}$$

$$O2 = S2 + B2 = \alpha \times S1 + \beta \times B1 \tag{3.19}$$

where

$$\alpha = \frac{S2}{S1} \tag{3.20}$$

$$\beta = \frac{B2}{B1} \tag{3.21}$$

so that S1 and B1 can be calculated from observed O1, O2 if we know α and β.

$$\begin{pmatrix} S1 \\ B1 \end{pmatrix} = \frac{1}{\beta - \alpha} \begin{pmatrix} \beta & -1 \\ -\alpha & 1 \end{pmatrix} \begin{pmatrix} O1 \\ O2 \end{pmatrix} \tag{3.22}$$

The parameters α and β are calculated from real electron pair sample and fake electron sample respectively.

The parameter "α" measurement The parameter "α" is determined by two methods. One method uses the nonisolated J/Ψ sample and another uses opposite sign pairs and same sign pairs (Ref. section 3.5.3). In order to make J/Ψ sample, tight cuts are applied to both electrons, so that total 165 opposite sign pairs and 3 same sign pairs are left. Assuming the number of backgrounds in the opposite sign pair is equal to that of same sign pairs, the background contamination is estimated to be 1.8 %. From this sample, the parameter "α" is determined to be 0.056 $\pm$ 0.011.

This parameter "α" was also calculated by another method. We obtained the E/P distribution of real electron by subtracting the E/P distribution of the same sign pairs from that of opposite sign pairs. To make the opposite and same sign pair samples, tight cuts are applied to both electrons. From this methods, the parameter "α" is determined to be 0.062 $\pm$ 0.012. The parameter "α" measured by two independent methods is consistent within a error. Fig 3.20 and Fig 3.21 show the E/P distribution of J/Ψ and N_{diff} sample. Since Et of electrons are required to be greater than 6 GeV and the track momentum is required to be greater than 4 GeV/c, no bias is caused by offline cuts in the E/P distribution in the region E/P $<$ 1.5.

The parameter "β" measurement To get the E/P distribution of non-electron backgrounds, Lshr $>$ 0.2 is applied to the 2nd electrons. At that time, we assumed the E/P distribution is independent of Lshr variable.

The parameter "β" depends on the source of backgrounds. If the interactive pion is dominant, the value "β" should be close to the value "α". On the other hand, if the π^0, $\pi^\pm$ overlapping is dominant, the "β" should be much smaller than "α". To get same backgrounds in our data sample for the inclusive electron Pt measurement, same kinematical cuts are applied, and the parameter "β" is calculated from the E/P distribution of the sample. It was measured to be 1.38 $\pm$ 0.087 which is 22.5 times bigger than the "α" of real electron sample.

Backgrounds estimation check In order to check whether this method works, the number of backgrounds in J/Ψ sample which was made requiring one tight and one loose cut electrons, is estimated by this method. One tight and one loose cut are applied in order to contain some backgrounds. After applying these cuts, 109 opposite sign pairs and 11 same sign pairs were left. We assumed 11 out of 109 came from non-electron backgrounds, then the number of backgrounds are estimated from the E/P distribution for the 1st and 2nd electrons respectively. The 1st electrons were estimated to contain no backgrounds and the 2nd electrons were estimated to have 12.3 $\pm$ 3.3 backgrounds. This backgrounds estimation is consistent with the number of same sign pairs.

Backgrounds estimation in the nonisolated pairs The number of backgrounds in the nonisolated pairs is estimated with this method to calculate the electron Pt distribution from heavy flavor decay. For opposite sign pairs, it is estimated that 14 % of electrons come from non-electron backgrounds, so that 26 % (1-0.86^2 = .26) of pairs have at least one non-electron. On the other hand, it was estimated that the same sign pairs contained 31 % of non-electron backgrounds, so

that 53 % of the pairs are treated as backgrounds. The number of backgrounds for the same and opposite sign pairs are consistent with each other. Further more the backgrounds contamination are estimated for cascade decay sample ($\delta\phi < \pi/2$) and direct decay from b's ($\delta\phi > \pi/2$). The background contaminations are estimated to be 6.1 % for cascade decay sample and 14.5 % for direct decay sample.

Other backgrounds

When we measure the Pt distribution of the heavy flavor decay electrons, J/Ψ , Υ have been subtracted using invariant mass of dielectrons. [12] Another background comes from Drell-Yan process. The Drell-Yan contamination has been estimated using both the CDF data and the Monte Carlo generator. The detail description is written in the section 3.2.4.

[12]The invariant mass 2.8 > M > 3.2 for J/Ψ and 9 > M > 12 for Υ events are subtracted

Chapter 4

Results and discussions

4.1 Drell-Yan and Z Production

In this chapter, the discussion points are focused on Z^0 and Drell-Yan production mechanism [1]. The outline of the analysis is as follows: The measured physics quantities are differential cross sections $\frac{d\sigma}{dM}$ and $\frac{d\sigma^2}{dMdY}$ of Drell-Yan electron pair production process. The final goal is the determination of K factor and the study of parton distribution function behavior at small x region (0.0067-0.017).

The production cross section measurement will be discussed first. A comparison is made of the result with theoretical predictions calculated using several parton distribution functions. The cross section can be written by the following formula in classical parton model [194][195][196]:

$$\frac{d\sigma^2}{dMdY} = \frac{8K\pi\alpha^2}{9Ms}\Sigma_i[Q_i^2(q_{p_i}(x_1)\cdot\bar{q}_{\bar{p}_i}(x_2) + \bar{q}_{p_i}(x_1)\cdot q_{\bar{p}_i}(x_2))]$$

As shown in above formula, the production cross section depends both on the K factor and the parton distribution functions, so that the discussion will be done from two points of view. First we assumed

> " The parton distribution function is correct, or is measured by another measurement, such as other deep inelastic experiment". Then we discuss whether the QCD higher order correction is a good approximation or not [44][204][205].

The second discussion starts from the assumption,

> The QCD perturbative calculation is good enough [206] [207] to explain the discrepancies between the lowest order Drell-Yan cross section calculation and the measured cross section [42][208] [209]. Then we looked at which parton distribution function reproduces the data best.

Since predictions for many important processes at hadron collider depend on reliable determination of parton distributions, these measurement take a very important role in the CDF experiment. Next, the properties of Drell-Yan dielectron production will be discussed [203]. First, the Pt distribution of the Z^0 or virtual photon and second, the electron Pt distribution in the center of mass system, third the Z^0 and virtual photon rapidity distribution and last, the electron angular distribution in the center of mass system will be discussed. The comparison of Drell-Yan and heavy flavor dielectron production properties will be touched at the next section

" B production [178][179][180] as backgrounds of Drell-Yan ".

4.1.1 Cross section measurement

Drell-Yan electron pair production cross section has been measured with the dielectron sample 1 adding $I_{max} < 0.1$ requirement. The kinematical acceptance, geometrical acceptance and CTC track reconstruction efficiency were estimated using the ISAJET Monte Carlo and the CDF detector simulation. A total of 30 pb^{-1} Drell-Yan events were simulated in order to estimate the acceptances for several measurements. Fig 4.1 and Fig 4.2 show the geometrical + kinematical acceptance for the differential cross section measurement $\frac{d\sigma}{dM}$ and $\frac{d^2\sigma}{dMdY}|_{Y=0}$. In order to measure the cross section $\frac{d^2\sigma}{dMdY}|_{Y=0}$, pairs in $-0.75 < Y < 0.75$ are used, where Y is the rapidity of virtual photon. In order to calculate the Drell-Yan cross section, the following corrections were applied.

- Electron offline cut efficiency

- Geometrical acceptance
- Level 1, Level 2 and Level 3 trigger efficiency (Pt dependent)
- Kinematical cut efficiency (Pt threshold and isolation)
- Backgrounds subtraction
- Calorimeter energy smearing
- QCD correction for geometrical acceptance calculation.

The calorimeter energy smearing effect has been estimated with the CDF detector simulation. Fig 4.3 shows the invariant mass distribution calculated from the event generation level kinematical variables and the simulated detector energy values.

The rapidity distribution of virtual photon Y has been calculated including QCD diagram up to the 1st order of α_s. The correction of the geometrical acceptance coming from this ambiguity was added only for the $\frac{d\sigma}{dM}$ measurement. Basically the geometrical acceptance was estimated with generated events using the EHLQ parton distribution function and " the lowest order Drell-Yan diagram + initial quark's gluon bremsstrahlung ".

Fig 4.4 shows the rapidity distribution of the virtual photon in generated events. Fig 4.5 shows the theoretical calculation of the rapidity distribution including only the lowest order and including up to the 1st order α_s diagram [152][151][210]. The correction factor

$$Cor \equiv \frac{ACC_{lowest}}{ACC_{1st}}$$

is plotted against invariant mass in Fig 4.6, where ACC_{lowest} is an acceptance calculated with the lowest order and ACC_{1st} is an acceptance calculated with the 1st order correction.

The differential cross sections $\frac{d\sigma}{dM}$ and $\frac{d^2\sigma}{dMdY}\ |_{Y=0}$ are measured respectively. For the $\frac{d\sigma}{dM}$ measurement, in order to check the consistency between the central

-central pair cross section and the central - plug pair cross section, it was measured individually at first. Fig 4.7 shows the Drell-Yan differential cross section which is calculated using only the central-central or the central-plug electron pairs. The two cross sections are consistent within the error, so that both data sets were combined. [1]

Fig 4.8 shows the differential cross section $\frac{d\sigma}{dM}$ with some theoretical calculations which include the QCD correction up to the 2nd order of α_s . Table 4.1 shows the differential cross section and the systematic and statistics errors in each mass region. In order to calculate the Z^0 cross section, the differential cross section was integrated from 75 GeV/c^2 to 105 GeV/c^2 [185][186].

The cross section of the Z^0 is

$$\sigma = 205.5 \pm 13.8 \text{ (sta)} \pm 16.0 \text{ (sys)} \pm 15.4 \text{ (lum)}$$

Fig 4.9 shows the minimum and maximum cross sections obtained by trying different parton distribution functions. The parton distribution functions used to calculate the Drell-Yan production cross sections are EHLQ set 1, EHLQ set 2 [169], Duke-Owens set 1, Duke Owens set 2 [170], DLFM set 1, DLFM set 2, DLFM set 3 [173], HMRSE, HMRSB [171][172].

In the 12 GeV/c^2 < M < 30 GeV/c^2 region, HMRSE gives minimum cross section and DLFM3 gives maximum cross section. The measured cross section is middle of these predictions. Fig 4.10 shows the QCD correction, for example compton or annihilation diagrams, to the Drell-Yan calculation [150]. After adding QCD correction to Drell-Yan cross section calculation, the theoretical prediction closed to the data. The detail discussion will be done in the next section.

Fig 4.11 shows $\frac{d^2\sigma}{dMdY}\ |_{Y=0}$ with some theoretical calculations (the lowest order calculation) [151][152][210]. In this plot, especially the cross section 12 GeV/c^2 < M < 30GeV/c^2 is important. In this region, the cross section is measured using

[1] Fig 4.7 dose not include energy smearing correction.

$-0.75 < Y < 0.75$, where Y is the rapidity of virtual gamma. And the distribution of Y is assumed to be flat in $-0.75 < Y < 0.75$. This assumption is reasonable from both theoretical point of view and experimental result. Fig 4.35 shows the measured parent virtual photon rapidity Y distribution with theoretical prediction in the mass region 15 GeV/c^2 < M < 40GeV/c^2. For above 40 GeV/c^2 invariant mass pairs, the correction was added using theoretical calculation including up to the 1st order QCD diagram. The difference between the mean cross section in $-0.75 < Y < 0.75$ and $\frac{d^2\sigma}{dMdY}\ |_{Y=0}$ is 0.4 - 3 %. Table 4.2 shows the correction factor in each mass region.

Fig 4.12 shows the CDF measurement $M^3\frac{d^2\sigma}{dMdY}\ |_{Y=0}$ in comparison with UA1 data and first-order theoretical predictions [151][190][193]. Table 4.3 shows the cross section and systematic and statistics error in each mass region. The theoretical prediction is consistent with the measured cross section within the error. In order to calculate $M^3\frac{d^2\sigma}{dMdY}\ |_{Y=0}$ from $\frac{d^2\sigma}{dMdY}\ |_{Y=0}$ for each mass bin, the following corrections are added.

- The value M was taken the middle of each mass bin.
- Calculate differential cross section in the lowest order diagram, then calculate the cross section weighted mean mass value M.
- The correction factor ϵ is defined by

$$\epsilon \equiv (\frac{d\sigma}{dMdY}, Y = 0, M = m)/(\frac{d\sigma}{dMdY}, Y = 0, M = m')$$

- Then multiply ϵ to the measured cross section.

4.1.2 Scaling

The scaling has been also observed and compared with several previous measurements in pp (rather than $p\bar{p}$) collisions. The cross section $M^3\frac{d^2\sigma}{dMdY}\ |_{Y=0}$ is plotted

as a function of the scaling variable [34][189] $\sqrt{\tau} = M_{ee}/\sqrt{s}$ in Fig 4.13. Compared with the previous experiment result, the CDF experiment measured the cross section down to much lower $\sqrt{\tau}$ than measured before. In these small x region, sea quark and gluon contributions are dominant to valence quarks, so that we can compare $p\bar{p}$ data with pp experiment result for scaling discussion. When we ignore the parton distribution function Q^2 dependence, the differential cross section becomes the function of Y and $\sqrt{\tau}$, and if we fix Y=0, the cross section has to depend on $\sqrt{\tau}$ only, and should not depends on $\sqrt{s}$ of each experiment. However, because of gluon bremsstrahlung of initial partons, the scaling should be violating. The scaling violation has been predicted by QCD, although it was difficult to prove it clearly, because it has been difficult to get large $\sqrt{s}$ collisions.

Let's start the discussion of scaling. Fig 4.13 shows the differential cross section $M^3\frac{d^2\sigma}{dMdY}\ |_{Y=0}$. When we look at the data only, the scaling seems to be valid. Although the center of mass energy of the CDF experiment is 30-60 times bigger than that of ISR energy ($\sqrt{s}$ =28, 53 and 68 GeV), the cross section seems to connect smoothly with each other.

In order to have detail discussion, they are compared with theoretical predictions of two different $\sqrt{s}$ in pp and $p\bar{p}$ collisions. Fig 4.14 shows $M^3\frac{d^2\sigma}{dMdY}\ |_{Y=0}$ with the cross section predictions of pp and $p\bar{p}$ at $\sqrt{s}$= 63 and 1800 GeV. In the small $\sqrt{\tau}$ region measured by CDF, the difference between pp and p$\bar{p}$ data is expected to be small, i.e. the sea quark and gluon contribution is dominant. But in the large $\sqrt{\tau}$ the cross section of pp drops faster than that of $p\bar{p}$. This indicates that the valence quark contributions become large in this region. The difference of the cross sections between $\sqrt{s}$=63 GeV and $\sqrt{s}$= 1800 GeV comes from Q^2 dependence of the parton distribution and indicates scaling violation.

Comparing the data with these prediction,

- The pp data of ISR energy region has a good agreement with theoretical

expectation at $\sqrt{\tau} > 0.06$.

- The CDF data has a good agreement with theoretical prediction of $\sqrt{s}$=1800 GeV in 0.006< $\sqrt{\tau}$ <0.02.
- In the 0.02< $\sqrt{\tau}$ <0.06, pp data tends to show larger cross section than theoretical expectations.

When we extrapolate $\sqrt{s}$=63 GeV data into $\sqrt{\tau} < 0.02$ using theoretical calculation and compared it with our data, you can see that the CDF data has a good agreement with theoretical prediction of $\sqrt{s} = 1800$ GeV, but almost twice as big as $\sqrt{s} = 63$ GeV prediction. It agrees with $\sqrt{s} = 1800$ GeV prediction well, but dose not fit that of $\sqrt{s} = 63$ GeV at $\sqrt{\tau} < 0.02$. On the other hand, ISR experiment data reproduces $\sqrt{s} = 63$ GeV prediction well, but dose not fit that of $\sqrt{s} = 1800$ GeV at $\sqrt{\tau} > 0.06$. This is one of the proof of scaling violation.

4.1.3 K factor

The theoretical K factor calculation [202] has been done including up to the 2nd order diagram. [2] [150][197][198][199] [200][201] Fig 1-2 shows the lowest order diagram and some of the 1st order diagram, and Fig 4.15 shows some of the 2nd order diagram. In this calculation, the standard model parameters were set as shown in Table 4.4. The calculation has been done using several parton distribution functions.

The K factor in the theoretical calculation was defined as

$$K^{(2)} \equiv \frac{\sigma^2}{\sigma^0}$$

and

$$K^{(1)} \equiv \frac{\sigma^1}{\sigma^0}$$

where

[2] This calculation has been done using the DIS scheme.

- σ^0 = The cross section including only the lowest order diagram
- σ^1 = The cross section including up to the 1st order diagram
- σ^2 = The cross section including up to the 2nd order diagram

Fig 4.16 shows the theoretical prediction of the K factor as a function of the invariant mass of lepton pairs. Numerically the K factor doesn't depend on the parton distribution function in the theoretical calculation. It is 1.2 including the 1st order diagram and 1.4 including the 2nd order calculation. Table 4.5 shows the contribution of each process. Fig 4.17 shows Y dependence of $K^{(1)}$ factor. $K^{(1)}$ factor is almost constant, but decrease a little in the large Y region.

The K factor in the experiment was defined as

$$K_{exp} \equiv \frac{\sigma^{exp}}{\sigma^0}$$

and

$$K^0_{exp} \equiv \frac{\sigma^{exp}_{Y=0}}{\sigma^0_{Y=0}}$$

where

- σ^{exp} = Measured cross section

So K_{exp} depends on the parton distribution function used to calculate the lowest order diagram. In order to measure K_{exp}, another correction has been added. Fig 4.18 shows the rapidity distribution of the parent virtual gamma calculated by several parton distribution functions at an invariant mass of 12.5 GeV/c^2. Since the longitudinal momentum of the parent virtual photon depends on the parton distribution function, the geometrical acceptance calculation depends on the parton distribution function. This ambiguity was taken as a systematic error when we discussed about the cross section, however, when we discussed the K factor, these differences were not taken as a systematic error, because the K factor assumes one of the structure

functions. Fig 4.19 and Fig 4.20 show the relative geometrical and kinematical acceptance as a function of invariant mass. EHLQ1 was taken as a reference.

Finally K_{exp} is plotted as a function of invariant mass against several parton distribution functions. Fig 4.21 shows K_{exp} and Fig 4.22 shows K^0_{exp}. Now, let's start the discussion from two points of view. The first discussion is " whether the QCD higher order correction is a good approximation or not". The recent deep inelastic scattering experiment [171] [172] measured the parton distribution function down to x = 0.07 $\sim$ 0.08 at Q^2 = 20 GeV^2. Fig 4.24 shows $F_2^{\mu p}$ measured in BCDMS ([171]). Using these data, the structure function in the Z^0 mass region is estimated. Since measured x region in the deep inelastic scattering experiment is close to that of Z^0, the ambiguity of the estimated structure function should be small, so that the parton distribution function dependence of the lowest order cross section calculation is small. For this discussion, in order to reduce the statistical error, the following item was assumed,

- K factor is constant in the invariant mass region
  75 GeV/c^2 < M < 105GeV/c^2.

The K_{exp} has been determined using the lowest order cross section calculated by integrating over the region 75 GeV/c^2 < M < 105GeV/c^2 against several parton distribution functions. Table 4.6 shows the K_{exp} factor in this region. And Table 4.7 shows the K^0_{exp} factor. From this table, you can see that K factor is almost consistent with theoretical predictions.

The next discussion point is the behavior of the parton distribution function. The parton distribution function differences are much more distinct in the low mass region. For this discussion, we made the following assumptions.

- the K factor measurement in Z^0 region is correct.
- the K factor behaves as theoretical prediction, i.e. it is almost constant in the

  mass region 10 GeV/c^2 < M < 105GeV/c^2

From Figs 4.22 and 4.23, the K^0_{exp} factor calculated with HMRSE, HMRSB is fairly flat in this mass region. On the other hand, DFLM and DO2 tend to overestimate the low mass Drell-Yan cross section. These results are consistent with the W asymmetry measurement [162] [163] [164].

4.1.4 The properties of the Drell-yan process

The Pt distribution of the parent gamma or Z^0

The Pt distribution of the parent Z^0 [188] or virtual photon is measured in the -0.75 < Y < 0.75 region, where Y is the rapidity of the Z^0 or virtual photon. The measurement is done in the four invariant mass regions, 15 GeV/c^2 < M < 25GeV/c^2, 40 GeV/c^2 < M < 75GeV/c^2 and 75 GeV/c^2 < M < 105GeV/c^2. For the first two mass regions, only the central-central electron pairs were used and for the last two mass regions, the central-plug pairs were added. In order to check whether there is any discrepancy between these two samples, the Pt distribution has been measured for each. Fig 4.25 shows the Pt distribution of the last two mass regions calculated only with the central -central pairs and only with the central-plug pairs. The two cross sections are consistent within the errors, so that they were combined. Fig 4.26 shows the Pt distribution of each mass region, (Pt has been measured by calorimeter information.) and a comparison with a Monte Carlo generator and theoretical calculation [187]. A total of 250, 000 events were generated with the Papageno Monte generator. The background subtraction has been done by the following procedure:

- Estimate the number of background events in each mass region from the isolation distribution.
- Look at the Pt distribution of nonisolated electron pairs, in order to see the Pt spectrum of the background.

- After normalization by the number of background events in each mass region, the background Pt spectrum was subtracted from the data.

This procedure was used for other physics measurements also. The inclusive Pt distribution is shown in Fig 4.27 (Invariant mass > 0.5 GeV/c^2) and compared to the ISAJET Monte Carlo generator. The data are all consistent with the theoretical prediction.

The Pt distribution of electrons

The electron Pt distribution in the dielectron center-of-mass system has been measured. Fig 4.28 shows the electron Pt vs. rapidity of the parent virtual gamma or Z^0 in Monte Carlo events. Since the CDF central detector covers only $|\eta_e| < 1.0$, the detectable Pt range depends on invariant mass. For example we can measure electron Pt down to 25-30 GeV/c in 15 GeV/c^2 $< M <$ 25GeV/c^2, but down to 4-5 GeV/c only in the Z^0 mass region. The measurement has been done in three mass regions, 15 GeV/c^2 $< M <$ 25GeV/c^2, 25 GeV/c^2 $< M <$ 40GeV/c^2 and 75 GeV/c^2 $< M <$ 105GeV/c^2. Fig 4.29 shows the generated electron Pt distribution and the accepted electron Pt distribution. From these plots, you can recognize that the measurable Pt region is very small, so that the mean Pt distribution depends on the Monte Carlo generator a lot if we discuss the Pt distribution in the complete η_e range. In order to reduce this uncertainty, the Pt distribution in $\eta_e < 1$ is also measured. η_e is the electron pseudorapidity in the center of mass system. The central-plug electron pairs were used only for the measurement of Pt over all η_e for the mass range 75 GeV/c^2 $< M <$ 105GeV/c^2. The consistency between the central-central and the central-plug samples was checked in Fig 4.30, Fig 4.30 shows the electron Pt distribution calculated with the central-central and the central-plug pairs individually. Although the measurable Pt region is different, both cross sections agree in the overlap region. Fig 4.31 shows the geometrical acceptance of the electron Pt measurement. Fig 4.32 shows the Pt distribution in each mass region with theoretical predictions. The theoretical predictions are calculated with ISAJET Monte Carlo (the Lowest order). Then K factor 1.4 is multiplied to obtain the cross sections $d\sigma/dPt$. The background subtraction is done using the same procedure described in the previous chapter. Except for the 25 GeV/c^2 $< M <$ 40GeV/c^2 region, the Pt distribution is consistent with the expected value. The disagreement in the region 25 GeV/c^2 $< M <$ 40GeV/c^2 will be discussed later.

Fig 4.33 shows the mean Pt distribution as a function of invariant mass. It is compared with the Papageno generator.

The parent particle angular distribution

The rapidity distribution of the Z^0 or virtual photon is measured in the two mass regions 15 GeV/c^2 $< M <$ 40GeV/c^2 and 75 GeV/c^2 $< M <$ 105GeV/c^2. The rapidity of the Z^0 or virtual photon is defined as

$$Y \equiv (\eta_1 + \eta_2)/2,$$

where η_1 and η_2 are the pseudorapidities of the electrons. Fig 4.34 shows the geometrical acceptance as a function of Y in the two mass regions. The rapidity distribution of the parent particle is shown in Fig 4.35 with the theoretical expectation in the two mass regions [210].

Produced electron angular distribution

The electron angular distributions are measured in the center of mass system. In order to calculate the polar angle in the center of mass system, both initial partons are assumed to have the same Pt, so that the angles are measured against the beam. The measurement is done in two invariant mass regions 15 GeV/c^2 $< M <$ 40GeV/c^2 and 75 GeV/c^2 $< M <$ 105GeV/c^2. Because of the trigger threshold, the plug electron is used only for the Z^0 mass region measurement. Fig 4.36 shows

the angular distribution for each mass region. The forward backward asymmetry is shown clearly in the Z^0 mass region. [153][154][155][156][157] [158][159][160][161]

4.2 B production as backgrounds of Drell-Yan

The dielectron decay from b and c quarks has been studied as backgrounds of the Drell-Yan process. In this chapter, the differences in the properties of Drell-Yan and heavy flavor dielectron production are discussed [189][191][192]. The dielectron sample 2 (Heavy flavor samples) are used for this study.

4.2.1 Inclusive dielectron Pt distribution

The inclusive dielectron Pt distribution has been measured in the rapidity region $\eta_e < 1.0$. The number of non-electron backgrounds are estimated from E/P distribution of electrons in the sample and these backgrounds are subtracted from the data. Fig 4.37A shows the inclusive di-electron Pt distribution of opposite sign pair above 6 GeV/c. In order to calculate the Pt distribution in laboratory system, the following corrections were applied.

- Electron offline cut efficiency
- Geometrical acceptance
- Level 1 and Level 2 trigger efficiency (Pt dependent)
- Kinematical cut efficiency (Pt threshold and isolation)
- Backgrounds subtraction

The source of these electrons are J/Ψ , $b\bar{b} and c\bar{c}$ leptonic decay, Drell-Yan, Z^0 and Υ . In order to reduce non-electron background contamination, tight cuts were applied to both electrons and if both electrons satisfied the cuts, two entries were added to the histogram. The background contamination has been estimated to be 26 %

for opposite sign pairs and 53 % for same sign pairs. The number of background events are same in opposite and same sign pairs, but S/N ratio is different. For this analysis, only the central calorimeter was used. Then the Pt distribution was measured process by process. Fig 4.37B shows the Pt distribution of Drell-Yan electrons. The backgrounds from heavy quark leptonic decay, J/Ψ and Υ were subtracted. The Drell-Yan electron Pt spectrum are calculated as follows:

- Require both electron η_e should be in $-1 < \eta_e < 1$
- Require I_{max} should be less than 0.1
- Estimate backgrounds from heavy flavor semileptonic decay and fake electron using I_{max} distribution and subtract them from the data.
- The isolation cut efficiency are calculated from Monte carlo simulation (corrected by efficiency in the Z^0 mass region)

Fig 4.37C shows the J/Ψ decay electron Pt distribution, and Fig 4.37D shows the Υ decay electron Pt distribution. These two samples are defined as follows.

- Require both electron η_e should be in $-1 < \eta < 1$
- The invariant mass is 2.8 GeV/c^2 $< M <$ 3.2GeV/c^2 are defined as J/Ψ , and 9 GeV/c^2 $< M <$ 11GeV/c^2 is defined as Υ .

Finally heavy flavor semileptonic decay electron Pt spectrum is measured. For heavy flavor semileptonic decay, electrons were separated into two criteria using the opening angle in the azimuthal plane, $d\phi < \pi/2$ and $d\phi > \pi/2$. The former comes from mainly cascade decay (diagram Fig 4.38) and the latter comes from direct decay from $b\bar{b}$ (diagram Fig 4.39). In addition to the standard corrections, the Level 2 trigger inefficiency correction was applied for small opening angle pairs. As discussed in the 'Trigger' Chapter, because of the size of the trigger tower, the

level 2 trigger is inefficient for small opening angle electron pairs. The opening angle dependence of the offline EM clustering inefficiency was also studied with a $b\bar{b}$ Monte carlo Generator and the CDF detector simulation. Fig 4.40 shows the efficiency as a function of opening angle. Using these corrections, the Pt distribution of heavy flavor decay electron was measured as follows:

- Require both electron η_e should be in $-1 < \eta_e < 1$
- Require I_{max} should be greater than 0.1 (reject Drell-Yan backgrounds)
- The invariant mass should be greater than 0.5 GeV/c^2.
- opening angle dependence efficiency corrections are applied
- J/Ψ and Υ backgrounds were subtracted from this sample requiring invariant mass is outside of J/Ψ and Υ mass region.
- Drell-Yan background contamination is estimated after applying $I_{max} > 0.1$ cut using Monte carlo data. Then it is subtracted from the data.

Fig 4.37E shows the opposite charge and same charge pair Pt distributions.

Fig 4.37F shows the dielectron Pt spectrum of $d\phi > \pi/2$ samples, and $d\phi < \pi/2$ samples. Fig 4.41 shows the invariant mass distribution of this nonisolated electron pairs. J/Ψ and Υ have been already subtracted. If the opposite sign electron pairs with the small opening angle come from cascade decay, the invariant mass are limited kinematically to be less than 5.2 GeV/c^2 which is the mass of b quark. Fig 4.42 shows the invariant mass distribution of $d\phi < \pi/2$ samples. From Fig 4.42, some events with the invariant mass greater than the mass of b quark can be seen, which may come from gluon splitting.

Fig 4.43 shows the 1st electron and the 2nd electron Pt distribution, process by process. We can see the effect of the neutrino in the nonisolated electron pair sample, i.e. the 1st and 2nd electron Pt distribution is almost the same in isolated

pairs, but the 2nd electron Pt distribution drops faster than that of the 1st electron in non-isolated pairs.

4.2.2 Decay properties

The decay properties are studied for isolated and nonisolated electron pairs.

Fig 4.44A shows the $\delta\ \phi$ distribution for Drell-Yan events. As in the previous chapter, heavy flavor leptonic decay backgrounds have been subtracted. Fig 4.44B shows the $\delta\ \phi$ distribution of the opposite sign and nonisolated electron pairs (the Drell-Yan contamination was subtracted). Two kinds of decay properties are observed in the plot, i.e. the direct leptonic decay from $b\bar{b}$ and the cascade decay. Fig 4.44C shows the same sign electron pair $\delta\ \phi$ distribution. Fig 4.45A, B and C show the correlation between the Pt of the two electrons. The Pt imbalance of the two electrons is observed clearly only in nonisolated electron pairs. In order to see the Pt unbalance, we required the 1st electron Pt should be greater than 12 GeV/c. Since we demands both electrons should have Pt $>$ 6 GeV/c, Pt2/Pt1 has no bias down to Pt2/Pt1$>$ 0.5, where Pt1 and Pt2 are the Pt of the 1st and 2nd electrons.

4.2.3 Comparison with electron + muon sample

The same analysis has been done on an electron + muon sample. In order to reduce backgrounds, tight cuts were applied to both the electron and muon with no trigger requirement. Other cuts were as same as for the dielectron analysis. Fig 4.46A and Fig 4.46B show the opening angle distributions of the same charge pairs and opposite charge pairs, respectively. The electron - muon Pt correlation is plotted in Fig 4.46C, Fig 4.46D; the Pt imbalance can be seem very well.

4.2.4 J/Ψ and Υ production

Since the dielectron trigger Et threshold was set to 5 GeV/c for the central calorimeters, only high Pt J/Ψ 's are detectable in dielectron decay mode. Fig 4.47C shows

the observed J/Ψ mass distribution, Fig 4.48B shows Pt distribution, opening angle distribution are shown in Fig 4.48A and decay electron Pt distribution is Fig 4.48C [165][166][167][168]. The Υ and Υ ' are also detected clearly. Fig 4.47A shows the observed Υ mass distribution, Pt distribution (Fig 4.49B), opening angle (Fig 4.49A) and decay electron Pt distributions (Fig 4.49C) are also shown. These distributions were all calculated using track momentum information.

The track momentum resolution in this region is 0.0017 $\times Pt^2$ = 0.04 - 0.2 $(GeV/c)^2$. From the J/Ψ sample, we can see radiative effects such as a tail in the negative direction. Fig 4.47D is the J/Ψ mass distribution calculated with calorimeter information. The energy resolution of this momentum region is E $\times\sqrt{0.017^2 + 0.013^2/Et}$ = 0.3 - 0.45 GeV. Compared with the tracking mass distribution, the mass distribution calculated with calorimeter tends to have a tail in the positive which may indicate J/Ψ 's from the χ state, because one of electrons can accompany the photon from χ_c decay in the same calorimeter tower.

4.3 Exotic event candidates

4.3.1 High Pt and High mass events

In the dielectron sample, there are some interesting events which have very high Pt or very large invariant mass. Table 4.8 is the list of those events. Though these events are not statistically significant, they will be one of the interesting topics in future runs. The selection criteria are:

- The central-central electron pair
- At least one electron should satisfy tight electron cuts
- Invariant Mass > 150 GeV/c^2 or Pair Pt > 150 GeV/c, or High Pt Υ (Pt > 50 GeV/c)

One of the interesting physics aspects from this sample is the existence of high Pt Υ . There are two high Pt Υ with values of Pt around 90 and 120 GeV/c. Both electron pairs have reasonable electron quantities. Fig 4.50 shows observed the Υ Pt distribution. Since these two events are far from the continuum of Υ Pt, they may come from different physics process. For example reference [184] mentioned that high Pt Υ indicates the existence of axigluons.

4.3.2 The possibility of a new particle

The Drell-Yan mass spectrum agrees with the theoretical prediction well, except for mass region 30 - 35 GeV/c^2 region. The K factor becomes large in this region and the isolated electron Pt distribution has also an excess around 16 GeV/c (Fig 4.51) and only isolated electrons show this behavior. Although more statistics are necessary to treat this peak as physics, if it indicates the existence of a new particle, the cross section times e^+e^- branching ratio is around 3 ± 2 pb .

Chapter 5

Conclusions

The Drell-Yan production mechanism and its QCD correction have been studied with a dielectron sample obtained by the $\bar{p}$ p collision at $\sqrt{s}$ =1800 GeV. The differential cross section was measured in the invariant mass region from 12 GeV/c^2 to 105 GeV/c^2 and the scaling property was compared with other $p\bar{p}, pp$ experiment results. Followings are main conclusions in this analysis.

- The Drell-Yan cross section times branching ratio ($\gamma^* \rightarrow e^+e^-$), $\frac{d\sigma}{dM}$, $\frac{d\sigma}{dMdY}$, at Y=0 have been measured down to M = 12 GeV/c^2. Recent deep inelastic scattering experiments measured parton structure function down to x=0.1, thus our low mass Drell-Yan cross section measurement is the first measurement of the parton structure function in the smaller x region. The cross section $\frac{d\sigma}{dMdY}$, at Y=0 in the low mass region is 8.05±3.0 ± 1.69(pb/GeV) for 12-15 GeV/c^2, 4.34±0.98 ± 0.50 (pb/GeV) for 15-20 GeV/c^2, 1.87±0.59 ± 0.27(pb/GeV) for 20-25 GeV/c^2 and 0.82±0.40 ± 0.13(pb/GeV) for 25-30 GeV/c^2. The first error comes from statistics and the second comes from systematic error. The other uncertainty comes from luminosity calculation, which is approximately 7%. The parton distribution function from the latest deep inelastic scattering experiment, HMRSB with the QCD higher order correction reproduces the

data well.

- The K_{exp} factor was calculated on the basis of the measured cross section and several parton distribution functions, then compared with a 2nd order QCD calculation. Because the uncertainty from the parton distribution function is small in the Z^0 mass region, the K_{exp} factor has been calculated in that range at first. Assuming the HMRSB parton distribution function, it has been measured to be 1.53 ± 0.4.

- Then the behavior of parton distribution function in the low mass region was discussed assuming the K^0_{exp} factor measured in Z^0 mass region.
  HMRSE and HMRSB parton distribution functions reproduce the data well. That is consistent with the result from W decay forward-backward asymmetry measurement [162] [163] [164].

- The properties of the Drell-Yan process are studied. The $P_{t(ee)}, P_{t(e)}$ at the center of mass system, $Y_{(ee)} and \eta_e$ are measured and compared with theoretical predictions. Each property agrees within the calculated experimental uncertainties.

- The properties of Drell-Yan dielectron production were compared with those of heavy flavor leptonic decay. There are distinctive differences between the two specifically in the opening angle distribution and the electron Pt unbalance.

- J/Ψ , Υ and Υ ' dielectron decays are detected clearly in the dielectron decay mode. It indicates the ability of the CDF detector for identification of low momentum electrons.

- For the dielectron sample, the electron Pt distribution in the laboratory frame was obtained for the inclusive electrons and electrons from each process of

Drell-Yan, heavy flavor leptonic decay, J/Ψ and Υ productions from 6 GeV/c

in the $\eta_e < 1$ region.

Bibliography

[1] S.D.Drell et al Phys Rev Lett 25 (1970) 316

[2] D.Antreasyan et al Phys Rev Lett 45 (1980) 863

[3] D.Antreasyan et al Phys Rev Lett 47 (1981) 12

[4] D.Antreasyan et al CERN-EP/81-116 (1981)

[5] Badier et al Phys Lett 86B (1979) 98

[6] Badier et al Phys Lett 86B (1979) 145

[7] Badier et al Phys Lett 93B (1980) 354

[8] Badier et al Phys Lett 104B (1981) 335

[9] Corden et al Phys Lett 76B (1978) 226

[10] Corden et al Phys Lett 96B (1980) 417

[11] Corden et al Phys Lett 96B (1980) 411

[12] Ito et al Phys Rev D 23 (1981) 604

[13] Smith et al Phys Rev Lett 46 (1981) 1607

[14] efrancois et al Proc Int Conf om High Energy Physics, Madison,AIP Conf Proc No68 (1980)1319

[15] Altarelli et al Nucl Phys B69 (1974) 531

[16] Breidenbach et al Phys Rev Lett 23 (1969) 930

[17] D.J.Bjorken and E.A.Paschos Phys Rev 185 (1969) 1975

[18] D.J.Bjorken and E.A.Paschos Phys Rev D13 (1970) 151

[19] D.J.Bjorken Phys Rev 179 (1969) 1547

[20] Bodek et al Phys Rev D20 (1980) 1471

[21] Gell-Man Phys Lett 8 (1964) 214

[22] Zweig CERN Rep 8419/TH412

[23] West Phys Rev Lett 24 (1970) 1206

[24] Yan Ann Rev Nucl Sci 26 (1976) 199

[25] Brodsky et al Phys Rev Lett 31 (1973) 1153

[26] Bosetti et al Nucl Phys B142 (1978) 1

[27] Altarelli et al Nucl Phys B126 (1977) 298

[28] Politzer Nucl Phys B129 (1977) 301

[29] Sachrajda Phys Lett B73 (1978) 185

[30] Baer Sov Phys JETP 21 (1965) 629

[31] Altarelli et al Phys Lett B76 (1978) 351,356

[32] Fritzsch et al Phys Lett B73 (1978) 80

[33] Scott Proc Moriond Workshop (1981)

[34] Kourkoumelis et al Phys Lett B91 (1980) 475

[35] Badier et al CERN-EP/80-36 (1980)

[36] C. Quigg 'Gauge Theories of the Strong, Weak and Electromagnetic Interaction' Benjamin/Cummings (1983)

[37] Kuti et al Phys Rev D 4 (1971) 3418

[38] Farrar Nucl Phys B 77 (1974) 429

[39] Field et al Phys Rev D 15 (1977) 2590

[40] Altarelli ' Proceedings of EPS Conference on High Energy Physics Geneva 1979' (1980) 727

[41] Altarelli et al Nucl Phys B 143 (1978) 521

[42] Kubar-Andre et al Phys Rev D 19 (1979) 221

[43] Contogouris et al Phys Rev D 19 (1979) 2207

[44] Altarelli et al Nucl Phys B157 (1979) 461

[45] Abad et al Phys Lett B78 (1978) 433

[46] Humpert Phys Lett B84 (1979) 327 , Phys Lett B85 (1979)293

[47] Harada et al Nucl Phys B155 (1979) 169

[48] Abbott et al Ann Phys 125 (1980) 276

[49] Buras et al Nucl Phys B132 (1978) 249

[50] M.Shibata, Doctoral Thesis, " Study of charged intermediate vector boson production in Proton-Antiproton collisions at $\sqrt{s}$ = 1.8 TeV " Univ. of Tsukuba, UTPP-31(1988)

[51] Y.Hayashide, Doctoral Thesis, " Characteristic of CDF ebdplug electromagnetic calorimeter" Univ. of Tsukuba, UTPP-26(1986)

[52] Abe et al., Nucl. Inst. and Meth. A271(1988)) 387.

[53] F.Snider et al., Nucl. Inst. and Meth. A268(1988) 75.

[54] U.S.NIM Commitee "FASTBUS Standard routines" DOE/ER-0325(1987)

[55] Nuclear Instruments and Detector Commitee of IEEE Nuclear and Plasma Sciences Society " IEEE Standard FASTBUS ¡odular High-Speed data Acquisition and Control System" ANSI/IEEE std 960-1986 (1986)

[56] G.Drake et al., Nucl. Inst. and Meth. A269(1988) 68.

[57] C.Blocker., CDF internal report CDF315.

[58] T.Mimashi, Master Thesis, " The Vertex time projection chamber for Proton-Antiproton collider experiment" Univ. of Tsukuba (1986)

[59] J.Huth et al., CDF internal report CDF564.

[60] M.Binkley et al., CDF internal report CDF350.

[61] R.J.Yarema et al., CDF internal report CDF363.

[62] R.J.Yarema et al., IEEE Trans. Ncul. Sci. NS33 (1986) 933.

[63] E.Bedeschi et al., Nucl. Inst. and Meth. A268(1988) 50.

[64] M.Atac et al., Nucl. Inst. and Meth. A269(1988) 40.

[65] S.Bhadra et al., Nucl. Inst. and Meth. A268(1988) 92.

[66] S.Bhadra et al., Nucl. Inst. and Meth. A269(1988) 33.

[67] G.Ascoli et al., Nucl. Inst. and Meth. A268(1988) 33.

[68] G.Ascoli et al., Nucl. Inst. and Meth. A268(1988) 41.

[69] K.Byrum et al., Nucl. Inst. and Meth. A268(1988) 46.

[70] L.Balka et al., Nucl. Inst. and Meth. A267(1988) 272.

[71] Y.Fukui et al., Nucl. Inst. and Meth. A267(1988) 280.

[72] G.Brandenburg et al., Nucl. Inst. and Meth. A267(1988) 257.

[73] S.Bertolucci et al., Nucl. Inst. and Meth. A267(1988) 301.

[74] CDF Design Report (1981) 100.

[75] S.Cihangir et al., Nucl. Inst. and Meth. A267(1988) 249.

[76] S.R.Hahn et al., Nucl. Inst. and Meth. A267(1988) 351.

[77] K.Yasuoka et al., Nucl. Inst. and Meth. A267(1988) 315.

[78] R.G.Wagner et al., Nucl. Inst. and Meth. A267(1988) 330.

[79] G.Drake et al., Nucl. Inst. and Meth. A269(1988) 68.

[80] E.Barsotti et al., Nucl. Inst. and Meth. A269(1988) 82.

[81] H.Minemura et al., Nucl. Inst. and Meth. A238(1985) 18.

[82] C.N.Holmes et al., CDF internal report CDF361.

[83] R.Yamada et al., Fermilab TM-1369 (1985)

[84] F.Abe et al., Phys. Rev. D 41 (1990) 2330.

[85] H.Frisch et al., CDF internal report CDF250.

[86] H.Frisch et al., CDF internal report CDF416.

[87] T.Liss et al., CDF internal report CDF552.

[88] H.B.Jensen., CDF internal report CDF770.

[89] R.Johnson., CDF internal report CDF876.

[90] M.Dell'Orso., CDF internal report CDF792.

[91] C.White et al., CDF internal report CDF1202.

[92] C.White et al., CDF internal report CDF1031.

[93] M.Bozzo et al., Phys Lett. 147B (1984) 392.

[94] M.Bozzo et al., Phys Lett. 198B (1987) 513.

[95] C.Blocker., CDF offline documentation C$DOC:ELCTRN.MEM

[96] C.Blocker., CDF offline documentation C$DOC:EMCLST.MEM

[97] C.Blocker., CDF offline documentation C$DOC:ELEFLT.MEM

[98] M.Binkley et al., CDF internal report CDF841.

[99] M.Miller et al., CDF internal report CDF1086.

[100] J.Proudfoot The proceedings of the workshop on calorimetry for the Superconducting Suppercollider, TUSCAL00SA 1989

[101] J.Proudfoot., CDF internal report CDF935.

[102] S.Errede et al., CDF internal report CDF1226.

[103] R.Blair et al., CDF internal report CDF641.

[104] A.B.Wicklund et al., CDF internal report CDF933.

[105] S.Kim et al., CDF internal report CDF967.

[106] M.Ninomiya et al., CDF internal report CDF914.

[107] S.Miyashita et al., CDF internal report CDF706.

[108] Y.Morita, Doctoral Thesis, 'Measurement of the intermediative Vector Boson Production cross section and mass at the Fermilab Proton-Antiproton collider' Univ. of Tsukuba, UTPP-33(1989)

[109] M.Sekiguchi, Doctoral Thesis, 'Multiplicity and transverse momentum distributions of charged particles in Proton-Antiproton collisions at $\sqrt{s}$=630 and 1800 GeV " Univ. of Tsukuba, UTPP-30(1988)

[110] T.Minashi., CDF internal report CDF974.

[111] J.J.Schmidt et al., CDF internal report CDF955.

[112] Private comunication to J.J.Schmidt .

[113] D.Baden et al., CDF internal report CDF845.

[114] U.Joshi et al., CDF internal report CDF486.

[115] D.Quarrie et al., CDF internal report CDF156, J.T.Caroll et al., CDF internal report CDF264, K.Chadwick et al., CDF internal report CDF227, M.Eaton et al., CDF internal report CDF365.

[116] M.Eaton et al., CDF internal report CDF292.

[117] T.Liss et al., CDF internal report CDF1080.

[118] D.Amidei et al., CDF internal report CDF802.

[119] D.Amidei et al., CDF internal report CDF945.

[120] T.J.Phillips et al., CDF internal report CDF956.

[121] J.C.Yun et al., CDF internal report CDF884.

[122] D.Baden et al., CDF internal report CDF569.

[123] D.Baden et al., CDF internal report CDF960.

[124] M.Franklin et al., CDF internal report CDF848.

[125] T.Kamon et al., CDF internal report CDF865.

[126] T.Kamon et al., CDF internal report CDF900.

[127] T.Kamon et al., CDF internal report CDF621.

[128] M.Atac et al., CDF internal report CDF544.

[129] Y.Morita et al., CDF internal report CDF996.

[130] Y.Morita et al., CDF internal report CDF997.

[131] M.Ninomiya et al., CDF internal report CDF1078.

[132] J.Proudfoot et al., CDF internal report CDF1011.

[133] W.Trischuk et al., CDF internal report CDF948.

[134] T.L.Watts et al., CDF internal report CDF956.

[135] J.Hauser., CDF internal report CDF966.

[136] J.Proudfoot., CDF internal report CDF1008.

[137] J.Proudfoot., CDF internal report CDF1223.

[138] G.W.Foster et al., CDF internal report CDF660.

[139] J.Freeman et al., Nucl. Inst. and Meth. A269(1988) 93.

[140] D.Amidei et al., CDF internal report CDF510.

[141] D.Amidei et al., Nucl. Inst. and Meth. A269(1988) 51.

[142] J.Proudfoot., CDF internal report CDF860.

[143] J.Proudfoot., CDF internal report CDF633.

[144] U.Joshi et al., Nucl. Inst. and Meth. A263(1988) 199.

[145] U.Joshi et al., 'Proceedings of SSC workshop on Trigger and Data acquisition' Toront CANADA (1989)

[146] F.Paige et al., ISAJET monte Carlo report BNL 38034 (1986)

[147] S.Errede., CDF internal report CDF524.

[148] M.Gold et al., CDF internal report CDF1094.

[149] A.Barbaro-Galtieri et al., CDF internal report CDF918.

[150] Private communication to Dr. T.Matsuura: Calculation has been done DIS scheme. [197][198][199][201]

[151] Private communication to Dr. W.J.Stirling Calculation has been done Msbar scheme.

[152] Private communication to Dr. H.Iso [210]

[153] P.Hurst et al., CDF internal report CDF1097.

[154] P.Hurst et al., CDF internal report CDF1126.

[155] P.Hurst et al., CDF internal report CDF1216.

[156] C.Blocker., CDF internal report CDF1114.

[157] C.Blocker., CDF internal report CDF1115.

[158] C.Blocker., CDF internal report CDF1116.

[159] C.Blocker., CDF internal report CDF1117.

[160] C.Blocker., CDF internal report CDF1118.

[161] C.Blocker., CDF internal report CDF1119.

[162] J.Hauser et al., CDF internal report CDF1110.

[163] S.Leone et al., CDF internal report CDF1091.

[164] S.Leone, Doctoral Thesis, 'Lepton Charge Asymmetry from $W^{\pm} \rightarrow l^{\pm}\nu$ at the Tevatron Collider' Univ. of Pisa, INFN PI/AE 90/7 (1990)

[165] V.Barger et al., Phys. Rev. D 31 (1985) 1051.

[166] B.van Eijk, Cern-Ep/88-38 (1988)

[167] B.van Eijk et al., Z. Phys. C 41 (1988) 489.

[168] C.Albajar et al., Phys. Lett. B 200 (1988) 380.

[169] E.Eichten et al., Rev. of Mod Phys. 56(1984) 599., 58 (1986) 1065(E)

[170] D.W.Duke et al., Phys. Rev. D 30 (1984) 49.

[171] W.J.Stirling et al., Preprint of Univ. of Durham DTP/90/46 RAL 90-053 (1990)

[172] W.J.Stirling et al., Rutherford Appleton Lab. DTP/90/04 RAL-90-007 (1990)

[173] M.Diemoz et al., Cern-Th CERN-TH 4751/87 (1987)

[174] Wu-Ki.Tung et al., Fermilab-Conf-89/26 (1989)

[175] Wu-Ki.Tung et al., Fermilab-Conf-87/122-T (1987)

[176] Wu-Ki.Tung et al., Fermilab-Pub-88/135-T (1988)

[177] A.Devoto et al., Phys Rev D 30 (1984) 541.

[178] H.Schroder., DESY88-101 ISSN 0418-9833 (1988)

[179] C.Albajar et al., CERN-EP/88-100 (1988)

[180] C.Albajar et al., Phys Lett B 186 (1988) 247.

[181] Guidoal.,Tareli Phys Reports 81 1 (1982) 1.

[182] R.K.Ellis., Fermilab-Conf-88/60-T (1988)

[183] R.K.Ellis., Fermilab-Conf-88/161-T (1988)

[184] Lars Bergstrom., Phys. Lett. 212B (1988) 386.

[185] C.Quigg, Rev of Modern Phys, 49 (1977) 297.

[186] Thomas Muller., CERN-EP/88-48 (1988)

[187] P.B.Arnold et al., Fermilab-Pub-88/168-T (1988)

[188] G.Altareri et al., Nucl Phys B246 (1984) 12.

[189] C.Albajar et al., Phys Lett. 186B (1987) 237.

[190] A.D. Martin et al., Z. Phys C-Particles and Fields 42 (1989) 277.

[191] G.Arnison et al.,. Phys. Lett. 155B (1985) 442.

[192] P.Bagnaia et al.,. Phys. Lett. 154B (1985) 338.

[193] C.Albajar et al., CERN-EP/88-46 (1988)

[194] F.Halzen et al., CERN-TH 4621/86 (1986)

[195] R.Tripiccione., CDF internal report CDF82.

[196] I.R.Kenyon Rep Prog Phys 45 (1982) 1261.

[197] T.Matsuura et al., Phys. Lett. B211 (1988) 171.

[198] T.Matsuura., Nucl. Phys. B319 (1989) 570.

[199] T.Matsuura., DESY preprint 90-031

[200] W.L.Van Neerven., Nucl Phys B268 (1986) 453.

[201] T.Matsuura et al., Preprint Univ of Leiden The Netherlands (1988)

[202] W.J.Stirling " Proceedings of the Drell-Yan Workshop Fermilab" Octorber 7,8 (1982) 131.

[203] E.L.Berger., " Proceedings of the Drell-Yan Workshop Fermilab" Octorber 7,8 (1982) 1.

[204] R.K.Ellis., Nucl Phys B173 (1980) 397.

[205] R.K.Ellis et al., Nucl Phys B211 (1983) 106.

[206] R.J.Gonsalves et al., Phys Rev D 28 (1983) 1542.

[207] B.Humpert et al., Nucl Phys B184(1981) 225.

[208] G.Altarelli et al., Phys Lett (1985) 457.

[209] F.Halzen et al., Phys Rev D 19 (1979) 216.

[210] J.Kubar et al.,. Nucl. Phys. B175 (1980) 251.

[211] M.Binkley et al CDF internal report CDF381

[212] J.C.Yun et al CDF internal report CDF953

[213] Private communication to S.Ogawa

[214] Private communication to M.Binkley

[215] M.Gold CDF internal report CDF913

[216] C.Campagnari et al CDF internal report CDF794

[217] C.Campagnari et al CDF internal report CDF795

[218] Private communication to M.Ninomiya

Tables

Group	Beam and target	$\sqrt{s}$ (GeV)	K_{exp}
Badier et al (1980) (NA3)	(p - $\bar{p}$):Pt	150	2.3 ± 0.4
Badier et al (1979) (NA3)	p:Pt	200	2.2 ± 0.4
Iso et al (1981) (CFS)	p:pt	300/400	$1.7^{+0.73}_{-0.58}$
Antreasyan et al (1981) (CHFMNP)	p:p	44,63	1.6±0.2
Smith et al (1981) (MNTW)	p:W	400	1.6±0.3
Kourkoumelis et al (1981)	p:p	44,63	1.7±
Lefrancois et al (1980) (NA3)	π^-:pt	200	2.2 ±0.3
Lefrancois et al (1980) (NA3)	π^+:pt	200	2.4 ±0.4
Lefrancois et al (1980) (NA3)	$\pi^- - \pi+$:pt	200	2.4 ±0.4
Annassontzis et al (1982) (AFMcMs) E-537	$\bar{p}$: W,Cu,Be	125	2.25±0.45
Annassontzis et al (1982) (AFMcMs) E-537	π^-:W,Cu,Be	125	2.5±0.5
Corden et al (1980) (Omega)	π^-:W	40	2.45 ±0.42
Corden et al (1980) (Omega)	π^+:W	40	2.52 ±0.49
Corden et al (1980) (Omega)	$(\pi^- - \pi^+)$:W	40	2.22 ±0.41

Table 1.1: The list of K_{exp} determined by previous experiments

Cut parameter	Central tight cut	Central Loose cut	Plug cut
Had/EM	<ABW	<ABW	<ABW
Good track	≥ 1(CTC)	≥ 1(CTC)	≥ 1(VTPC)
CDF fiducial volume cut	On	On	On
Lshr	<0.2	<0.2	*
E/P	<1.5	*	*
Strip χ^2	<10	*	*
CTC track matching $\mid \delta Z \mid$	<3 cm	*	*
CTC track matching $\mid \delta\phi \mid$	<1.5 cm	*	*
VTPC hit occupancy	>0.2	>0.2	*
VTPC track matching $\mid \delta\eta \mid$	*	*	<0.06
Lateral shower profile $\chi^2_{3\times3}$	*	*	<10

Table 3.1 Two kinds of cut parameter sets, 'tight cut parameter set' and 'loose cut parameter set' are defined for the central electron identification. For the plug electron, only one parameter set is defined. ABW means 0.055+0.00045 × (Energy of EM cluster).

The cut parameter	Applied cut
Central electron	
Had/EM	E/P, $\mid \delta Z \mid$,$\mid \delta X \mid$, VTPC
Lshr	E/P, $\mid \delta Z \mid$,$\mid \delta X \mid$, VTPC
E/P	Lshr, Had/EM, $\mid \delta Z \mid$,$\mid \delta X \mid$, VTPC
Strip χ^2	E/P, $\mid \delta Z \mid$,$\mid \delta X \mid$, VTPC
CTC track matching $\mid \delta Z \mid$	Lshr, Had/EM, E/P, VTPC
CTC track matching $\mid \delta\phi \mid$	Lshr, Had/EM, E/P, VTPC
VTPC hit occupancy	Lshr, Had/EM, E/P, $\mid \delta Z \mid$,$\mid \delta X \mid$
Plug electron	
Had/EM	VTPC track matching $\mid \delta\eta \mid$
VTPC track matching $\mid \delta\eta \mid$	Lateral shower profile $\chi^2_{3\times3}$, Had/EM
Lateral shower profile $\chi^2_{3\times3}$	VTPC track matching $\mid \delta\eta \mid$

Table 3.2 In order to determine the cut value for each cut parameter, it is neccesary to see the distribution of each cut parameter of pure electrons. To get pure electron sample, the electron pairs whose invariant mass is in J/Ψ and Z^0 mass region are used and other cut parameters which are independent of the cut that we talk about, are applied. The table shows which cuts are applied to study each cut efficiency

Cut parameter	J/Ψ (Isolated)	J/Ψ (Nonisolated)	Z^0(Isolated)
Lshr	99.1 ±1.5	89.5 ±2.4	96.9±1.7
Had/EM	100.0±0.2	96.3 ±1.5	96.9±1.7
Strip χ^2	90.8 ±5.0	93.5 ±1.9	90.6±3.0
E/P	100.0±0.2	100.0±0.2	96.9±1.7
VTPC hit occupancy	98.3 ±2.2	96.1 ±1.5	97.9±1.6
CTC track matching δx	96.7 ±3.1	99.0 ±0.7	99.0±1.0
CTC track matching δz	100.0±0.2	100.0±0.2	99.0±1.0
Tight cut parameter sets	85.7 ±6.0	74.3 ±3.4	77.1±4.9
Loose cut parameter sets	96.6 ±3.0	83.8 ±2.9	91.7±2.9

Table 3.3: The central electron identification efficiencies calculated by methode 1. The efficiencies for high Pt electrons are calculated with the Z^0 sample, and the J/Ψ sample is used for low Pt electrons.

Cut parameter	Z^0(Isolated)
Had/EM	100±0.2
Lateral shower profile $\chi_{3\times3}$	95.1±1.9
VTPC Hit > 0.6	92.6±2.4
VTPC track matching $\mid \eta \mid < 0.06$	91.8±2.5
VTPC track matching $\mid \phi \mid < 0.06$	90.1±3.2
VTPC track matching $\mid \phi \mid < 0.06$ + $\mid \eta \mid < 0.06$	85.5±4.0

Table 3.4: The plug electron identification efficiencies calculated by methode 1. The efficiencies are calculated with Z^0 sample. There is a big correlation between VTPC η and ϕ matching so that if VTPC η matching is good, ϕ matching efficiency is 93 ± 2.9 %.)

Mass	Estimated backgrounds	Opposite sign pair $I_{max} < 0.1$	Opposite sign pair $0.1 < I_{max} < 0.5$	Same sign pair $I_{max} < 0.1$	Same sign pair $0.1 < I_{max} < 0.5$
12-15	1.99	14	63	1	44
15-20	2.80	32	99	0	60
20-25	1.15	16	48	2	25
25-30	0.37	9	11	0	13
30-40	0.41	17	18	1	8
40-60	0.22	9	5	0	5
60-75	0.0	6	3	0	0
75-80	0.0	1	1	0	0
80-85	0.0	10	2	0	0
85-90	0.0	38	1	0	0
90-95	0.0	45	0	0	0
95-100	0.0	14	1	0	0
100-110	0.0	2	0	0	0
110<	0.0	2	2	0	0

Table 3.5 : The backgrounds estimation for Drell-Yan process has been done with the isolation distribution of electrons. The table shows the number of opposite and same sign isolated electron pairs ($I_{max} < 0.1$) and that of nonisolated pairs ($0.1 < I_{max} < 0.5$) in the central calorimeter. These samples are used to calculate the differential cross section $\frac{d\sigma}{dM}$. The estimated number of backgrounds are also in the table.

Mass	Estimated backgrounds	Isolated pair $I_{max} < 0.1$	Nonisolated pair $0.1 < I_{max} < 0.5$
40-60	0.33	10	14
60-75	0.17	4	4
75-80	0.03	2	3
80-85	0	10	0
85-90	0.07	25	5
90-95	0.08	44	2
95-100	0.03	16	1
100-110	0	5	0
110<	0.03	1	1

Table 3.6: The backgrounds estimation for Drell-Yan process has been done with the isolation distribution of electrons. The table shows the number of isolated electron ($I_{max} < 0.1$) and nonisolated ($0.1 < I_{max} < 0.5$) The central-plug electron pairs. These samples are used to calculate the differential cross section $\frac{d\sigma}{dM}$. The estimated number of backgrounds are also in the table.

Mass	Estimated backgrounds	Opposite sign pair $I_{max} < 0.1$	Opposite sign pair $0.1 < I_{max} < 0.5$	Same sign pair $I_{max} < 0.1$	Same sign pair $0.1 < I_{max} < 0.5$
12-15	1.96	15	57	1	41
15-20	3.13	29	92	0	56
20-25	1.45	15	45	2	24
25-30	0.31	7	10	0	12
30-40	0.51	15	18	1	8
40-60	0.13	9	5	0	5
60-75	0.08	5	3	0	0
75-80	0.0	0	1	0	0
80-85	0.05	9	1	0	0
85-90	0.0	35	0	0	0
90-95	0.03	42	0	0	0
95-100	0.0	12	0	0	0
100-110	0.0	2	0	0	0
110<	0.0	2	2	0	0

Table 3.7: The background estimation for Drell-Yan process has been done with the isolation distribution of electrons. The table shows the number of opposite and same sign isolated electron pairs ($I_{max} < 0.1$) and that of nonisolated pairs ($0.1 < I_{max} < 0.5$) in parent particle rapidity $-0.75 < Y < 0.75$. The central calorimeter is only used. These samples are used to calculate the differential cross section $\frac{d\sigma}{dMdY}$ at Y=0. The estimated number of backgrounds are also in the table.

Mass (GeV)	Central-Central pairs	Central-Plug pairs
12-15	0.3	*
15-20	0.3	*
20-25	0.3	*
25-30	0.6	*
30-40	1.0	0.3
40-60	0.6	0.4
60-75	0.0	0.0
75-105	0.0	0.0

Table 3.8 The number of expected $Z \rightarrow \tau\tau \rightarrow ee$ backgrounds in the 4.76 pb^{-1} data was estimated by ISAJET Monte Carlo and the CDF detector simulation. Both decay electrons are required to be within the CDF fiducial volume in the central or end plug calorimeter.

Mass	$d^2\sigma/dMdY$	statistical error	Luminosity error	systematic error	sys (1)	sys (2)	sys (3)
12-15	109.9	39.4	9.69	19.63	13.4	4.0	13.8
15-20	30.6	6.5	2.4	3.2	2.3	0.89	2.0
20-25	12.4	3.8	1.0	1.8	1.3	0.43	1.1
25-30	6.43	2.7	0.61	1.2	1.0	0.40	0.44
30-40	5.08	1.4	0.39	0.79	0.70	0.26	0.23
40-60	1.37	0.33	0.10	0.20	0.002	0.003	0.016
60-75	0.982	0.32	0.069	0.18	0.0023	0.003	0.016
75-105	7.01	0.46	0.49	0.53	0.06	0.06	0.32

Table 4.1: Differential cross section $\frac{d\sigma}{dMdY}$

Mass	$d^2\sigma/dMdY$ Y=0	statistical error	Luminosity error	systematic error	sys (1)	sys (2)	sys (3)
12-15	8.05	3.0	0.70	1.69	1.26	0.29	1.08
15-20	4.340	0.98	0.34	0.50	0.37	0.13	0.32
20-25	1.87	0.59	0.15	0.27	0.19	0.065	0.18
25-30	0.82	0.40	0.081	0.13	0.097	0.054	0.075
30-40	0.91	0.26	0.069	0.10	0.081	0.046	0.048
40-60	0.26	0.097	0.020	0.034	0.030	0.011	0.011
60-75	0.21	0.10	0.016	0.028	0.023	0.009	0.013
75-105	2.33	0.24	0.16	0.104	0.094	0.050	0.01

Table 4.3: Differential cross section $\frac{d^2\sigma}{dMdY}|_{Y=0}$ Systematic error (1) comes from acceptance estimation, (2) comes from electron trigger efficiency,identification efficiency and isolation efficiency estimation. (3) comes from back ground estimation.

The contributions taken into account are :

- pure Z contribution
- pure photon contribution
- photon-Z interference

DIS mass factorization scheme
Input parameters :

1. sqrt(S) : 1.80 TeV
2. Mass of Z boson : 90.90 GeV
3. Width of Z boson : 3.81 GeV
4. Mass of W boson : 79.70 GeV
5. Width of W boson : 1.93 GeV
6. Factor. scale : 12.50 GeV
7. Renorm. scale : 12.50 GeV
8. Weinberg angle : 0.231
9. Cabibbo mixing angle: 0.050
10. Number of flavours : 5
11. QCD scale : 0.200 GeV
12. α_s : 0.165
13. Fermi coupling constant: 1.16637 * 10^{-5}
14. QCD scale

HMRSE: 0.1 ,HMRSB: 0.19,DO1 : 0.2 ,DO2 : 0.4,EHLQ1: 0.2,
EHLQ2: 0.29,DFLM1: 0.16,DFLM2: 0.26,DFLM3: 0.36

Table 4.4: Standard model parameters used to calculate Drell-Yan cross section

Example of out put of QCD calculation
The results are in nbarn :
Invariant Mass = 90.9,Parton distribution function:Duke ans owens 1,

- 0th order, q qb : 7.67526E-01
- 1st order, q qb, singular : 2.70429E-01
- 1st order, q qb, regular : -4.95197E-02
- q g : -4.02647E-02
- 1st order contribution : 1.80645E-01
- Cross-section up to 1st order : 9.48171E-01
- 2nd order, q qb, singular : 8.74880E-02
- 2nd order, q qb, regular : 5.88995E-03
- g g, : 1.16112E-03
- q q + qb qb : 1.00427E-03
- q qb, singlet : 1.83946E-03
- 2nd order contribution : 9.73828E-02
- Cross-section up to 2nd order : 1.04555E+00

Table 4.5: Contribution of QCD higher order processes to the Drell-Yan cross section calculation

Structure function	K_{exp}
EHLQ set 1	1.95 ± 0.40
EHLQ set 2	1.93 ± 0.42
Duke and Owens set 1	1.68 ± 0.41
Duke and Owens set 2	1.70 ± 0.40
HMRSE	1.39 ± 0.41
HMRSB	1.53 ± 0.41
DFLM set 1	1.80 ± 0.38
DFLM set 2	1.82 ± 0.38
DFLM set 3	1.85 ± 0.38

Table 4.6: K_{exp} value for several parton distribution functions

Structure function	K^0_{exp}
EHLQ set 1	1.92 ± 0.38
EHLQ set 2	1.85 ± 0.37
Duke and Owens set 1	1.80 ± 0.37
Duke and Owens set 2	1.74 ± 0.35
HMRSE	1.77 ± 0.35
HMRSB	1.76 ± 0.35
DFLM set 1	1.71 ± 0.34
DFLM set 2	1.72 ± 0.34
DFLM set 3	1.75 ± 0.34

Table 4.7: K^0_{exp} value for several parton distribution functions

High Mass events	RUN:17864, EVENT:767
	Mass: 189.83 (GeV/c^2),Opening angle: 3.03 (rad)
	Et of the pair 92.24 (GeV)
Electron	η_e : $-0.28, \phi_e$: 1.00, E_t: 107.24 (GeV), Lshr: -0.03, E/P: 1.22
	Isolation: 0.04, χ^2_{strip} : 2.53, χ^2_{wire}: 2.70, VTPC Hit fraction: 1.0
	Track-Cluster match:: δ Z: 1.09 (cm),$\delta\phi$: 0.23 (cm), Had/Em: 0.04
Positron	η_e : $-0.52, \phi_e$: $-2.24, E_t$: 95.88 (GeV), Lshr: -0.04, E/P: 0.75
	Isolation: 0.08, χ^2_{strip} : 2.76, χ^2_{wire}: 2.30, VTPC Hit fraction: 1.0
	Track-Cluster match:: δ Z: 0.32 (cm),$\delta\phi$: 0.36 (cm), Had/Em: 0.08
High Pt Υ	RUN:17332, EVENT:2517
	Mass: 10.39 (GeV/c^2),Opening angle: 0.02 (rad)
	Et of the pair 116.60 (GeV)
Electron	η_e : $-0.41, \phi_e$: 3.72, E_t: 27.95 (GeV), Lshr: -0.05, E/P: 1.07
	Isolation: 2.66, χ^2_{strip} : 0.24, χ^2_{wire}: 1.93, VTPC Hit fraction: 0.96
	Track-Cluster match:: δ Z: 0.40 (cm),$\delta\phi$: 0.08 (cm), Had/Em: 0.01
Positron	η_e : $-0.65, \phi_e$: $-2.55, E_t$: 72.39 (GeV), Lshr: -0.22, E/P: 0.94
	Isolation: 0.41, χ^2_{strip} : 219.5, χ^2_{wire}: 8.81, VTPC Hit fraction: 1.0
	Track-Cluster match:: δ Z: 4.43 (cm),$\delta\phi$: -0.07 (cm), Had/Em: 0.08
High Pt Υ	RUN:19157, EVENT:10816
	Mass: 9.04 (GeV/c^2),Opening angle: 0.03 (rad)
	Et of the pair 91.51 (GeV)
Electron	η_e : 0.46, ϕ_e : 1.94, E_t: 84.64 (GeV), Lshr: 0.03, E/P: 1.29
	Isolation: 0.24, χ^2_{strip} : 3.11, χ^2_{wire}: 25.38, VTPC Hit fraction: 1.00
	Track-Cluster match:: δ Z: -0.58 (cm),$\delta\phi$: -0.94 (cm), Had/Em: 0.02
Positron	η_e : 0.73, ϕ_e : 1.90, E_t: 17.82 (GeV), Lshr: -0.01, E/P: 0.97
	Isolation: 4.90, χ^2_{strip} : 2.05, χ^2_{wire}: 8.87, VTPC Hit fraction: 1.0
	Track-Cluster match:: δ Z: -0.82 (cm),$\delta\phi$: 0.88 (cm), Had/Em: 0.01
High Pt Z^0	RUN:18895, EVENT:40027
	Mass: 89.99 (GeV/c^2),Opening angle: 0.37 (rad)
	Et of the pair 200.6 (GeV)
Electron	η_e : $-0.04, \phi_e$: $-2.27, E_t$: 97.14 (GeV), Lshr: -0.05, E/P: 1.05
	Isolation: 0.02, χ^2_{strip} : 0.73, χ^2_{wire}: 1.81, VTPC Hit fraction: 1.00
	Track-Cluster match:: δ Z: 0.78 (cm),$\delta\phi$: 0.26 (cm), Had/Em: 0.02
Positron	η_e : $-0.79, \phi_e$: 4.35, E_t: 121.42 (GeV), Lshr: -0.06, E/P: 1.29
	Isolation: 0.03, χ^2_{strip} : 3.43, χ^2_{wire}: 2.91, VTPC Hit fraction: 0.92
	Track-Cluster match:: δ Z: 1.1 (cm),$\delta\phi$: -0.03 (cm), Had/Em: 0.03
High Pt Z^0	RUN:18172, EVENT:8850
	Mass: 89.78 (GeV/c^2),Opening angle: 1.35 (rad)
	Et of the pair 221.61 (GeV)
Electron	η_e : 0.69, ϕ_e : -0.12, E_t: 37.75 (GeV), Lshr: -0.03, E/P: 1.11
	Isolation: 0.01, χ^2_{strip} : 13.35, χ^2_{wire}: 16.72, VTPC Hit fraction: 1.00
	Track-Cluster match:: δ Z: -1.56 (cm),$\delta\phi$: 0.57 (cm), Had/Em: 0.00
Positron	η_e : 0.94, ϕ_e : 1.20, E_t: 151.53 (GeV), Lshr: -0.08, E/P: 1.08
	Isolation: 0.01, χ^2_{strip} : 5.53, χ^2_{wire}: 12.36, VTPC Hit fraction: 1.00
	Track-Cluster match:: δ Z: -0.60 (cm),$\delta\phi$: -0.20 (cm), Had/Em: 0.01

Table 4.8: High Transverse or high mass event list

Figures

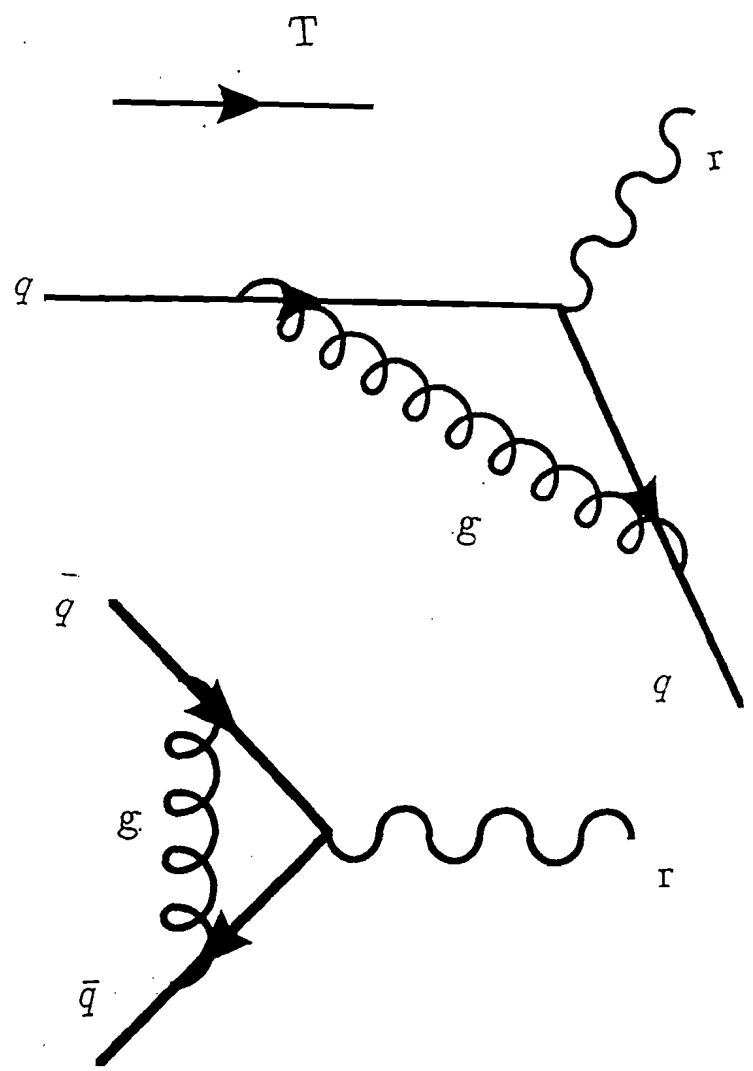

Figure 1.1: One gluon correction to the Born diagram. This figure shows one of the example of transformation from 'Space-like Q^2' (deep inelastic scattering) to 'Time-like Q^2' (Drell-Yan lepton pair production).

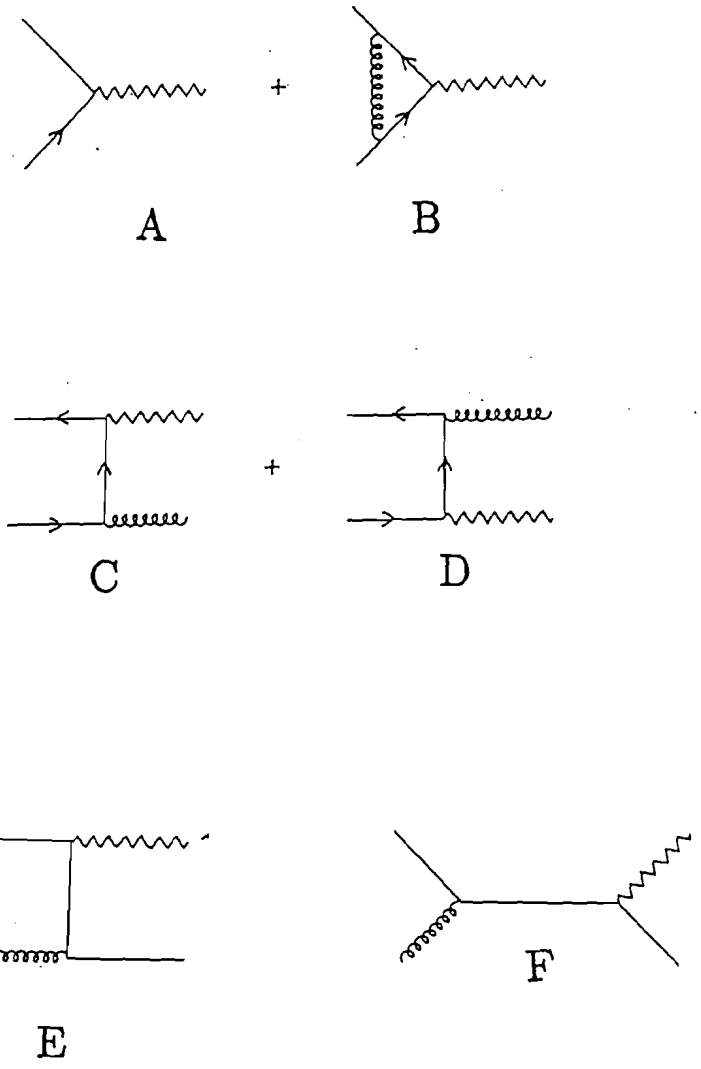

Figure 1.2: The lowest diagram of Drell-Yan process is the annihilation of a quark-antiquark pair to a virtual photon with $q^2 = m^2$. and some of the first order α_s diagram. The diagram of B is a gluon exchang between the quark and antiquark. In the diagram of C-D, a gluon is emitted in addition to the virtual photon, they are called as 'annihilation diagram'. The diagram of E-F shows one of the quark in the two colliding hadrons interacts with a gluon of the other hadron, and emit a virtual photon. These are called as 'Compton diagrams'.

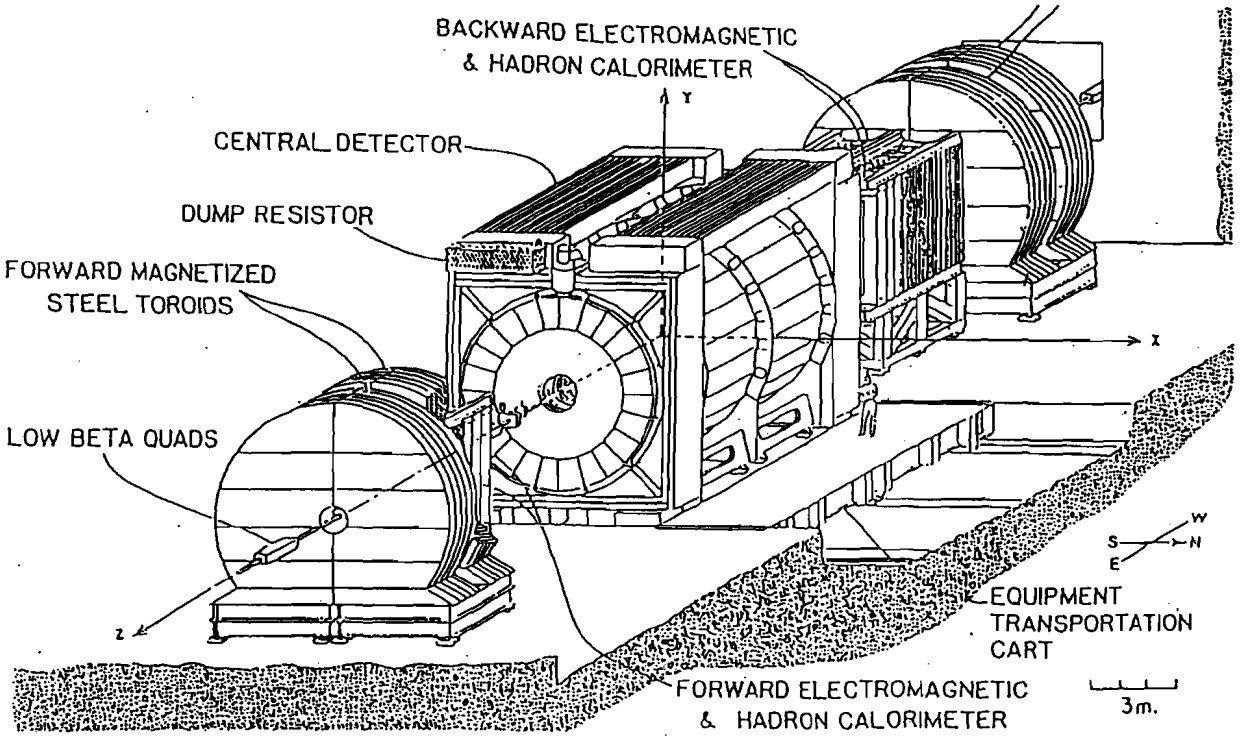

Figure 2.2: A perspective view of the Collider Detector at Fernilab (CDF). The detector composed of Central detector and identical Forward/Backward detector

128

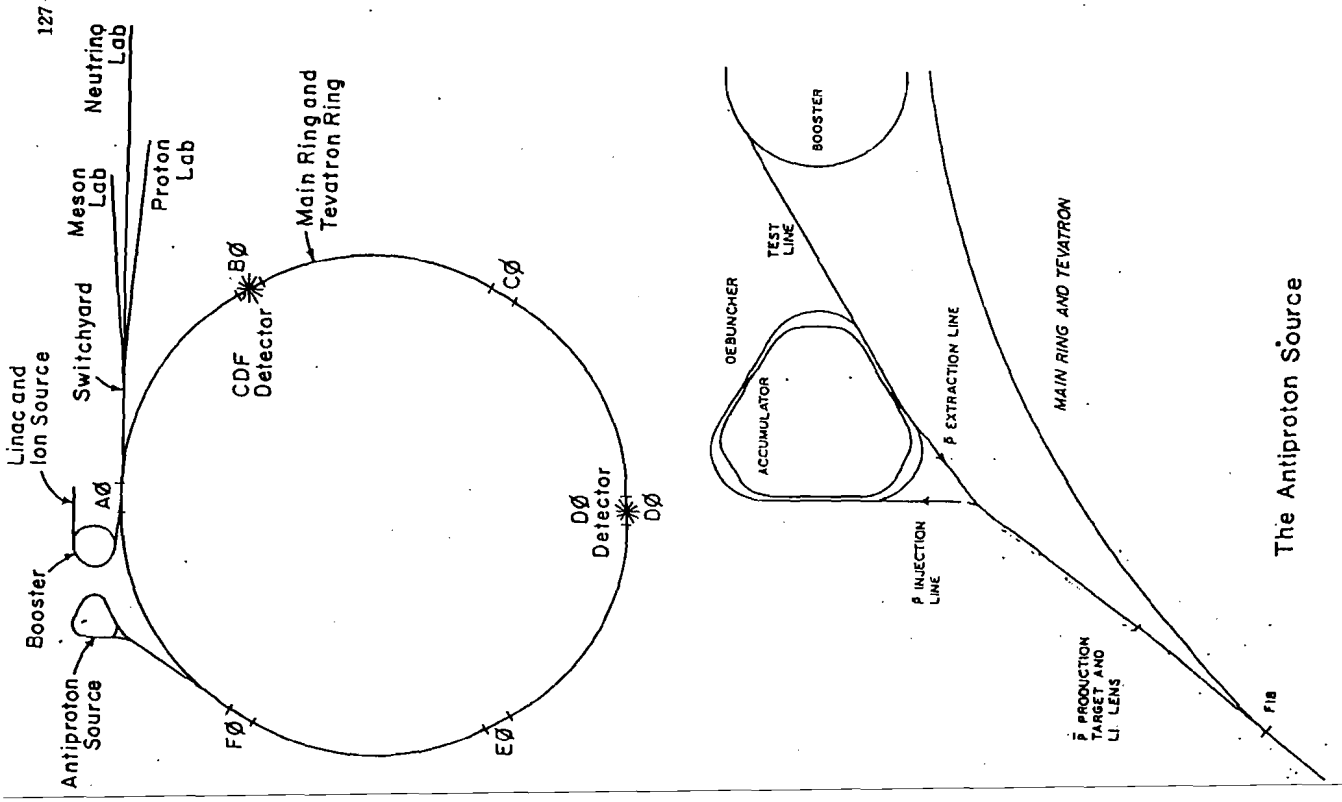

Figure 2.1: The schematic drawing of the Tevatron accelerator

127

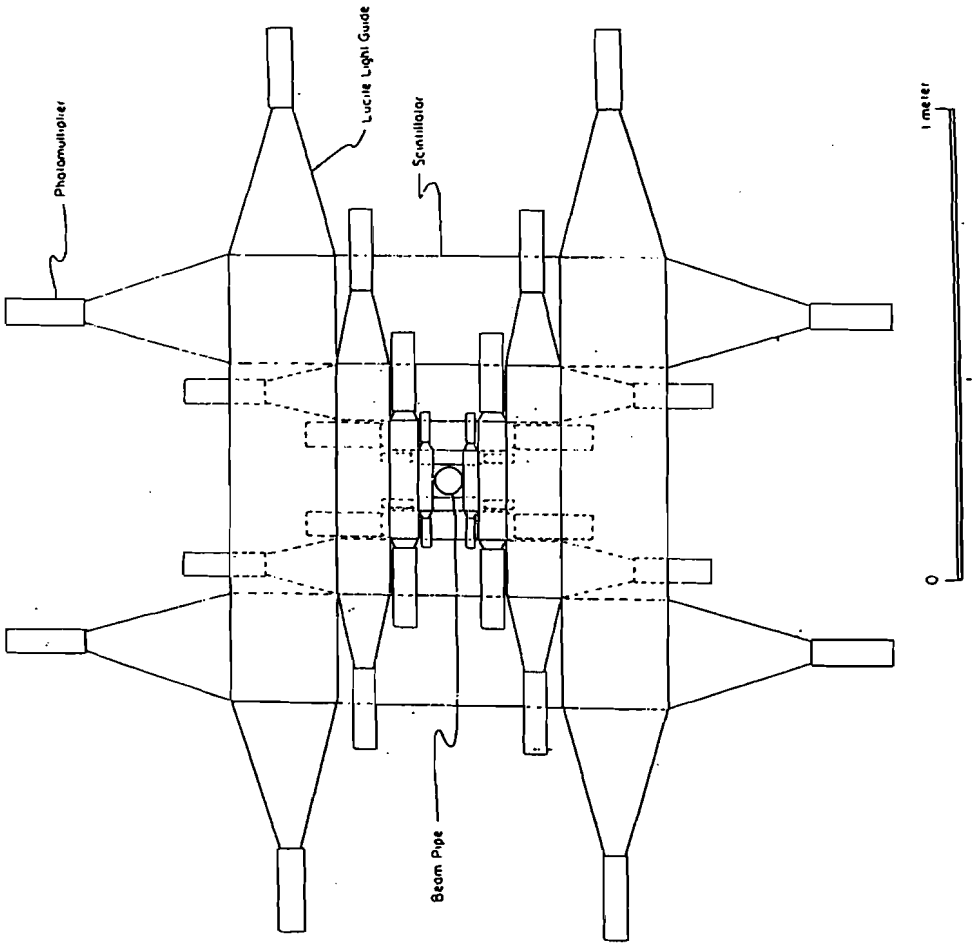

Figure 2.4: A beam eye view of Beam-Beam counter. The counter is made from single layer 2.5 cm thick SCSN23 scintillator, and arranged in rectangle surrounding the beam pile. It covers $0.317 < \theta < 4.47 (3.24 < \eta < 5.89)$.

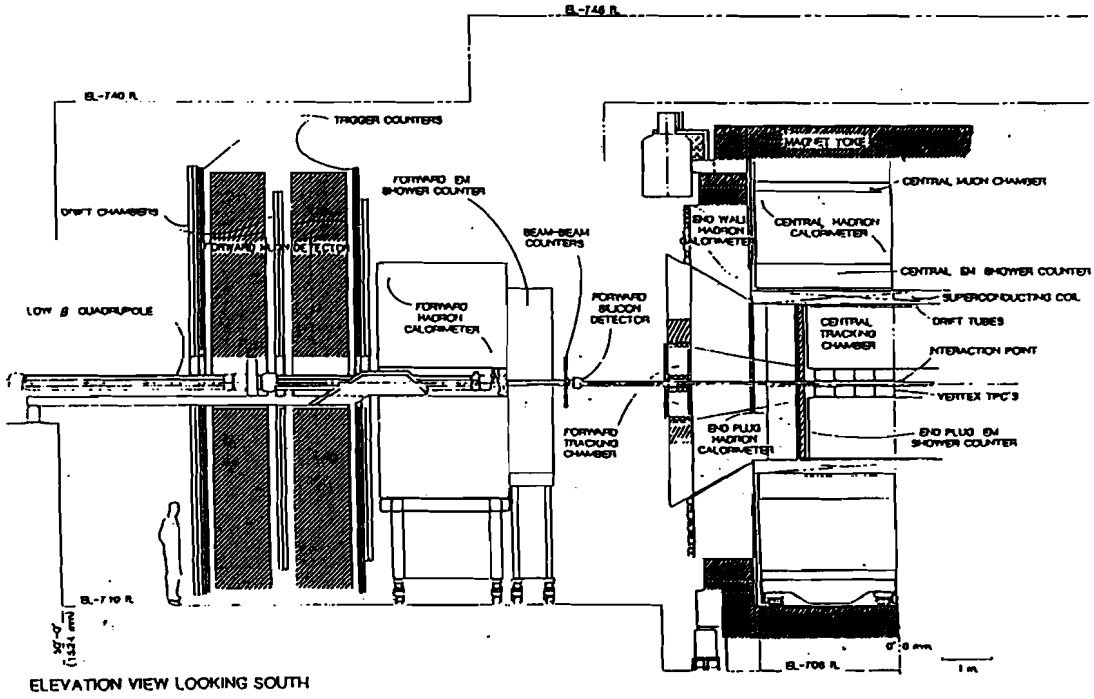

Figure 2.3: A vertical view of CDF detector. Normal collision point is right side of this picture, and from right side, Central detector with End plug calorimeter, and Forward Calorimeter, Toroidal magnet and Forward muon chamber.

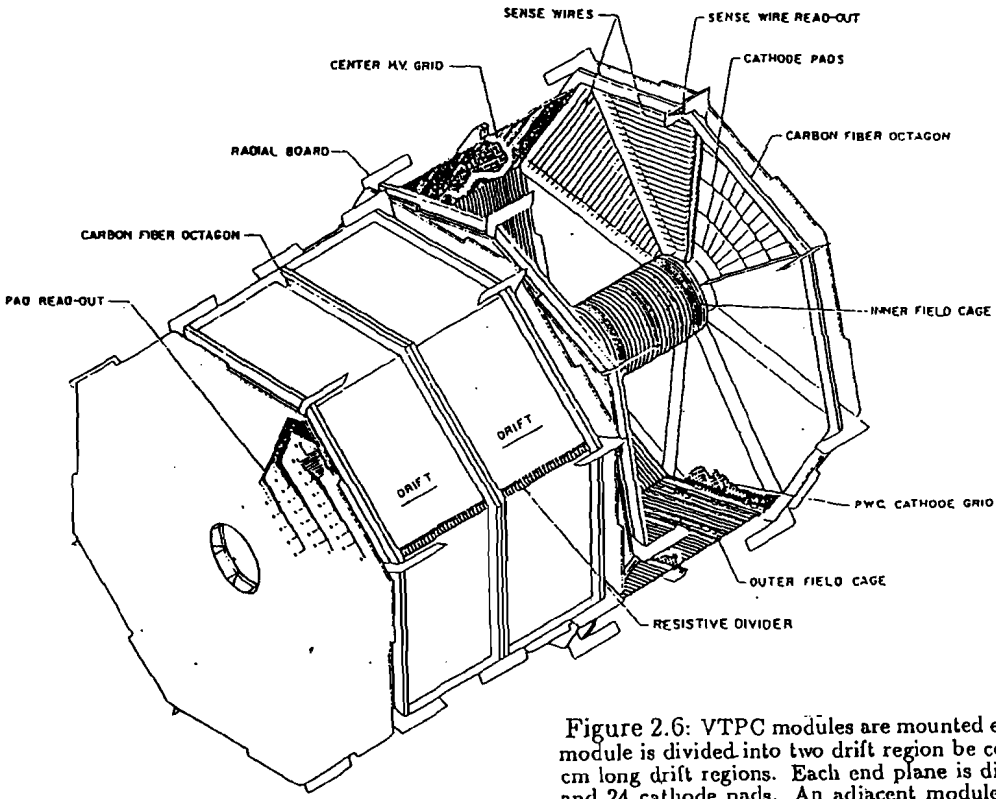

Figure 2.6: VTPC modules are mounted end to end surrounding beam pipe. One module is divided into two drift region be center high voltage grid. Each has 15.25 cm long drift regions. Each end plane is divided into octants with 24 sense wires and 24 cathode pads. An adjacent modules have a relative rotation angle of $\phi =$ arctan (0.2) around beam axis, so that it provide ϕinformation from small angle stereo, and eliminate the clack caused by octant boundary.

132

131

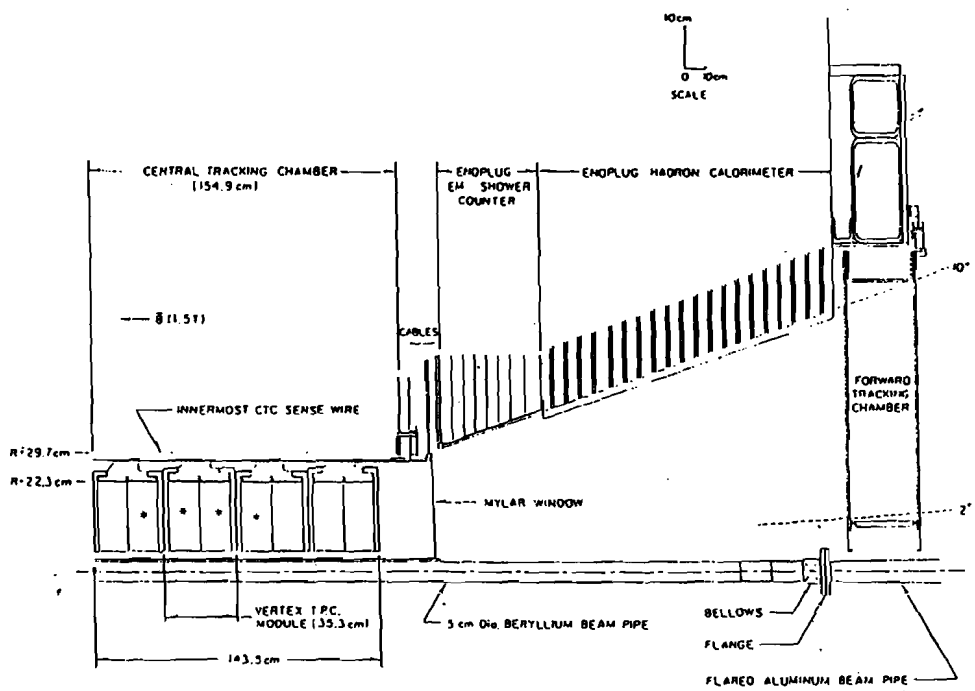

Figure 2.5: VTPC location at Central detector. The half modules marked with *, are pad implemented modules.

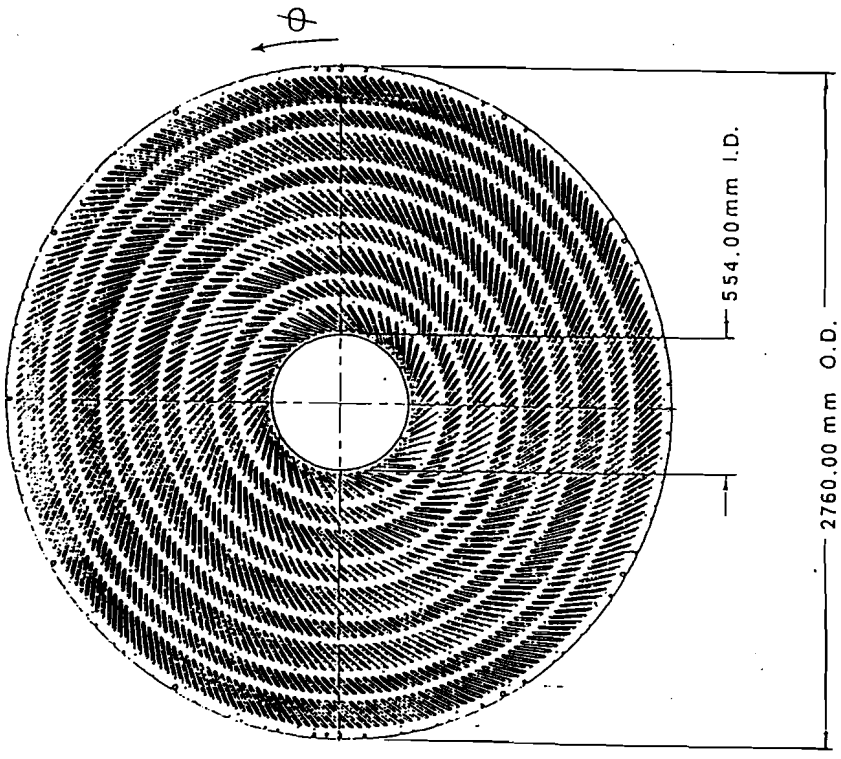

Figure 2.8: An end plate of Central tracking cahmber. The 84 layers of sense wires are held as nine supper layers.

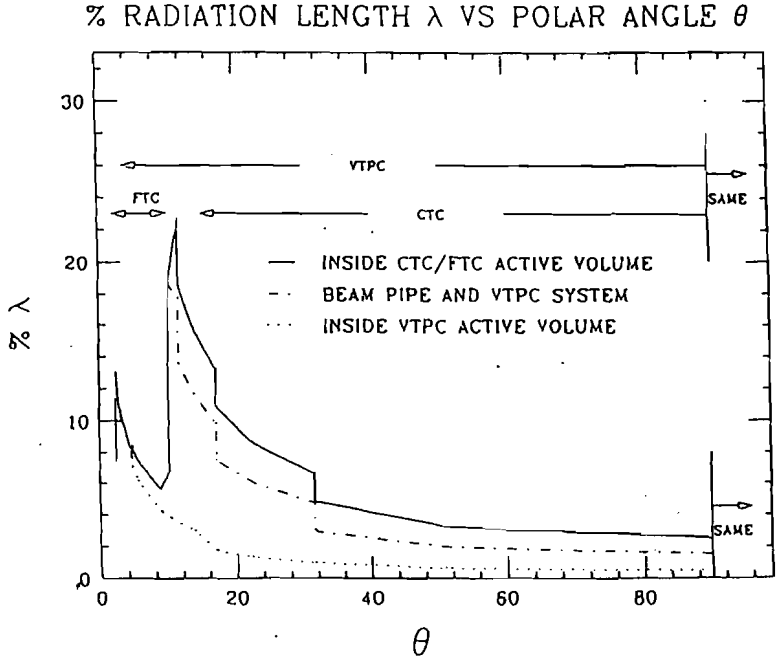

Figure 2.7: The amount of material in tracking system (as function of polar angle.The dotted line means material of Be beam pipe. The dot-dashed line includes beam pipe and material of VTPC system. The solid line include these two and material of CTC inner wall.

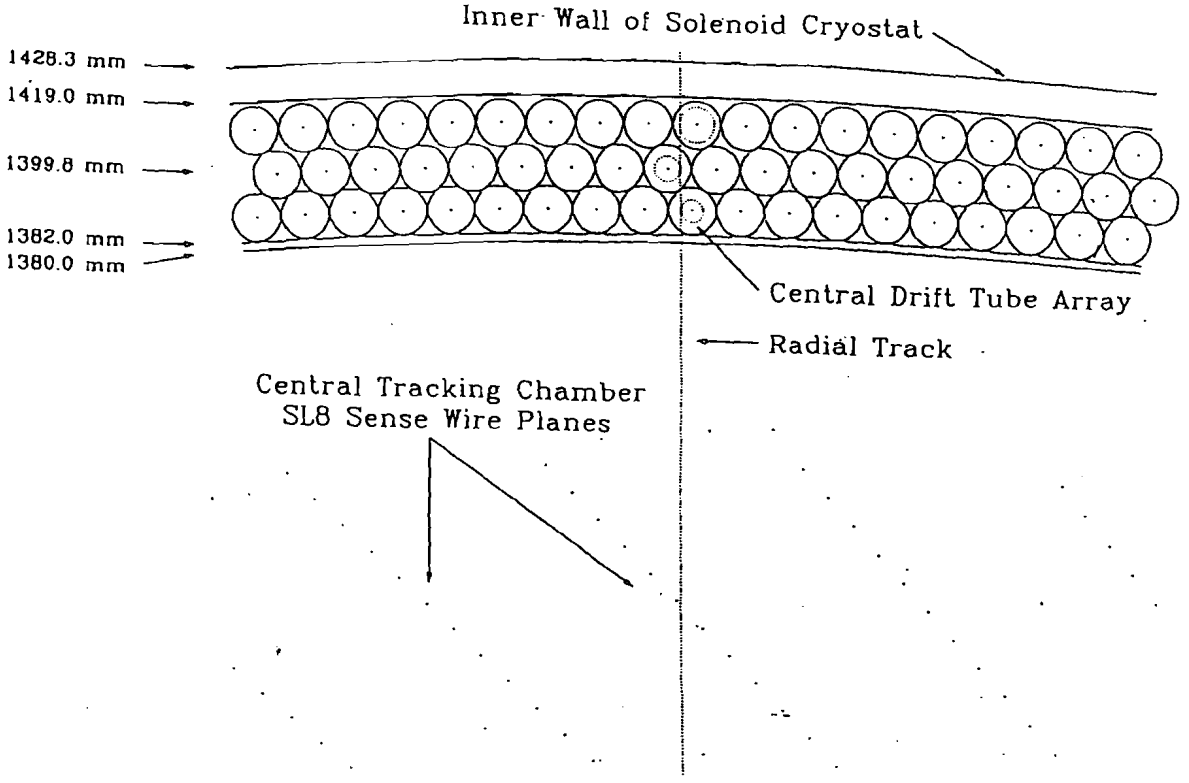

Figure 2.10: A cross section of Central Drift Tube. The CDT is composed of three layers of 3 m long, 1.27 cm diameter stainless steel tubes.

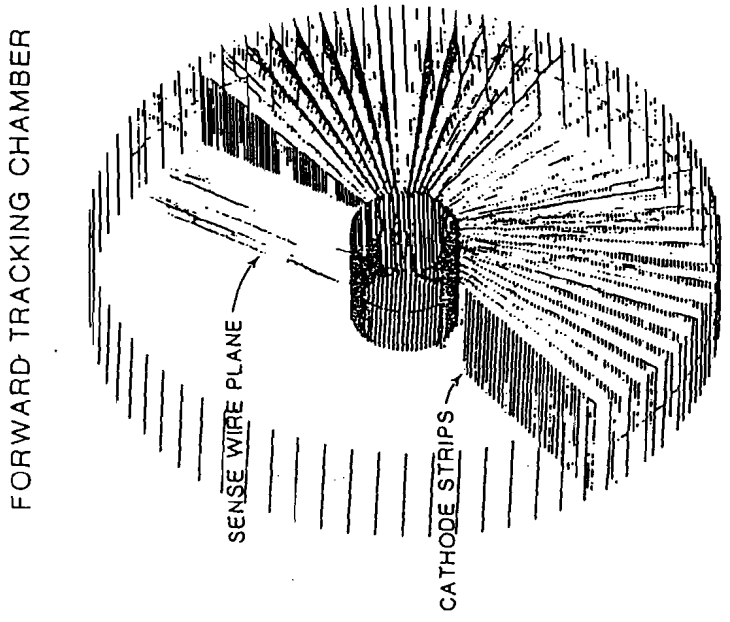

Figure 2.9: An isometric view of Forward tracking chamber The FTC is composed of 72 wedge shape cells, and each cell contains planes of radial anode and field shaping wires, and planes of cathode strip. The planes are slanted by 2 degree relative to the beam axis

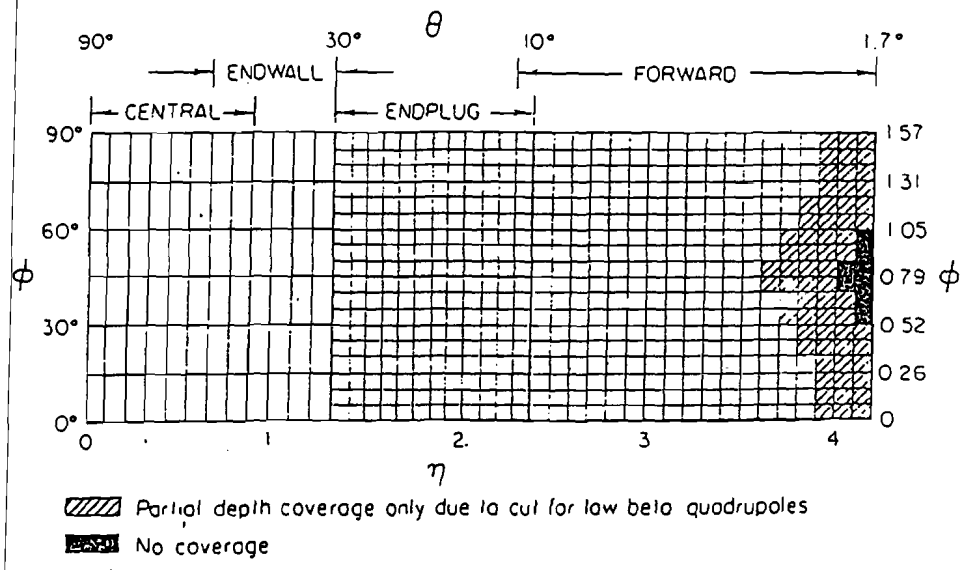

Figure 2.11: Calorimeter segmentation in $\eta - \phi$ space. The electromagnetic and hadron calorimeters have approximately uniform granularity in rapidity-azimuthal angle, and constructed in tower geometry pointing at interaction region. Typical tower size is set 0.1 in $\delta\eta$ and 15° in $\delta\phi$ for Central scintillator calorimeter, and 5° in Plug and Forward/backward gas calorimeters.

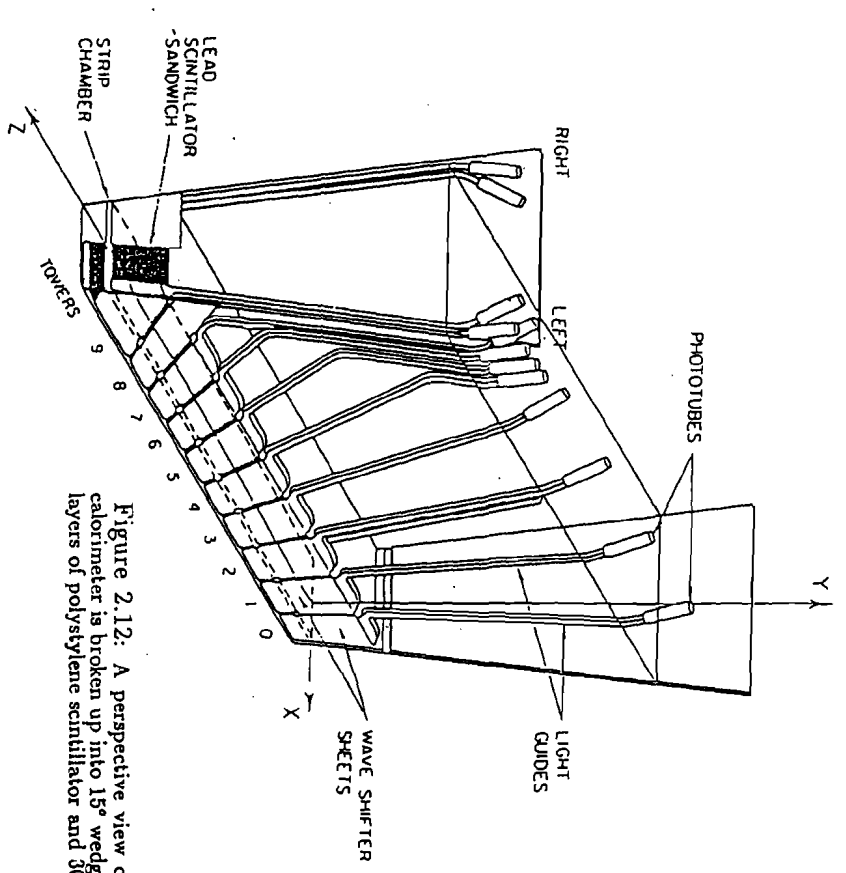

Figure 2.12: A perspective view of Central electromagnetic calorimeter, The calorimeter is broken up into 15° wedge style tower geometry. It is composed of 31 layers of polystylene scintillator and 30 layers of lead absorber.

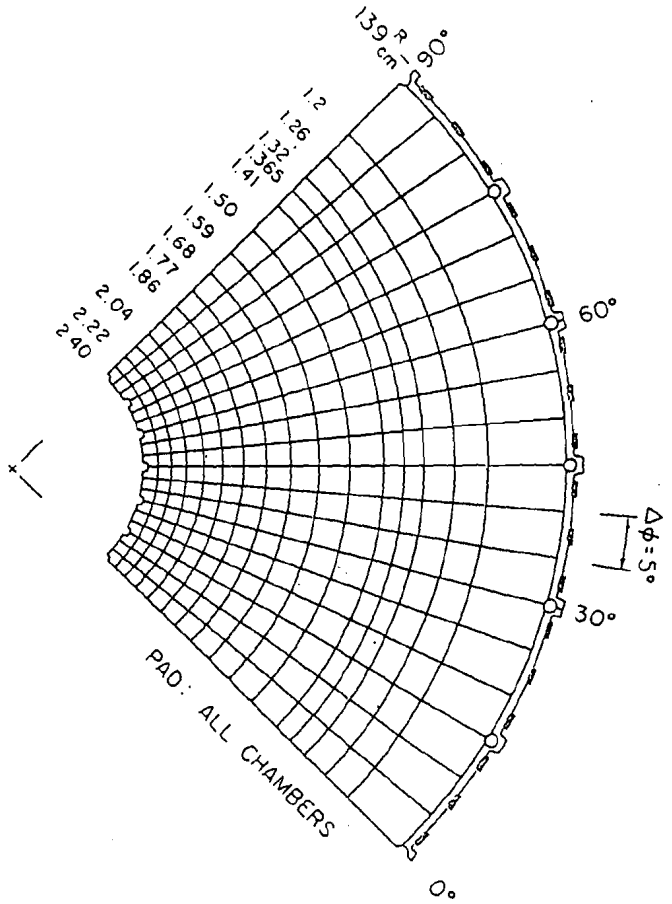

Figure 2.13: The segmentation of Endplug electromagnetic calorimeter. The calorimeter tower size are $\delta\eta = 0.09$ at $1.41 < \eta < 2.4$, $\delta\eta = 0.045$ at $1.1 < \eta < 1.41$, and $\delta\phi = 5°$.

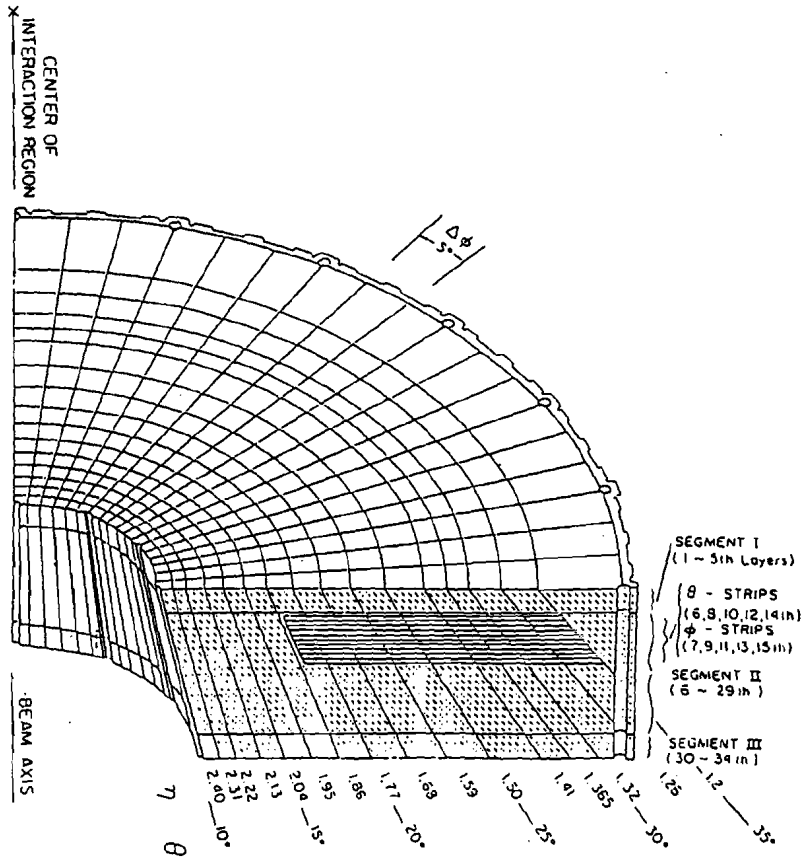

Figure 2.14: The detector consists of 34 layers of proportional counters and 2.7 mm lead plate absorber. The pad signals are ganged in longitudinal direction, and readout as three depth segment.

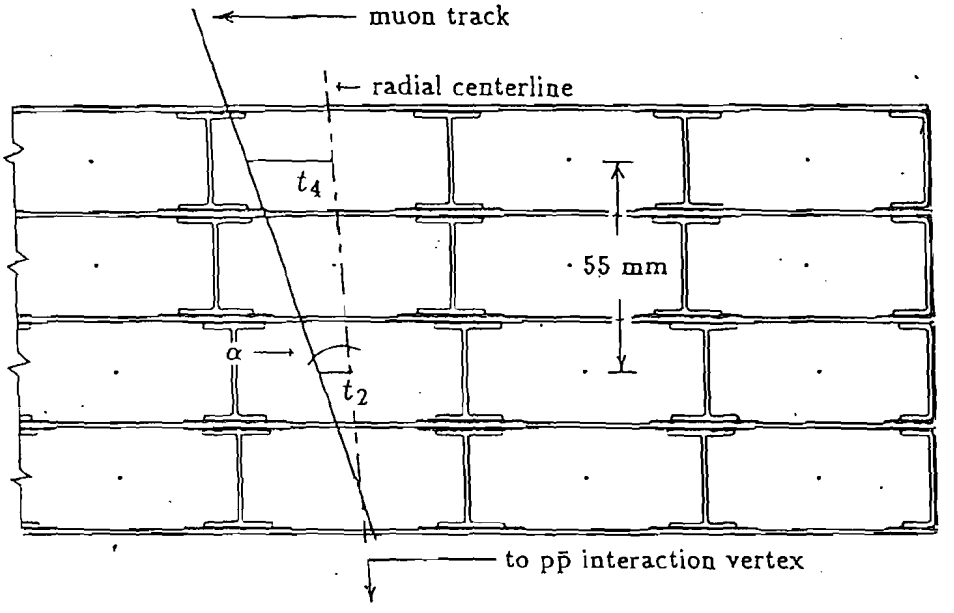

Figure 2.17: A cross section of Central muon chamber. The central muon chamber consists of three layers of drift chamber and measures azimuthal position using drift time, and z coordinate from the charge division sense wires.

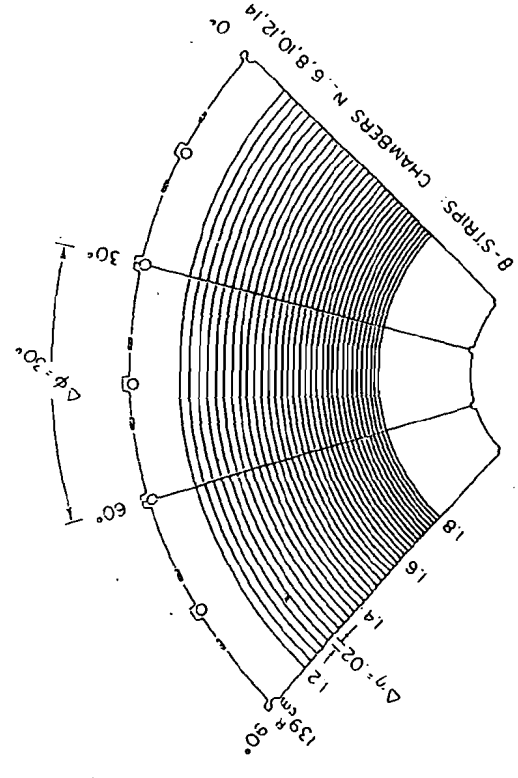

Figure 2.15: The patterns of η strip in Endplug electro magnetic calorimeter. Two kinds of strip patterns are implemented around the shower maximum of the calorimeter. These are orthogonal with each other.

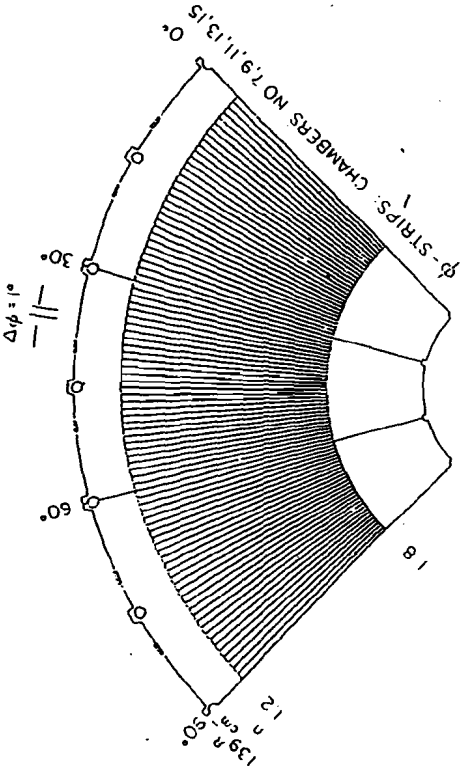

Figure 2.16: The patterns of ϕ strip in Endplug electro magnetic calorimeter

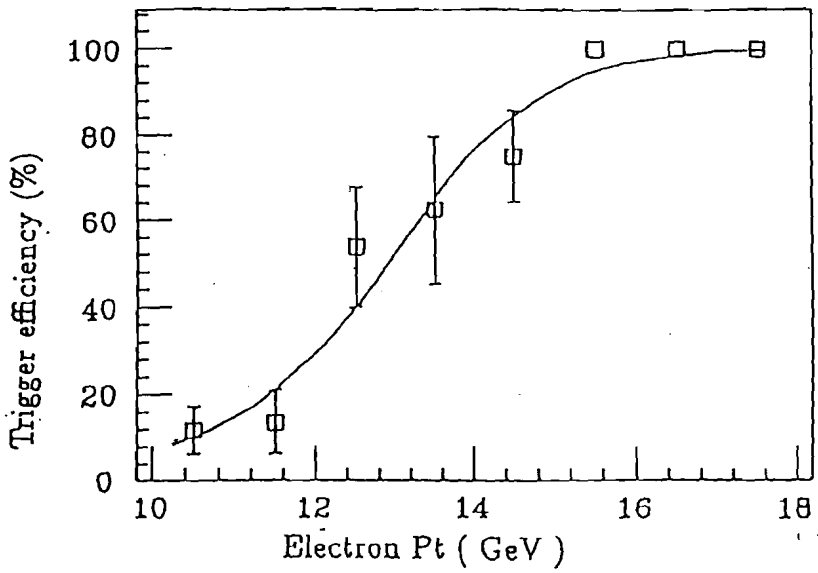

Level 2 Central 12 GeV electron trigger efficiency

Figure 3.1: Nonisolated electron trigger efficiency of central calorimeter as a function of electron transverse momentum.

144

143

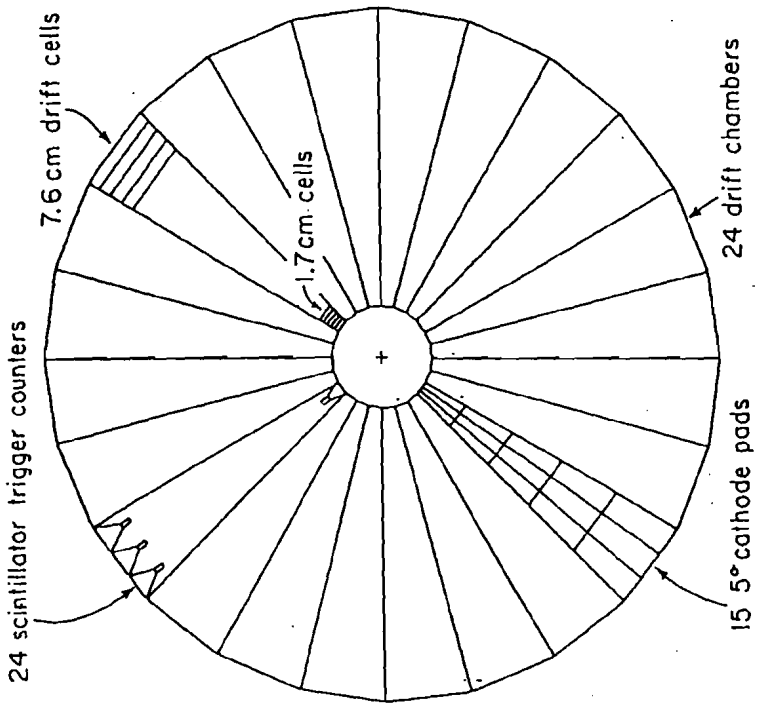

Figure 2.18: A beam eye view of Forward muon chamber. The forward muon chamber covers $3° < \theta < 16°, 164° < \theta < 177°$.

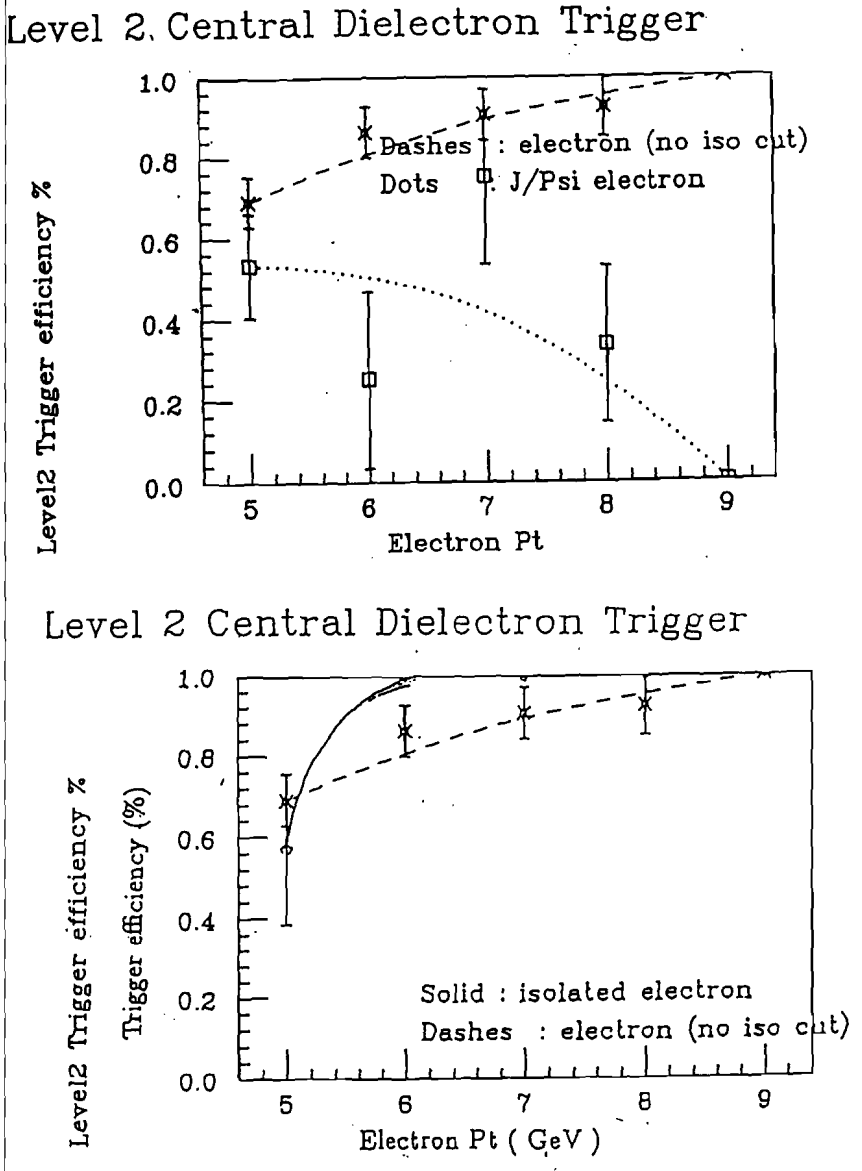

Figure 3.2: 5 GeV electron level 2 trigger efficiency has been studied using second electron of dielectron sample whose first electron is triggered by Central 12 GeV electron trigger.

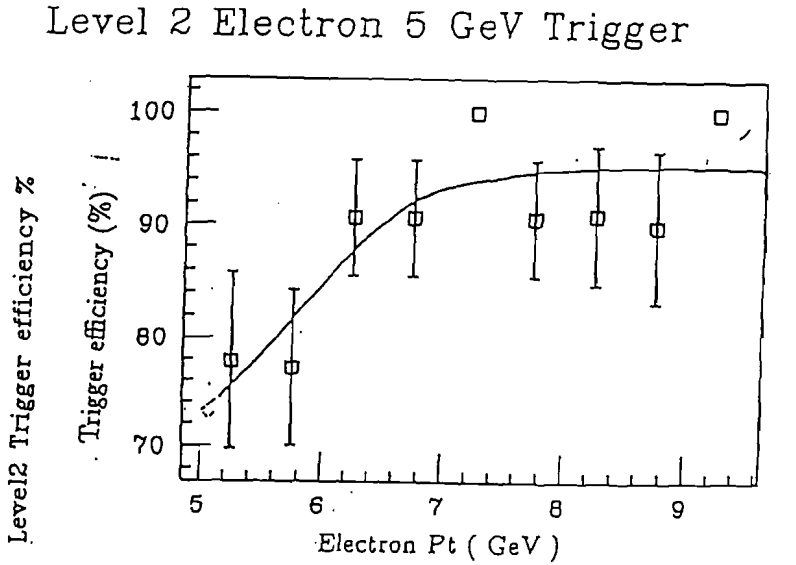

Figure 3.3: 5 GeV electron level 2 trigger efficiency has been studied using events triggered by Central muon triggers.

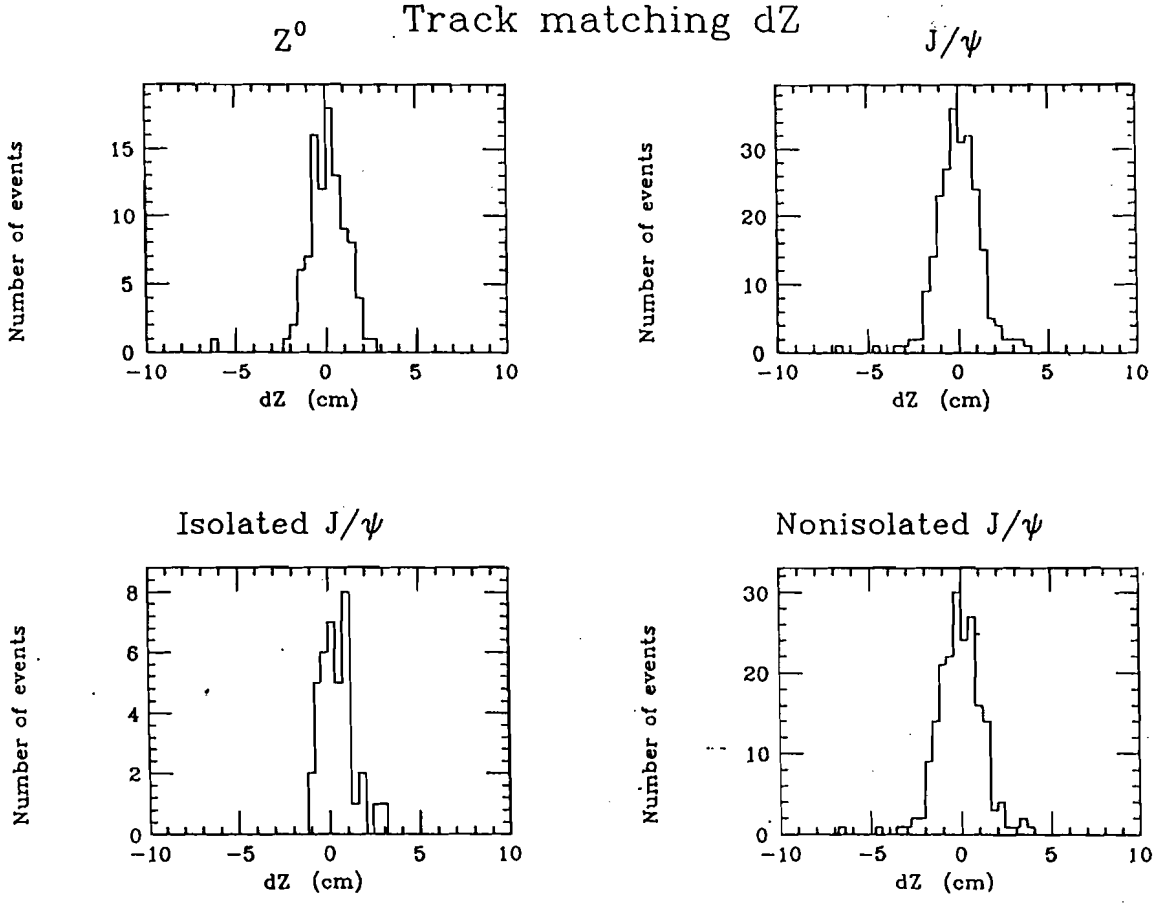

Figure 3.5: the distribution of Central electron cut parameters of 2nd electron for four different electron samples, Z0,J/Ψ ,isolated J/Ψ ,nonisolated J/Ψ .

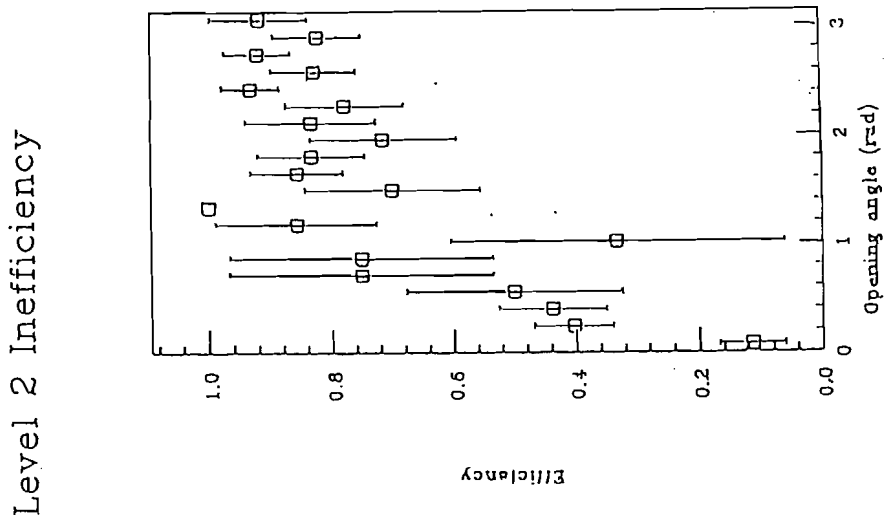

Figure 3.4: Level 2 trigger efficiency is plotted as a function of opening angle of two electrons.

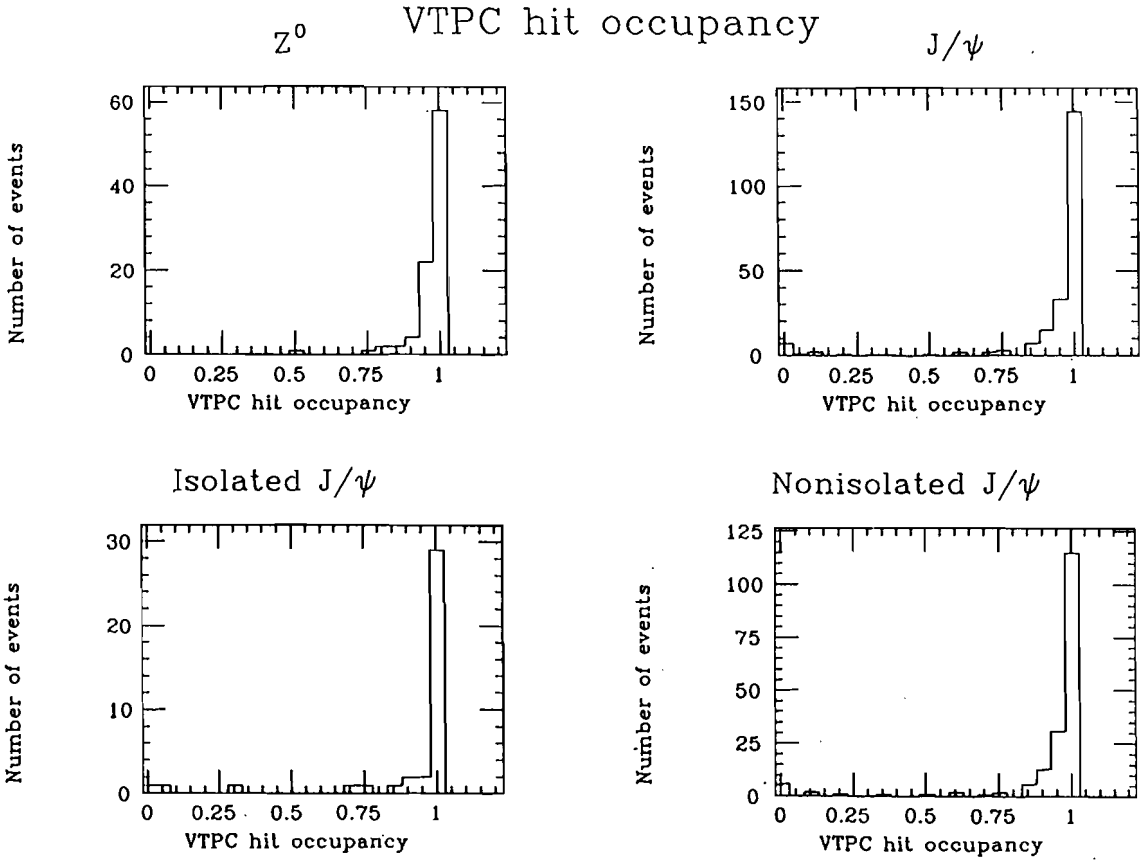

Figure 3.5: The distribution of Central electron cut parameters of 2nd electron for four different electron samples, Z0,J/Ψ,isolated J/Ψ,nonisolated J/Ψ.

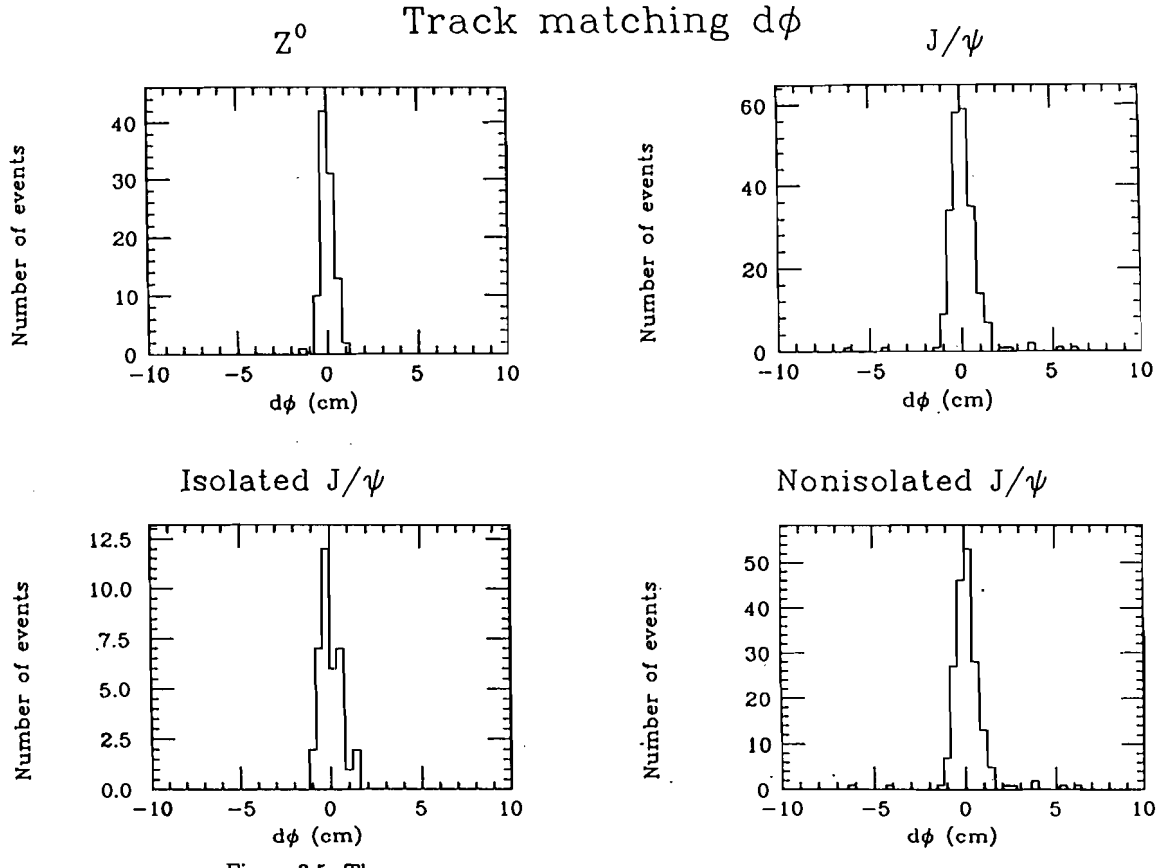

Figure 3.5: The distribution of Central electron cut parameters of 2nd electron for four different electron samples, Z0,J/Ψ,isolated J/Ψ,nonisolated J/Ψ.

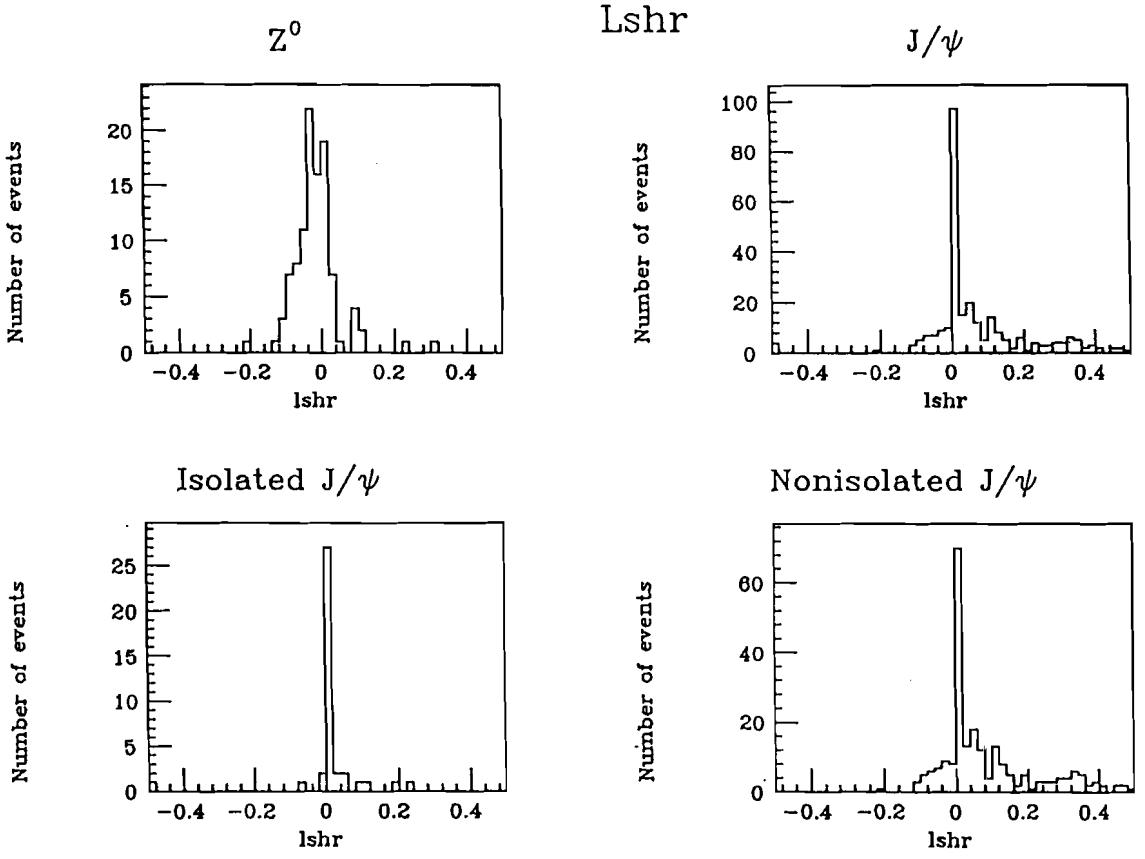

Figure 3.5: The distribution of Central electron cut parameters of 2nd electron for four different electron samples, Z0,J/Ψ,isolated J/Ψ,nonisolated J/Ψ.

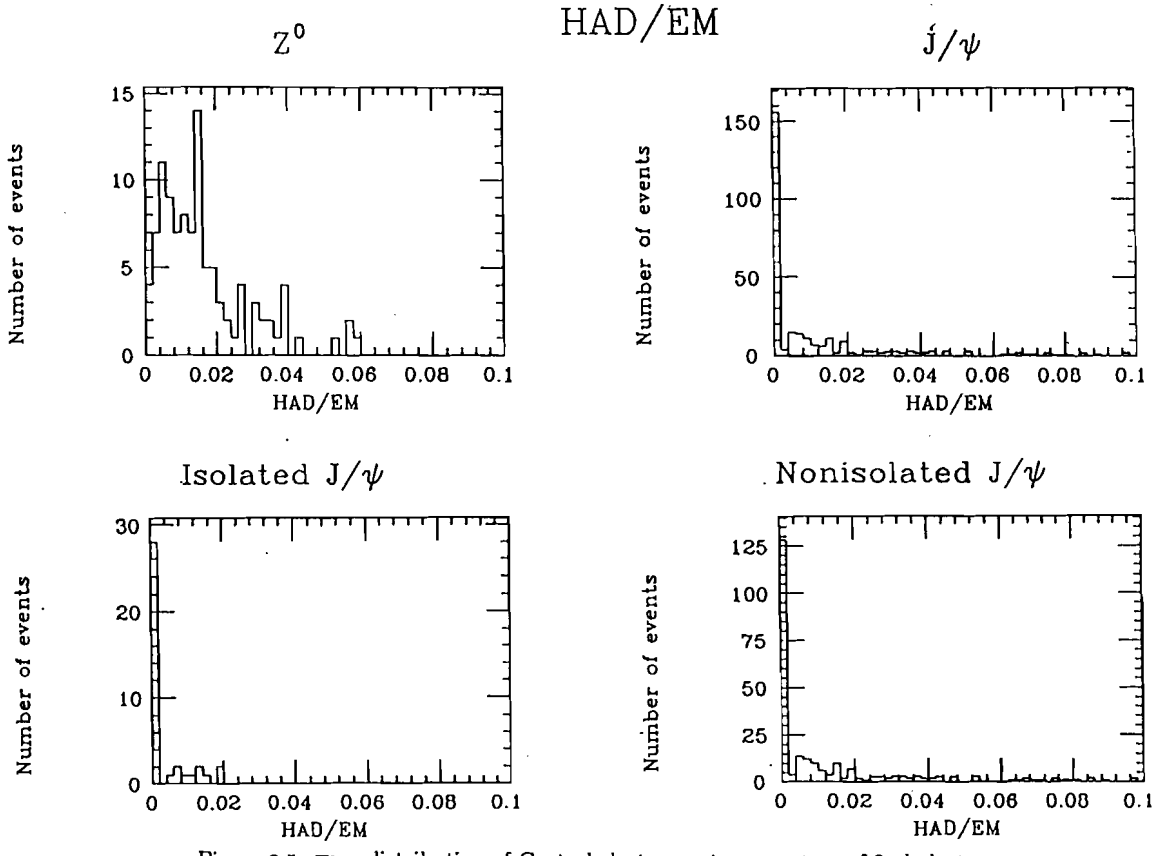

Figure 3.5: The distribution of Central electron cut parameters of 2nd electron for four different electron samples, Z0,J/Ψ,isolated J/Ψ,nonisolated J/Ψ.

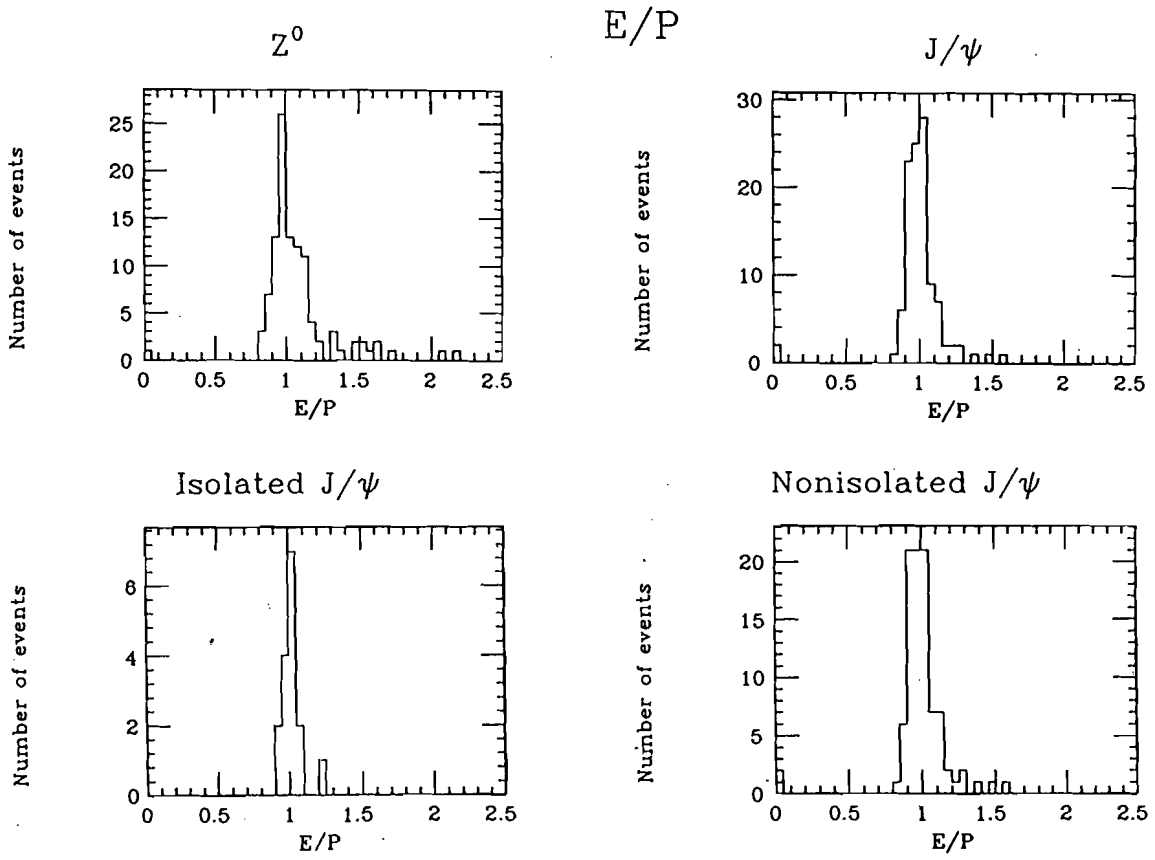

Figure 3.5: The distribution of Central electron cut parameters of 2nd electron for four different electron samples, Z0,J/Ψ,isolated J/Ψ,nonisolated J/Ψ.

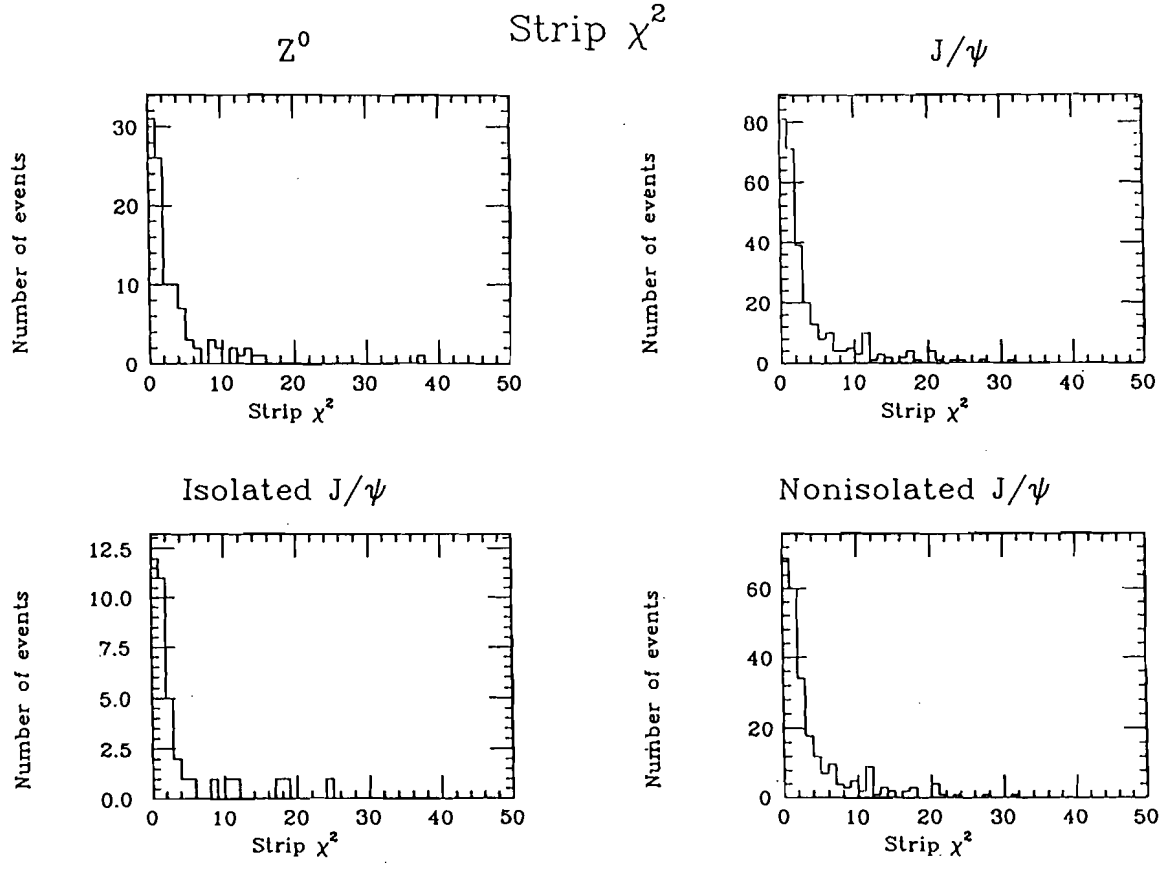

Figure 3.5: The distribution of Central electron cut parameters of 2nd electron for four different electron samples, Z0,J/Ψ,isolated J/Ψ,nonisolated J/Ψ.

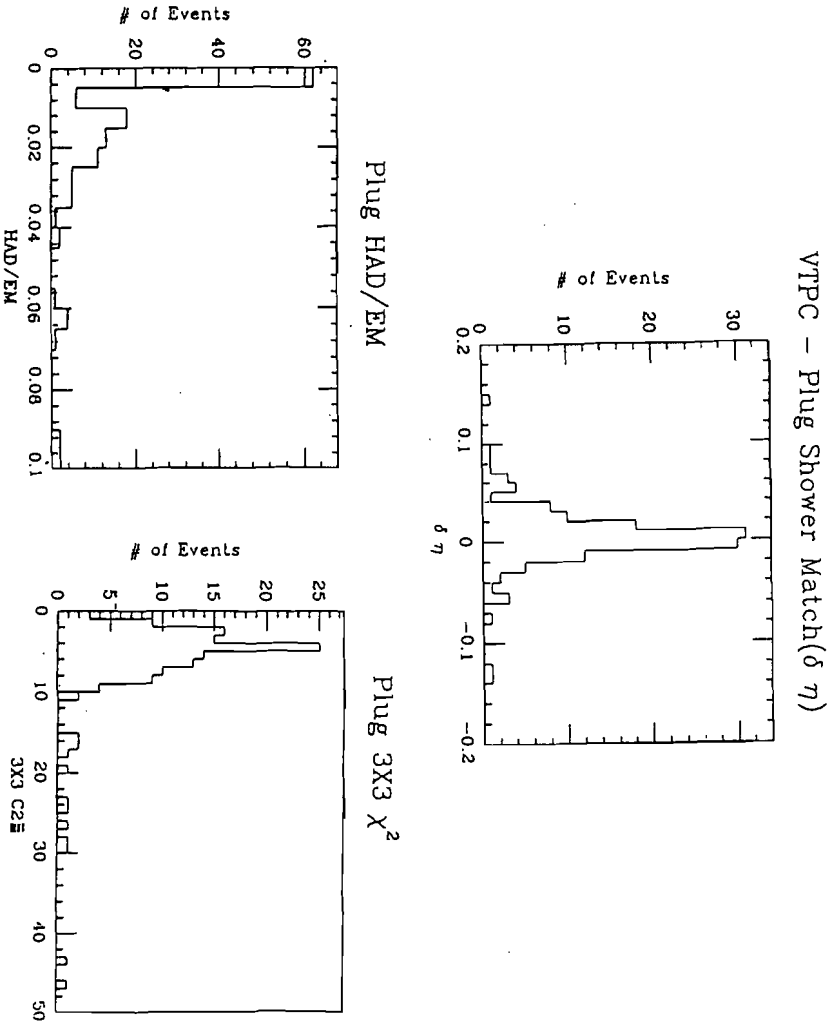

Figure 3.6: the distribution of Plug electron cut parameters of 2nd electron ZOs

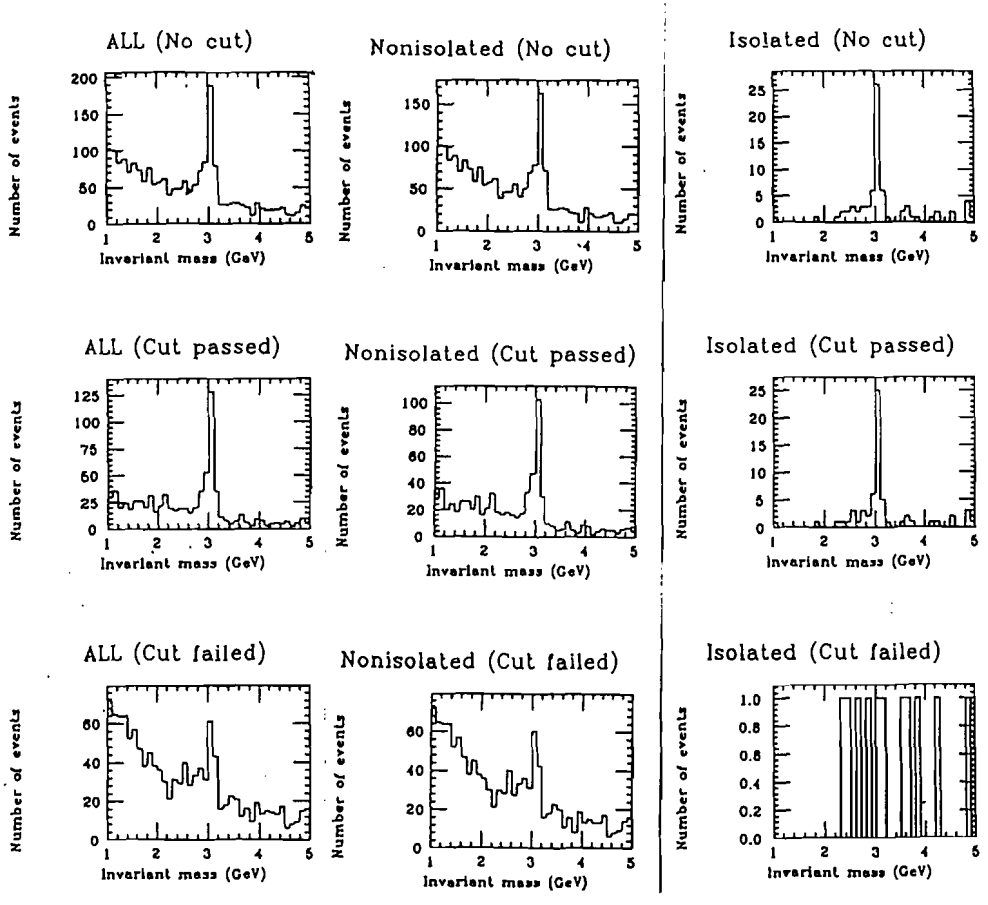

Figure 3.7: Signal to backgrounds ration around J / P mass peak.
Tight cuts are applied to the one electron in upper three figures for all, isolated (I_{max}< 0.1) and nonisolated (I_{max}> 0.1) electron pairs. The middle three figures show the mass distribution of the events that passed one tight electron and one loose electron cuts. The lower three figure shows the mass distribution which failed 2nd electron cut.

Figure 3.8 (B1) : ALL

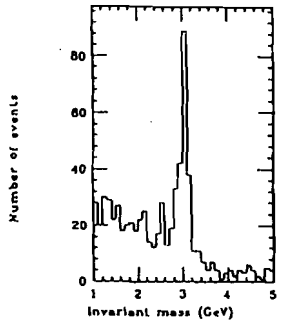

Figure 3.8 (B2) : E/P

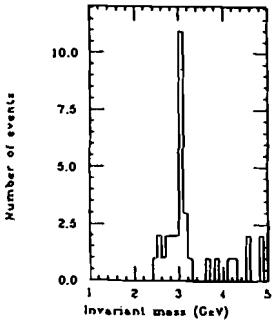

Figure 3.8 (B3) : Nonisolated

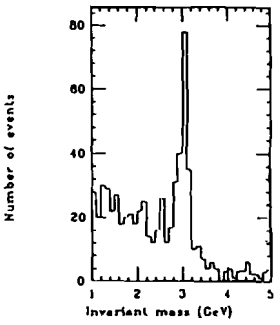

Figure 3.8 (B4) ALL

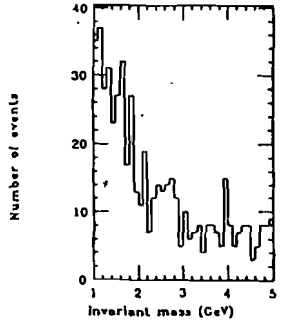

Figure 3.8 (B5) Isolated

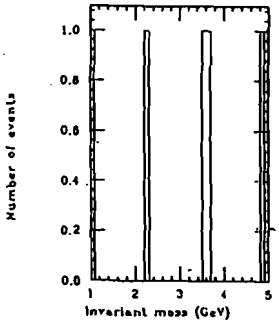

Figure 3.8 (B6) Nonisolated

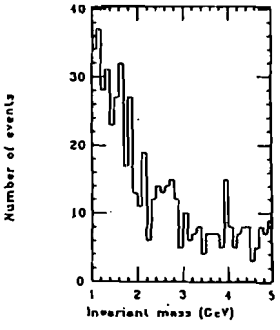

Figure 3.8(B): Central electron cut inefficiencies. The upper three figures (B1 - B3) are invariant mass distribution of lepton pairs which satisfied E/P cuts around the J/Ψ. The lower three figures (B4-B6) are that of lepton pairs that dose not satisfied the E/P cuts.

158

Figure 3.8 (A1) : ALL

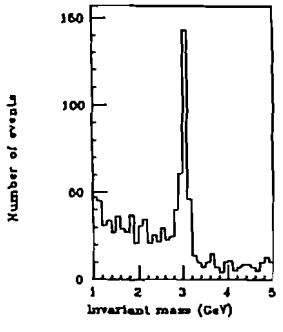

Figure 3.8 (A2) : Lshr

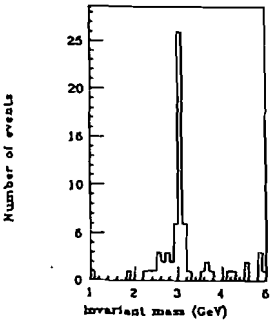

Figure 3.8 (A3) : Nonisolated

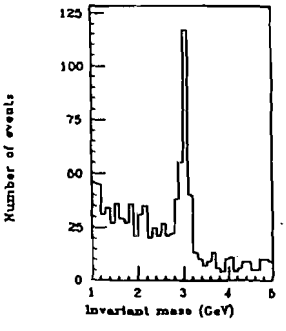

Figure 3.8 (A4) : ALL

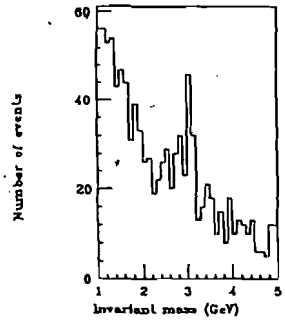

Figure 3.8 (A5) : Isolated

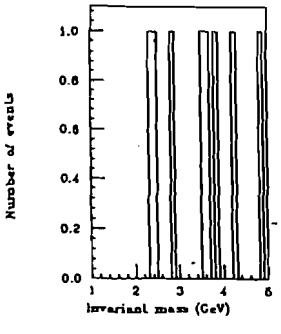

Figure 3.8 (A6) : Nonisolated

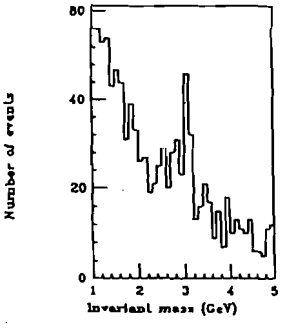

Figure 3.8(A): Central electron cut inefficiencies. The upper three figures (A1 - A3) are invariant mass distribution of lepton pairs which satisfied LSHR cuts around the J/Ψ. The lower three figures (A4-A6) are that of lepton pairs that dose not satisfied the LSHR cuts.

157

Figure 3.8 (D1) : ALL Strip chi2 Figure 3.8 (D2) : Nonisolated Figure 3.8 (D3) :

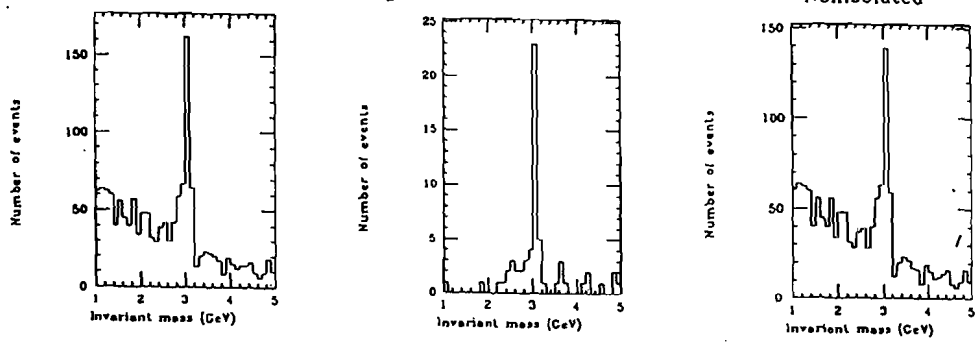

Figure 3.8 (D4) ALL Figure 3.8 (D5) Isolated Figure 3.8 (D6) Nonisolated

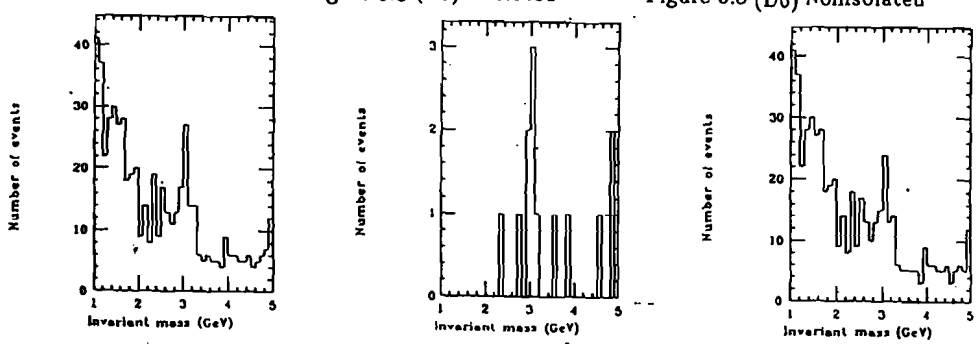

Figure 3.8(D): Central electron cut inefficiencies. The upper three figures (D1 - D3) are invariant mass distribution of lepton pairs which satisfied Strip χ^2 cuts around the J/Ψ. The lower three figures (D4-D6) are that of lepton pairs that dose not satisfied the Strip χ^2 cuts.

Figure 3.8 (C1) : ALL Figure 3.8 (C2) : HAD/EM Figure 3.8 (C3) : Nonisolated

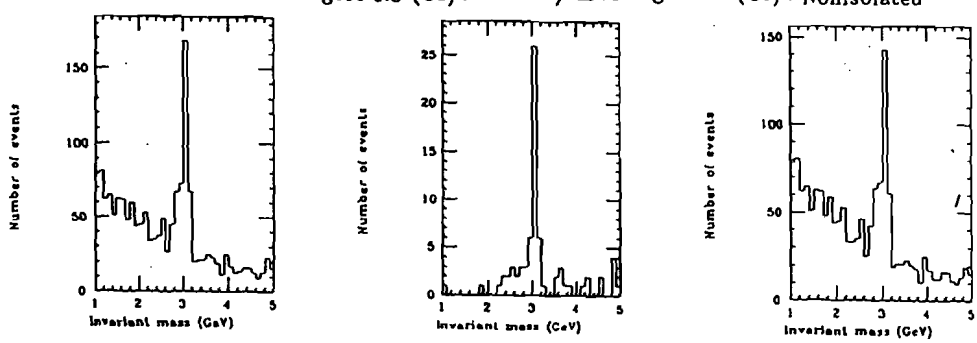

Figure 3.8 (C4) : ALL Figure 3.8 (C5) : Isolated Figure 3.8 (C6) : Nonisolated

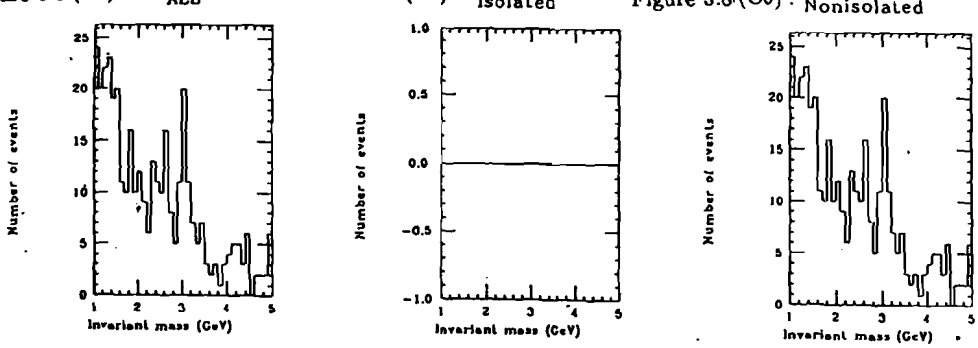

Figure 3.8(C): Central electron cut inefficiencies. The upper three figures (C1 - C3) are invariant mass distribution of lepton pairs which satisfied HAD/EM cuts around the J/Ψ. The lower three figures (C4-C6) are that of lepton pairs that dose not satisfied the HAD/EM cuts.

Figure 3.8 (F1) : ALL

Track matching dphi

Figure 3.8 (F2)

Figure 3.8 (F3) : Nonisolated

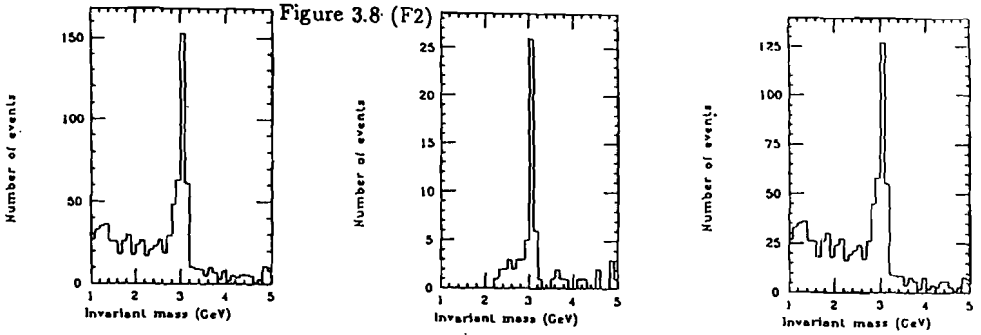

Figure 3.8 (F4) : ALL

Figure 3.8 (F5) : Isolated

Figure 3.8 (F6) : Nonisolated

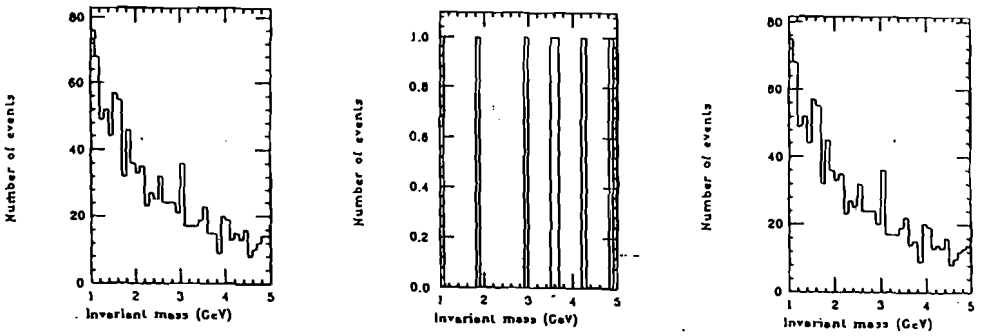

Figure 3.8(F): Central electron cut inefficiencies. The upper three figures (F1 - F3) are invariant mass distribution of lepton pairs which satisfied a cut of a match between an extrapolated track position and shower center. The lower three figures (F4-F6) are that of lepton pairs that dose not satisfied the cuts.

Figure 3.8 (E1) : ALL

track matching dZ

Figure 3.8 (E2)

Figure 3.8 (E3) : Nonisolated

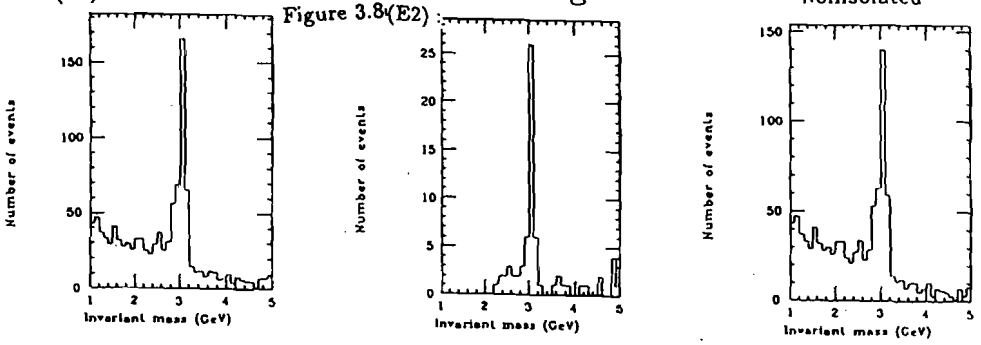

Figure 3.8 (E4) : ALL

Figure 3.8 (E5) : Isolated

Figure 3.8 (E6) : Nonisolated

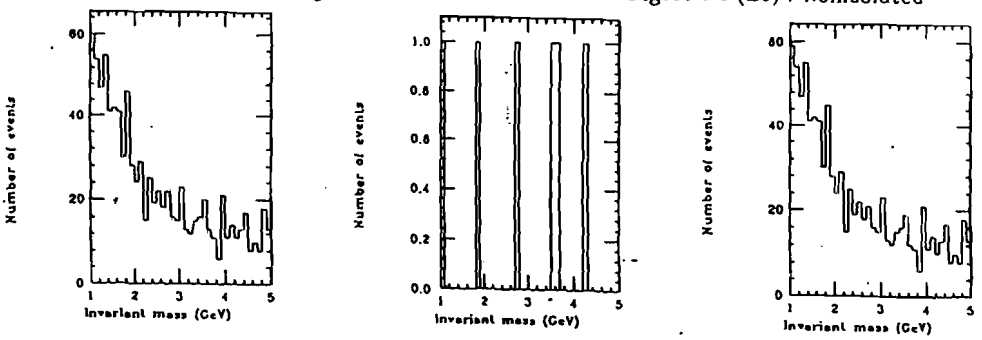

Figure 3.8(E): Central electron cut inefficiencies. The upper three figures (E1 - E3) are invariant mass distribution of lepton pairs which satisfied a cut of a match between an extrapolated track position and shower center. The lower three figures (E4-E6) are that of lepton pairs that dose not satisfied the cut.

Figure 3.8 (H1) : ALL

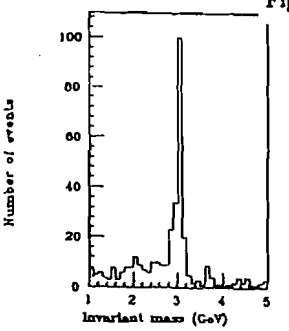

Figure 3.8 (H2) Tight cut

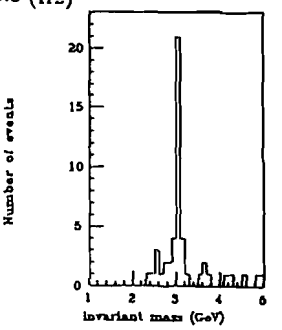

Figure 3.8 (H3) : Nonisolated

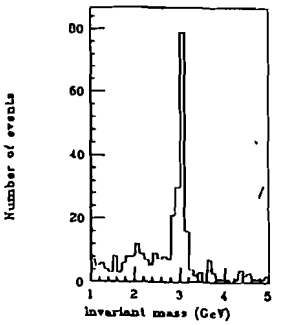

Figure 3.8 (H4) : ALL

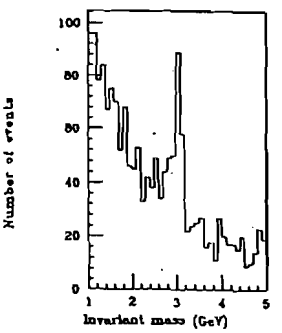

Figure 3.8 (H5) : Isolated

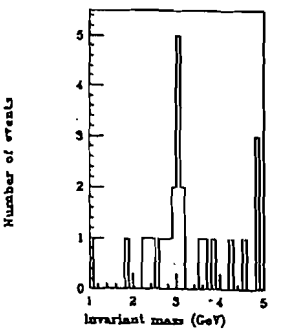

Figure 3.8 (H6) : Nonisolated

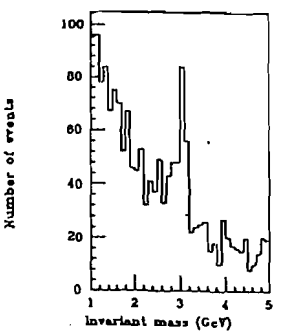

Figure 3.8(H): Central electron cut inefficiencies. The upper three figures (H1 - H3) are invariant mass distribution of lepton pairs which satisfied tight cuts around the J/Ψ. The lower three figures (H4-H6) are that of lepton pairs that dose not satisfied the tight cuts.

Figure 3.8 (G1) : ALL

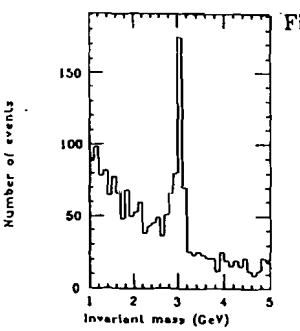

VTPC hit occupancy

Figure 3.8 (G2)

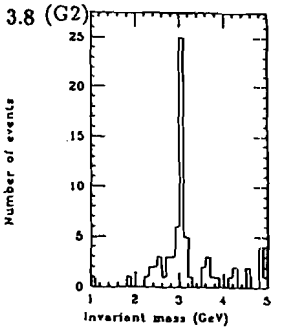

Figure 3.8 (G3) : Nonisolated

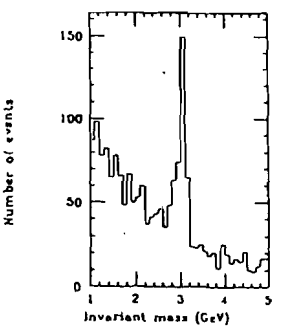

Figure 3.8 (G4) : ALL

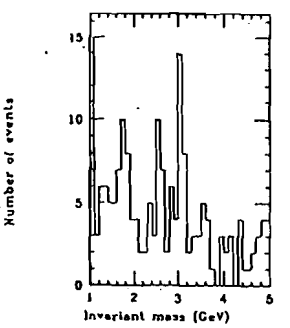

Figure 3.8 (G5) : Isolated

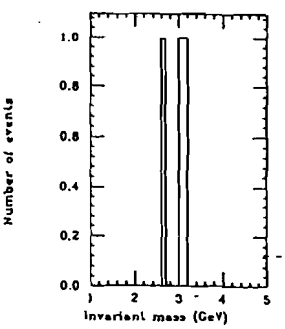

Figure 3.8 (G6) : Nonisolated

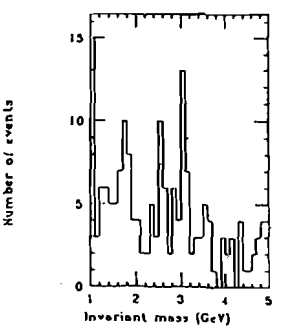

Figure 3.8(G): Central electron cut inefficiencies. The upper three figures (G1 - G3) are invariant mass distribution of lepton pairs which satisfied VTPC hit occupancy cuts around the J/Ψ. The lower three figures (G4-G6) are that of lepton pairs that dose not satisfied the VTPC hit occupancy cuts.

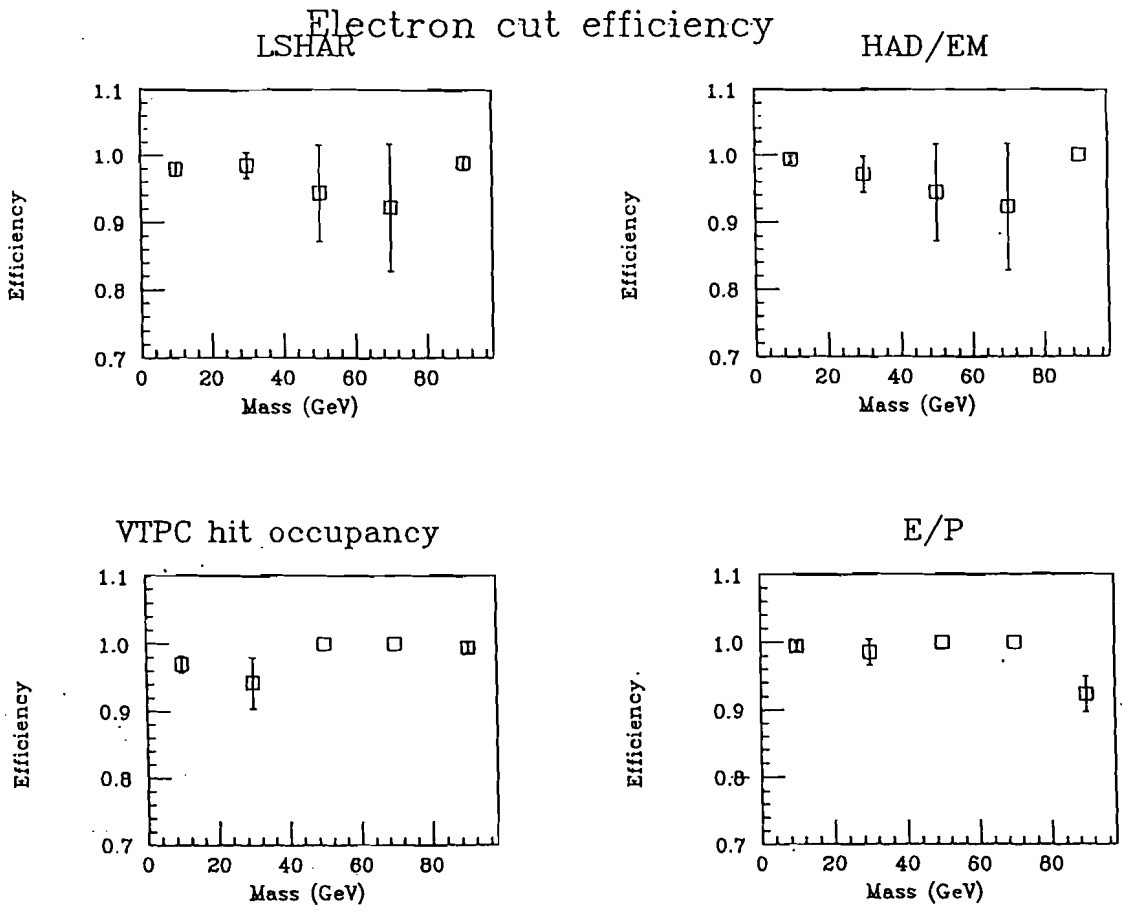

Figure 3.9: Central isolated electron identification efficiency invariant mass dependence

Figure 3.8 (I1) : ALL

Figure 3.8 (I2) : Loose cut

Figure 3.8 (I3) : Nonisolated

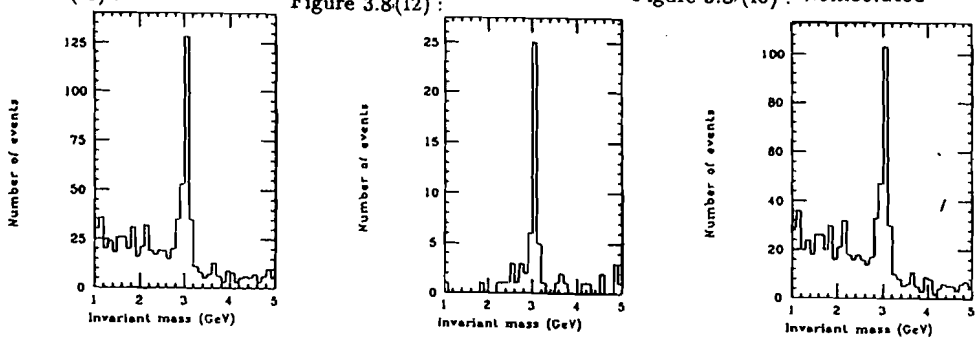

Figure 3.8 (I4) : ALL

Figure 3.8 (I5) : Isolated

Figure 3.8 (I6) : Nonisolated

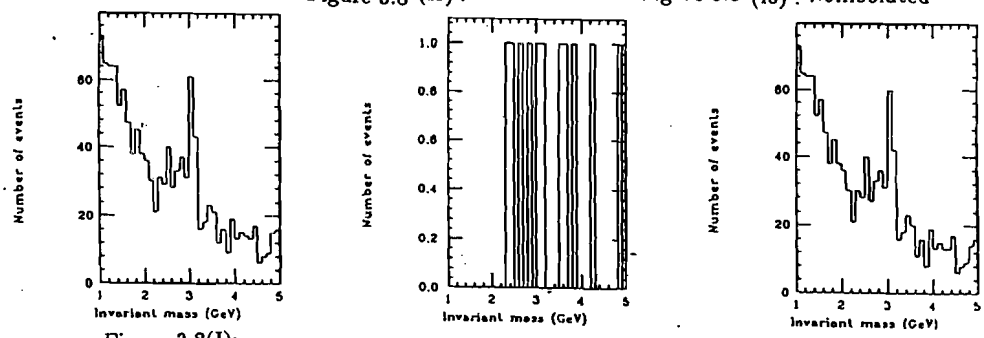

Figure 3.8(I): Central electron cut inefficiencies. The upper three figures (I1 - I3) are invariant mass distribution of lepton pairs which satisfied loose cuts around the J/Ψ. The lower three figures (I4-I6) are that of lepton pairs that dose not satisfied the loose cuts.

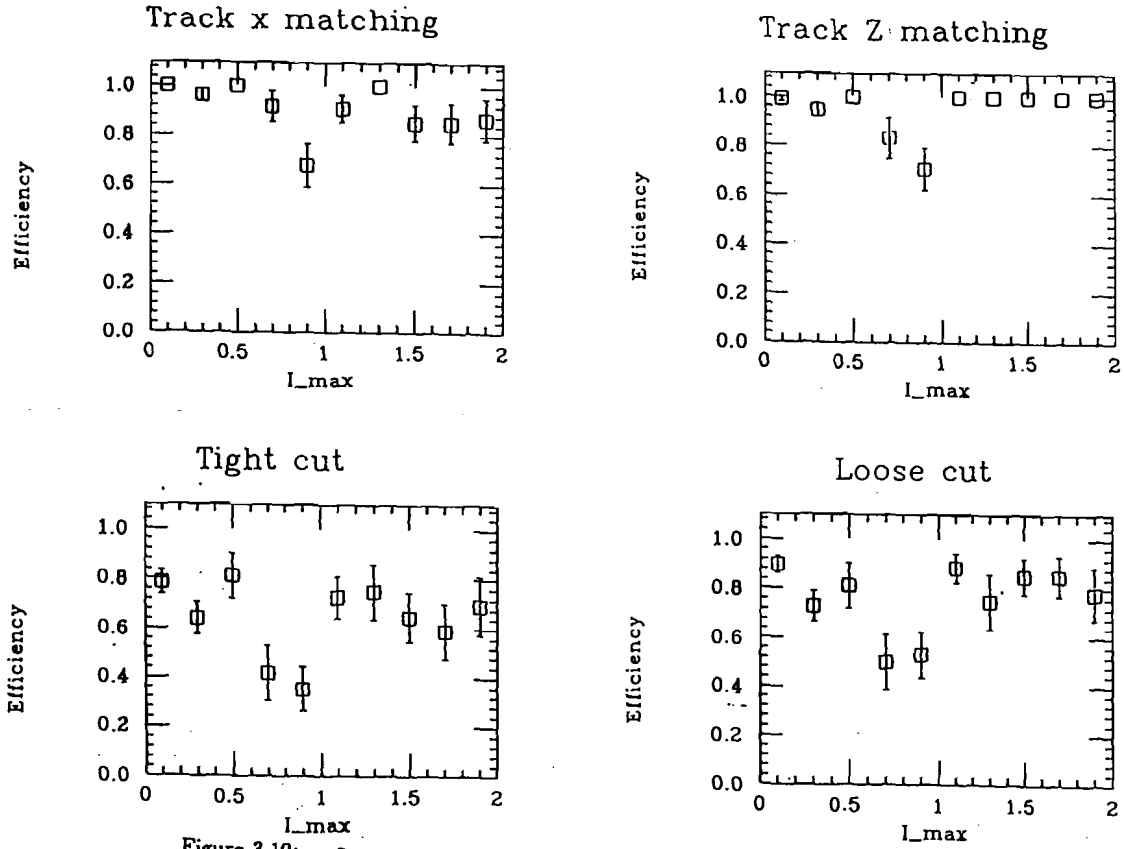

Figure 3.10: Central electron identification efficiency isolation dependence are investigated using $J\Psi$ electrons.

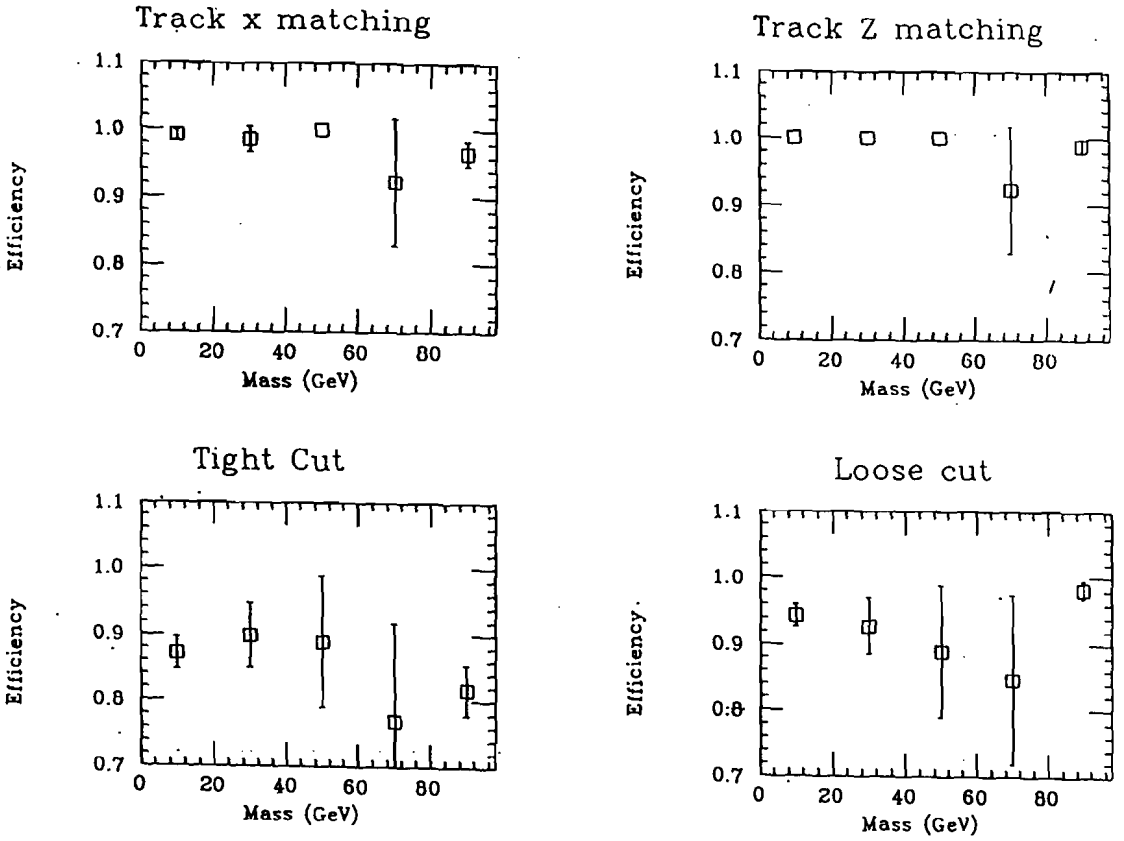

Figure 3.9: Central isolated electron identification efficiency invariant mass dependence

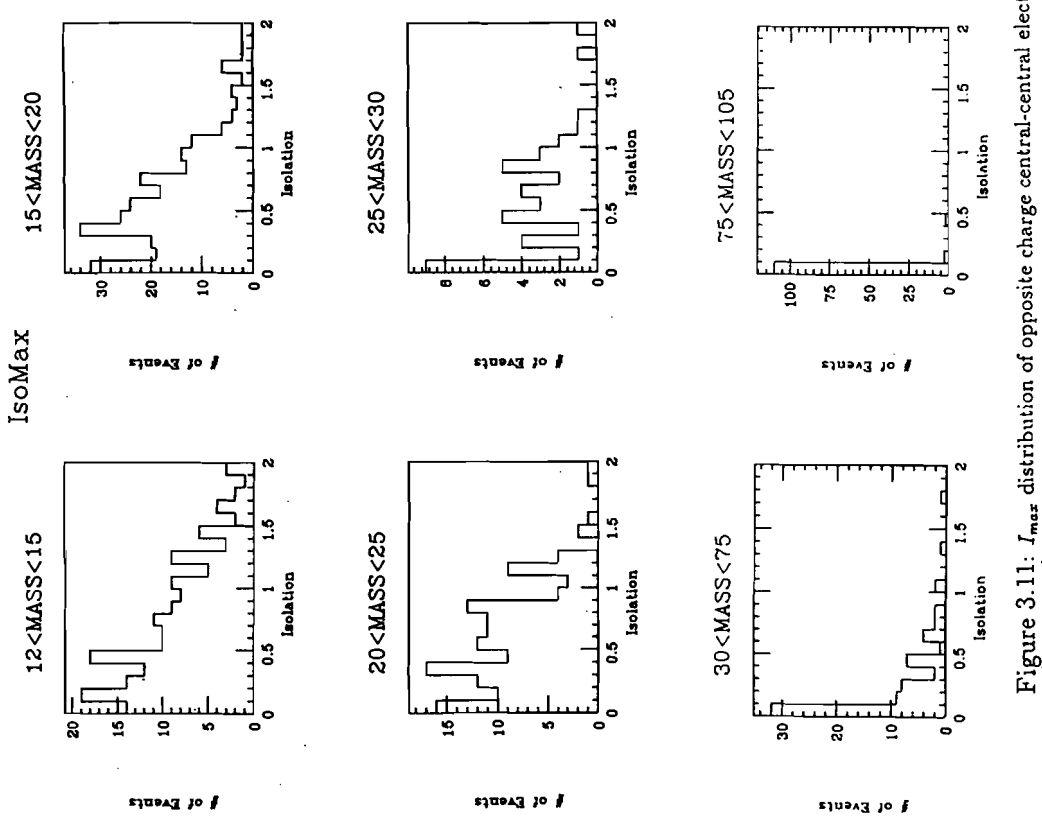

Figure 3.11: I_{max} distribution of opposite charge central-central electron pairs in each mass region.

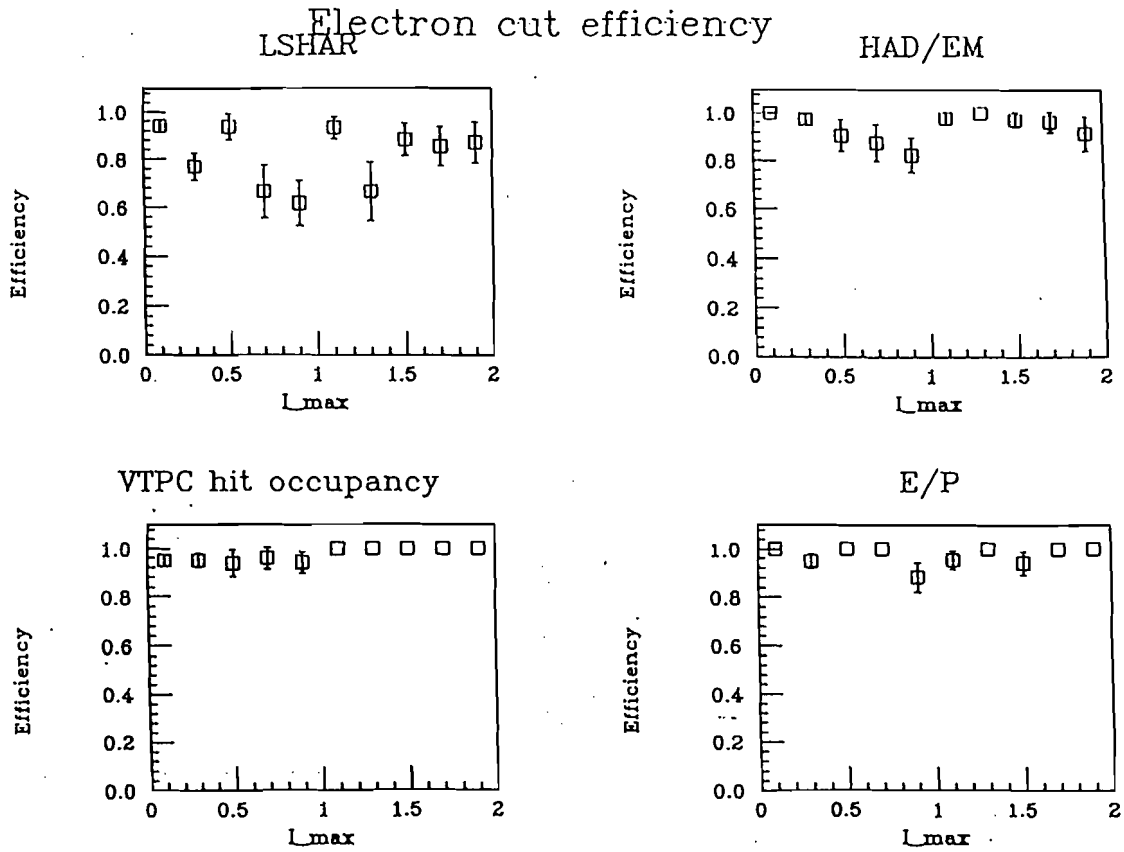

Figure 3.10: Central electron identification efficiency isolation dependence are investigated using $J\Psi$ electrons.

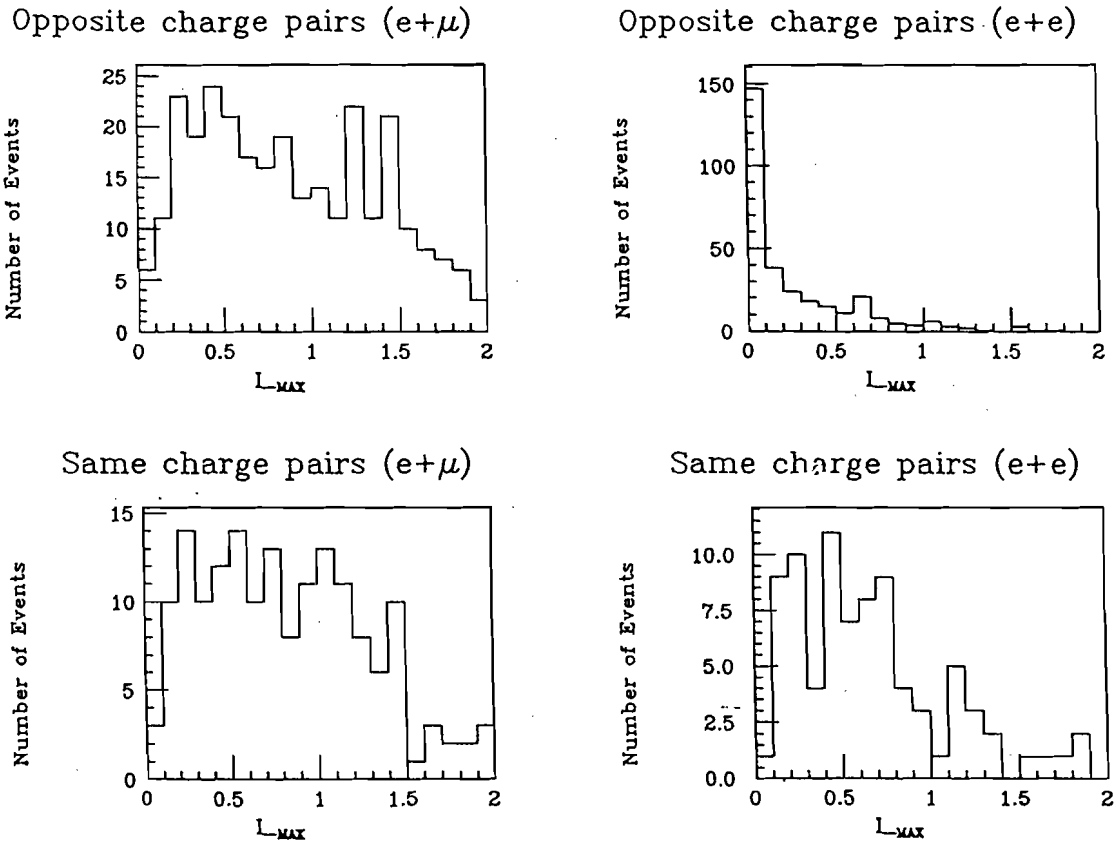

172

Figure 3.13: I_{max} distribution of opposite/same sign 'electron+muon' sample. These distributions are compared two tight cut same sign electron pairs I_{max} distributions.

171

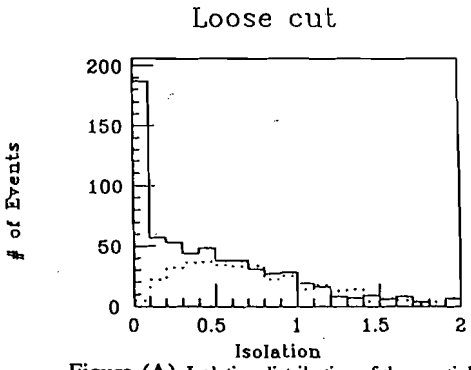

Figure (A): Isolation distribution of the one tight and one loose cut electron pairs. The cuts are identical to the cuts used to calculate Drell-Yan cross section.

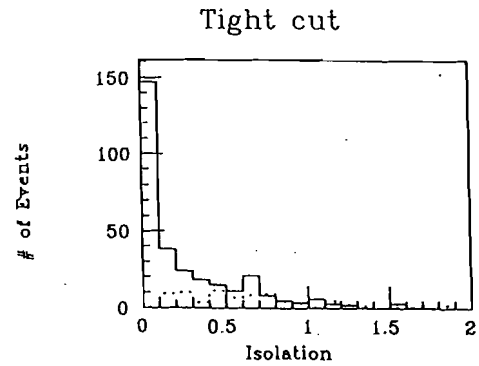

Figure (B): Isolation distribution of the two tight cut electron pairs. The cuts are identical to the cut used to calculate di-electron Pt distributions.

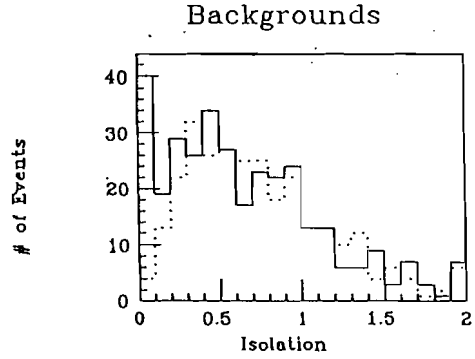

Dots : Same charge pairs

Solid: Opposite charge pairs

Figure 3.12: Fig A is isolation distribution of the one tight and one loose cut electron pairs. The cuts are identical to the used cut to calculate Drell-Yan cross section. Fig B is that of the two tight cut electron pairs. The cuts are identical to the cut used to calculate di-electron Pt distribution. And C is the difference between previous two plots.

Figure (C): The plot is the difference between previous two plots.

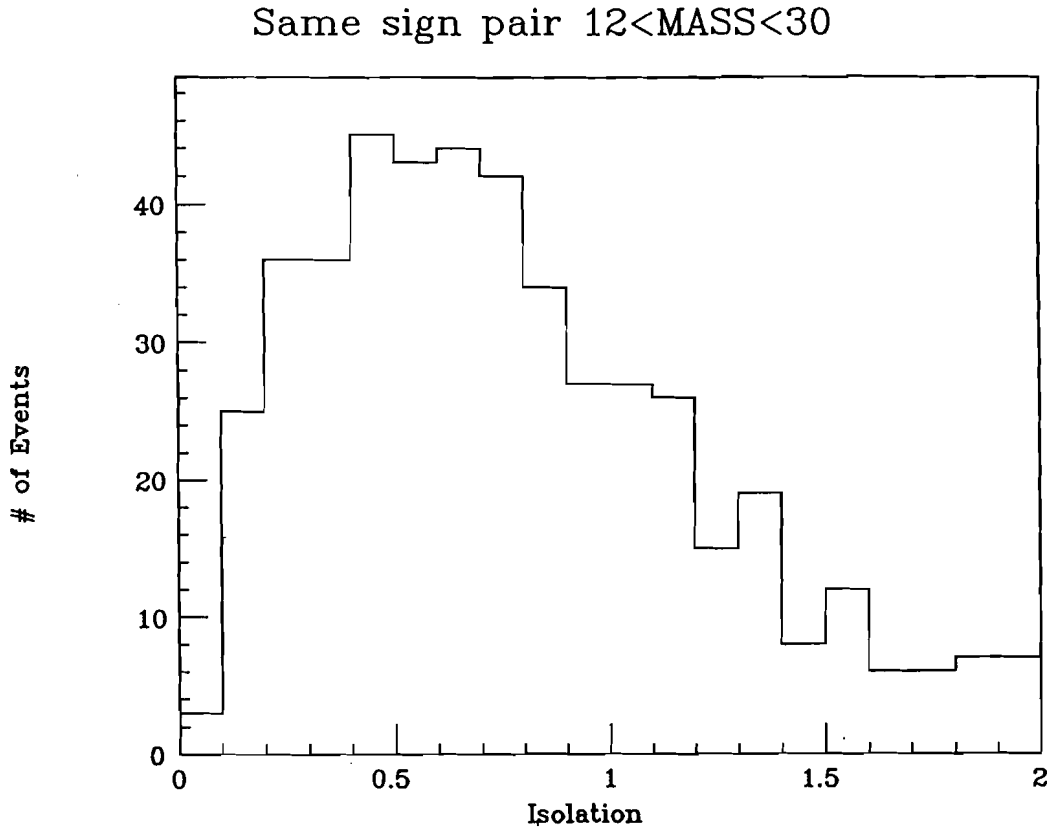

Figure 3.15: I_{max} distribution of same sign electron pairs. For this plot the pairs whose invariant mass is greater than 12 GeV are used.

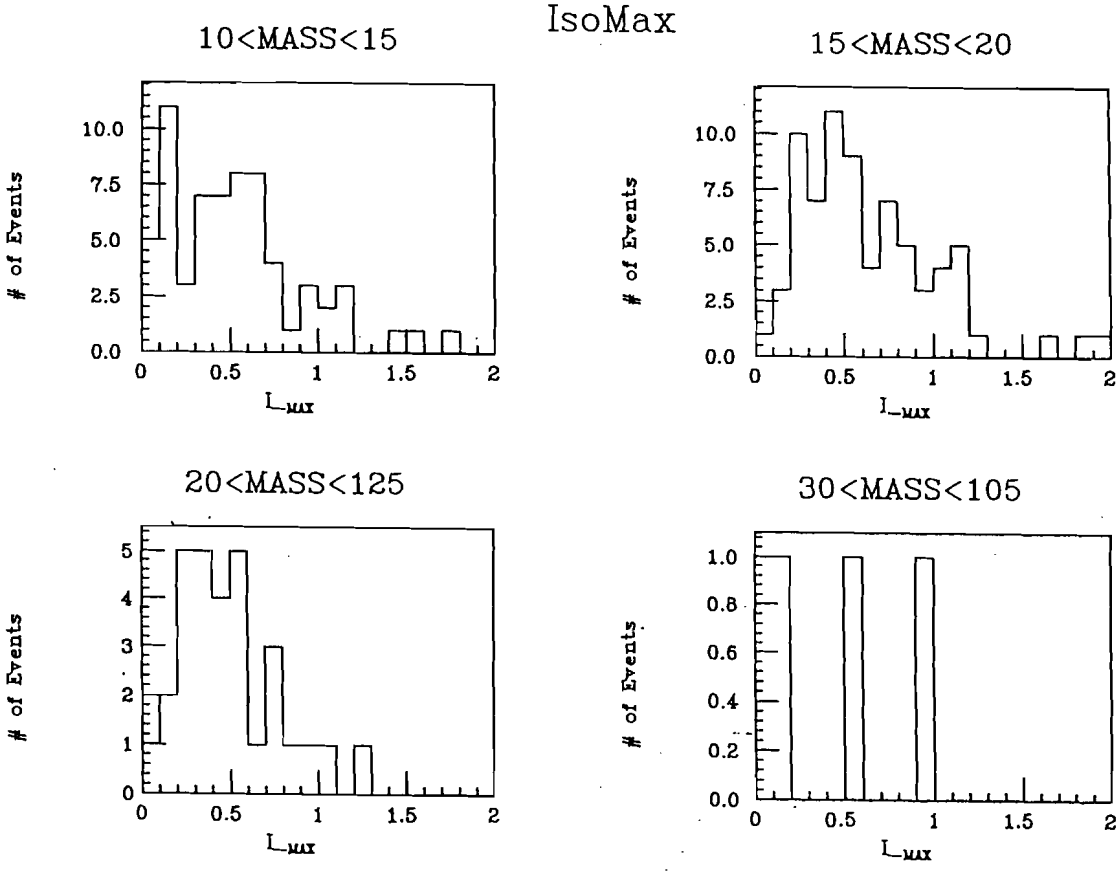

Figure 3.14: I_{max} distribution of electron pairs from the $b\bar{b}$ ISAJET Monte Carlo generator

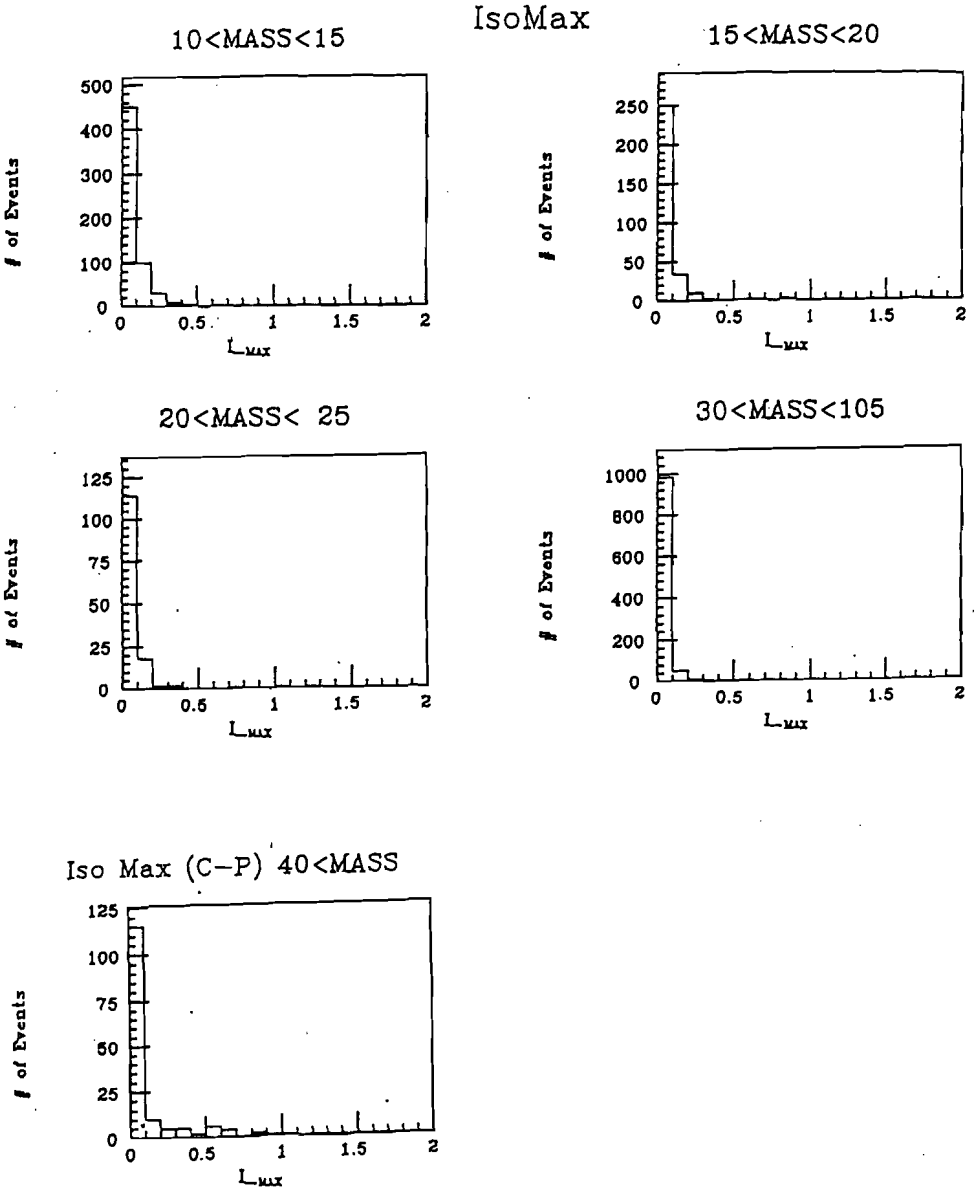

Figure 3.16: I_{max} distribution of electron pairs from the Drell-Yan ISAJET Monte Carlo generator

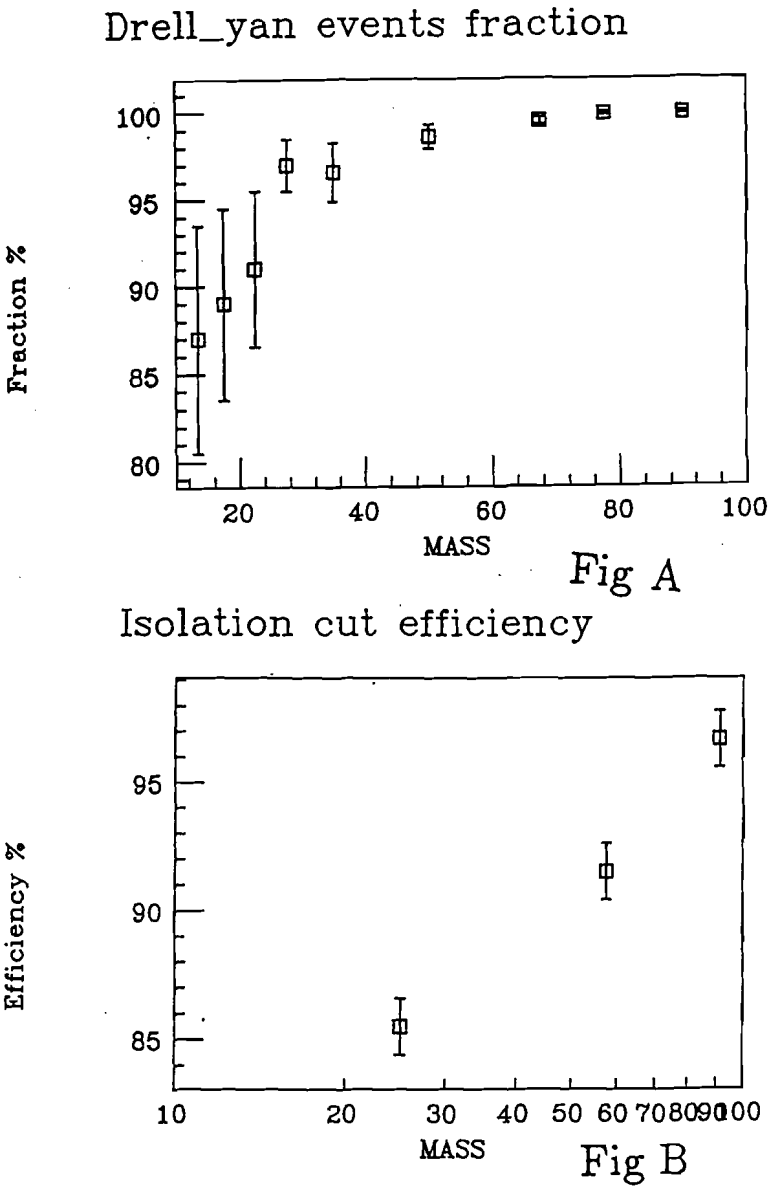

Figure 3.17: The invariant mass dependence of isolation cut efficiency has been estimated from Monte Carlo generator, then it was calibrated at Z0 mass region using real data.

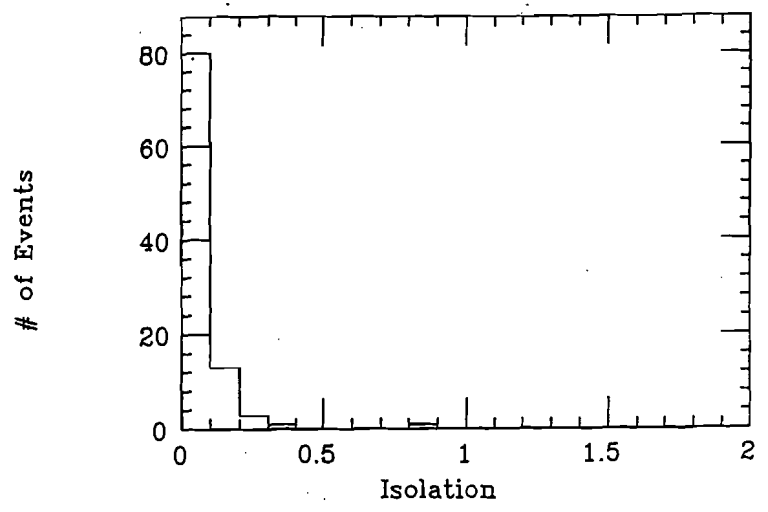

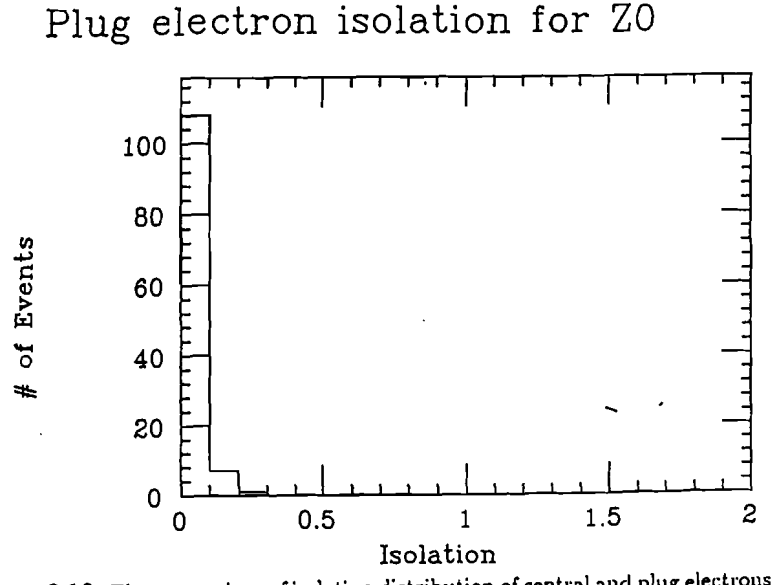

Figure 3.18: The comparison of isolation distribution of central and plug electrons at $75 < Mass < 105$ region. One tight cut electron is required and another loose cut electron is required in either central or plug region. This distribution includes only that of 2nd electron. And it include both same sign and opposite sign pairs.

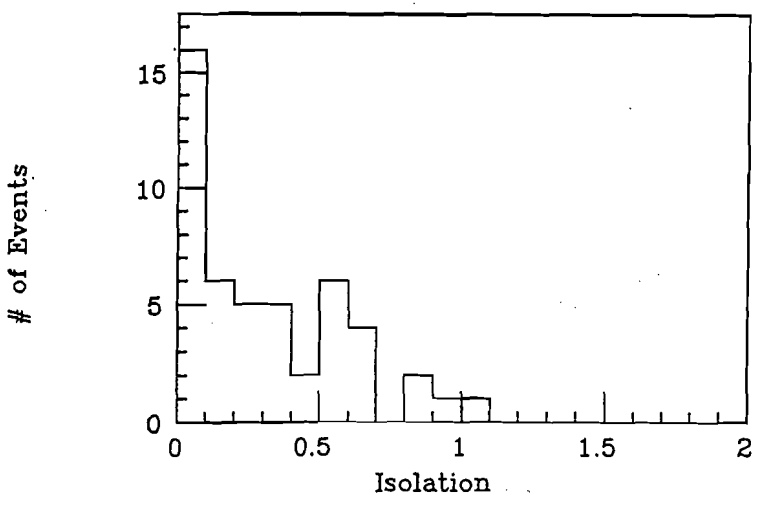

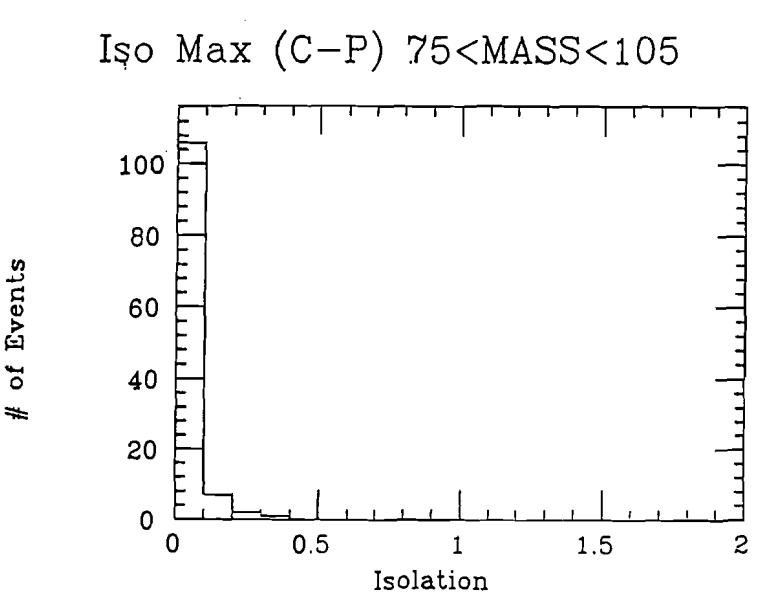

Figure 3.19: I_{max} distribution of central-plug electron pairs in each mass region.

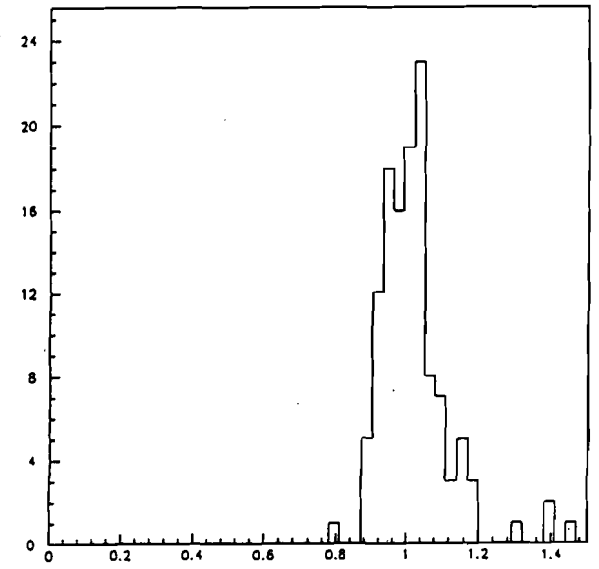

Figure 3.20: E/P distribution of J/Ψ decay electron. The ratio was calculated from corrected energy and vertex constrained momentum.

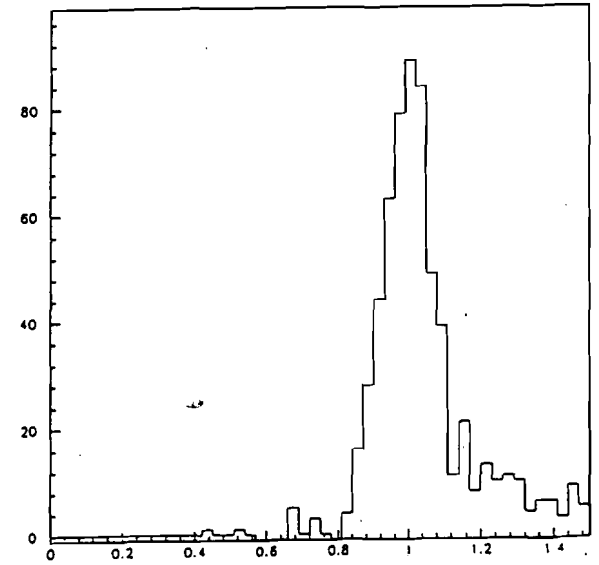

Figure 3.21: E/P distribution of N_{diff} sample. The ratio was calculated from corrected energy and vertex constrained momentum.

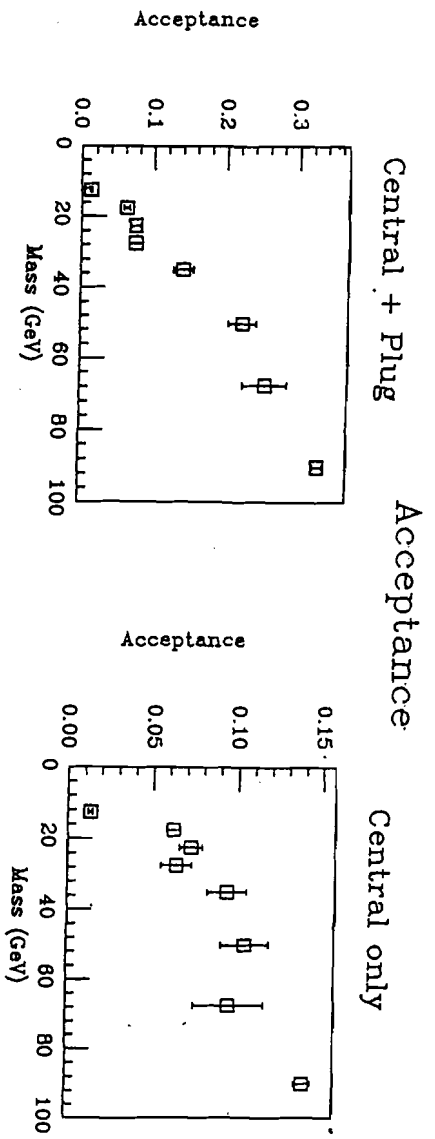

Figure 4.1: Geometrical and kinematical acceptance for $\frac{d\sigma}{dm}$ measurement has been estimated ISAJET Monte Carlo and CDF detector simulation

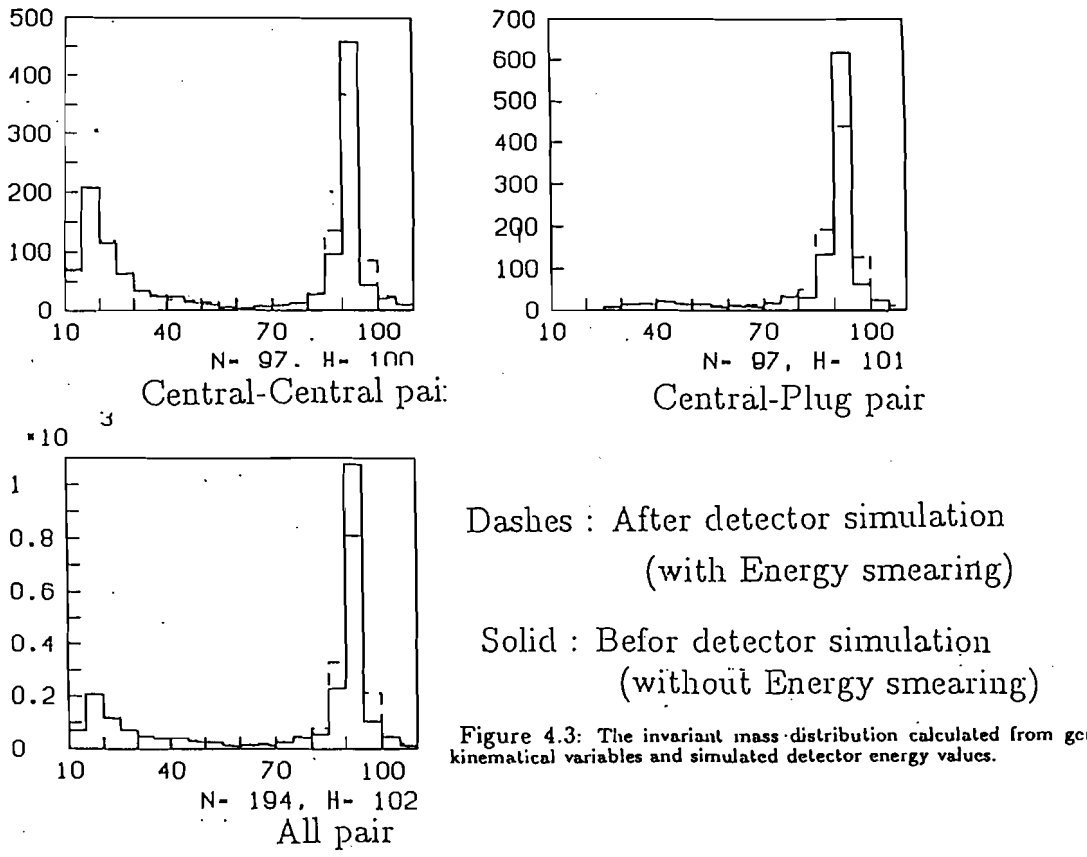

Figure 4.3: The invariant mass distribution calculated from generation level kinematical variables and simulated detector energy values.

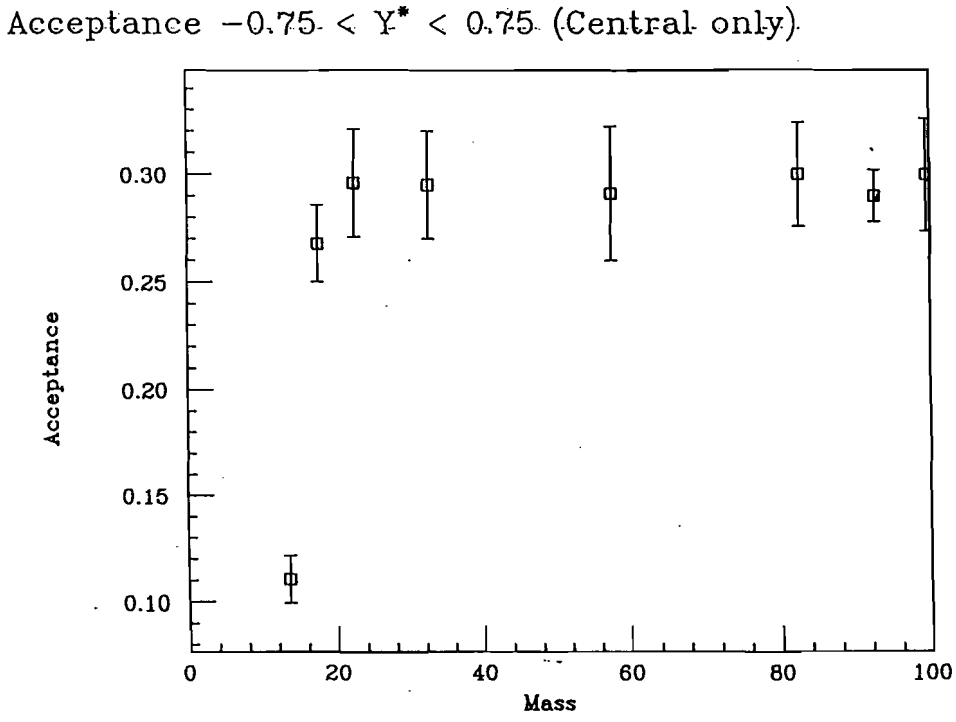

Figure 4.2: Geometrical and kinematical acceptance for $\frac{d\sigma^2}{dmdy}y=0$ measurement has been estimated ISAJET Monte Carlo and CDF detector simulation. $-0.75 < Y < 0.75$ data are used to calculate $\frac{d\sigma^2}{dmdy}y=0$

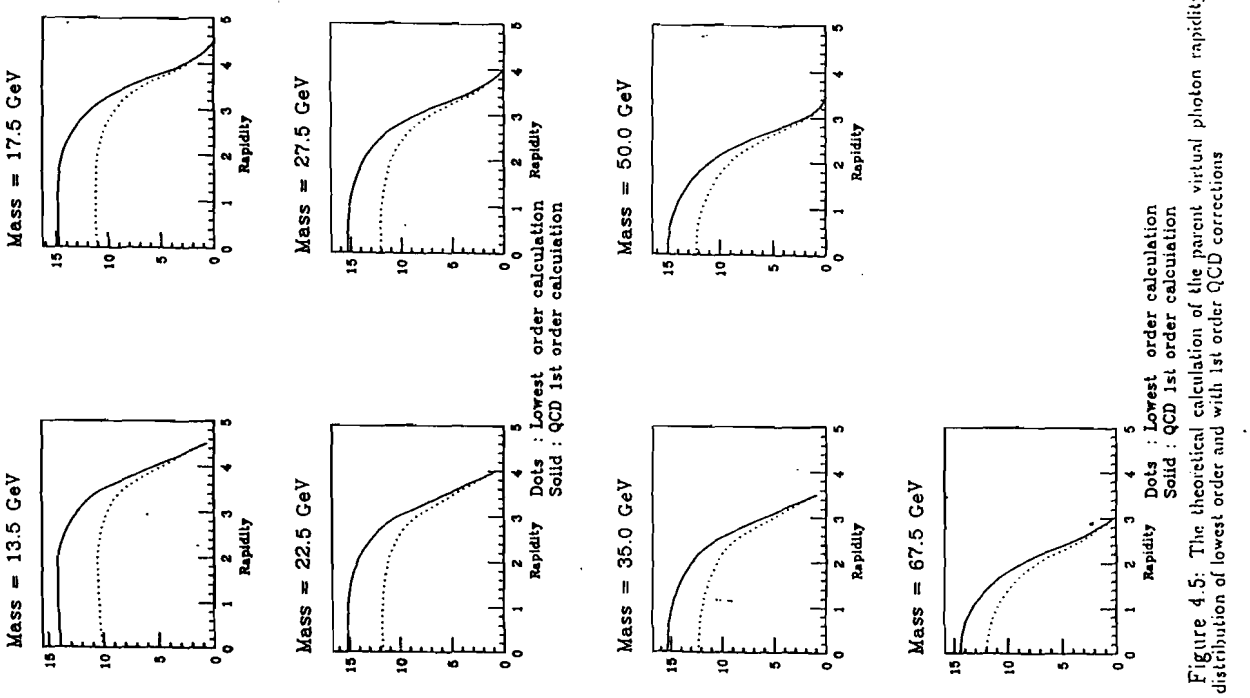

Figure 4.5: The theoretical calculation of the parent virtual photon rapidity distribution of lowest order and with 1st order QCD corrections

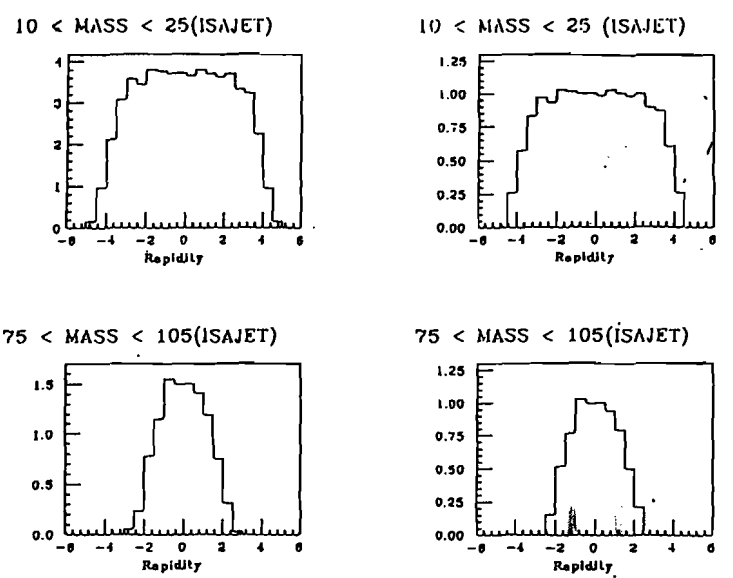

Figure 4.4: Rapidity distribution of parent virtual photon in ISAJET Monte carlo

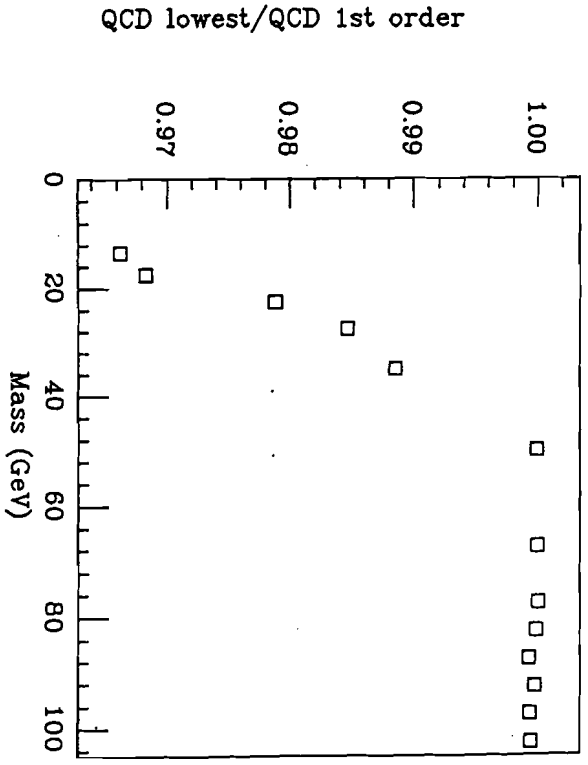

QCD Acceptance correction C

Figure 4.6: The correction of Geometrical and kinematical acceptance for QCD higher order process

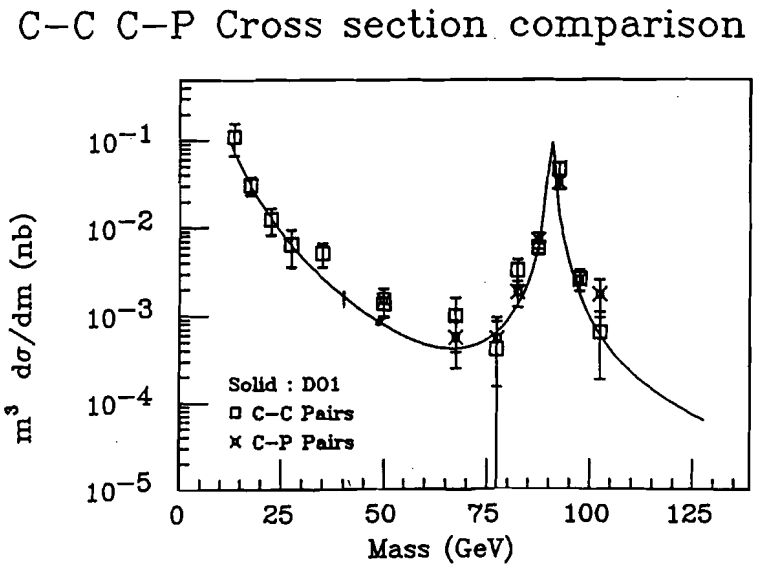

Figure 4.7: The consistency between the Central -Central pair cross section, and the Central - Plug pair cross section is checked. The differential cross section $\frac{d\sigma}{dM}$ is measured individually and compared with each other.

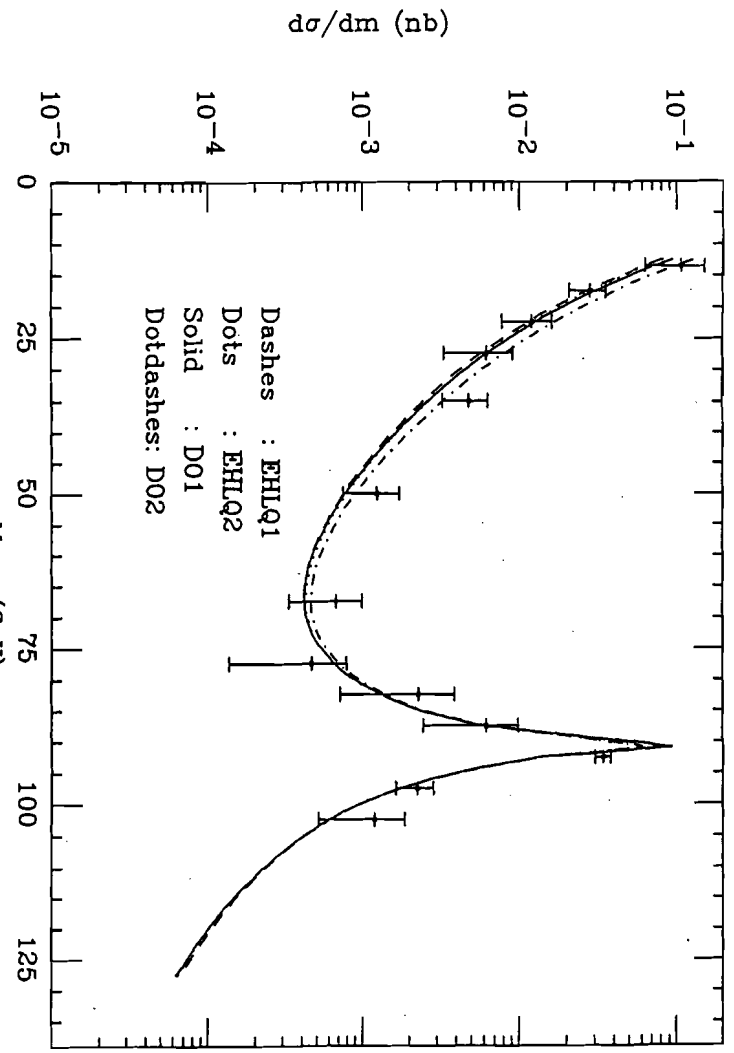

Figure 4.8: Drell-Yan dielectron decay differential cross section $\frac{d\sigma}{dM}$ with some theoretical calculations which include the QCD correction up to 2nd order.

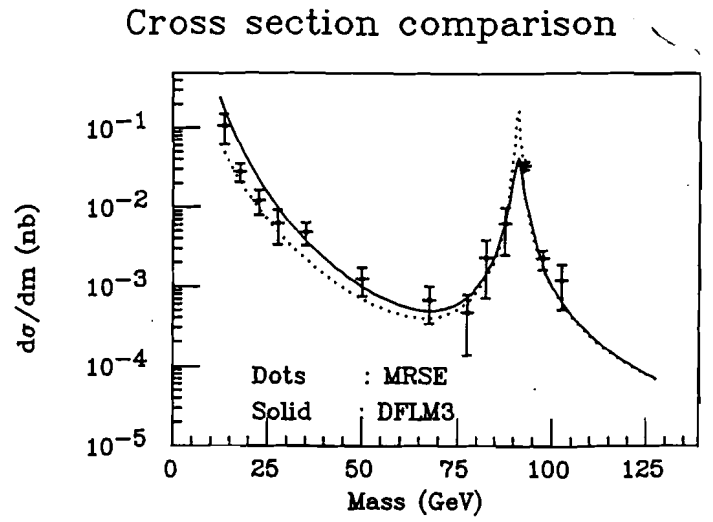

Figure 4.9: The minimum and maximum cross sections obtained by trying different parton distribution functions are plotted with real data

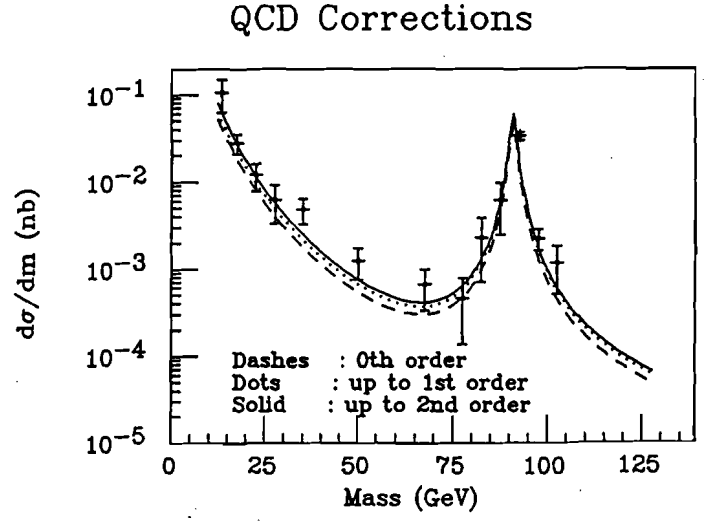

Figure 4.10: The Drell-Yan differential cross section $\frac{d\sigma}{dm}$ is calculated including upto 1st and 2nd order diagram. The calculated cross sections are plotted with data and lowest order cross section calculation

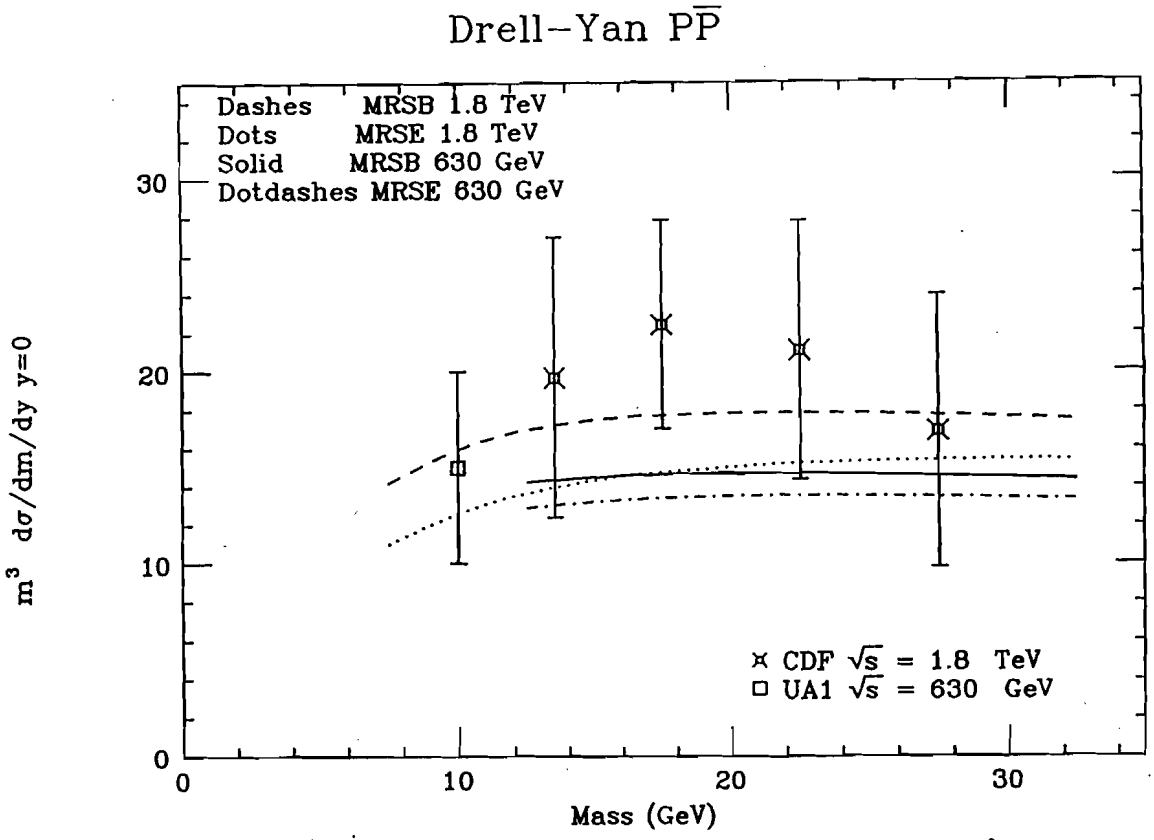

Figure 4.12: Drell-Yan dielectron decay differential cross section $\frac{d^2\sigma}{dMdY_{Y=0}}$ for $30 > M > 12$ with theoretical calculations including up to 1st order

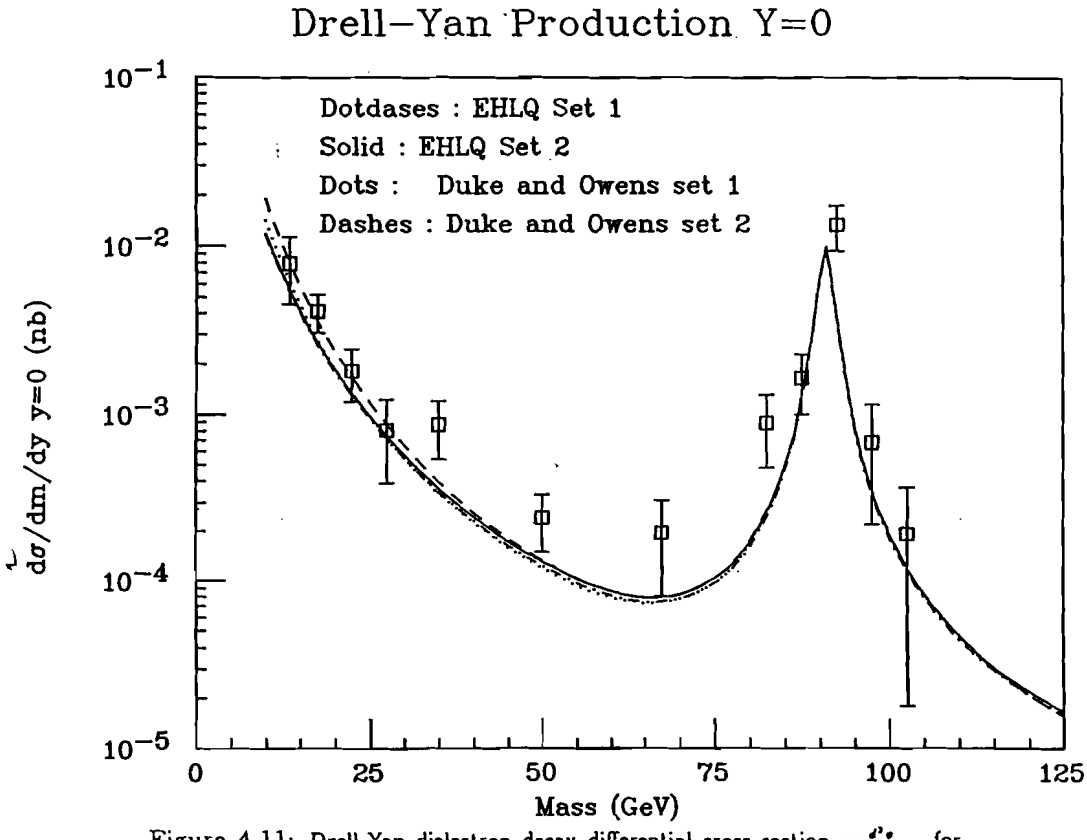

Figure 4.11: Drell-Yan dielectron decay differential cross section $\frac{d^2\sigma}{dMdY_{Y=0}}$ for whole region with theoretical calculations (lowest order calculation)

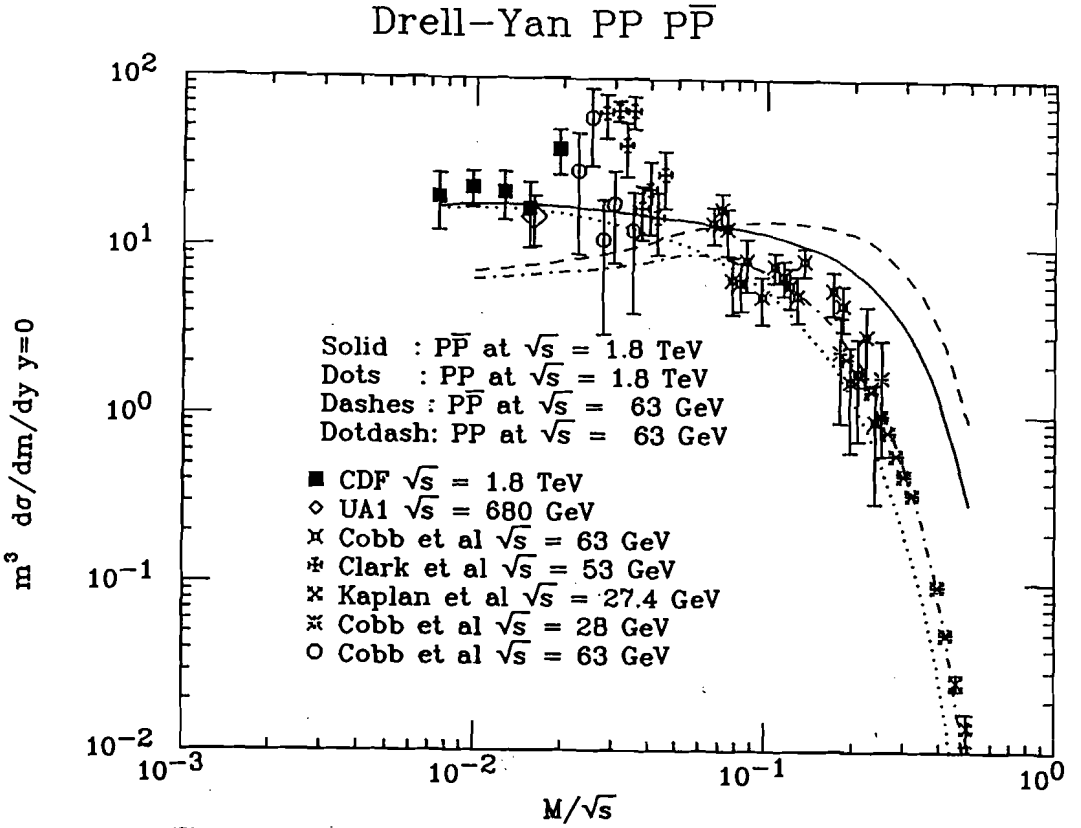

Figure 4.14: The cross section $M^3 \frac{d^2\sigma}{dM\,dY_{Y=0}}$ is plotted as a function of the scaling valuable $\sqrt{\tau} = M_{ee}/\sqrt{s}$ with theoretical expectations.

192

191

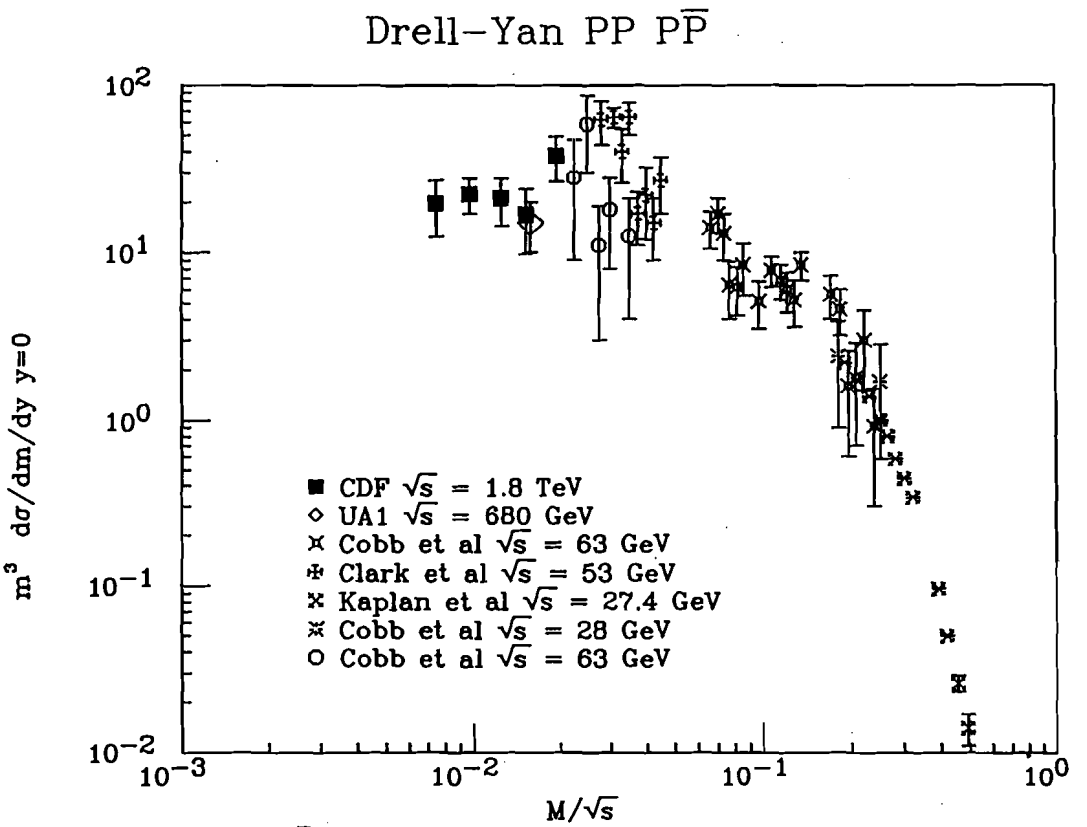

Figure 4.13: The cross section $M^3 \frac{d^2\sigma}{dM\,dY_{Y=0}}$ is plotted as a function of the scaling valuable $\sqrt{\tau} = M_{ee}/\sqrt{s}$

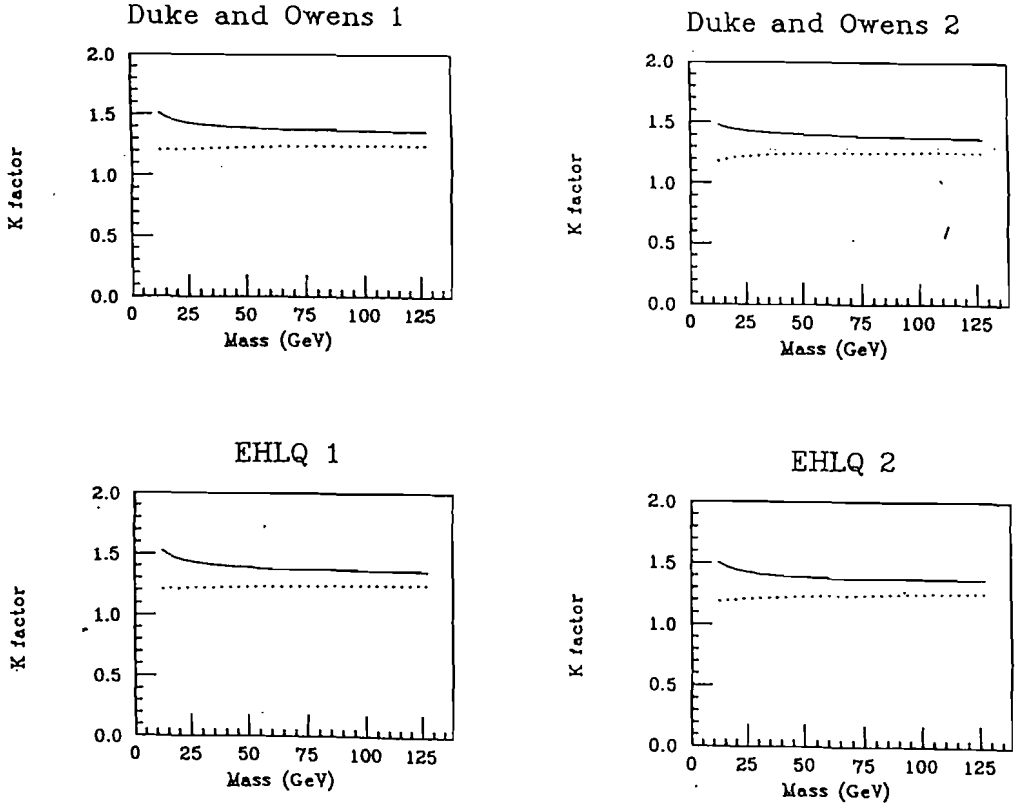

Figure 4.16 The theoretical prediction of the K factor calculated using several parton distribution functions. The doted line include upto QCD 1st order diagram, and solid line include upto 2nd order QCD diagram

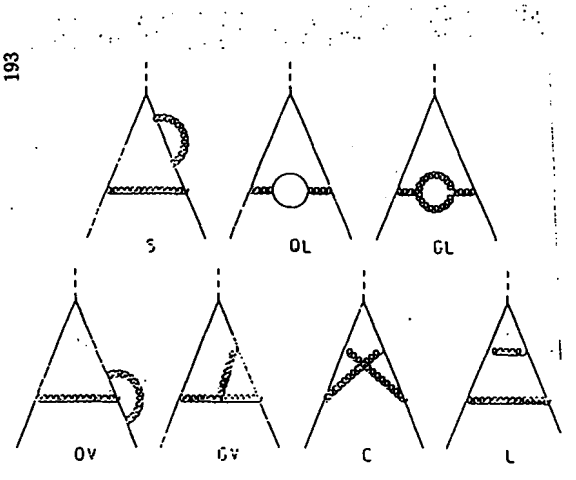

Order α_s^2 contribution to the quark form factor

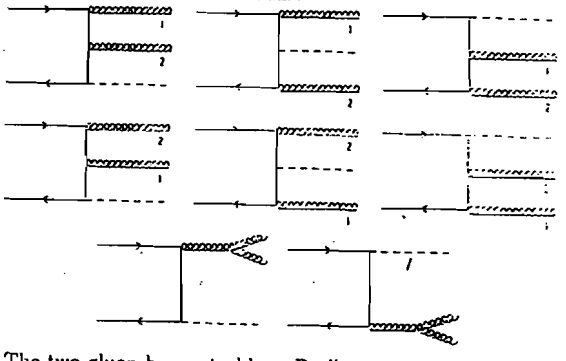

The two gluon bremsstrahlung Drell-Yan Process: $q(p_1) + \bar{q}(p_2) \rightarrow V(q) + g(k_1) + g(k_2)$.

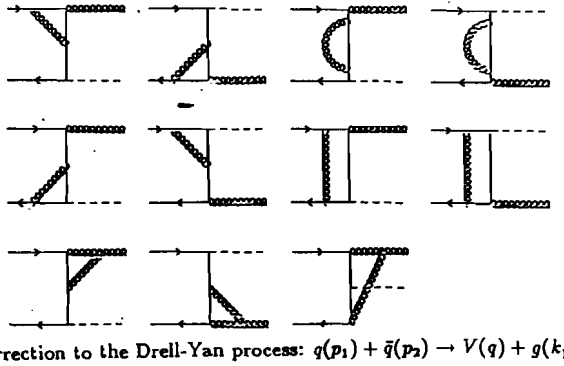

$O(\alpha_s)$ correction to the Drell-Yan process: $q(p_1) + \bar{q}(p_2) \rightarrow V(q) + g(k_1)$

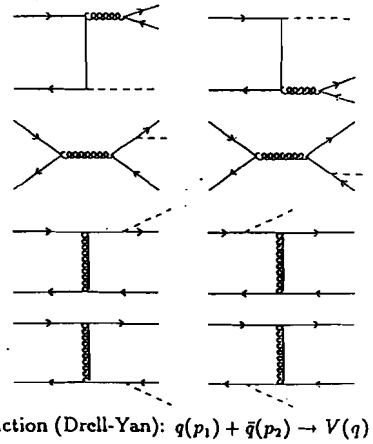

Quark production (Drell-Yan): $q(p_1) + \bar{q}(p_2) \rightarrow V(q) + q(k_1) + \bar{q}(k_2)$

Figure 4.15 Drell-Yan QCD 2nd order diagrams Ref. T.Matsuura et al Nucl. Phys B139 (1989) 5

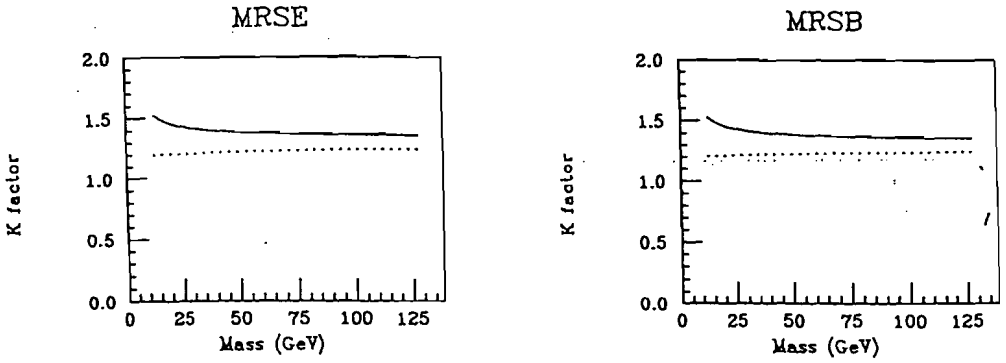

Figure 4.16 The theoretical prediction of the K factor calculated using several parton distribution functions. The doted line include upto QCD 1st order diagram, and solid line include upto 2nd order QCD diagram

196

195

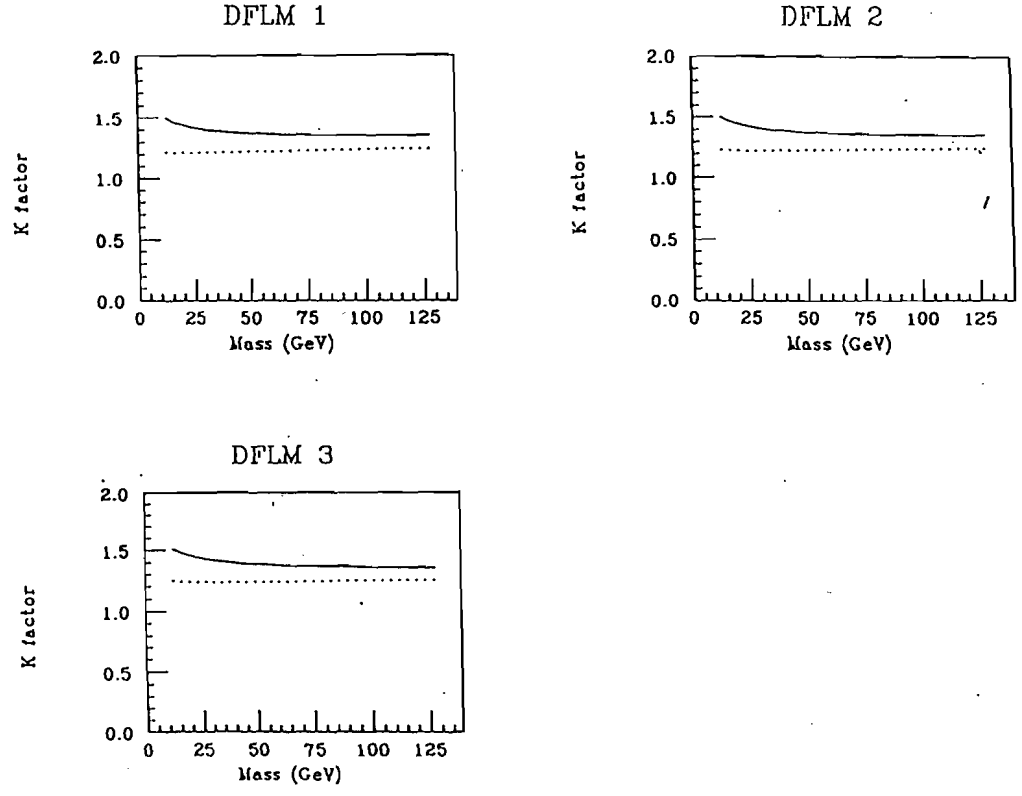

Figure 4.16 The theoretical prediction of the K factor calculated using several parton distribution functions. The doted line include upto QCD 1st order diagram, and solid line include upto 2nd order QCD diagram

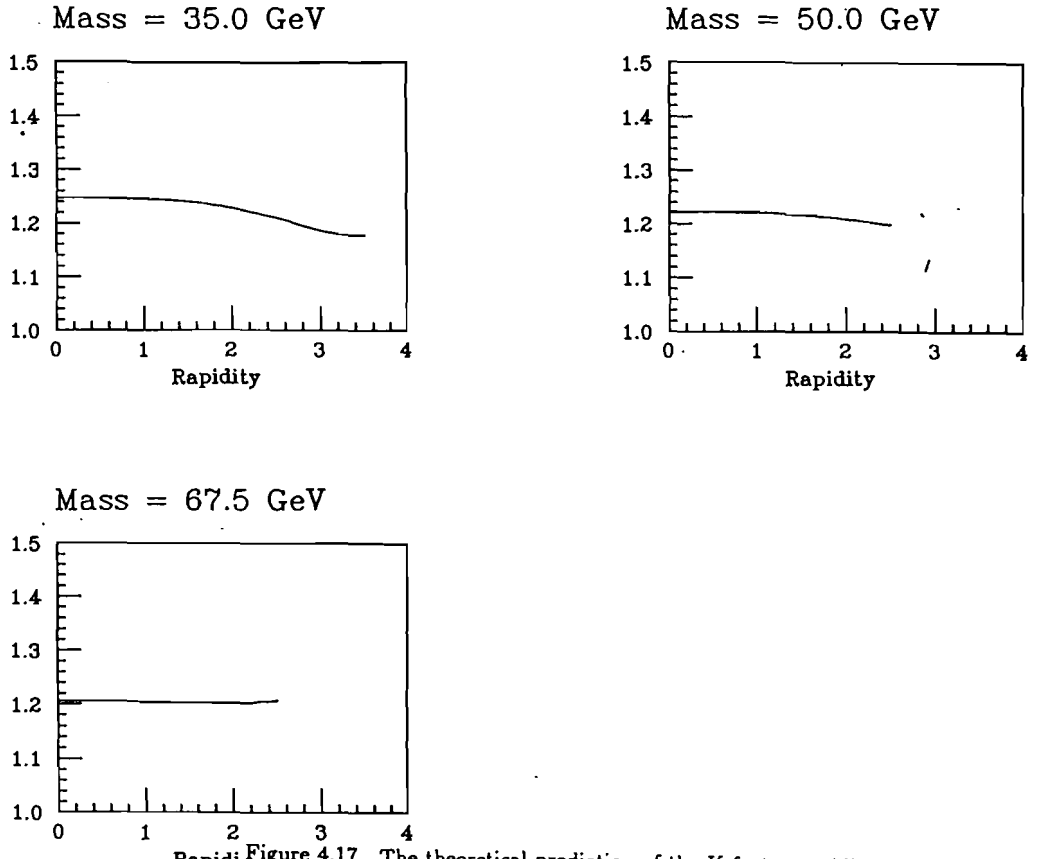

198

Figure 4.17 The theoretical prediction of the K factor rapidity dependence
Solid : QCD 1st order calculation

197

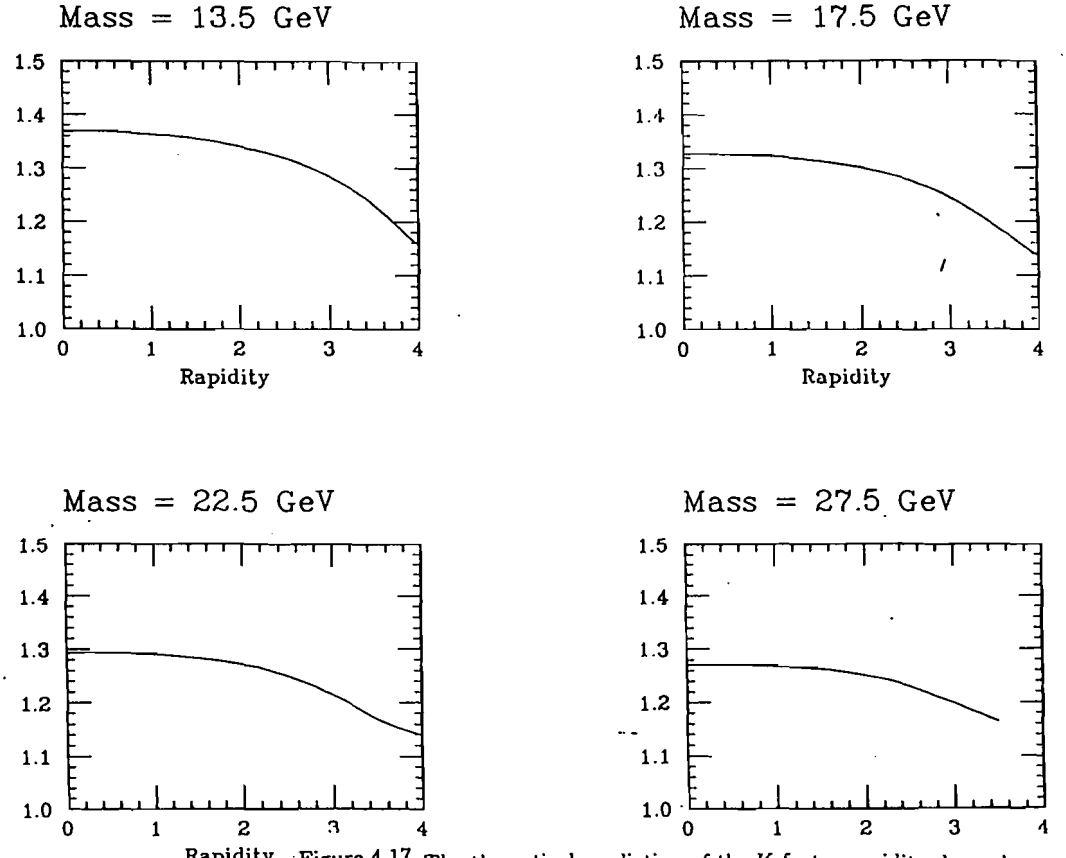

Figure 4.17 The theoretical prediction of the K factor rapidity dependence
Solid : QCD 1st order calculation

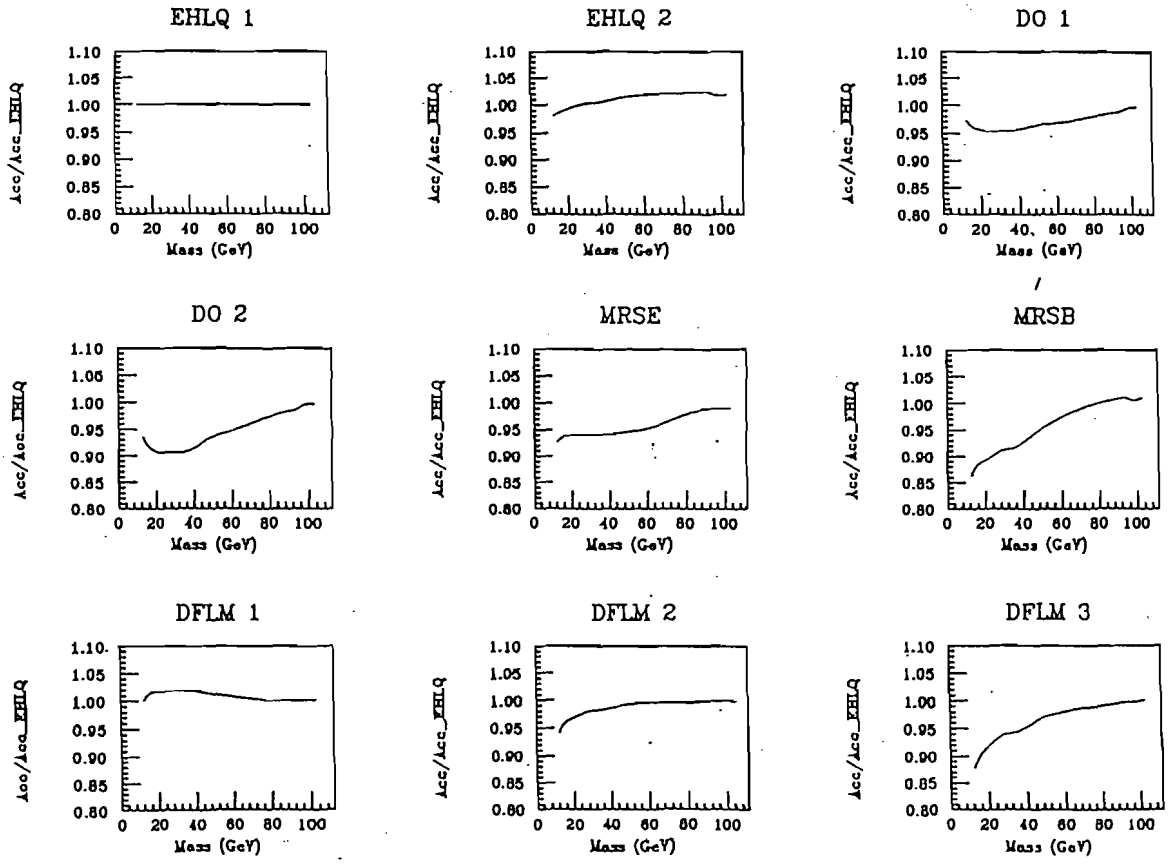

Figure 4.19: The parton distribution function correction for geometrical and Kinematical acceptance estimation for Central- Central pair only

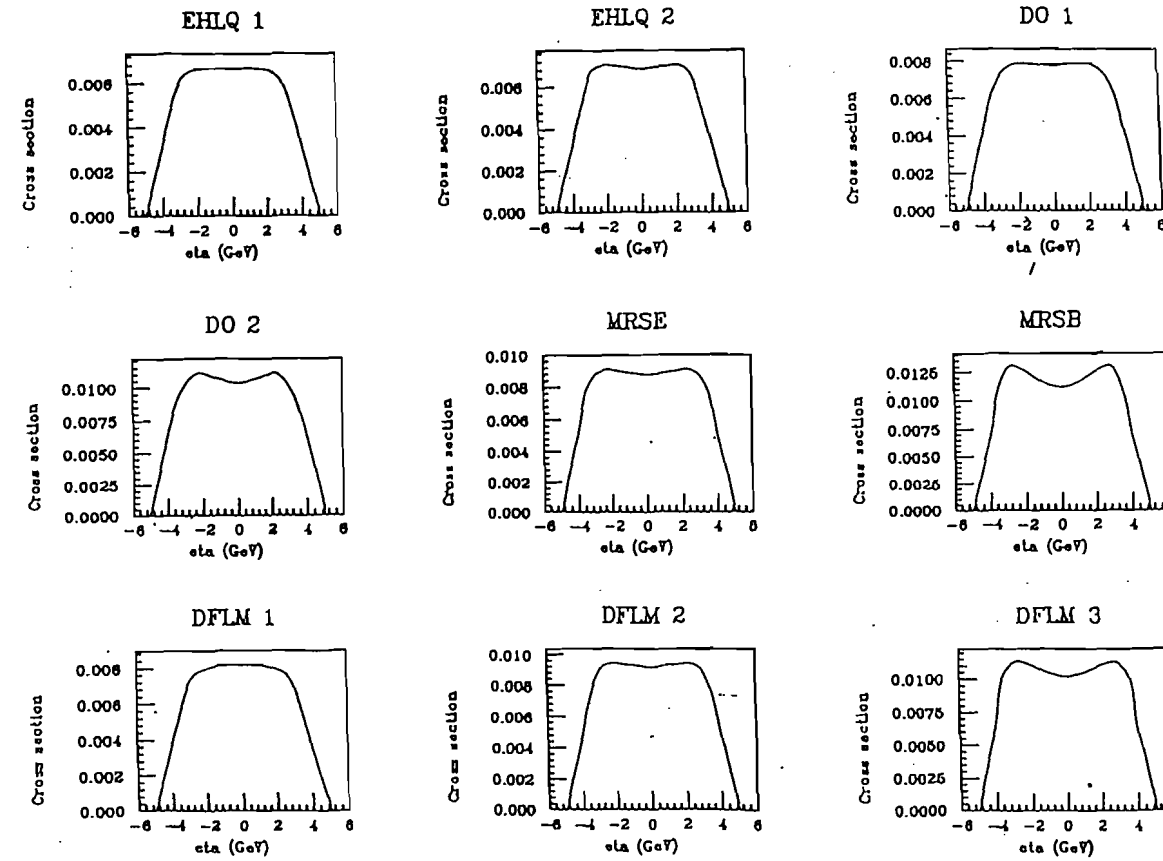

Figure 4.18: The rapidity distribution of the parent virtual photon parton distribution function dependence

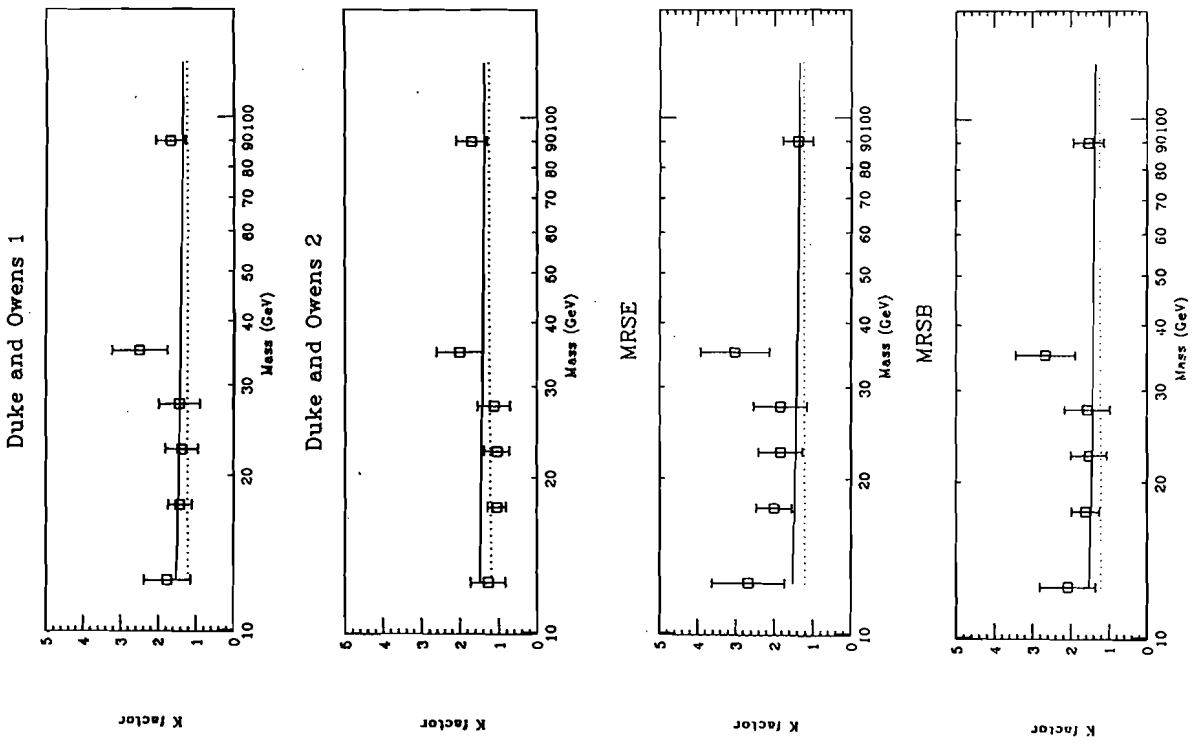

Figure 4.21: K_{exp} factor distribution integrated over whole Y region calculated against several parton distribution functions

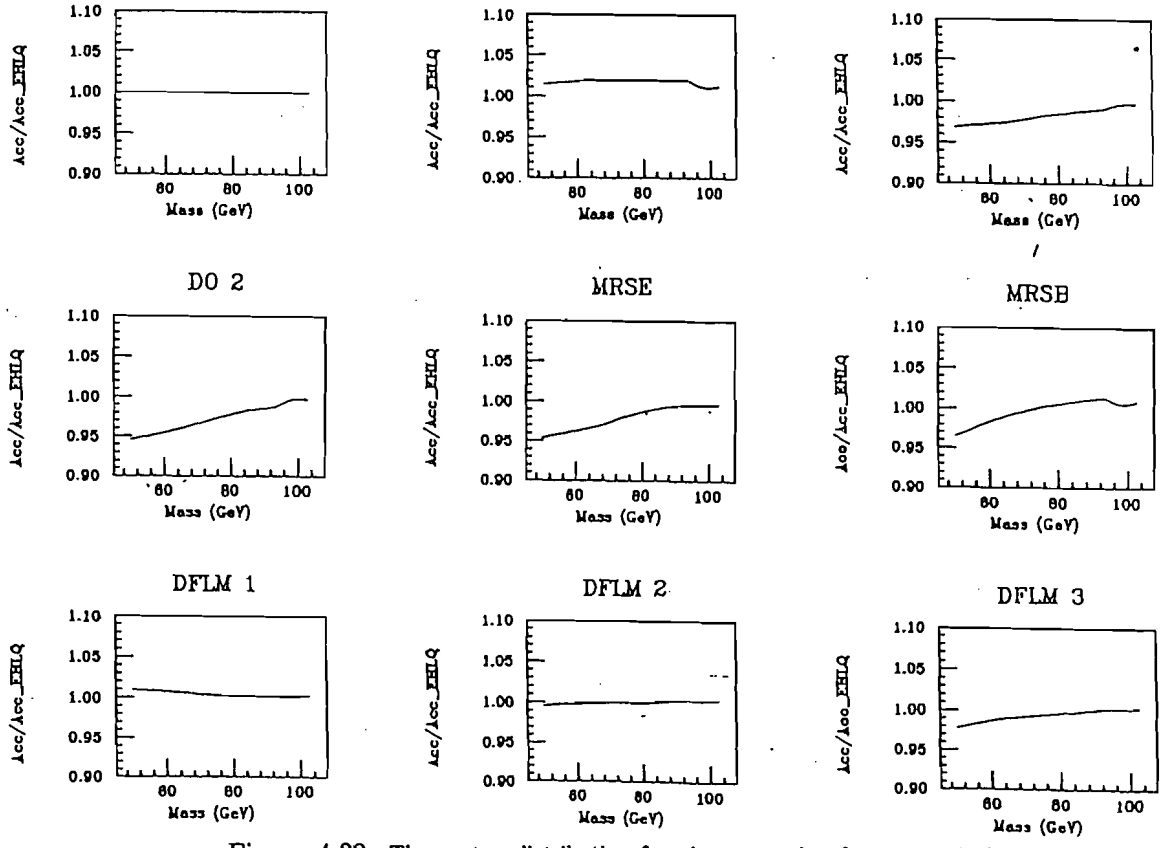

Figure 4.20: The parton distribution function correction for geometrical and Kinematical acceptance estimation for Central- Central pair and Central-Plug pair

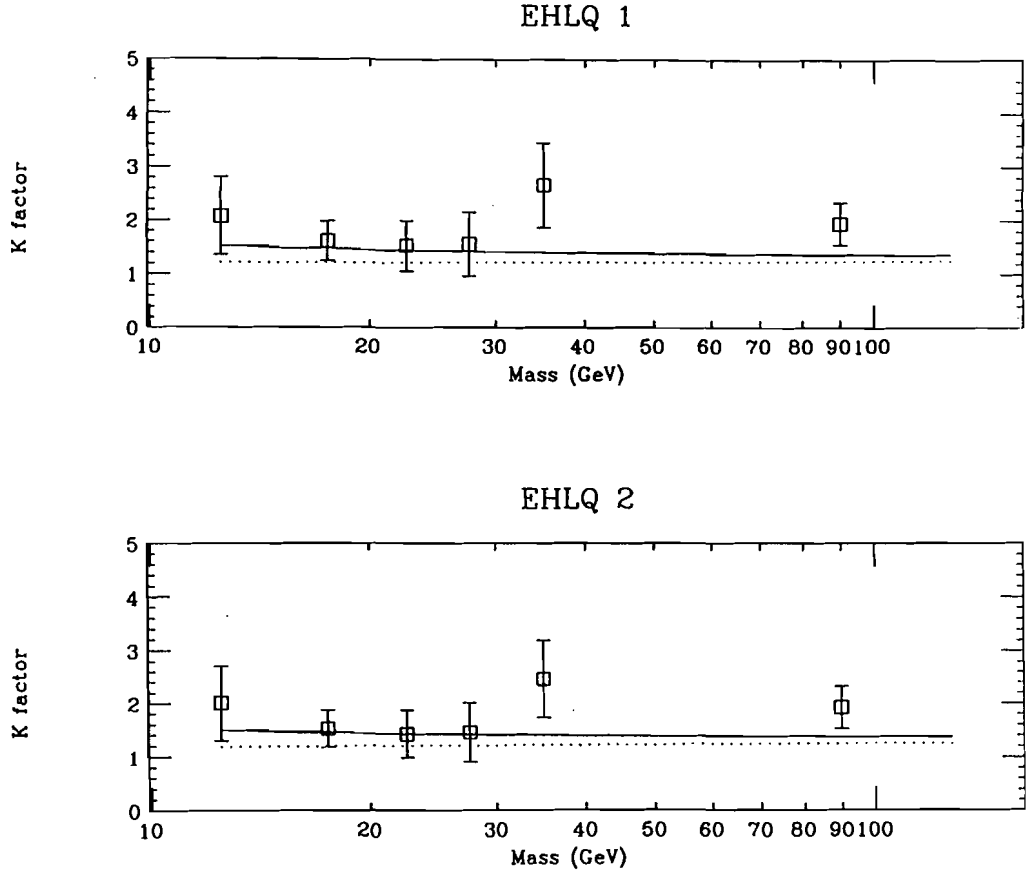

Figure 4.21: K_{exp} factor distribution integrated over whole Y region calculated against several parton distribution functions

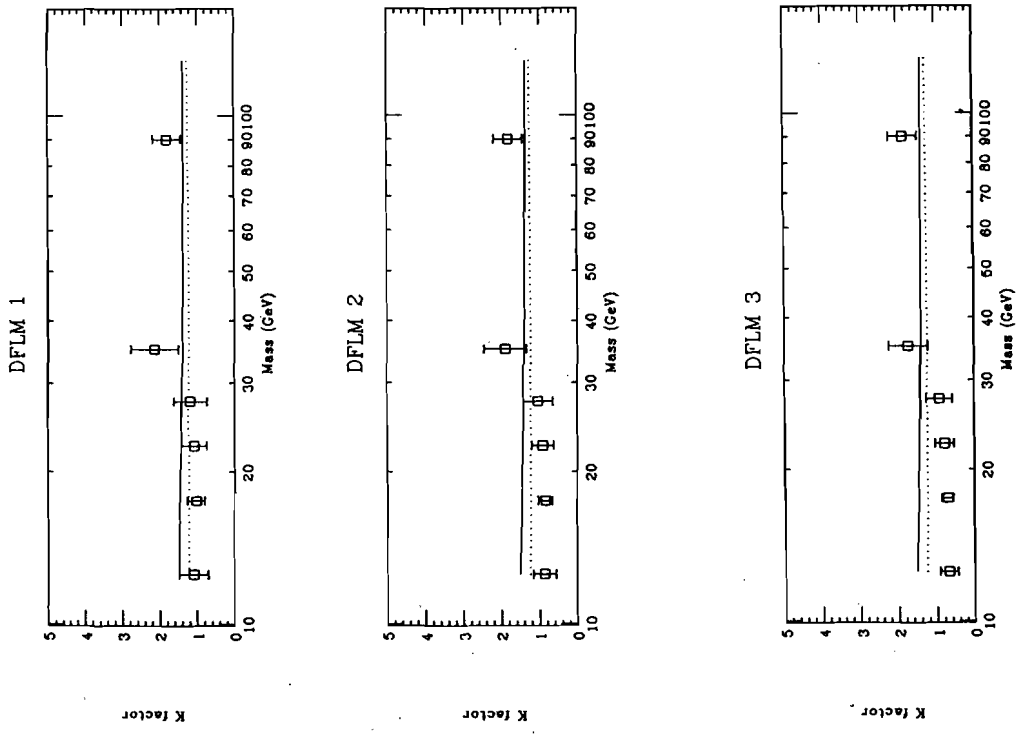

Figure 4.21: K_{exp} factor distribution integrated over whole Y region calculated against several parton distribution functions

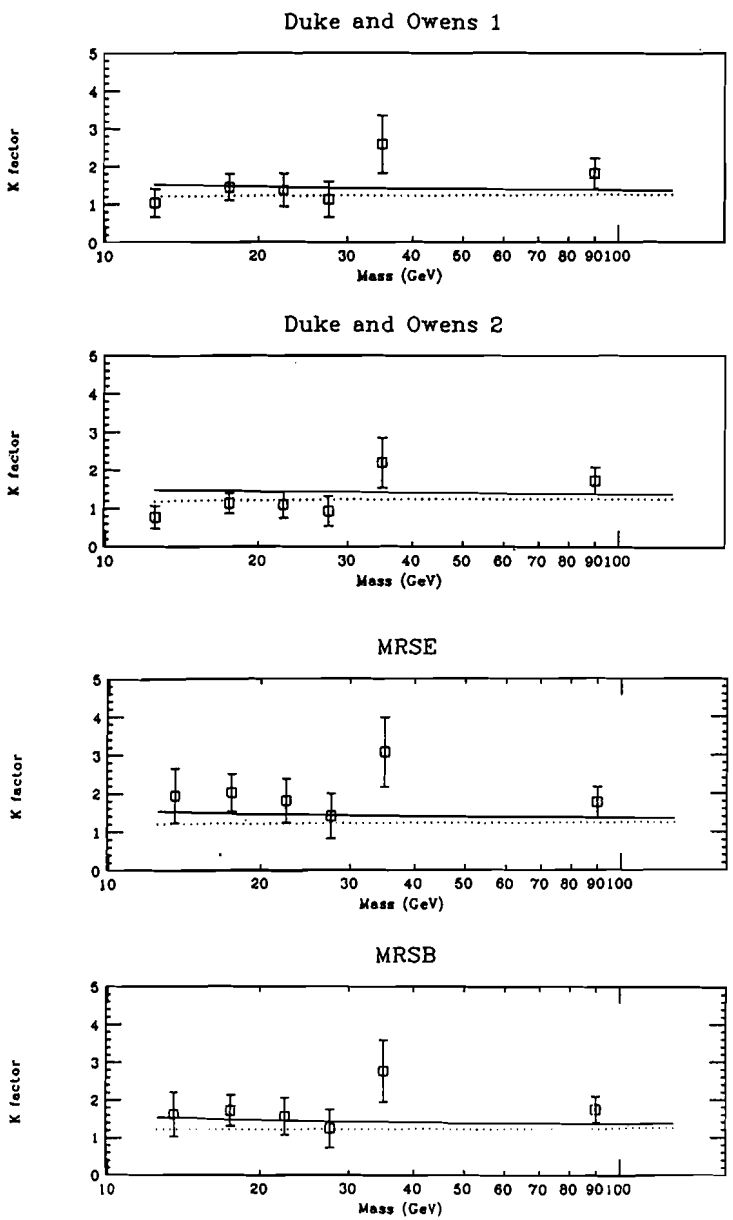

Figure 4.22: K^0_{exp} factor distribution at Y = 0

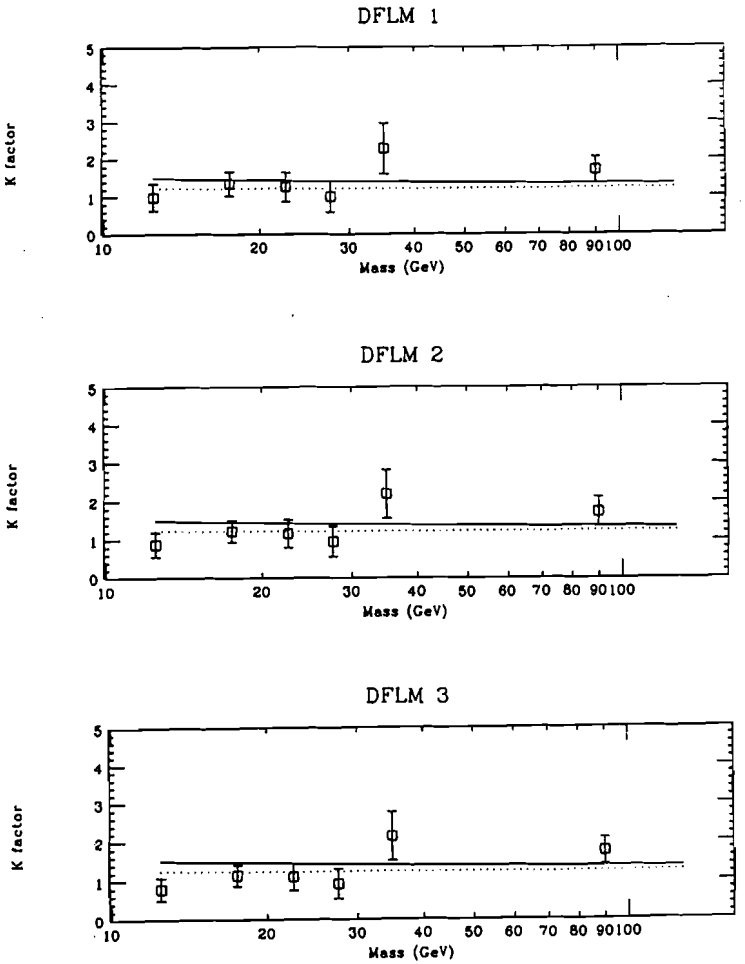

Figure 4.22: K^0_{exp} factor distribution at Y = 0

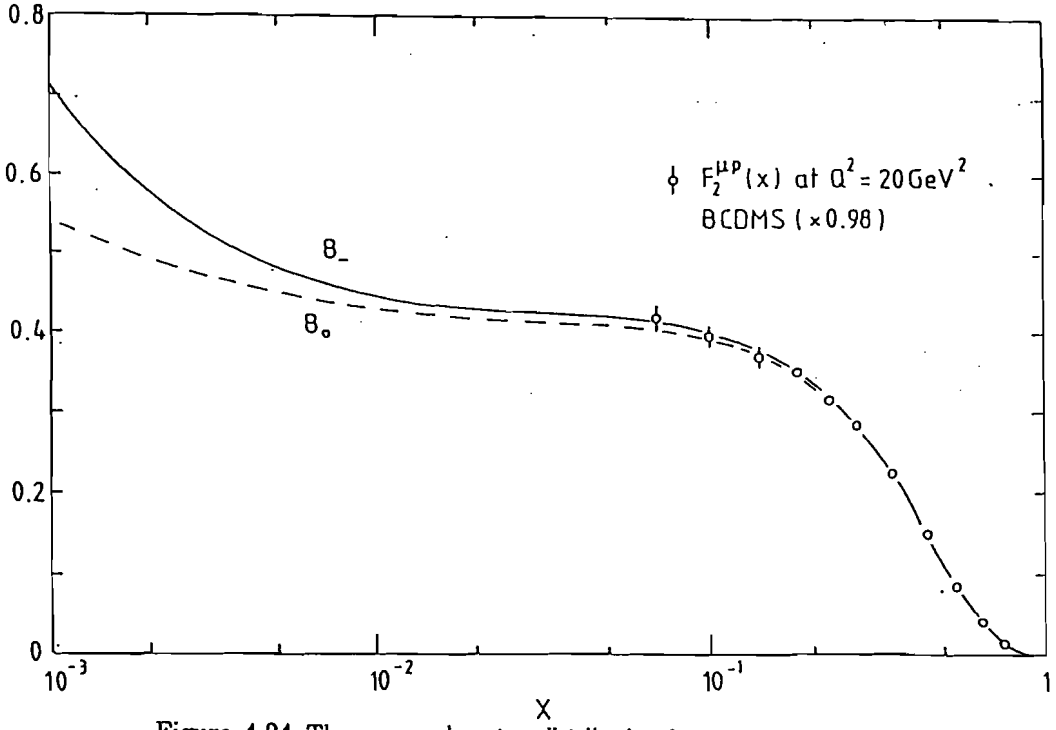

Figure 4.24: The measured parton distribution function $F_2^{\mu p}$ in deep inelastic scattering (BCDMS) at Q^2 is 20 GeV^2

208

207

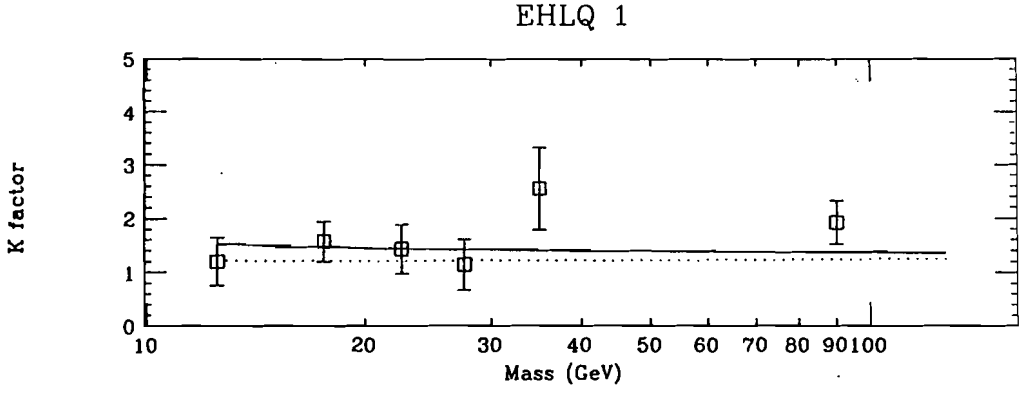

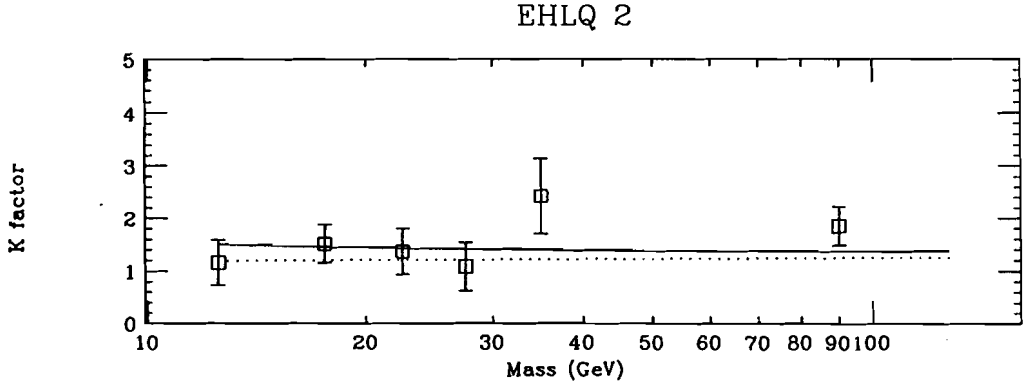

Figure 4.22: K^0_{exp} factor distribution at Y = 0

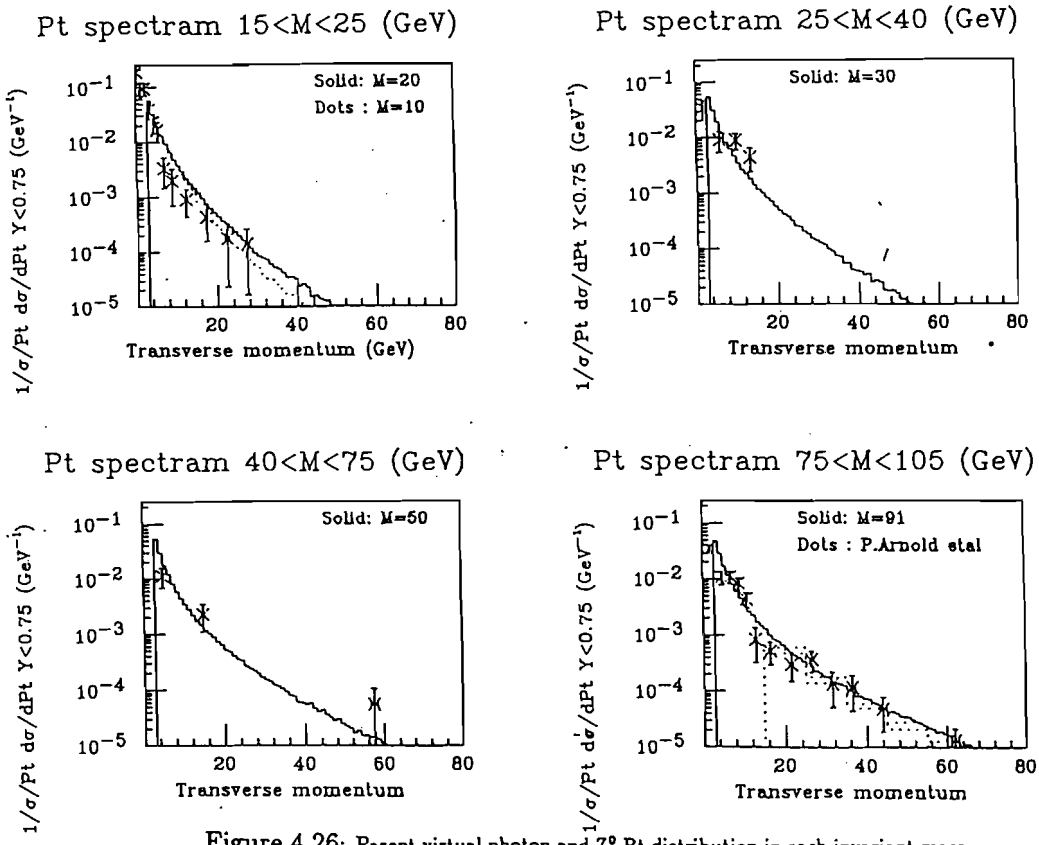

Figure 4.26: Parent virtual photon and Z^0 Pt distribution in each invariant mass (Pt has been measured by calorimeter information.) and a comparison with a Monte Carlo generator and theoretical calculation

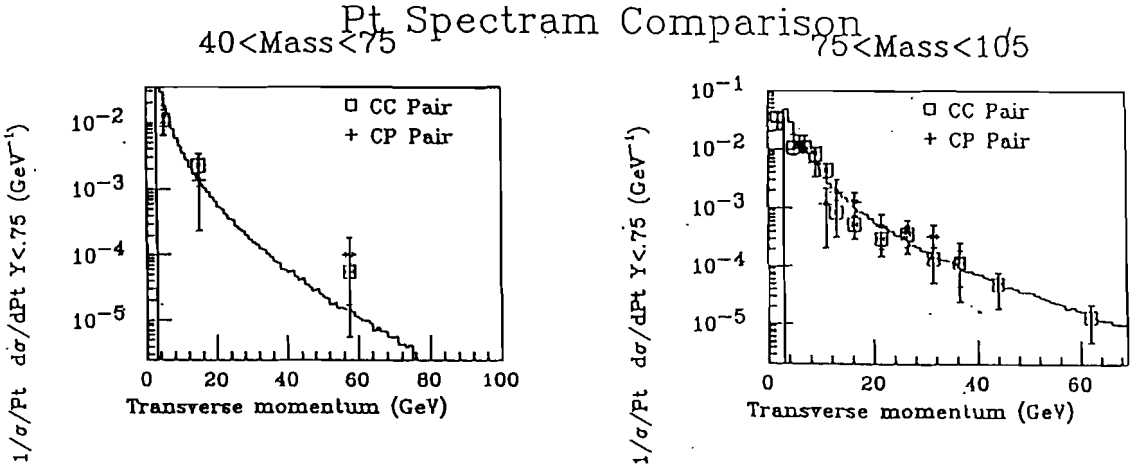

Figure 4.25: Parent virtual photon and Z^0 Pt distribution comparison. Pt distribution of Central-Central electron pairs and Central-Plug pairs.

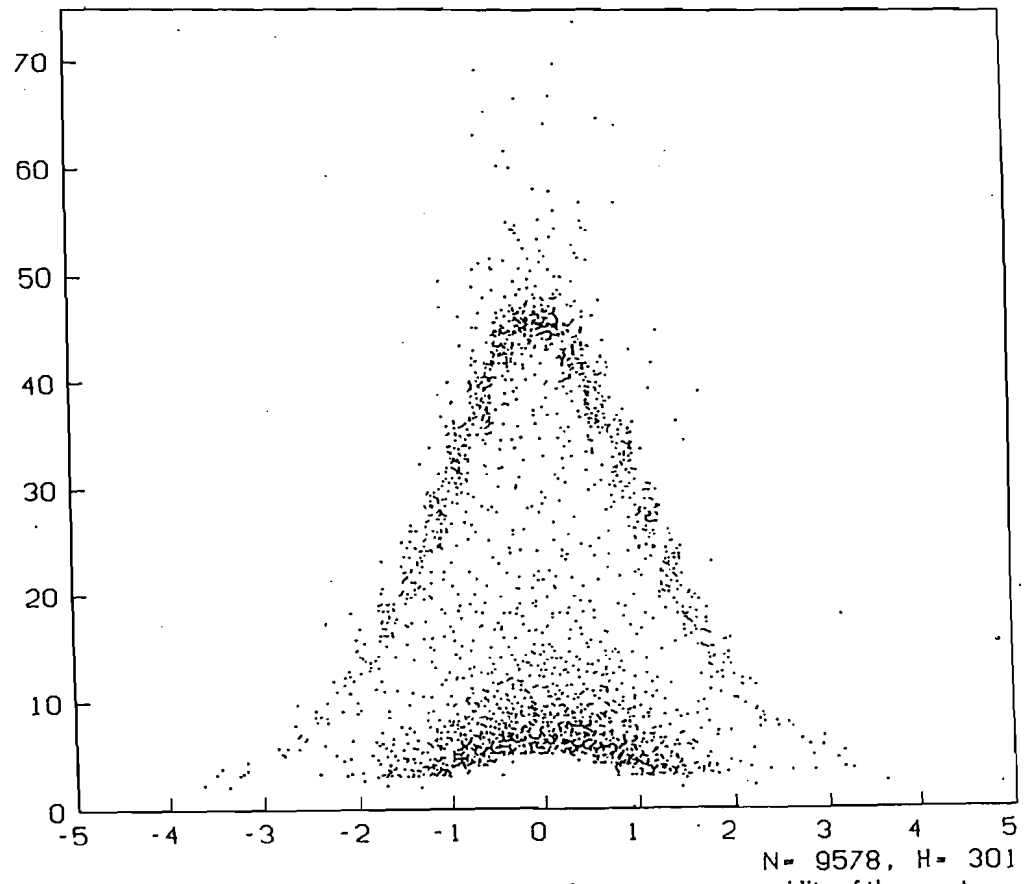

Figure 4.28: The electron Pt in center of mass system vs. rapidity of the parent virtual gamma or Z0 in Monte Carlo events

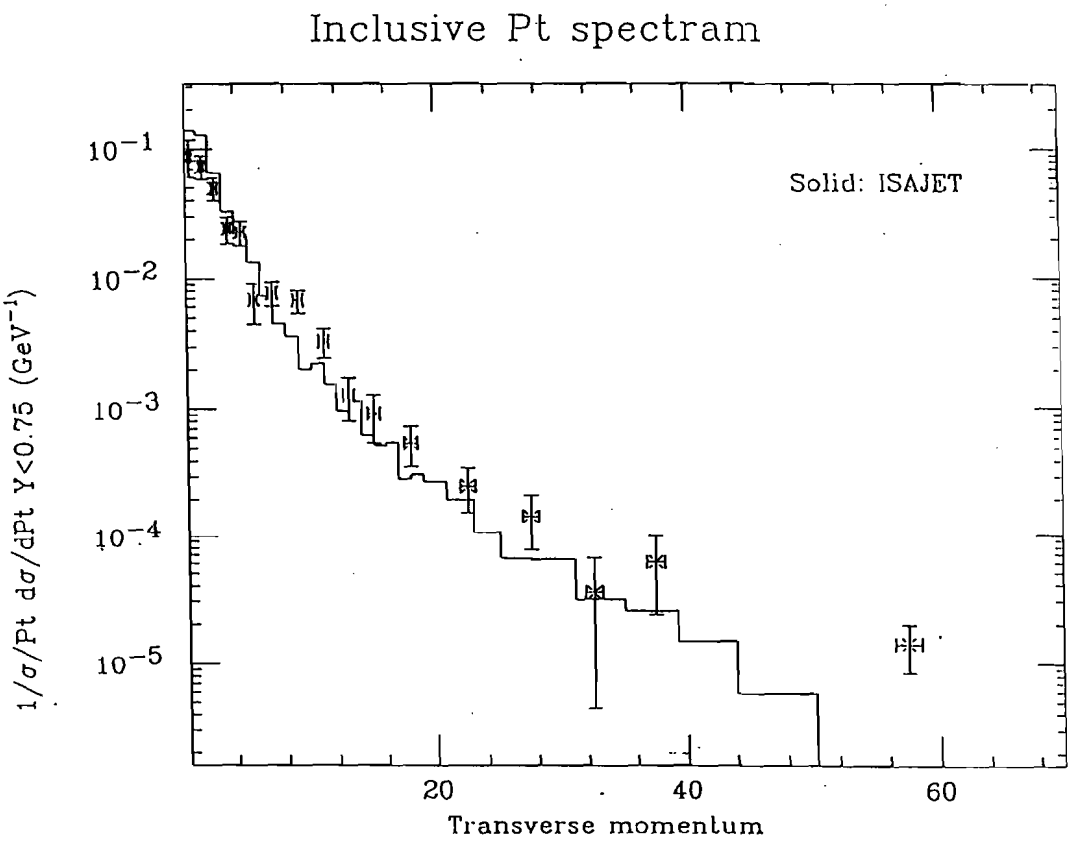

Figure 4.27: Parent virtual photon and Z^0 Pt distribution integrated over whole mass range and a comparison with a Monte Carlo generator

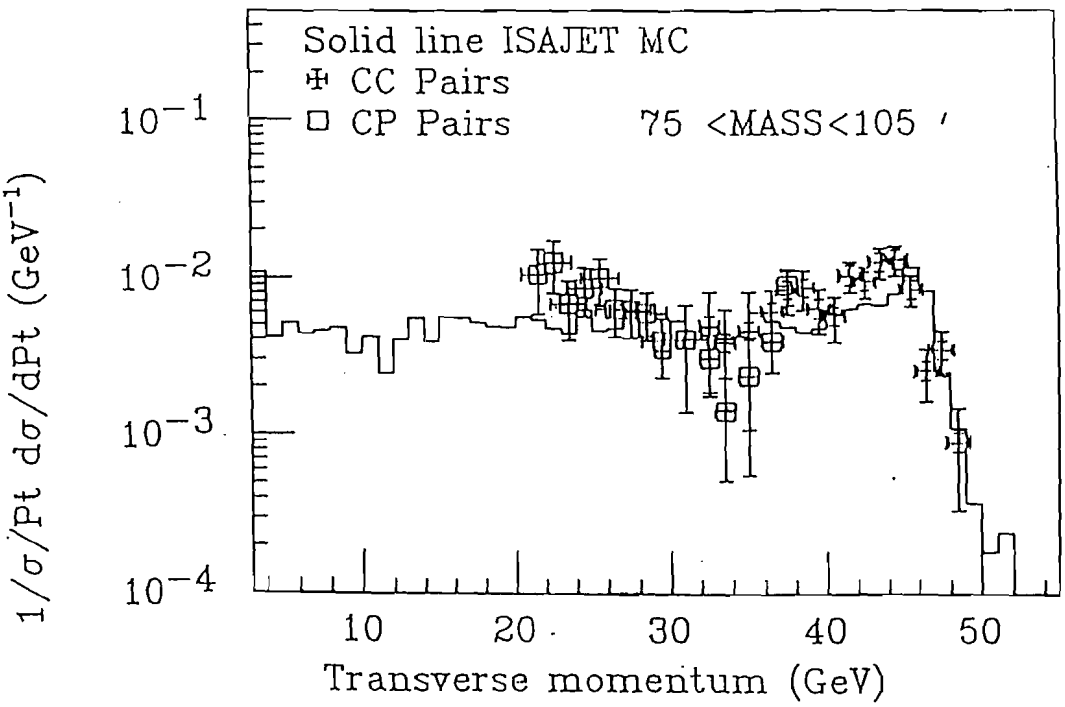

Figure 4.30: Decay electron Pt distribution comparison in center of mass system. the electron Pt distribution are calculated with Central-Central and Central-Plug pairs individually.

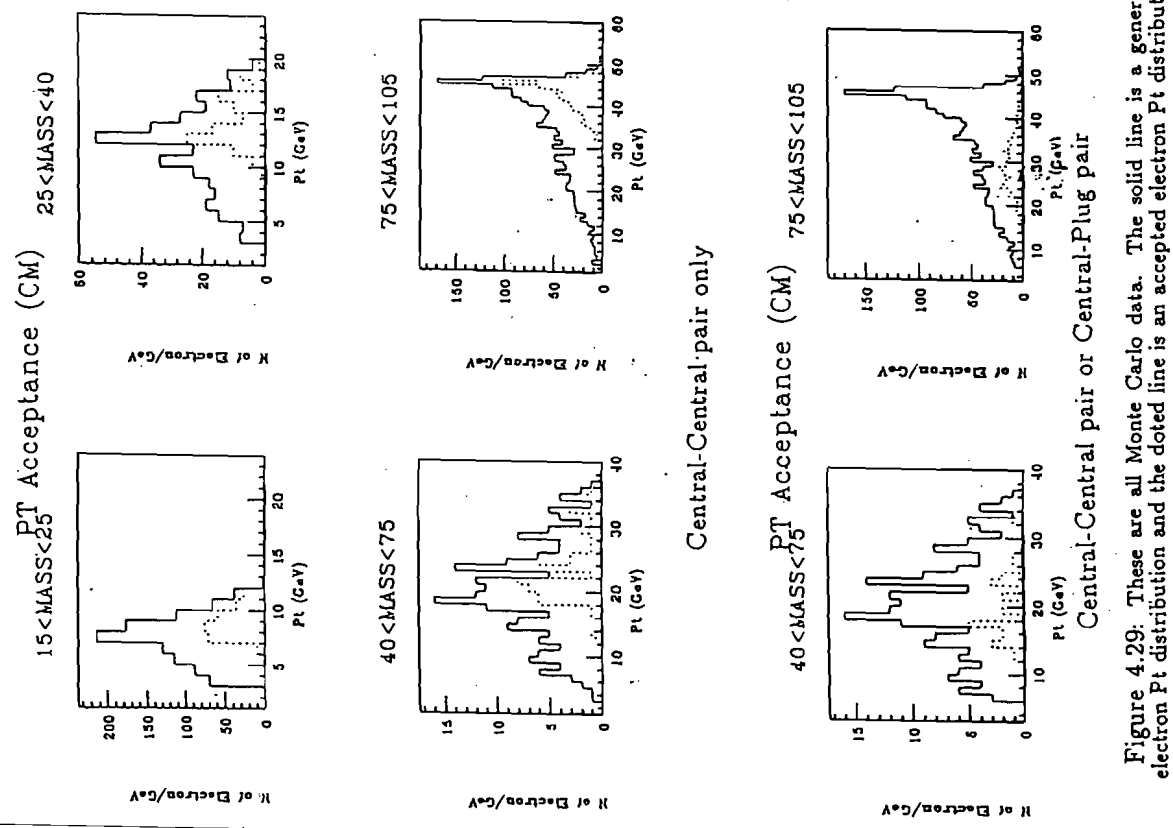

Figure 4.29: These are all Monte Carlo data. The solid line is a generated electron Pt distribution and the doted line is an accepted electron Pt distribution.

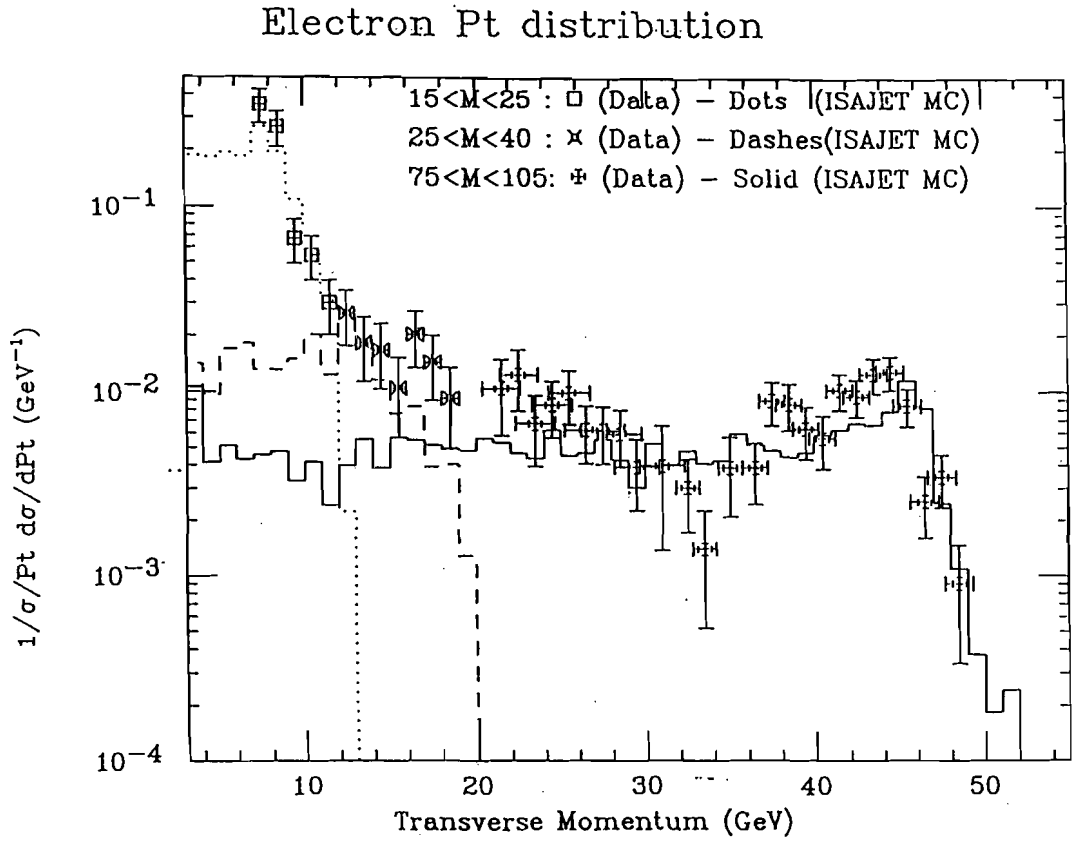

Figure 4.32: Decay electron Pt distribution at center of mass system for each mass region, where the line is theoretical prediction which has been calculated with ISAJET Monte Carlo (Lowest order) and then K factor 1.4 is multiplied

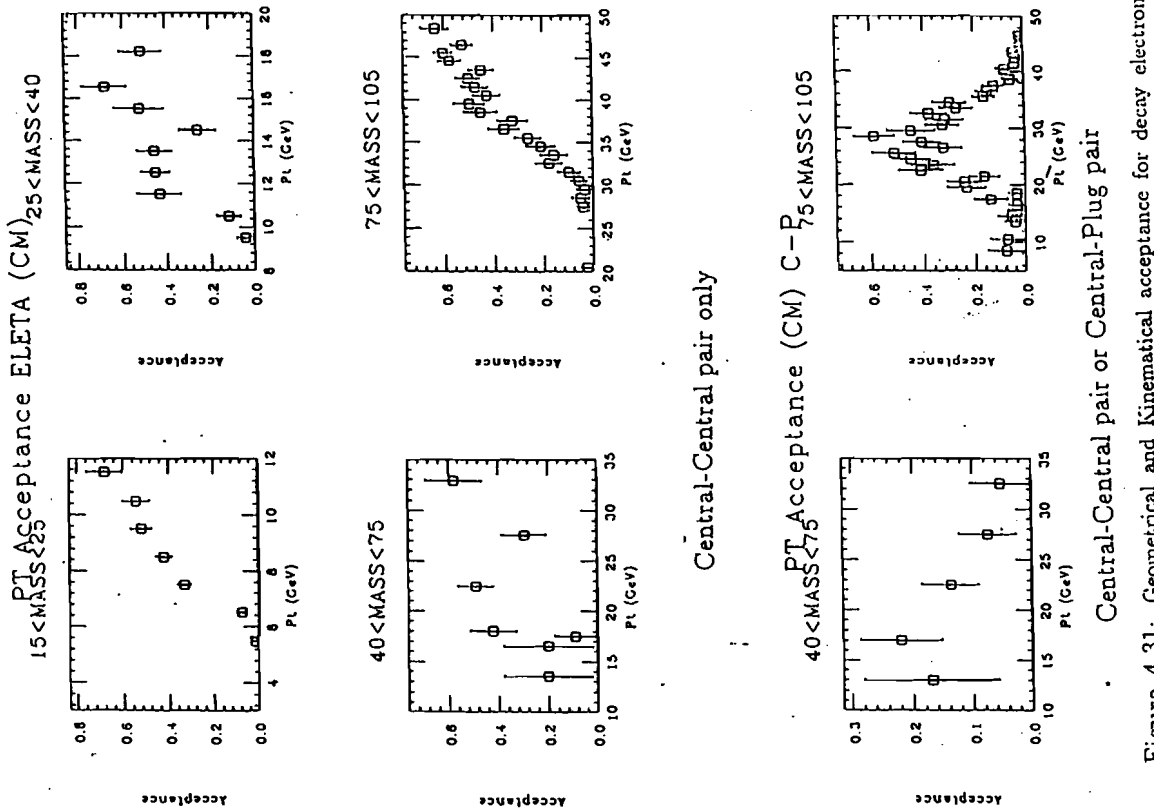

Figure 4.31: Geometrical and Kinematical acceptance for decay electron Pt distribution measurement at center of mass system

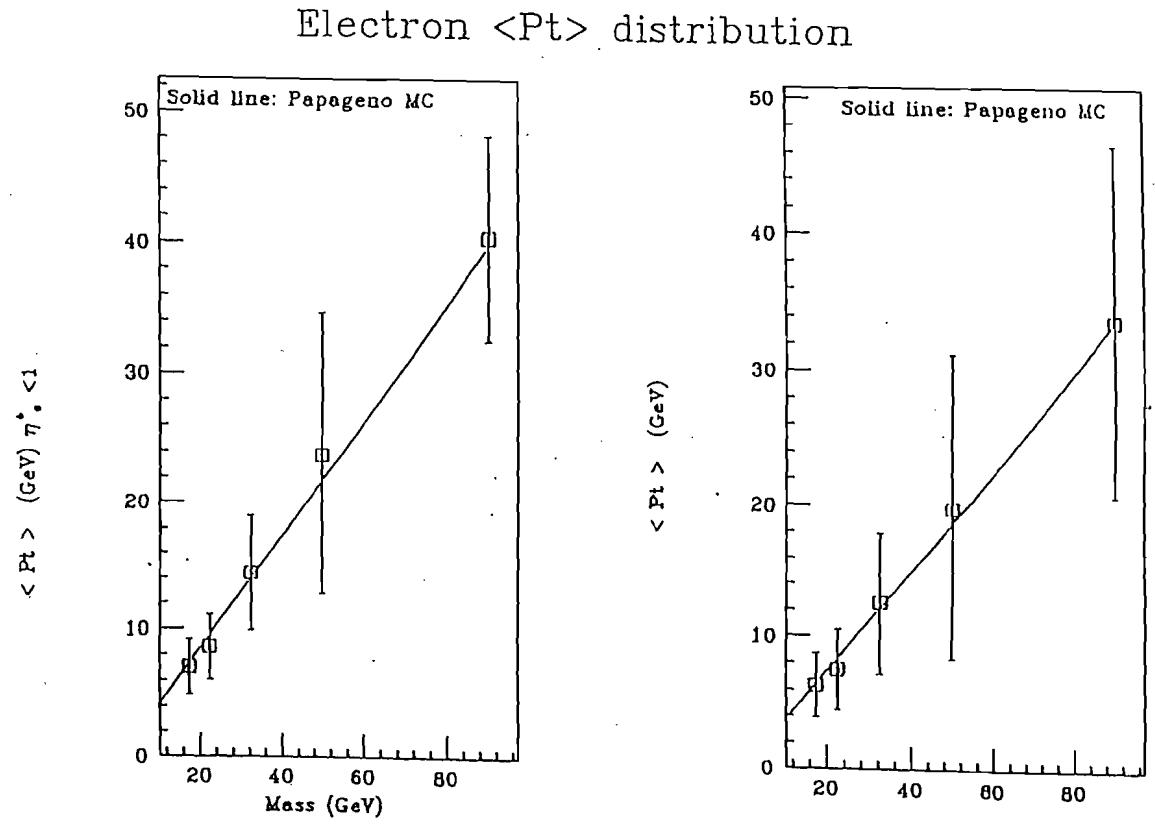

Figure 4.33: The decay electron mean Pt in the center of mass system distribution as a function of invariant mass with Monte carlo prediction. The left side plots are mean Pt of the electron in $\eta_e < 1$ of the center of mass system, and right side plot integrate over all η region assuming Monte Carlo generator

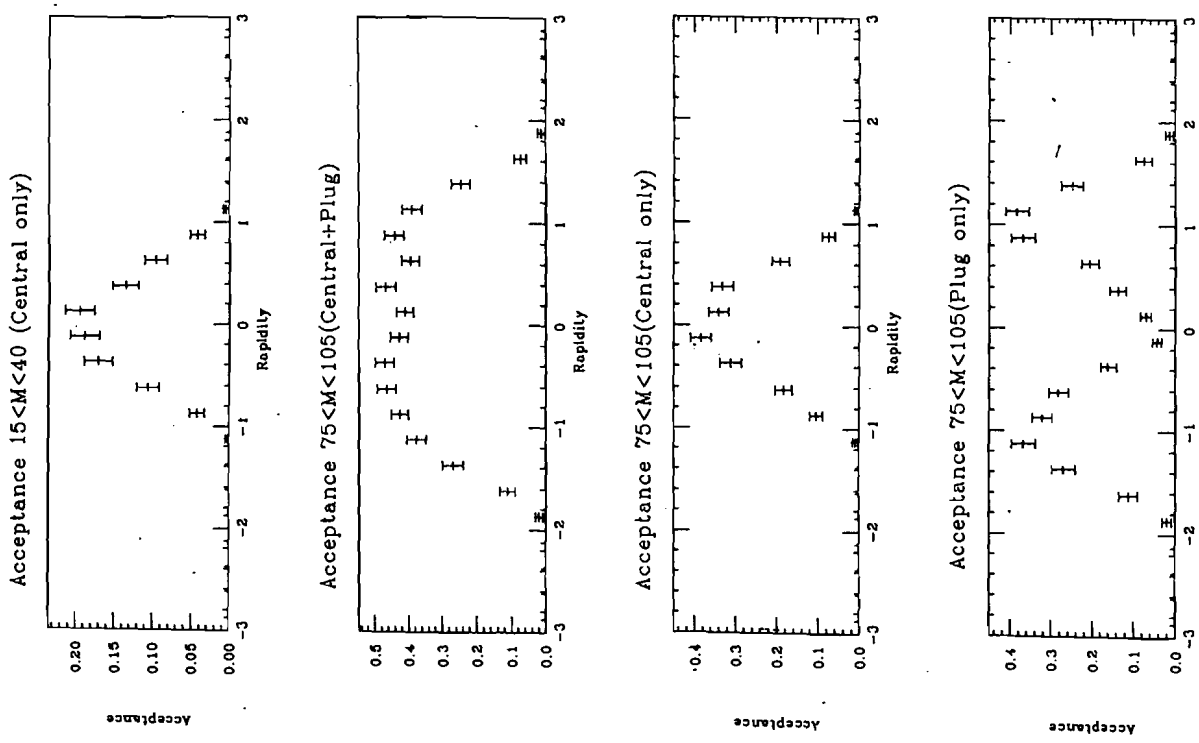

Figure 4.34: The geometrical and Kinematical acceptance as a function of rapidity of parent particle

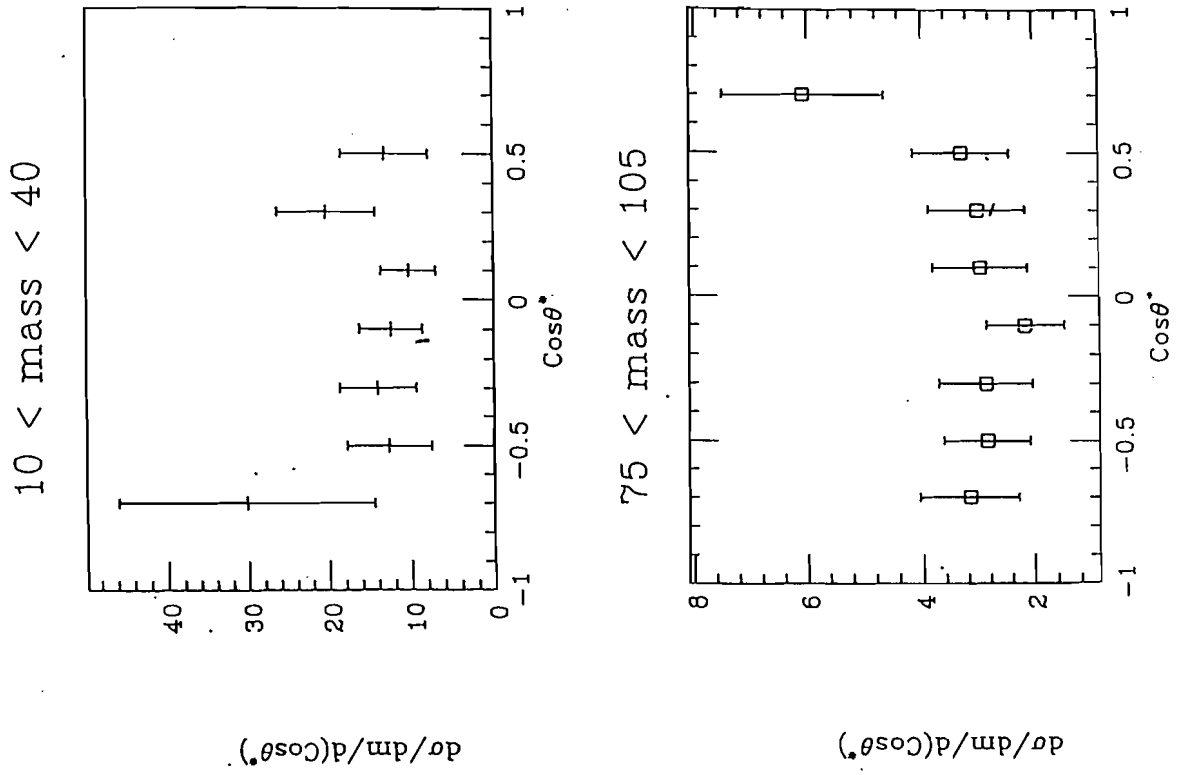

Figure 4.36: Decay electron angular distribution at the electron pair rest frame in $15 < M < 40, 75 < m < 105$ invariant mass region

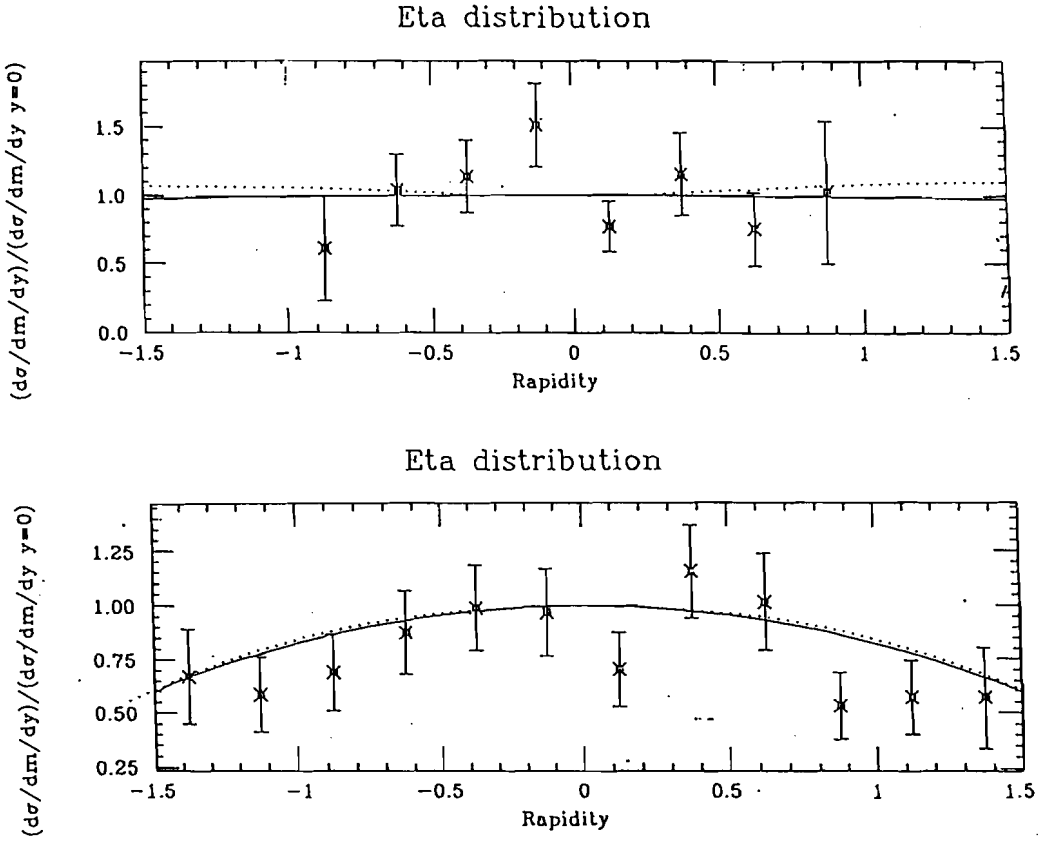

Figure 4.35: The parent particle normalized rapidity distribution with the theoretical expectation

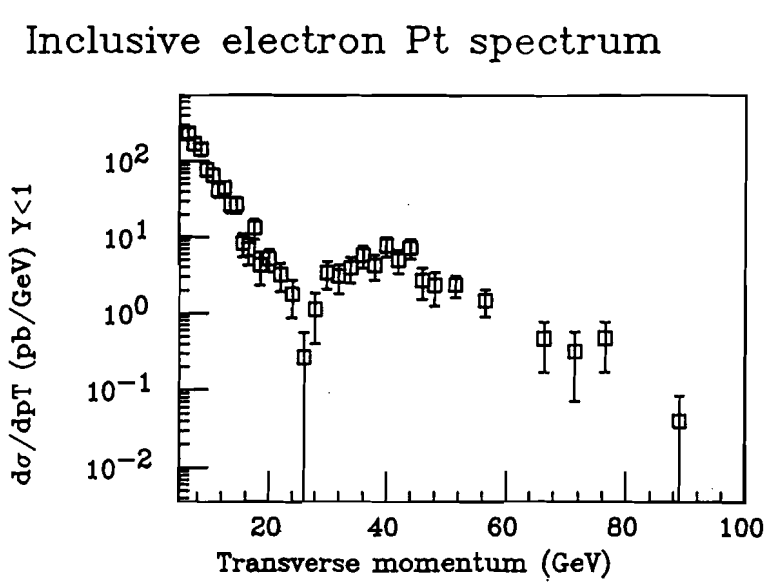

Figure 4.37 (A): The inclusive di-electron Pt distribution of opposite sign pair above 6 GeV

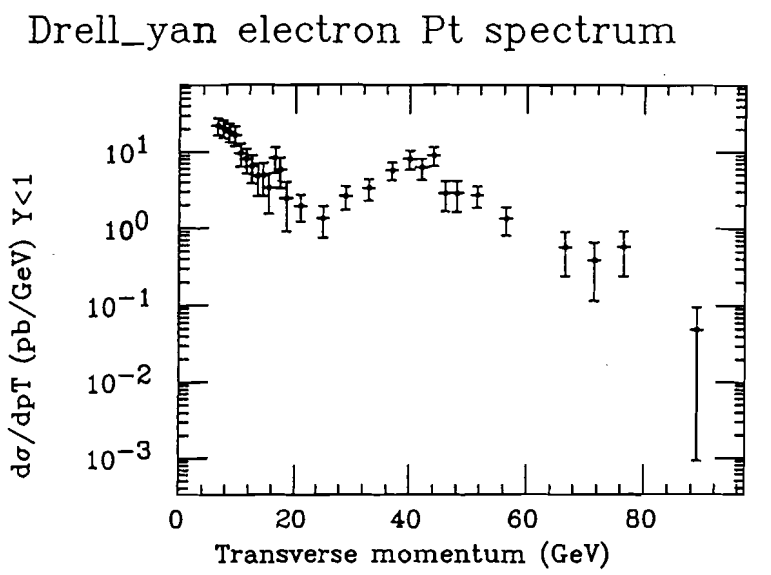

Figure 4.37 (B): The Drell-Yan di-electron Pt distribution of loboratory system above 6 GeV

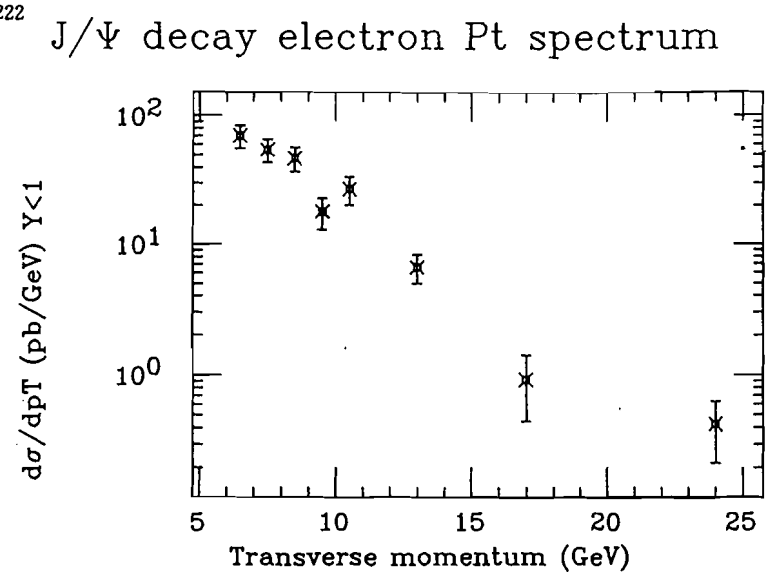

Figure 4.37 (C): The observed J/Ψ decay electron Pt distribution at laboratory system above 6 GeV

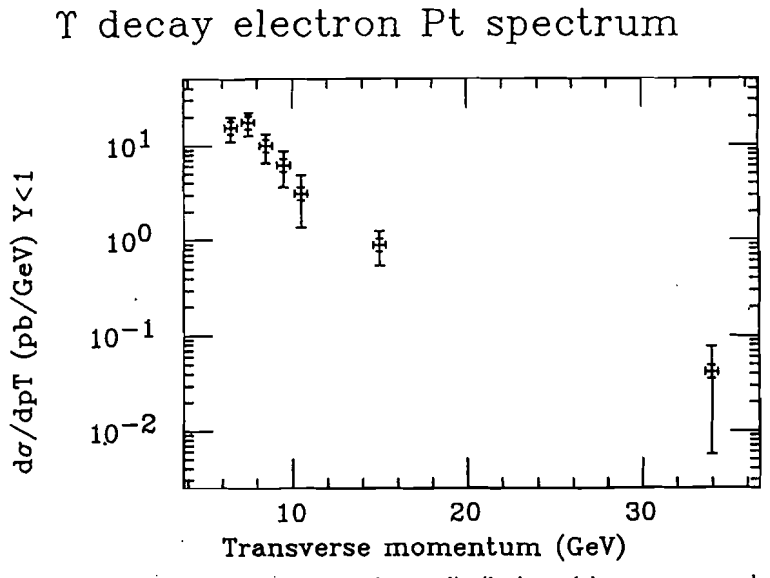

Figure 4.37 (D): The observed ϒ decay electron distribution at laboratory system above 6 GeV

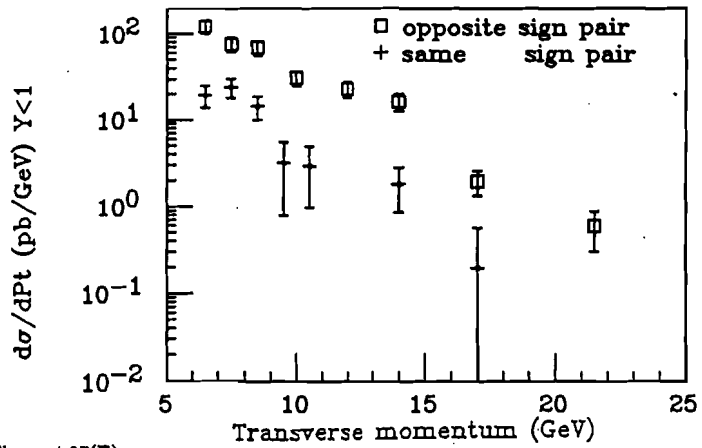

Figure 4.37(E): The nonisolated the opposite sign and same sign pair Pt distributions above 6 GeV

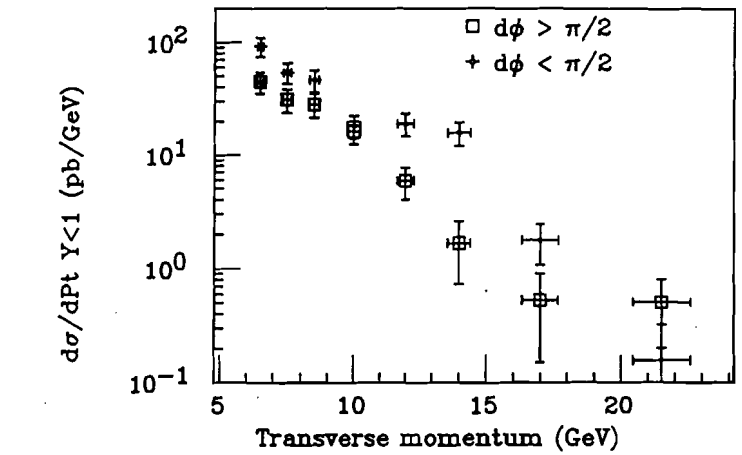

Figure 4.37(F): The nonisolated opposite pair Pt spectrum of $d\phi > \pi/2$ samples, and $d\phi < \pi/2$ samples

Figure 4.37: Fig A is the inclusive di-electron Pt distribution of opposite sign, and B is Drell-Yan di-electron Pt distribution, C and D are that of the observed J/Ψ and Υ decay electron. The nonisolated the opposite sign and same sign pair Pt distributions are plotted respectively in Fig E. The nonisolated opposite pair Pt spectrum are also plotted in Fig F for $d\phi > \pi/2$ and $d\phi < \pi/2$ samples. These all Pt distributions are measured above 6 GeV.

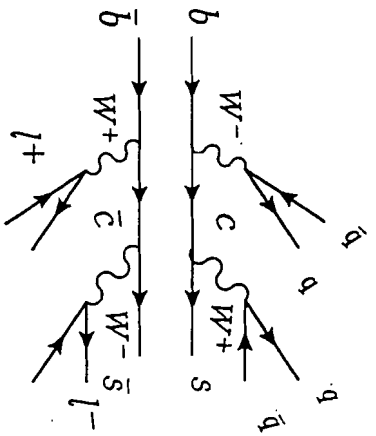

Figure 4.38(A): The cascade semileptonic decay of b quark (Opposite sign pair)

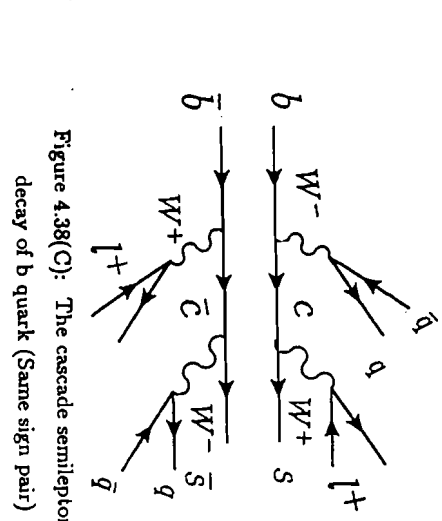

Figure 4.38(C): The cascade semileptonic decay of b quark (Same sign pair)

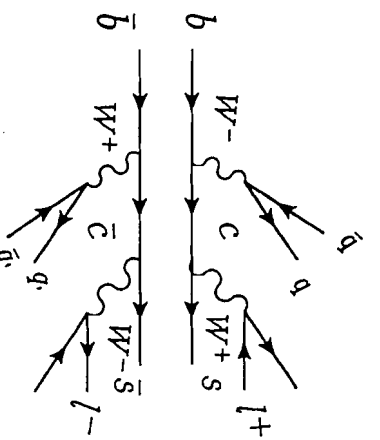

Figure 4.38(B): The cascade semileptonic decay of b quark (Opposite sign pair)

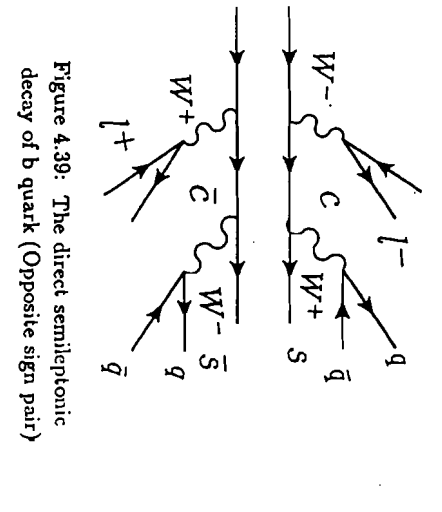

Figure 4.39: The direct semileptonic decay of b quark (Opposite sign pair)

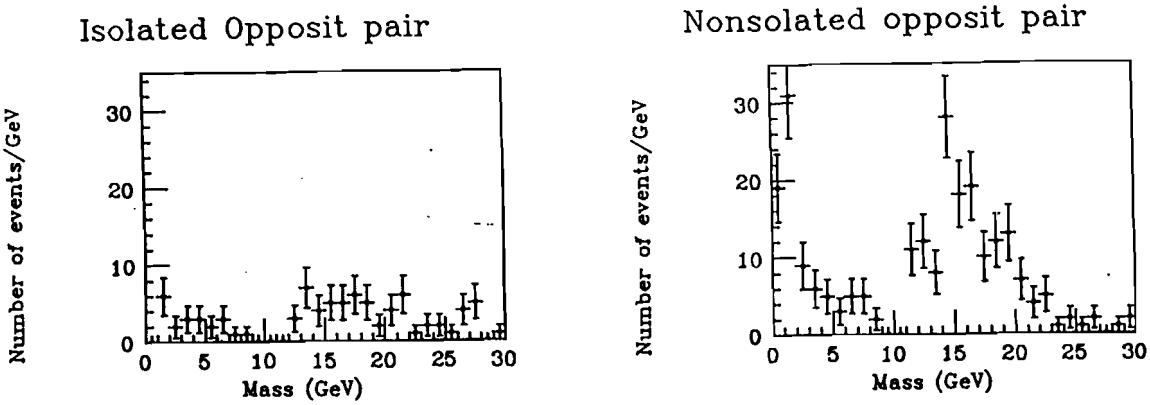

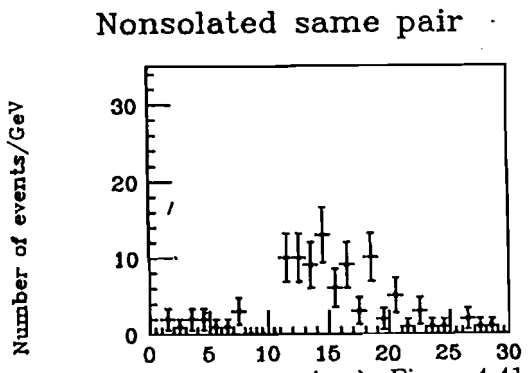

Figure 4.41: The invariant mass distribution of nonisolated electron pairs. J/Ψ, Υ have already subtracted.

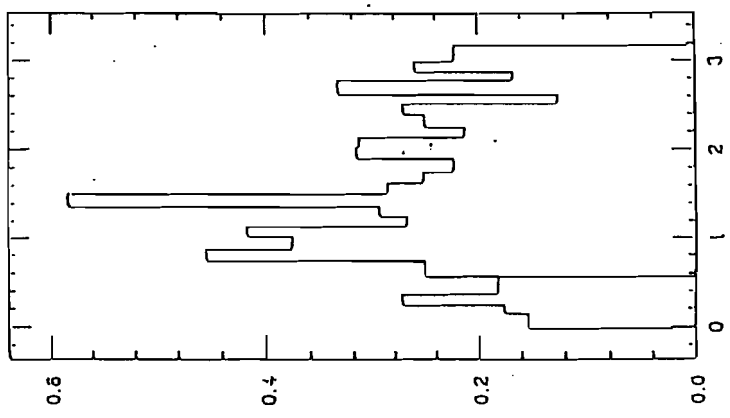

Figure 4.40: Offline electron identification efficiency opening angle dependence

Figure 4.43 (A):The 1st and 2nd electron Pt distribution of nonisolated opposite sign electron pairs.

Figure 4.43 (B):The 1st and 2nd electron Pt distribution of nonisolated same sign electron pairs.

Figure 4.42: The invariant mass distribution of nonisolated electron pairs with small opening angle $d\phi < \pi/2$. J/Ψ , Υ have already subtracted.

Nonisolated opposite charge pair (direct)

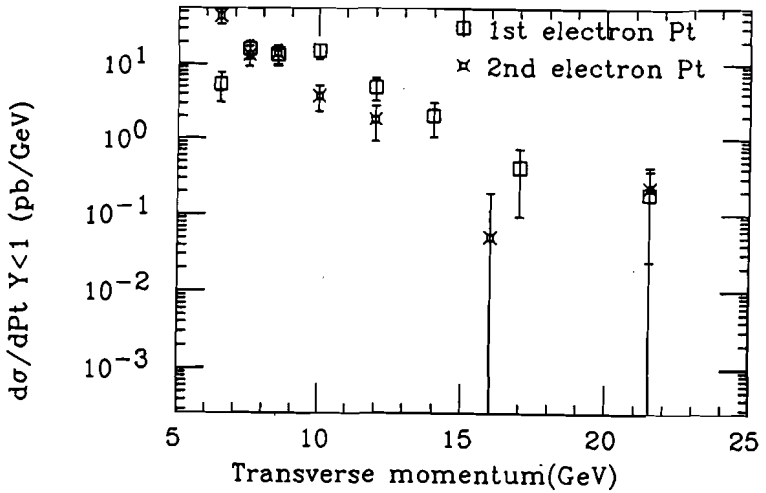

Figure 4.43 (C):The 1st and 2nd electron Pt distribution of nonisolated opposite sign electron pairs. ($d\phi > \pi/2$)

Nonisolated opposite charge pair (cascade)

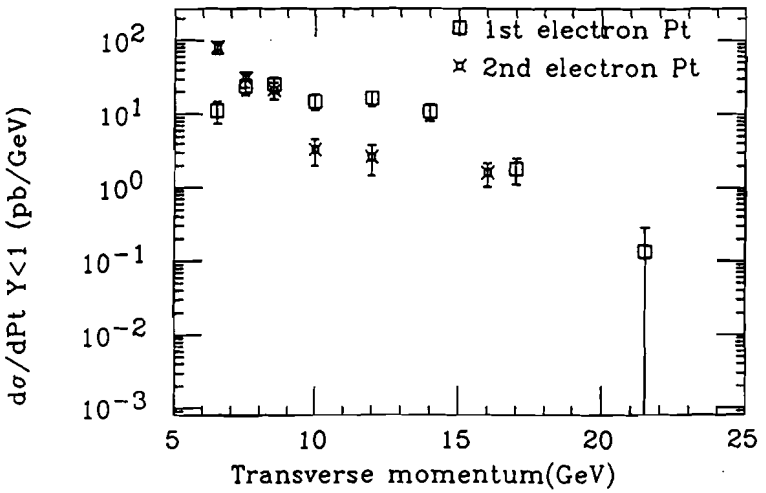

Figure 4.43 (D):The 1st and 2nd electron Pt distribution of nonisolated opposite sign electron pairs. $d\phi < \pi/2$)

Isolated opposite charge pair

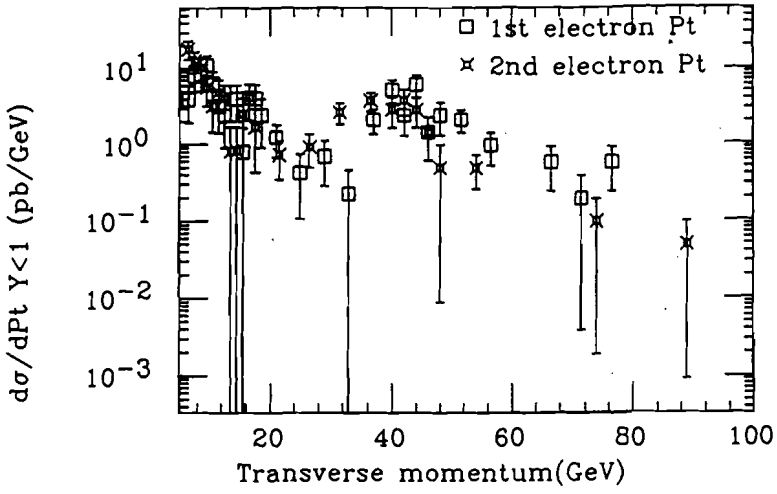

Figure 4.43(E): The 1st electron and 2nd electron Pt distribution for isolated electron pair sample above 6 GeV.

Inclusive opposite charge pair

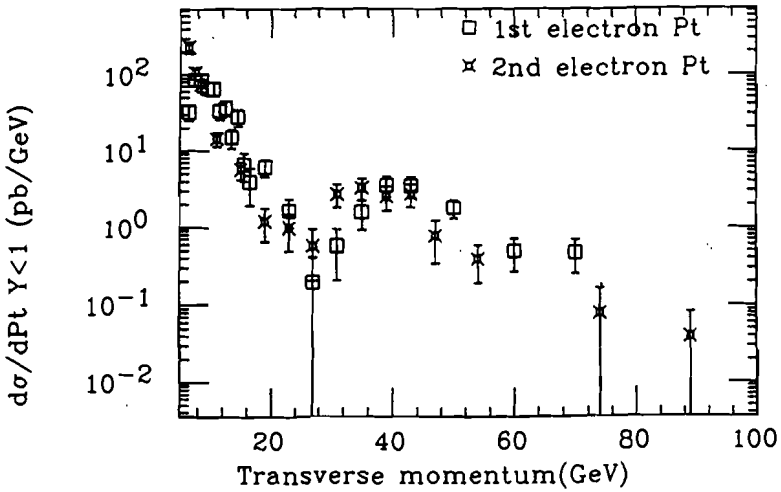

Figure 4.43(F): The 1st electron and 2nd electron Pt distribution for inclusive di-electron sample above 6 GeV.

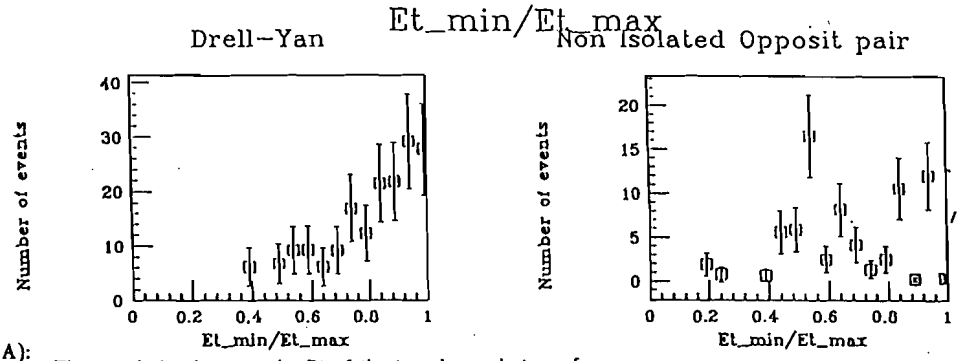

Figure 4.45(A): The correlation between the Pt of the two decay electrons for Drell-Yan sample. the 1st electron Pt is required to be greater than 12 GeV, and the 2nd electron Pt is required to be greater than 6 GeV

Figure 4.45(B):: The correlation between the Pt of the two decay electrons for nonisolated opposite sign pair sample. the 1st electron Pt is required to be greater than 12 GeV, and the 2nd electron Pt is required to be greater than 6 GeV

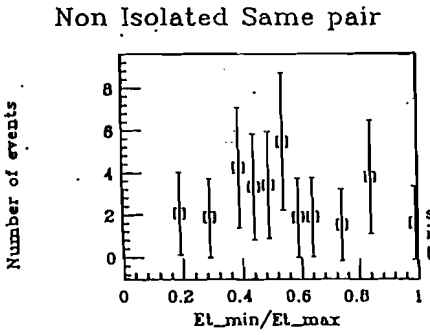

Figure 4.45: The correlation between the Pt of the two electrons in the final state. Fig A is Drell-Yan sample, B is nonisolated opposite sign pair sample, and C is nonisolated same sign pair sample. The 1st electron Pt is required to be greater than 12 GeV, and the 2nd electron Pt is required to be greater than 6 GeV

Figure 4.45(C):.. The correlation between the Pt of the two decay electrons for nonisolated same sign pair sample. the 1st electron Pt is required to be greater than 12 GeV, and the 2nd electron Pt is required to be greater than 6 GeV

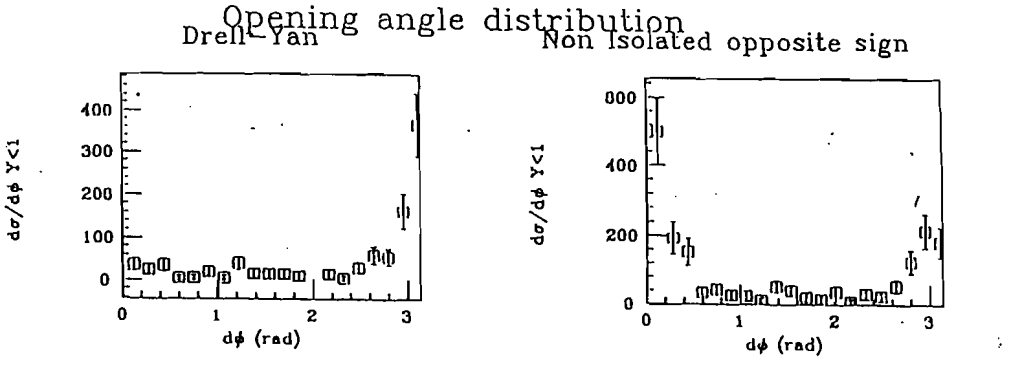

Figure 4.44(A):: Opening angle distribution for Drell-Yan events

Figure 4.44(B): Opening angle distribution for nonisolated opposite sign pairs

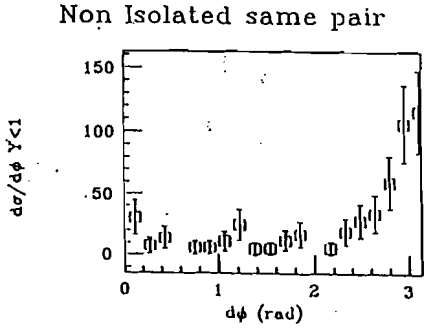

Figure 4.44: Fig A is opening angle distribution for Drell-Yan events and B is that of nonisolated opposite sign pairs, and C is for nonisolated same sign pairs.

Figure 4.44(C):: Opening angle distribution for nonisolated same sign pairs

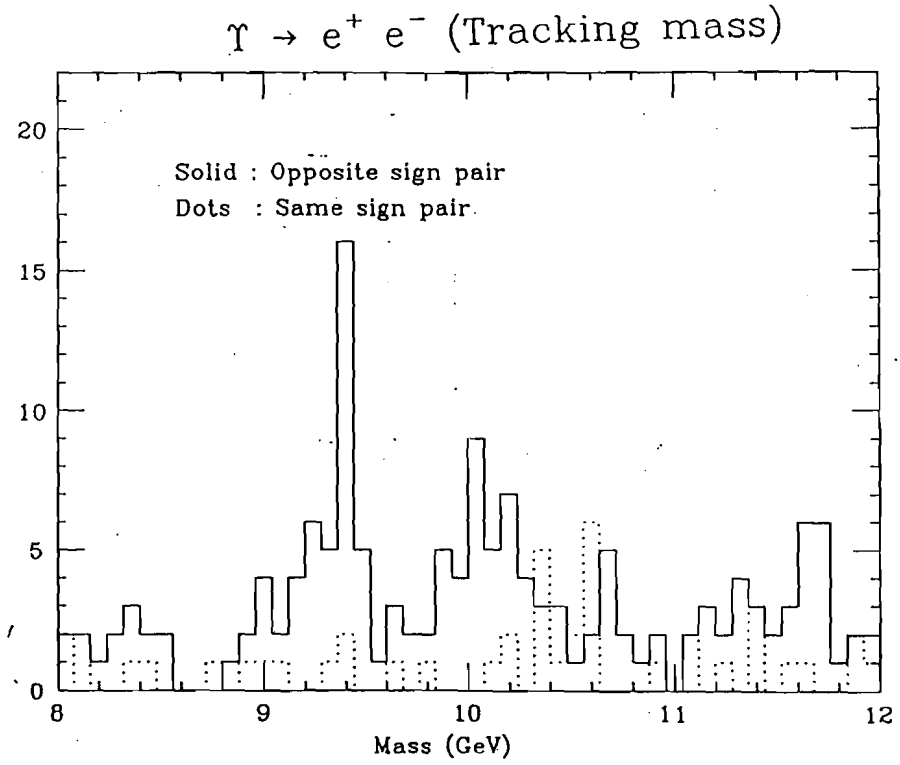

Figure 4.47(A) Υ mass distribution. Mass is calculated using the tracking momentum information.

234

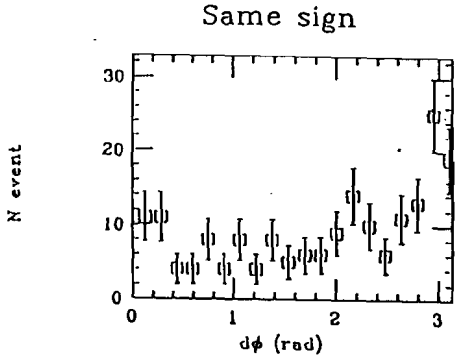

Figure 4.46(A): Opening angle distribution for electron + muon same sign pair

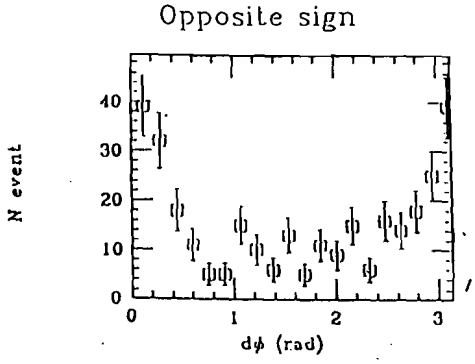

Figure 4.46(B): Opening angle distribution for electron + muon opposite sign pair

233

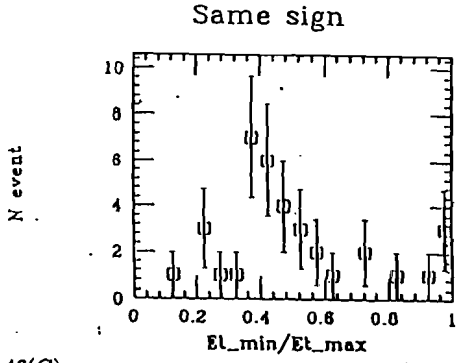

Figure 4.46(C): The correlation between the Pt of the two leptons for same sign electron + muon sample

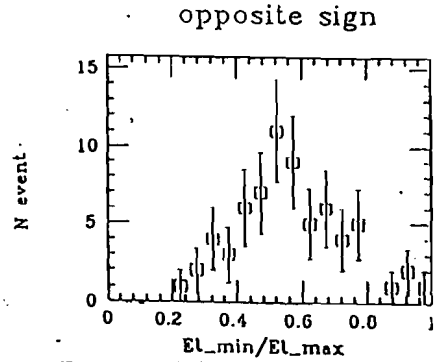

Figure 4.46(D): The correlation between the Pt of the two leptons for opposite sign electron + muon sample

Figure 4.46: Fig A is opening angle distribution for electron + muon same sign pair and B is that of opposite sign pairs. Fig C shows The correlation between the Pt of the two leptons (electron and muon) for same sign pairs and D is that of opposite sign pairs.

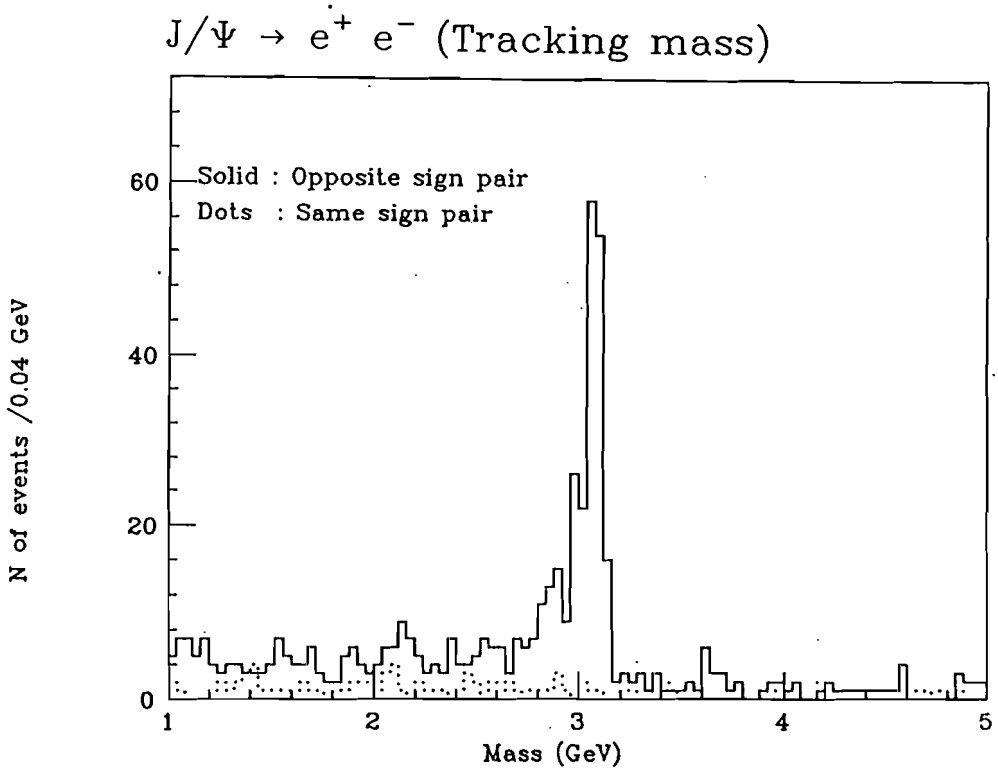

Figure 4.47(C) J/Ψ mass distribution. Mass is calculated using the tracking momentum information.

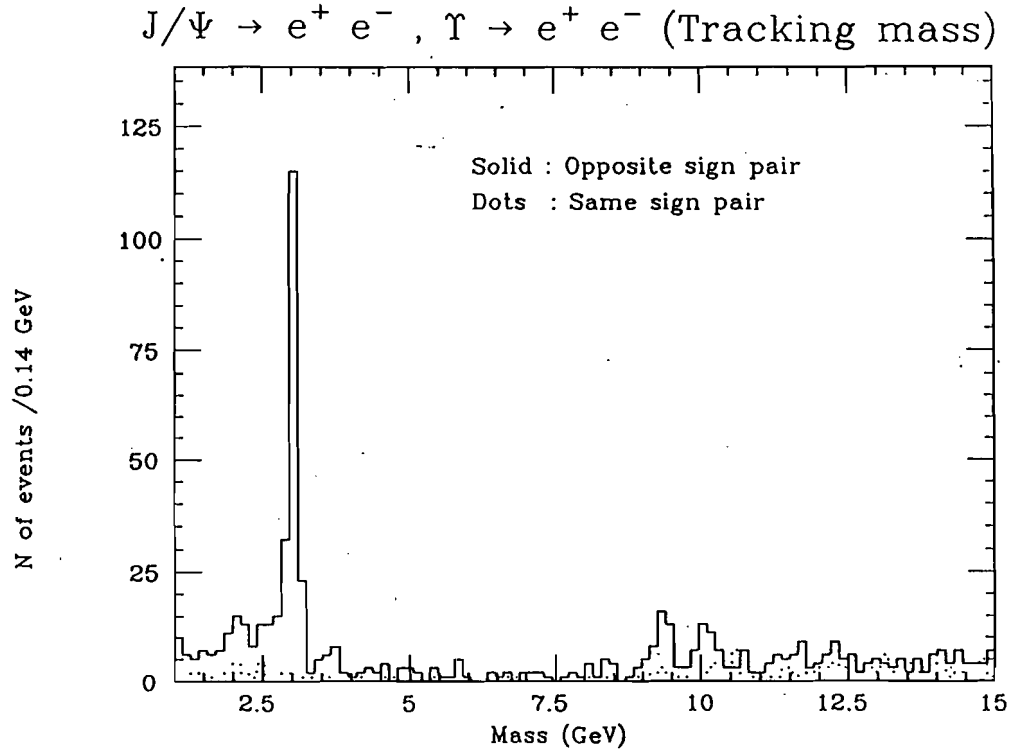

Figure 4.47(B) J/Ψ and Υ mass distribution. Mass is calculated using the tracking momentum information.

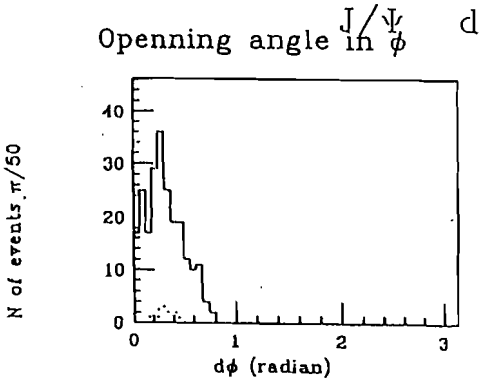

Figure 4:48(A): J/Ψopening angle distribution

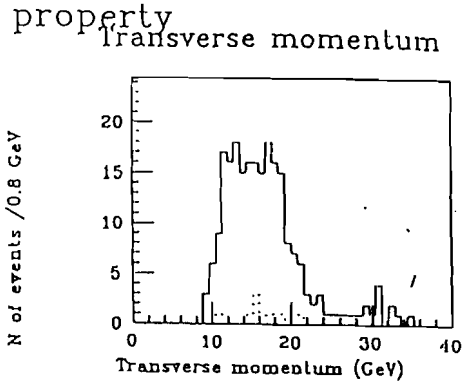

Figure 4.48(B) : J/ΨPt distribution

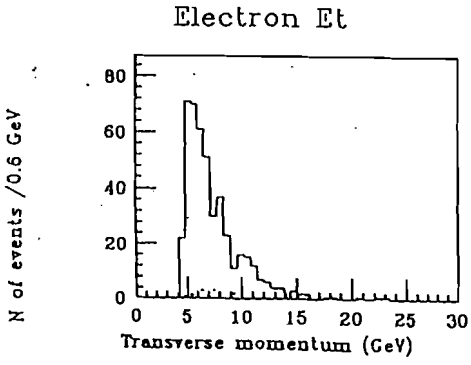

Figure 4.48(C) : J/Ψdecay electron Pt distribution

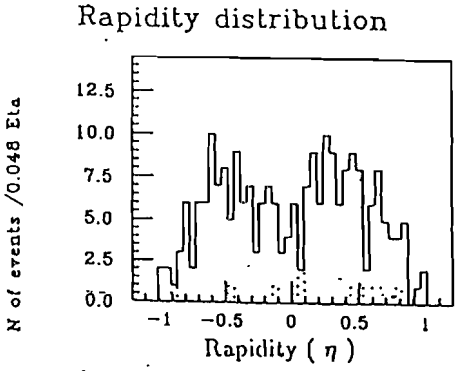

Figure 4.48(D) : J/Ψrapidity distribution

238

Figure 4.48: The decay properties of observed J/Ψin electron pair mode. Fig A is opening angle distribution, B is Pt distribution and C is Pt distribution of electrons in the final state. Fig D is rapidity distribution of J/Ψ's

237

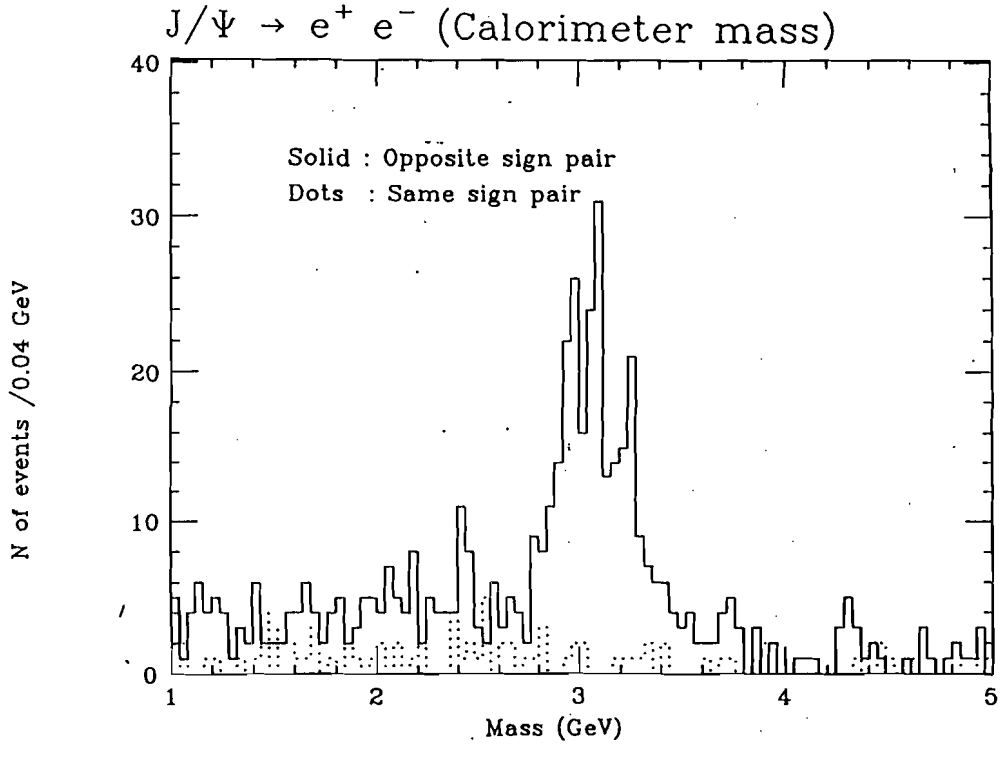

Figure 4.47(D) J/ψ mass distribution. Mass is calculated using the calorimeter information.

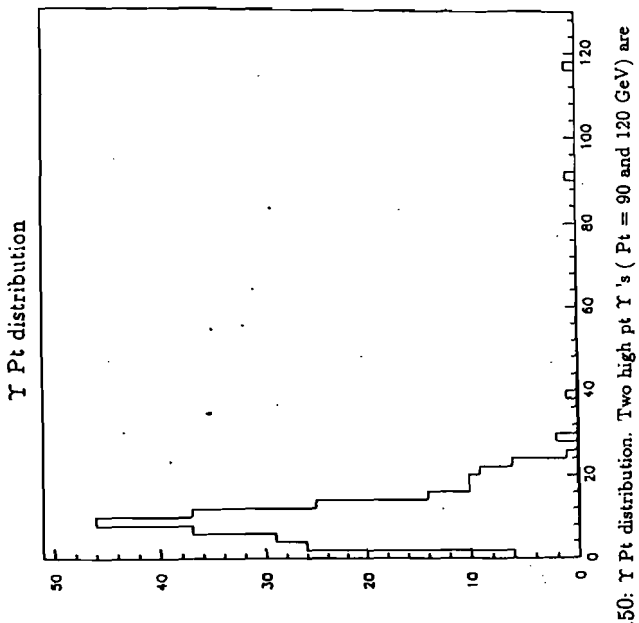

Figure 4.50: Υ Pt distribution. Two high pt Υ 's (Pt = 90 and 120 GeV) are detected.

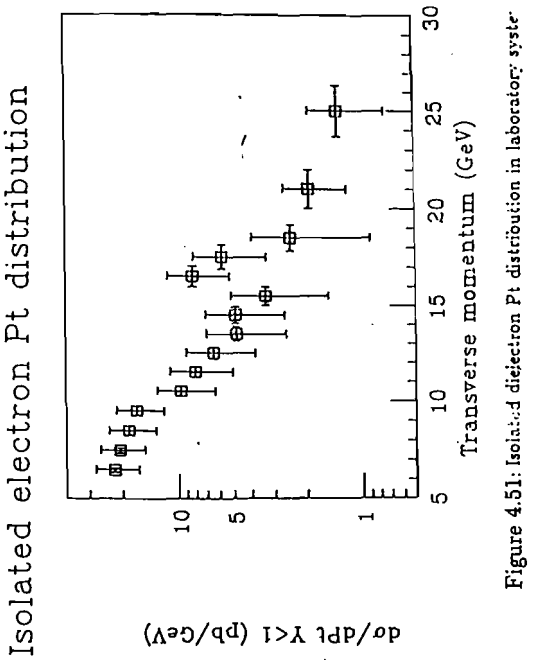

Figure 4.51: Isolated dielectron Pt distribution in laboratory syste

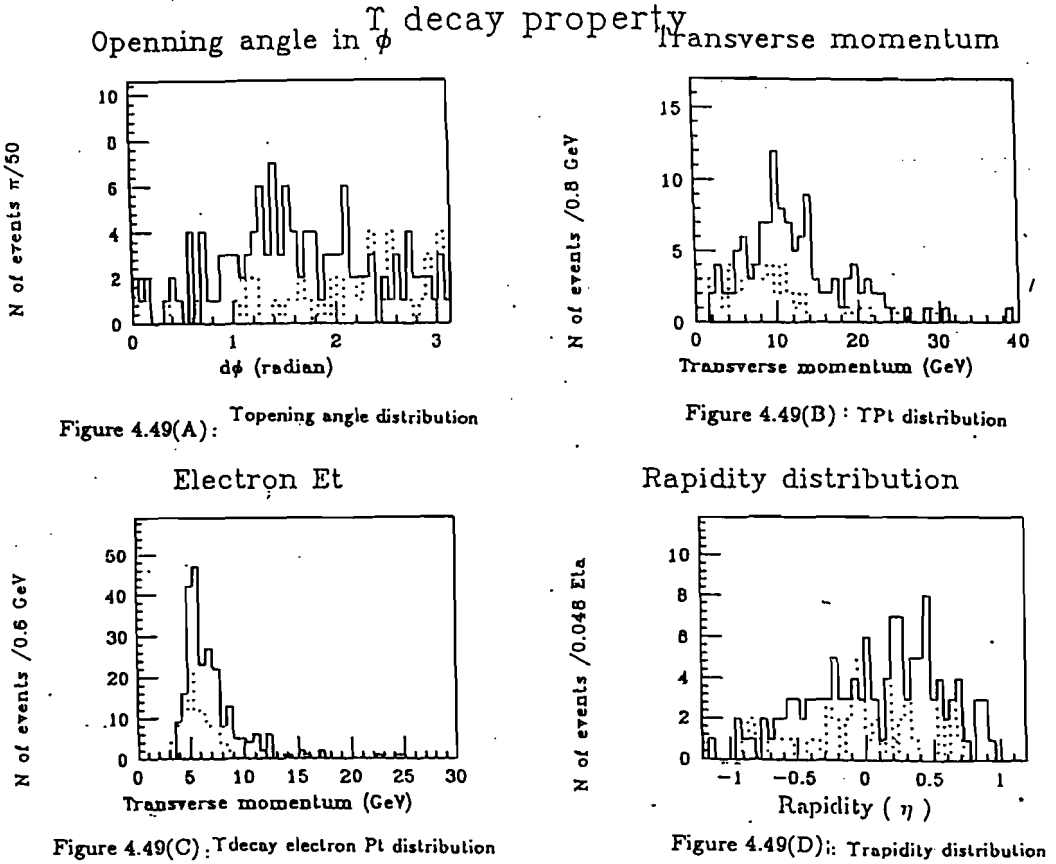

Figure 4.49(A): Topening angle distribution

Figure 4.49(B) : ΥPt distribution

Figure 4.49(C) : Υdecay electron Pt distribution

Figure 4.49(D): Υrapidity distribution

Figure 4.49: The decay properties of observed Υin electron pair mode. Fig A is opening angle distribution, B is Pt distribution and C is Pt distribution of electrons in the final state. Fig D is rapidity distribution of Υ's

Appendix

Appendix A

CDF collaboration

F. Abe,[8] D. Amidei,[4] G. Apollinari,[11] M. Atac,[4] P. Auchincloss,[14] A. R. Baden,[6] A. Bamberger,[4],[a] A. Barbaro-Galtieri,[9] V. E. Barnes,[12] F. Bedeschi,[11] S. Behrends,[3] S. Belforte,[11] G. Bellettini,[11] J. Bellinger,[18] J. Bensinger,[3] A. Beretvas,[4] J. P. Berge,[4] S. Bertolucci,[5] S. Bhadra,[7] M. Binkley,[4] R. Blair,[1] C. Blocker,[3] A. W. Booth,[4] G. Brandenburg,[6] D. Brown,[6] E. Buckley,[14] A. Byon,[12] K. L. Byrum,[18] C. Campagnari,[3] M. Campbell,[3] R. Carey,[6] W. Carithers,[9] D. Carlsmith,[18] J. T. Carroll,[4] R. Cashmore,[4],[a] F. Cervelli,[11] K. Chadwick,[4] G. Chiarelli,[5] W. Chinowsky,[9] S. Cihangir,[4] A. G. Clark,[4] D. Connor,[10] M. Contreras,[2] J. Cooper,[4] M. Cordelli,[5] D. Crane,[4] M. Curatolo,[5] C. Day,[4] S. Dell'Agnello,[11] M. Dell'Orso,[11] L. Demortier,[2] P. F. Derwent,[3] T. Devlin,[14] D. DiBitonto,[15] R. B. Drucker,[9] J. E. Elias,[4] R. Ely,[9] S. Errede,[7] B. Esposito,[5] B. Flaugher,[14] G. W. Foster,[4] M. Franklin,[6] J. Freeman,[4] H. Frisch,[3] Y. Fukui,[8] Y. Funayama,[16] A. F. Garfinkel,[12] A. Gauthier,[7] S. Geer,[6] P. Giannetti,[11] N. Giokaris,[13] P. Giromini,[5] L. Gladney,[10] M. Gold,[9] K. Goulianos,[13] H. Grassmann,[11] C. Grosso-Pilcher,[3] C. Haber,[9] S. R. Hahn,[4] R. Handler,[18] K. Hara,[16] R. M. Harris,[9] J. Hauser,[3] T. Hessing,[15] R. Hollebeek,[10] L. Holloway,[7] P. Hu,[14] B. Hubbard,[9] B. T. Huffman,[12] R. Hughes,[10] P. Hurst,[7] J. Huth,[4] M. Incagli,[11] T. Ino,[16] H. Iso,[16] H. Jensen,[4] C. P. Jessop,[6] R. P. Johnson,[4] U. Joshi,[4] R. W. Kadel,[4] T. Kamon,[15] S. Kanda,[16] D. A. Kardelis,[7] I. Karliner,[7] E. Kearns,[6] R. Kephart,[4] P. Kesten,[2] R. M. Keup,[7] H. Keutelian,[7] S. Kim,[16] L. Kirsch,[2] K. Kondo,[16] S. E. Kuhlmann,[1] E. Kuns,[14] A. T. Laasanen,[12] J. I. Lamoureux,[18] W. Li,[1] T. M. Liss,[7] N. Lockyer,[10] C. B. Luchini,[7] P. Maas,[4] M. Mangano[11] J. P. Marriner,[4] R. Markeloff,[18] L. A. Markosky,[18] R. Mattingly,[2] P. McIntyre,[15] A. Menzione,[11] T. Meyer,[15] S. Mikamo,[8] M. Miller,[3] T. Mimashi,[16] S. Miscetti,[5] M. Mishina,[8] S. Miyashita,[16] Y. Morita,[16] S. Moulding,[2] A. Mukherjee,[4] L. F. Nakae,[2] I. Nakano,[16] C. Nelson,[4] C. Newman-Holmes,[4] J. S. T. Ng,[6] M. Ninomiya,[16] L. Nodulman,[1] S. Ogawa,[16] R. Paoletti,[11] A. Para,[4] E. Pare,[6] J. Patrick,[4] T. J. Phillips,[6] R. Plunkett,[4] L. Pondrom,[18] J. Proudfoot,[1] G. Punzi,[11] D. Quarrie,[4] K. Ragan,[10] G. Redlinger,[3] J. Rhoades,[18] M. Roach,[17] F. Rimondi,[4],[a] L. Ristori,[11] T. Rohaly,[10] A. Roodman,[3] D. Saltzberg,[3] A. Sansoni,[5] R. D. Sard,[7] A. Savoy-Navarro,[4] V. Scarpine,[7] P. Schlabach,[7] E. E. Schmidt,[4] M. H. Schub,[12] R. Schwitters,[6] A. Scribano,[11] S. Segler,[4] Y. Seiya,[16] M. Sekiguchi,[16] P. Sestini,[11] M. Shapiro,[6] M. Sheaff,[18] M. Shochet,[3] J. Siegrist,[9] P. Sinervo,[10] J. Skarha,[18] K. Sliwa,[17] D. A. Smith,[11] F. D. Snider,[3] R. St. Denis,[6] A. Stefanini,[11] R. L. Swartz, Jr.,[7] M. Takano,[16] K. Takikawa,[16] S. Tarem,[2] D. Theriot,[4] M. Timko,[15] P. Tipton,[9] S. Tkaczyk,[4] A. Tollestrup,[4] G. Tonelli,[11] J. Tonnison,[12] W. Trischuk,[6] Y. Tsay,[3] F. Ukegawa,[16] D. Underwood,[1] R. Vidal,[4] R. G. Wagner,[1] R. L. Wagner,[4] J. Walsh,[10] T. Watts,[14] R. Webb,[15] C. Wendt,[18] W. C. Wester, III,[9] T. Westhusing,[11] S. N. White,[13] A. B. Wicklund,[1] H. H. Williams,[10] B. L. Winer,[9] A. Yagil,[4] A. Yamashita,[16] K. Yasuoka,[16] G. P. Yeh,[4] J. Yoh,[4] M. Yokoyama,[16] J. C. Yun,[4] F. Zetti[11]

[1] *Argonne National Laboratory, Argonne, Illinois 60439*

[2] *Brandeis University, Waltham, Massachusetts 02254*

[3] *University of Chicago, Chicago, Illinois 60637*

[4] *Fermi National Accelerator Laboratory, Batavia, Illinois 60510*

[5] *Laboratori Nazionali di Frascati, Istituto Nazionale di Fisica Nucleare, Frascati, Italy*

[6] *Harvard University, Cambridge, Massachusetts 02138*

[7] *University of Illinois, Urbana, Illinois 61801*

[8] *National Laboratory for High Energy Physics (KEK), Tsukuba, Ibaraki 305, Japan*

[9] *Lawrence Berkeley Laboratory, Berkeley, California 94720*

[10] *University of Pennsylvania, Philadelphia, Pennsylvania 19104*

[11] *Istituto Nazionale di Fisica Nucleare, University and Scuola Normale Superiore of Pisa, I-56100 Pisa, Italy*

[12] *Purdue University, West Lafayette, Indiana 47907*

[13] *Rockefeller University, New York, New York 10021*

[14] *Rutgers University, Piscataway, New Jersey 08854*

[15] *Texas A&M University, College Station, Texas 77843*

[16] *University of Tsukuba, Tsukuba, Ibaraki 305, Japan*

[17] *Tufts University, Medford, Massachusetts 02155*

[18] *University of Wisconsin, Madison, Wisconsin 53706*

Appendix B

Electron cut efficiency calculation

The electron cut efficiencies are calculated in the following procedures, using J/Ψ and Z^0 sample. To measure the electron cut efficiencies from the J/Ψ and Z^0 sample, we required a set of tight electron cuts on one central electron first, and then the cut is applied to another EM cluster in the central region. Since we need the tight cut electron efficiency to calculate the other cut efficiencis, the tight cut electron efficiency has been measured first by method 1, then each cut efficiency has been calculated with method 2.

1) The cut efficiency calcuation for only one cut parameter set

$$N1 = N0 * P * P$$

$$N2 = N0 * 2 * P * (1 - P)$$

$$N3 = N0 * (1 - P) * (1 - P)$$

so that

$$P = 2 * \frac{N1}{(2 * N1 + N2)},$$

where

- N0: Number of total /Jpsi (or Z)
- N1: Number of /Jpsi (or Z) that both electron satisfied the cut
- N2: Number of /Jpsi (or Z) that only one electron satisfied the cut
- N3: Number of /Jpsi (or Z) that both electron dose not satisfy the cut
- P : Cut efficiency

2) The cut efficiency calcuation for two different cut parameter sets

$$N1 = N0 * P1 * P1$$

$$N2 = N0 * 2 * P1 * (P2 - P1)$$

$$N3 = N0 * 2 * P1 * (1 - P2)$$

$$N4 = N0 * (1 - P1) * (1 - P1)$$

so that

$$P2 = \frac{(2 * (N1 + N2) + P1 * N3)}{2 * (N1 + N2 + N3)}$$

(P1 should be calcuated first with 1) method)

Where

- P1 : Cut efficiency (Tight cut)
- P2 : Cut efficiency (loose cut)
- P2 > P1
- N0: Number of total /Jpsi (or Z)
- N1: Number of /Jpsi (or Z) that both electron satisfied the tight cut
- N2: Number of /Jpsi (or Z) that only one electron satisfied the tight cut and the other electron satisfied the loose cut

- N3: Number of /Jpsi (or Z) that only one electron satisfied the tight cut and the other electron dose not satisfied the loose cut
- N4: Number of /Jpsi (or Z) that both electron dose not satisfy the tight cut

APPENDIX B. ELECTRON CUT EFFICIENCY CALCULATION

Appendix C

The track and the end plug EM cluster matching

The track-cluster matching in the end plug EM calorimeter has been studied for the end plug electron identification. Basically the track reconstruction has been done with Version 5.1 production code. Then new matching algorithm are applied for these samples. First the detail of the matching algorithm between VTPC tracks and EM cluster in the end plug calorimeter will be described. Then the space charge correction and the geometry calibration will be discussed. Finally, the matching quarity of the track and the centroid of the EM cluster in the end plug calorimeter will be described.

C.1 Matching algorithm

C.1.1 η matching algorithm

The VTPC is composed of 8 double-drift-space time projection chambers. The module number was defined from 0 to 7. Each module was divided into 8 ϕ slices called octant. Fig 2.6 shows two VTPC modules. Adjacent modules have a relative rotation angle of $\phi = \arctan(0.2)$, but each odd (even) module was set to the same rotation. This is because

- The relative rotation eliminated inefficiencies near the octant boundaries for the tracks passing more than one module.
- The relative rotation provides ϕ information of tracks from small angle stereo.

This is very important for the end plug region ($10° < \theta < 30°$ and $150° < \theta < 170°$), because tracks in this region pass more than one module. VTPC tracks were reconstructed in R-Z plane at first with wire TDC data, then track azimuth angle was calculated with pad FADC data for each R-Z track. Basically two reconstruction algorithms exist in R-Z plane track reconstruction. One is the histogramming method and the other is the TDC-hit-search method' [109]. The histogramming method has been applied first. It reconstructs R-Z track in each even/odd module independently. Since these tracks do not have ϕ information, they are called a 2D track (Two dimensional track). If the track passed more than one module, i.e. a track have 2D track segments in both even and odd modules, these two 2D track segments were merged and its azimuthal angle was calculated using small stereo wire. Next, TDC-hit-search method is applied to reconstruct low momentum tracks and weak tracks. This method tries to reconstruct 3D tracks directly, it means it uses both even and odd module informations in the first stage. VTPC tracks and the end plug shower center matching algorithm is as follows:

- The road is assumed between the event vertex and the shower center of plug electron candidates.
- Check whether the road passed near the octant boundary. If the road passed even (odd) module octant boundary, only odd (even) module information was used. [1] And if the number of expected hits in odd

[1] If d ϕ between the road and closest octant boundary is less than 0.035 radians, it was excluded from fiducial volume.

(even) module is less than 4, only even (odd) module information has been used.

- Scan all 2D tracks and pick up the best matched track from each rotation module. 3D tracks reconstructed by the histogram method were split into two 2D tracks. Since azimuthal angle is not calculated in this stage, only η matching are evaluated. But we require that the VTPC ϕ slice number that a track passed, is consistent with EM cluster ϕ position. In order to calculate η matching, the track ϕ was assumed to be the same as that of cluster.
- If the difference between a track η and a calorimeter η is less than 0.1, the 2D track was defined as "good track candidates".
- If both even and odd modules have good track candidates which come from the same vertex, these two 2D tracks are merged into one 3D track.
- Next, all tracks reconstructed by TDC-Hit search were scanned and the best matched track is picked up.
- Finally, the best matched track reconstructed by Histogramming method is compared with the track reconstructed by TDC-Hit search.

C.1.2 ϕ matching algorithm

For each track in R-Z plane, the azimuthal angle was calculated from VTPC pad FADC data if it was available. VTPC pad was installed to cover the plug region as shown in Fig 2.5. The VTPC $\phi - Z$ tracks are reconstructed in the every 0.2 dη bins independent of wire R-Z tracks. Only FADC data is used. Then each $\phi - Z$ track are combined to the best matched R-Z wire track. A $\phi - Z$ track in the η bin around an EM cluster is used as track ϕ value if the number of expected pad data is enough to calculate track ϕ value. More than

10 FADC time bins are required. If it has not enough FADC time bins, and the stereo ϕ quality is good, then the stereo ϕ is taken as track ϕ value. The both rotation modules are required to have more than 6 hits.

C.2 Space charge effect on VTPC ϕ measurement

Since the space charge effect of VTPC has been discussed some previous CDF notes [211][212], only space charge effect of the VTPC ϕ measurement is discussed in this section. Because of the slow drift velocity of positive ion, the electric field are distorted and an electron tends to go inner side in the outer radius, and tends to go outer in the inner radius. Since the magnetic field are parallel to the beam axis, when the drift electron has the velocity along to the transverse direction caused by the space charge electric field distortion, it gets the ExB force. This effect always makes track ϕ value large at the inner radius, and make track ϕ small at the outer radius. It doesn't depend on the drift direction. Since the positive ion density is higher in the inner radius than that of outer radius, the bigger ϕ distortion was observed in the small radius. The analysis of the space charge effect has been done with CTC tracks [109]. First, VTPC module geometry correction has been done with low luminosity data. The method of geometry calibration is almost the same as that of space charge effect study [109]. Good CTC tracks are taken as real track trajects. Then all FADC data are converted from ADC count to ϕ position. For each CTC track, closest ϕ hits are picked up, and R value of each ϕ hit is calculated with the cotan of the track and time information of each hit. Then the distance between extrapolated CTC tracks and reconstructed ϕ position of VTPC pad hits were plotted. The analysis has been done at three different luminosities. Since the ExB force comes from both space charge field distortion and module misalignment, the ExB effect

was studied module by module. The drift length dependence of the distortion are plotted at three radius points, the inner radius: $R < 10$ (cm), the middle of radius: 13 (cm) $< R <$ 17 (cm) and the outer radius: 20 (cm) $< R$ for three different instantaneous luminosities. Fig C.1 shows the distance between the extrapolated CTC tracks and ϕ position reconstructed by VTPC pad as a function of drift time at the half module 9 inner radius. Fig C.2 and Fig C.3 show the distance at the middle and outer radius of same half module. Fig C.4 shows the radius dependence of the distortion. As mentioned before, the direction of the distortion is opposite for inner and outer side. When we used nonvertex constraint fit, the space charge gave a big effect, because the direction of the distortion is opposite in the inner and outer radius. In order to avoid the problem, the vertex constraint fit was used.

C.3 Geometry calibration

The geometry calibration for the matching between VTPC tracks and the center of electromagnetic cluster in the end plug calorimeter has been done using isolated W and Z^0 samples. The calibration were done for 2D tracks in even/odd modules and 3D tracks individually. Figs C.5 show η and ϕ matching as a function of track azimuthal angle before and after applying the geometry corrections.

C.4 The resolution of track-cluster matching

The end plug region track matching performance has been studied with isolated W sample.

C.4.1 Event selection

The isolated W samples in the end plug calorimeter were selected with the following cuts [213].

- Missing Et > 20
- Electron Et > 15
- EM/Had < 0.055+0.045*Energy /100.
- Dijet Cut (No jet Cluster (Et > 5 GeV opposite side)
- 3 x 3 $\chi^2 < 10$
- Depth $\chi^2 < 5$
- Fiducial cut
- Isolation cut (< .1)
  1. Isolation (R < .4) is the energy around the electron within the corn normalized by electron energy.
- Loose VTPC hit occupancy cut (> .5)

C.4.2 The matching resolutions

After applying the geometry calibration and the correction of space charge effect, the matching resolution has been estimated. The standard deviation of the fitted gaussian of ϕ matching distribution is 0.6 degree, this corresponds 3 mm at the outer radius of VTPC, and that of $\delta\ \eta$ distribution is 0.012 which corresponds to 2 mm at the outer radius of VTPC. Fig C.6 and Fig C.7 show the $\delta\ \eta$ distribution and $\delta\ \phi$ distribution. For Pt 10 GeV electrons, the probability misidentifying the sign of electron charge is 16 % at $\eta = 1.8$, and for 30 GeV Pt electron, η should be smaller than 1.2 to get same probability.

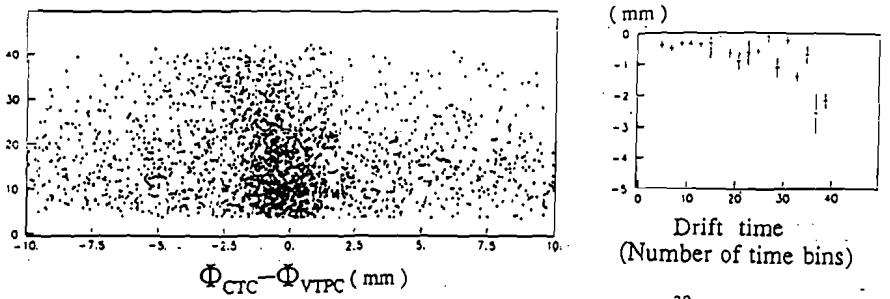

A : Instantaneous luminosity is $0.3 * 10^{30}$

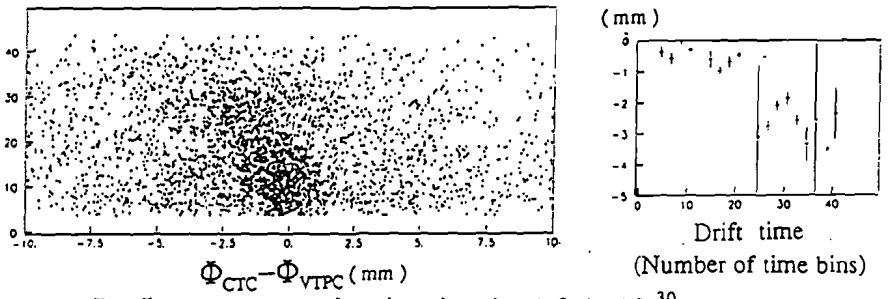

B : Instantaneous luminosity is $1.0 * 10^{30}$

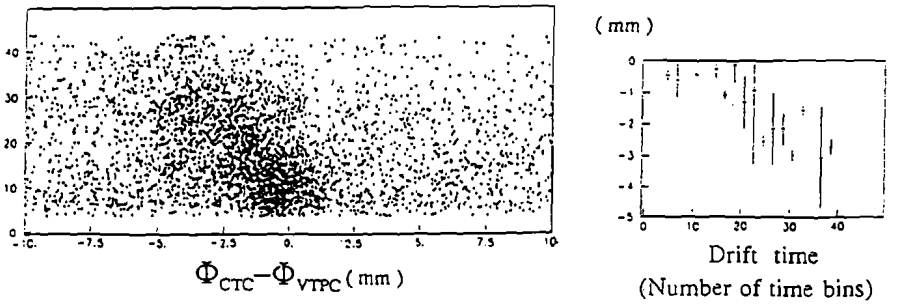

C : Instantaneous luminosity is $1.5 * 10^{30}$

Figure C.1 : VTPC space charge track distortion drift time dependence at inner radius (One time bin corresponds to 94 nsec)

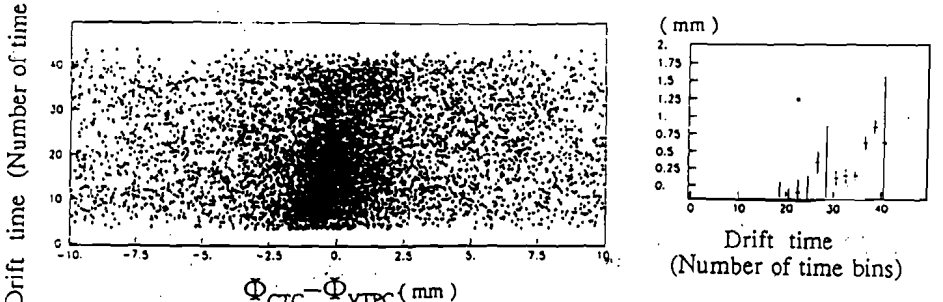

A : Instantaneous luminosity is $0.3 * 10^{30}$

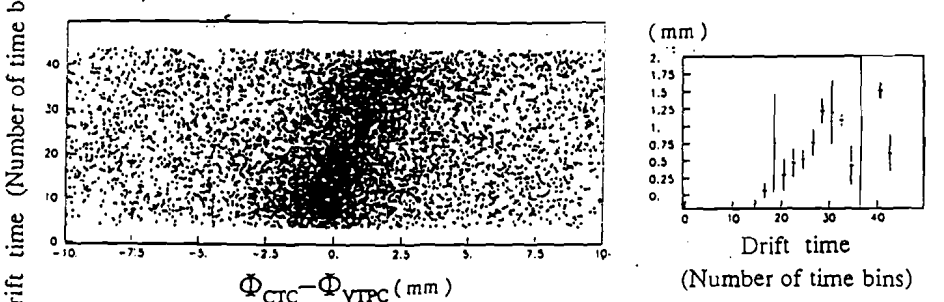

B : Instantaneous luminosity is $1.0 * 10^{30}$

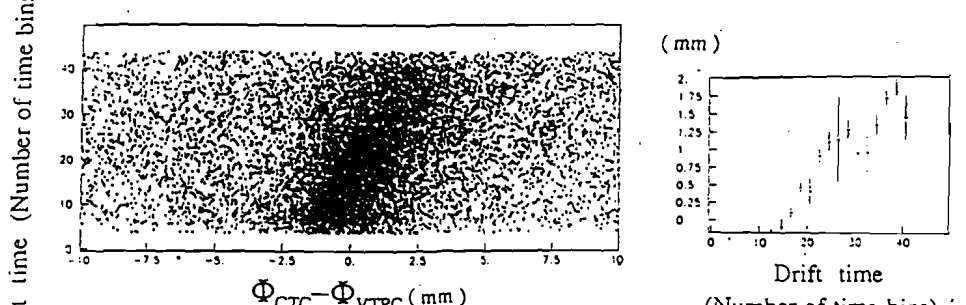

C : Instantaneous luminosity is $1.5 * 10^{30}$

Figure C.2 : VTPC space charge track distortion drift time dependence at middle of radius (One time bin corresponds to 94 nsec)

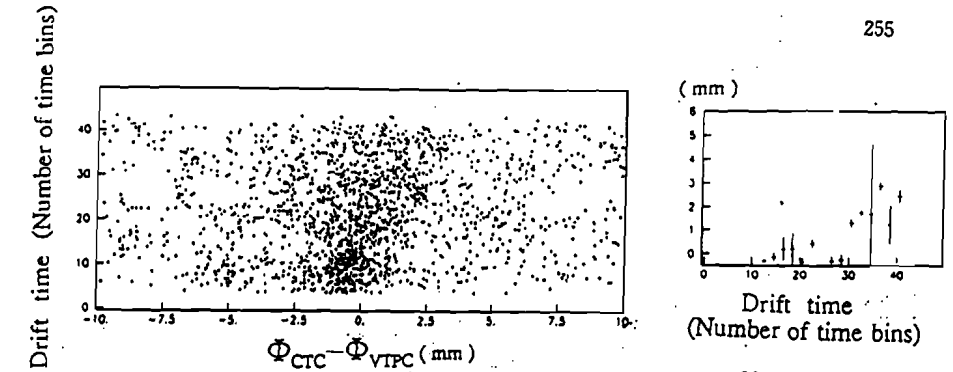

A : Instantaneous luminosity is $0.3 * 10^{30}$

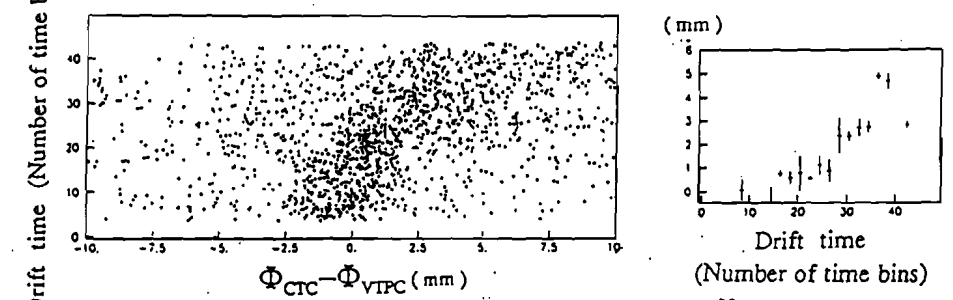

B : Instantaneous luminosity is $1.0 * 10^{30}$

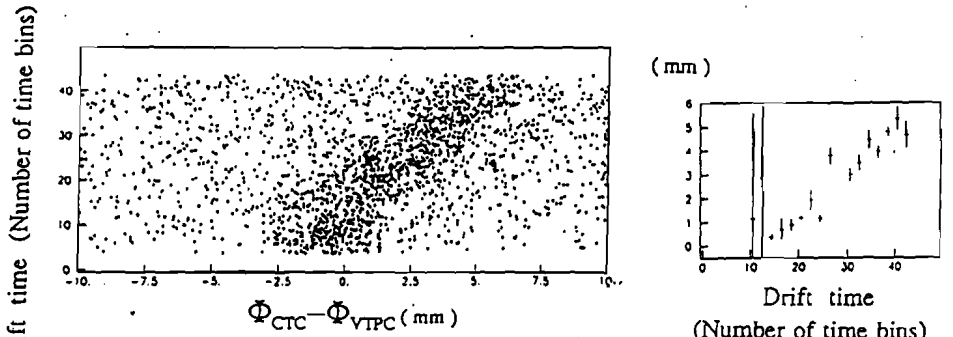

C : Instantaneous luminosity is $1.5 * 10^{30}$

Figure C.3 : VTPC space charge track distortion drift time dependence at outer radius (One time bin corresponds to 94 nsec)

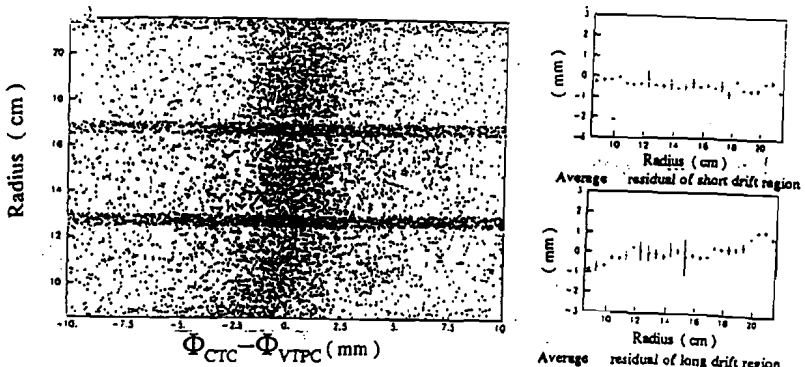

A : Instantaneous luminosity is $0.3 * 10^{30}$

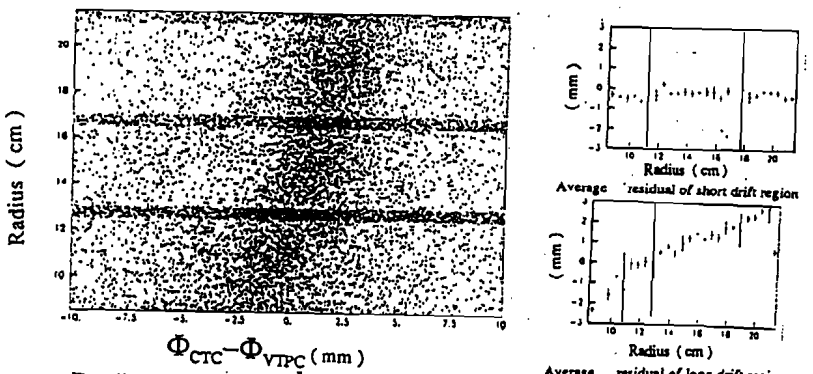

B : Instantaneous luminosity is $1.0 * 10^{30}$

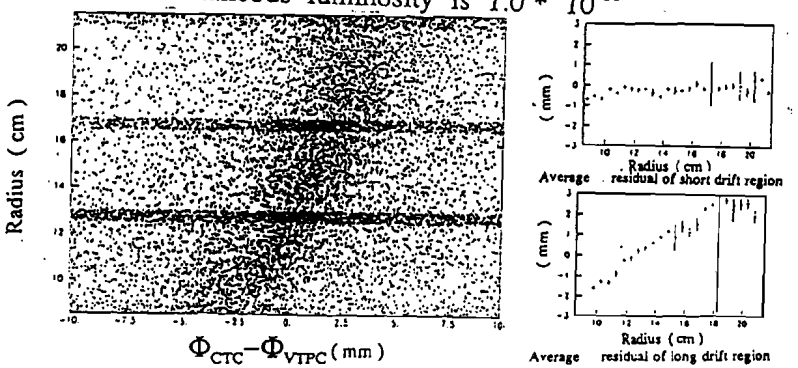

C : Instantaneous luminosity is $1.5 * 10^{30}$

Figure C.4 : VTPC space charge track distortion radius dependence

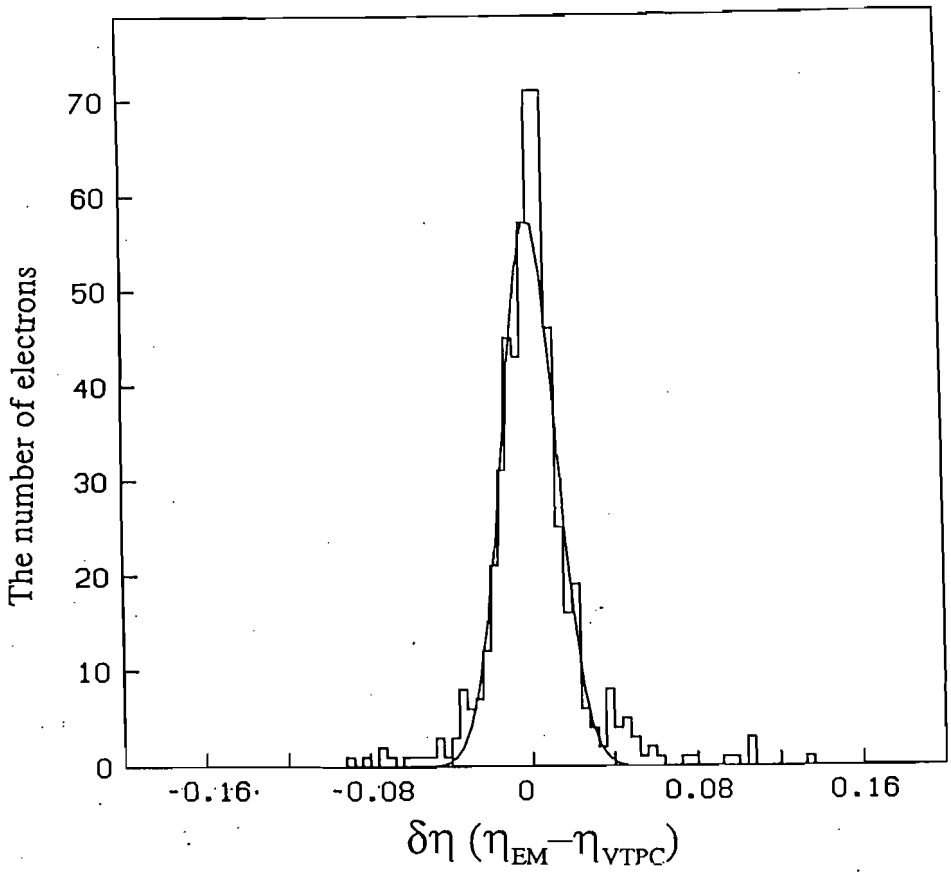

Figure C.6 A match between VTPC track extrapolated position and the end plug electromagnetic cluster centroid in η.

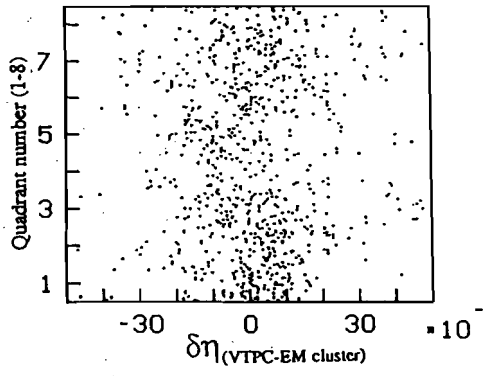

Figure C.5-A VTPC-Plug EM cluster η matching before geometry calibration

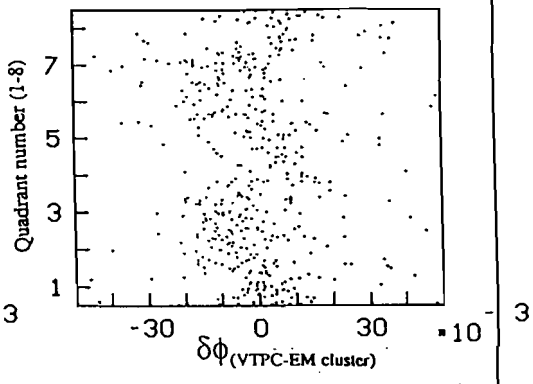

Figure C.5-B VTPC-Plug EM cluster φ matching before geometry calibration

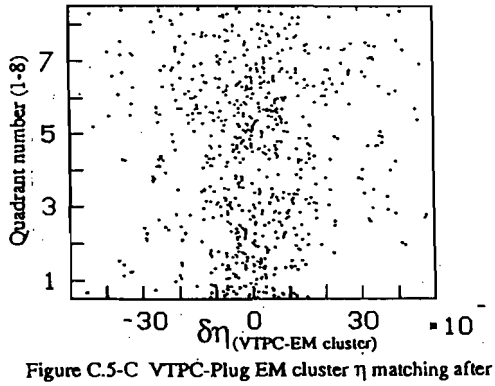

Figure C.5-C VTPC-Plug EM cluster η matching after geometry calibration

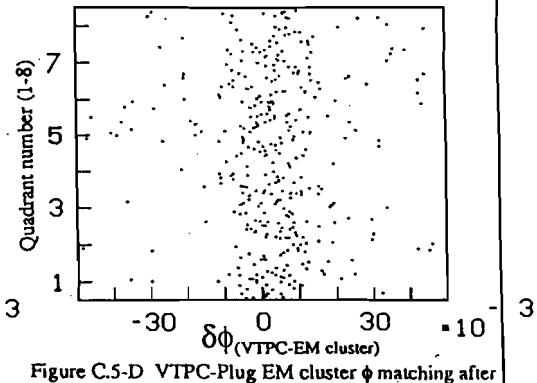

Figure C.5-D VTPC-Plug EM cluster φ matching after geometry calibration

Figure C.5 The geometry calibrations for a match between the VTPC track and the center of EM calorimeter.

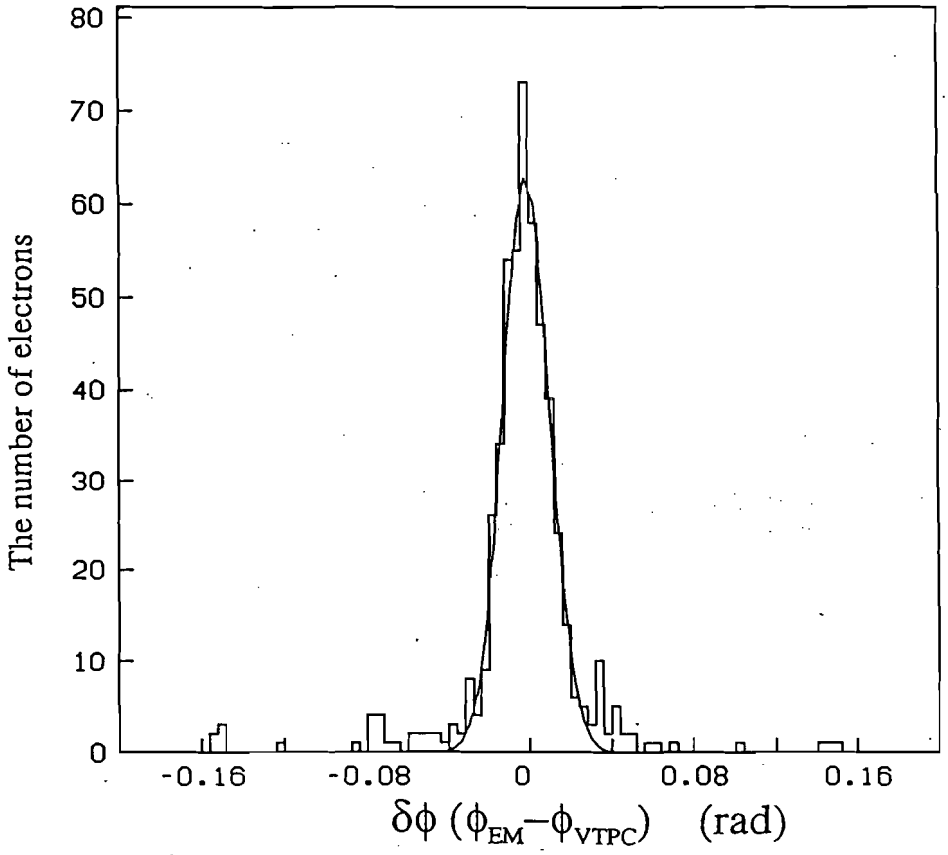

Figure C.7 A match between VTPC track extrapolated position and the end plug electromagnetic cluster centroid in ϕ.

Appendix D

The study of gamma conversion at the end plug region

The study of gamma conversions at the end plug region is discussed in this section. The dE/dx measurement for identifying a conversion electron pair, the pad road finder efficiency and SSP memory overflow rate are discussed. According to the previous VTPC wire road finder study [98][214], when the road is set at random, 10 % of the road had more than 70 % occupancy. The 7 % of electron candidates have only good activity on VTPC wire and have low pad occupancies. This is consistent with the analysis result.

Another goal of this section is to estimate the number of gamma conversions in the end plug electron candidates. In the central electron gamma conversion study [215], it is mentioned that 30 % of the electron candidates come from gamma conversions. 70 % of these gammas converted at out side of VTPC, and the other 30 % are converted at the beam pipe. In my analysis, 65% of the end plug electron candidates have both good VTPC wire and pad hits occupancies. The source of these electron candidates are real electrons and the beam pipe gamma conversion electrons. The 30 % of the plug electron candidates which have good activities both on VTPC wire and pad have more than 170% dE/dx of a minimum ionized track. If we assume that these come from beam pipe gamma conversions, the ratio between the gamma conversions at the beam pipe and out side of VTPC is 0.5 : 1. This is

consistent with the central region analysis and the amount of material.

D.1 SSP memory overflow problem

Inclusive electron samples are striped out from CDF spin production output [216][217]. Total 13822 events are analyzed for this study. VTPC wire SSP memory overflow rate is 0.7 % (95 events) and pad SSP memory overflow rate is 1.84 % (255 events).

D.1.1 Wire SSP overflow

The central and plug electrons are picked up from this sample. Each electron is required to have more than 10 expected wire hits. Total 9451 electron satisfied this cut. 40 electrons (0.42 %) passed the octant module whose data are readout not completely because of SSP memory overflow. The number of rejected electron because of SSP memory overflow was also counted. After requiring 80 % occupancy, 2354 electrons out of 9451 are rejected by hit occupancy cut. And 14 electrons of them are rejected because of SSP memory overflow. This is 0.6 % of rejected electrons.

D.1.2 Pad SSP overflow

The central and plug electrons which passed the VTPC pad implemented modules are selected. Each electron is required to have more than 10 expected FADC time bins. Total 3658 electrons satisfied this cut and 56 electrons (1.5 % of them) passed the VTPC pad SSP memory overflow modules. When 80 % VTPC pad hit occupancy is required, 721 out of 3658 electrons are rejected. 17 electrons of them were rejected because of SSP memory overflow. This is 2.36% of rejected electrons.

D.2 VTPC road finder

D.2.1 The study of road finder

The VTPC pad road finder was written for the plug electron identification. For given road, the code looks at closest three pads in each row, then sums ADC value over these pads. After subtracting the pedestal, if summed ADC value is bigger than 10, the time bin is counted as an active time bin. If a road is close to radial boards, the time bin is excluded from the number of expected time bins.

For the study of wire hit occupancy, the road width are set to 0.035 (rad) in azimuthal angle and $0.01 \times \sqrt{1 + cotan^2}$ in η. Only electrons having more than 10 expected wire hits are used for this study. In addition to the cut, each electron candidate is required to have more than 10 FADC expected time bins. Then the number of active hits is counted. In order to make the central and plug electron sample, the following cuts were required.

For the central electrons,

- Had/EM $< 0.055 + 0.00045 * Energy$
- NTRACK > 0
- LSHR < 0.2
- $\chi^2_{Strip} < 15.$
- Track matching $d\phi$ $<$ 1.5 cm , $dZ < 3.0$ cm
- E/P < 1.5

For the plug electrons,

- Had/EM $< 0.055 + 0.00045 * Energy$
- CTC hit occupancy > 0.5

- $\chi^2_{3x3} < 10.$

In the central, 83 % of the electrons have good activities both in wire and pad, and 0.4 % of electrons has only good occupancy in wire, and 3.4 % electrons have only good activity on pad, the other 12.8 % didn't have enough activity neither wire nor pad. On the other hand, for the plug electrons, 64.7 % electrons have satisfied occupancy cut both wire and pad, 4.3% electrons satisfied only wire occupancy cut, 12.1 % electrons satisfied only pad occupancy cut, and 18.7% electrons didn't satisfy neither wire nor pad occupancy cut. Since VTPC pad has 5 cm long in R direction, the pad road finder is overefficient when the track density in real space is high. Since the track density is relatively high in the central region, it doesn't help to reject accidental track in the VTPC wire road finder, but it is useful for the plug and forward electron identification. According to the previous analysis [218], when the road was set at random, 10 % of the road had good occupancies. Pad road finder reduced this ration from 10% to 3 %.

D.2.2 Gamma conversion study

Using both VTPC wire and pad road finder, inclusive electrons gamma conversion rate are studied. To remove nonconverted π^0 and γ s, CTC activities were required. A track has been required for the central electron candidates and a good CTC hit occupancy has been required for the plug electrons. We started the gamma conversion study using only VTPC wire data to look at the consistency of previous analysis [214]. The electron candidates having more than 70 % of wire hit occupancy are defined as real electrons, and others are defined as conversions. In the central region, 83 % of the electrons have good occupancy. This is consistent with the previous analysis [214]. The analysis mentioned that 20-30 % of the electron candidates come from gamma conversions. 70 % of these conversions are produced at outside of the VTPC and 30 % of them are converted at the beam pipe so that

80-86 % of electron candidates should have good activities in the VTPC wire signal. For the plug electron, 68% of the electron candidates had good wire occupancies and other 32% come from conversion electrons which converted at outside of VTPC. Fig D.1 and Fig D.2 show correlation between VTPC wire and pad hit occupancies of the central and plug electrons.

D.3 The dE/dx calculation

VTPC pad signals are read out with Flash Analog to Digital Converter (FADC) to measure the ϕ position of tracks in the 1988/89 Run. These FADC data are also useful to calculate the dE/dx (Energy deposit normalized by track length) to improve two tracks separation and identify gamma conversions. The study of dE/dx measurement has been done using isolated low angle tracks, the plug region W samples and the inclusive electron samples.

D.3.1 Introduction

Vertex Time Projection Chamber (VTPC) is composed of 8 TPC modules. Each module has two proportional chamber at the both end. In the 1988/89 run, 8 pad planes out of 16 planes, total 1536 channels are read out with FADC. Fig 2.5 shows the location of the half modules with pad readout. They are implemented to cover whole plug region. The FADC sampling speed is 10.6 MHz. The number of time bins which corresponds to maximum drift time is 44 bins. As shown in the Fig 2.6, there are three pad rows in each octant module. The inner, middle and outer pad rows have 6, 8, 10 pads individually, and each pad row covers almost 8 sense wires. Typical pad size is 1.5 cm in the ϕ direction, and 5 cm in the R direction.

D.3.2 Calibration for the dE/dx measurement

Various corrections are applied for the dE/dx calculations. The followings are the list of the corrections.

- VTPC pad electronics gain and pedestal calibration
- Module ϕ dependence correction
- Drift time dependence correction
- Track $cot\theta$ dependence correction
- Radius dependence correction (Wire position dependence)
- Shower position on pad correction
- Pressure dependence in the VTPC

The gain and pedestal calibration of the electronics have been done with the charge injection. The gain distribution and pedestal distribution of one of the calibration run are shown in Fig D.3 and Fig D.4. After calibrating electronics gain and subtracting the pedestal, other corrections are studied with real data.

One of the difficult points of the pad dE/dx calculation is that more than one wire hit induce the charge on a pad plane at the same time, so that when we try to apply position dependence correction, it is difficult to identify the wire number which induces the charge in the pads.

To avoid the problem and get each geometry correction factors, the studies were done with isolated low angle tracks, because each wire hit of isolated low angle tracks induces the charge on a pad at different time interval. The tracks were required to be

- Less than three tracks passed in a octant
- $cot\theta$ of the track must be greater than 1.5

The dE/dx was calculated for each wire hit individually. At that time, only the ADC counts of the pad row just below the wire, are used to calculate the dE/dx,

so that the dE/dx tends to be small at the boundary of each row. Fig D.5-A shows this effects. The dE/dx local ϕ dependence in each row is shown in Fig D.6-A. Since the inner 3 sense wires and outer most wire are not covered with pads, the charge induced by these wires are very small so that hits of these sense wire are not used in the dE/dx calculation. Because of the radial board effect, the dE/dx value becomes small near the edge of the octant(Fig D.6-A). The position dependence in a pad is shown Fig D.7-A. Drift time dependence is shown in Fig D.8-A . The dE/dx tends to be big at the short drift distance. Fig D.5-B, Fig D.6-B, Fig D.7-B and Fig D.8-B are the corrected dE/dx value of each quantities. Fig D.9 shows the dE/dx module dependence, the variation of dE/dx between these modules are small so that it is ignored in calculating the dE/dx.

D.3.3 The dE/dx calculation algorithm

After processing all track reconstruction, a track dE/dx was calculated with these corrections. There are two steps to calculate the charge and track length.

- Step 1: Track length is calculated for each wire hit. After multiplying several correction factors, the track length of each wire hit is summed in each module. The ADC value of the nearest three pads are summed over all expected time bins. When we calculate the sum of ADC counts in each module, the ADC counts that are more than two times bigger than the mean of the ADC counts in the module are truncated.

- Step 2: The sum of ADC counts in each module was recognised as the total energy deposit of the track and it was divided by the sum of the corrected track length in each module.

The amount of energy deposit and track length which need large correction factor are deweighted and summed to calculate the dE/dx. Finally $cot\theta$ correction factor is multiplied and normalized so that the dE/dx of a minimum ionizing particle

becomes 100 %. The dE/dx distribution as the function of cot θ is shown in Fig D.10-A and Fig D.10-B before and after applying the cot θ correction.

D.4 Performance

D.4.1 Resolution of the dE/dx

After applying these corrections, the dE/dx of each track is calculated. Fig D.11 shows isolated track dE/dx distributions, and Fig D.12 shows dE/dx distribution of no isolation cut tracks. The RMS of the dE/dx distribution is between 15 - 20% of the peak value for isolated tracks. Fig D.13-A and Fig D.14-A show the dE/dx distribution error dependence and the number of used time bins dependence for the isolated tracks, Fig D.13/14-B show the mean of dE/dx value as functions of error and the number of data. Fig D.13/14-C show the RMS width of the dE/dx distributions. The dE/dx of the tracks which has the number of time bins greater than 15 are calculated. Momentum dependence also measured with both CTC tracks and VTPC pad tracks. Fig D.15 shows the momentum dependence of the dE/dx value. Each VTPC tracks are linked with CTC tracks, and momentum of each tracks are calculated with CTC informations. And Fig D.16 are the dE/dx momentum dependence calculated by VTPC pad. Momentum resolution of the VTPC pad are almost 30 % for the 1 GeV track [109].

D.4.2 The dE/dx measurement of the end plug electrons

To identify the beam pipe gamma conversions, the dE/dx of electron candidates are calculated. Fig D.17 shows the dE/dx distribution of the plug W electron sample. Fig D.18 shows the dE/dx distribution of inclusive plug electron sample. The cut value of these samples are

Plug W cuts

- Missing Et cut

1) Missing Et > 20 GeV

2) (Missing Et)/(Total Et) > 2.4

3) Dijet Cut : No jet cluster (Et > 5 GeV) in opposite side of EM cluster

- Electron cuts

1) $\chi^2_{3\times3} < 10.$

2) VTPC wire hit occupancy > 0.5

The end plug inclusive electron cuts

- Electron cuts

1) $\chi^2_{3\times3} < 10.$

2) VTPC wire hit occupancy 0.5

Fig D.19 shows the end plug gas calorimetry pressure from Feb. 17 1989 to May 21 1989 [218]. We assume that the gas pressure of VTPC is the same as the pressure of the end plug gas calorimetry and made a gas gain correction. Fig D.20 and Fig D.21 shows plug $\chi^2_{3\times3}$ distribution of these samples. Although there is a big difference on the dE/dx distribution between W sample and inclusive electron sample, $\chi^2_{3\times3}$ distribution looks same. If the dE/dx is measured correctly, it means we can not reject gamma conversion with $\chi^2_{3\times3}$. From Figs D.18, we can see the gamma conversion peak around 200 %, even in the W/Z sample small conversion peak are seen. From this distribution, the tracks having less than 170 % dE/dx are defined as real electrons, and more than 170 % dE/dx is defined as beam pipe conversions. 30 % of good electron candidates are identified as conversion electrons in the plug region.

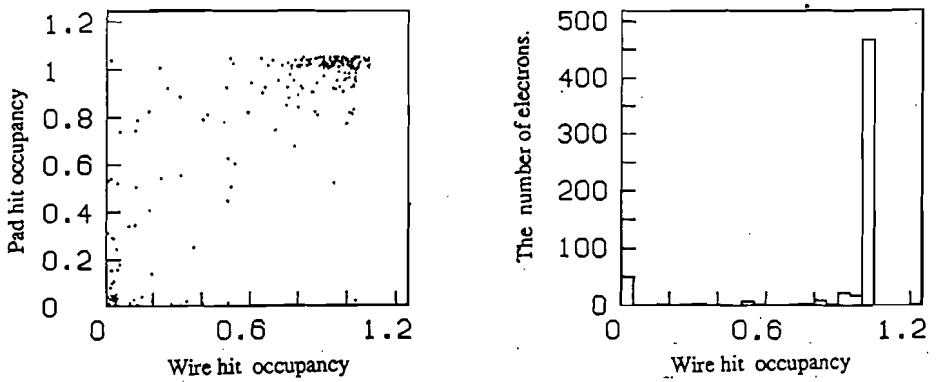

Figure D.1: VTPC wire hit occupancy VS pad occupancy (The central electron candidates)

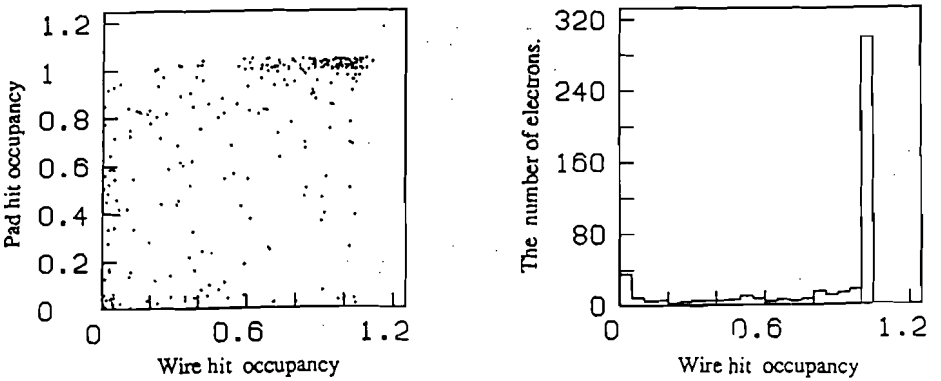

Figure D.2: VTPC wire hit occupancy VS pad occupancy (The end plug electron candidates)

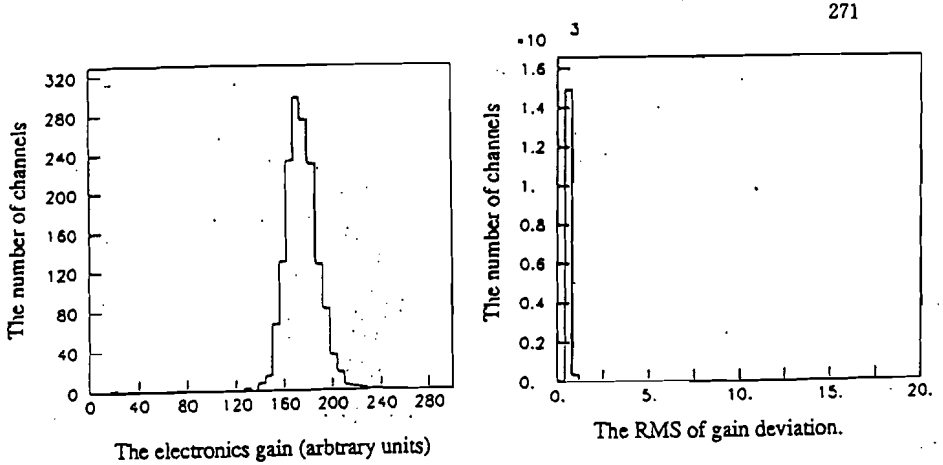

Figure D.3 Flash ADC gain deviation
The charge injection tests are done 50 times for each channel.
Figures are average and RMS of the electronics gain values.

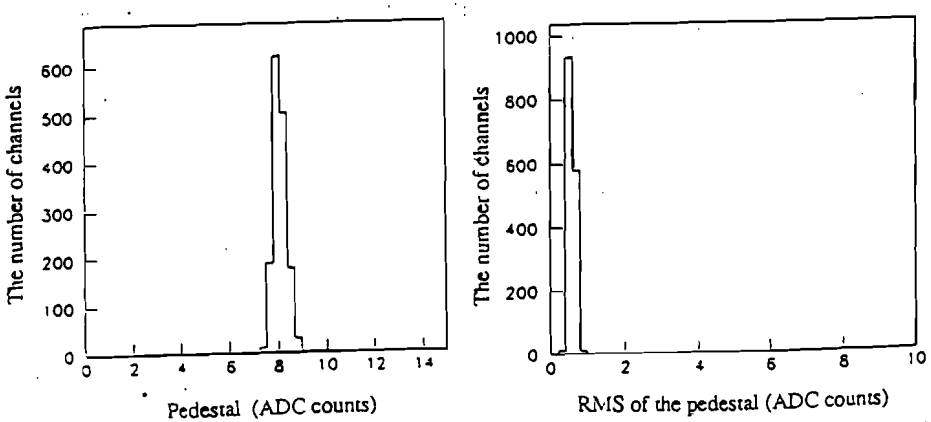

Figure D.4 Flash ADC pedestal deviation

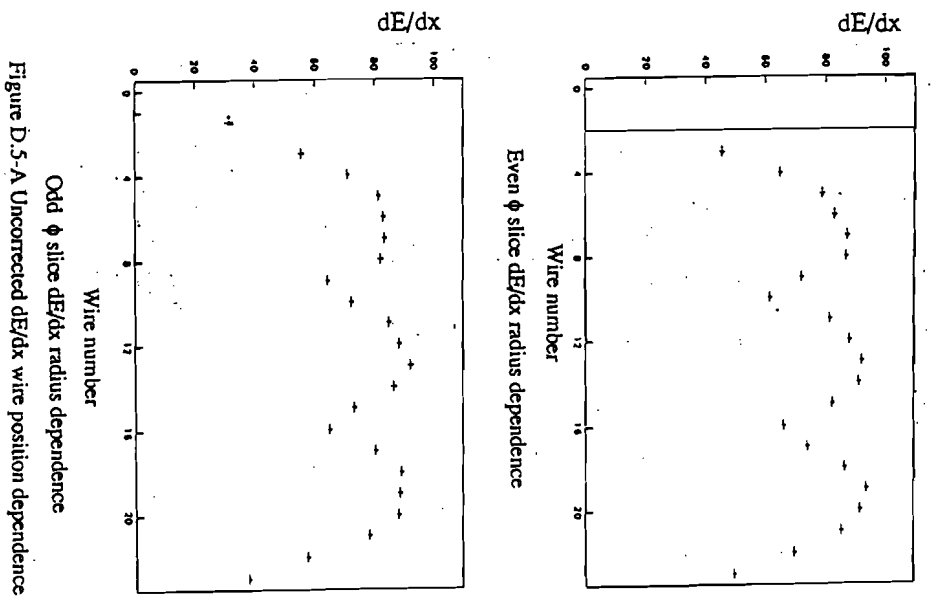

Figure D.5-A Uncorrected dE/dx wire position dependence

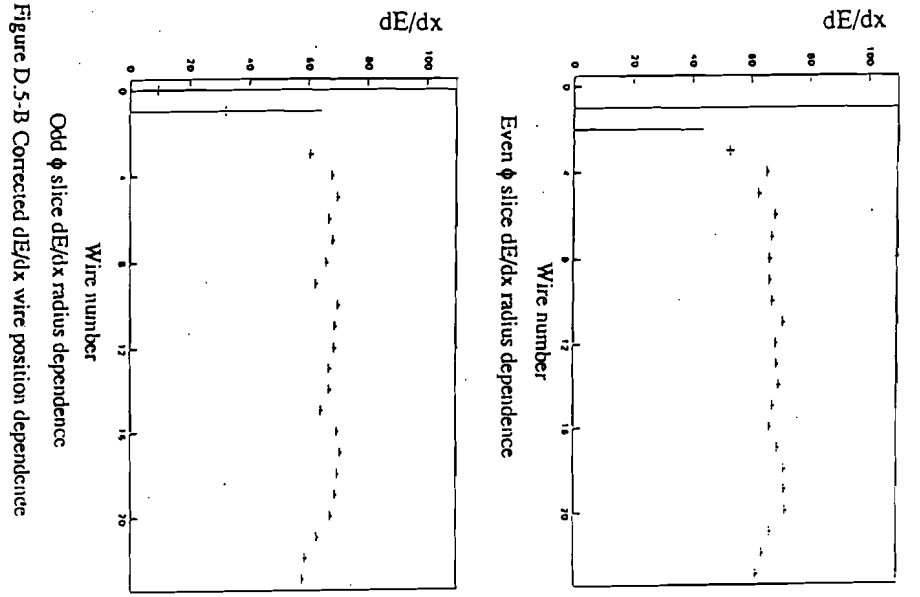

Figure D.5-B Corrected dE/dx wire position dependence

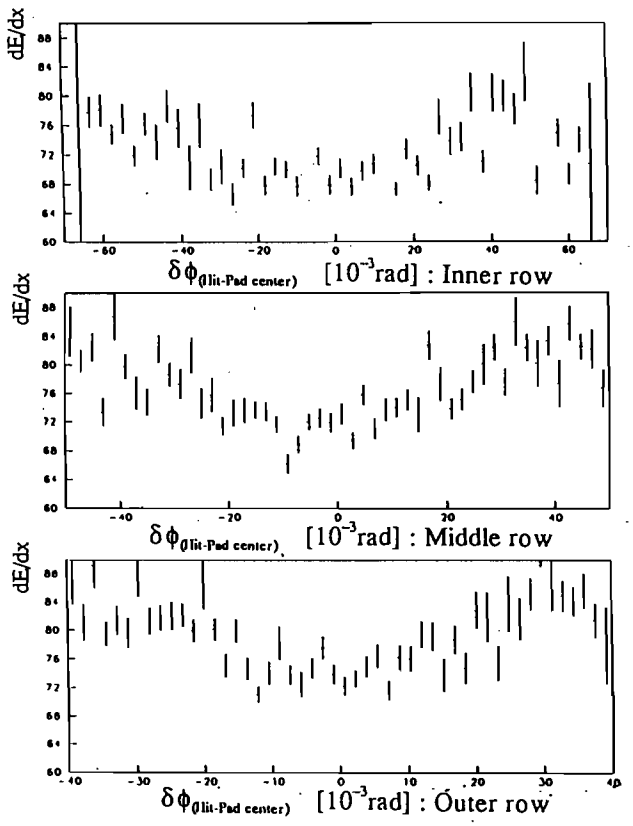

Figure D.7-A Uncorrected ϕ position dependence in side a pad

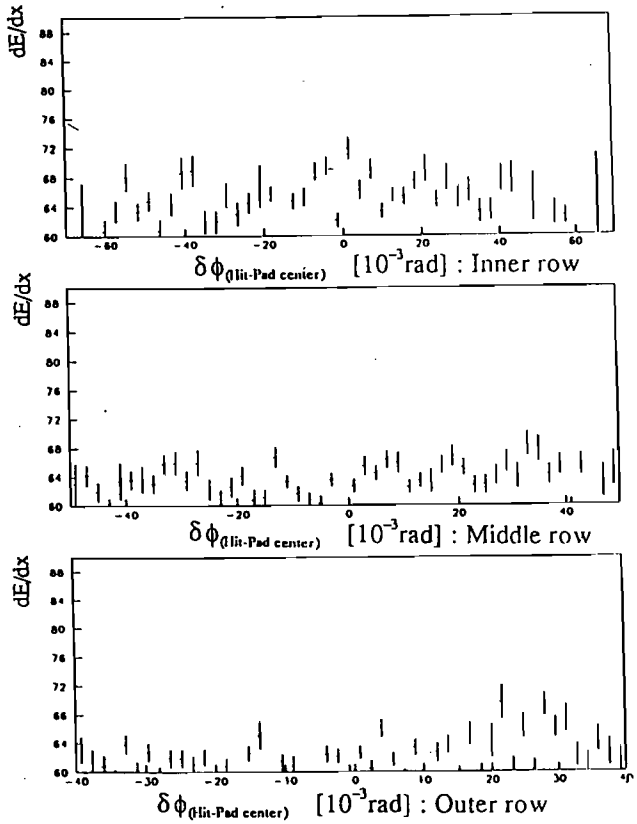

Figure D.7-B Corrected ϕ position dependence in side a pad

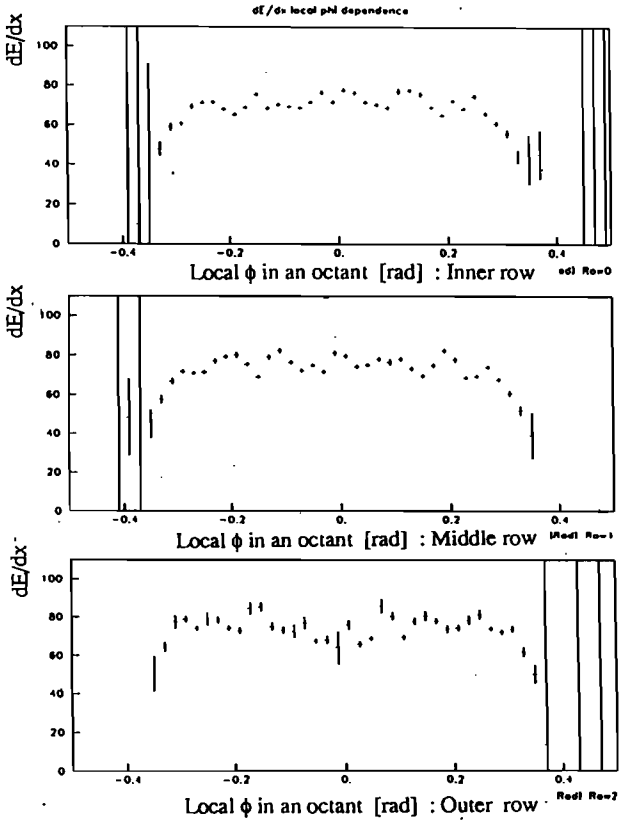

Figure D.6-A Uncorrected dE/dx local ϕ dependence ıce

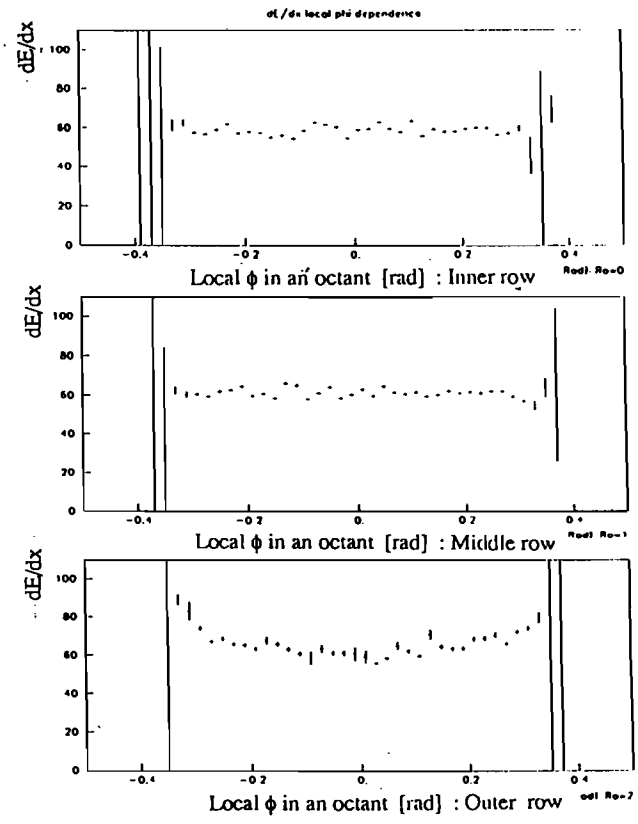

Figure D.6-B Corrected dE/dx local ϕ dependence

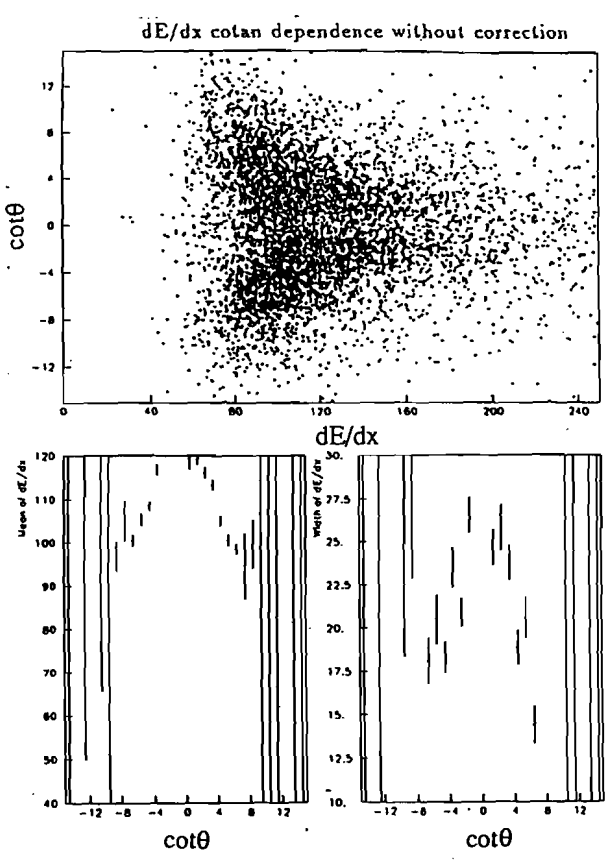

Figure D.10-A Uncorrected dE/dx track cotθ dependence

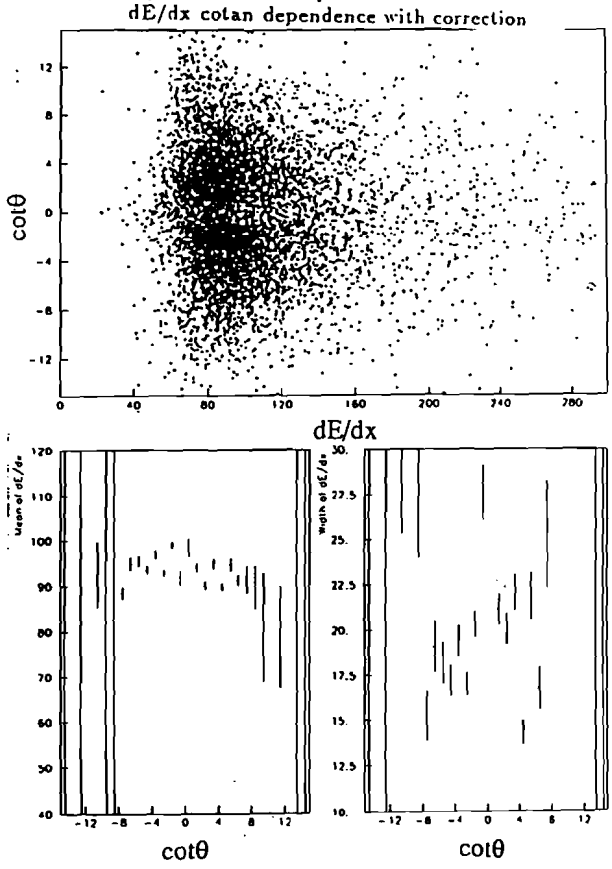

Figure D.10-B Corrected dE/dx track cotθ dependence

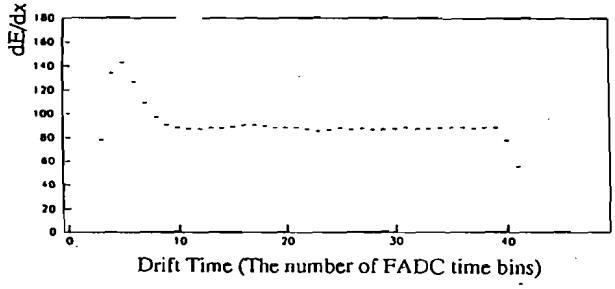

Figure D.8-A Uncorrected dE/dx drift time dependence

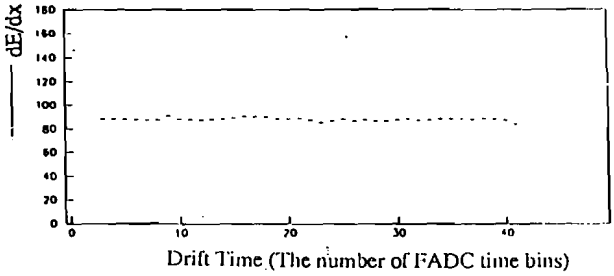

Figure D.8-B Corrected dE/dx drift time dependence

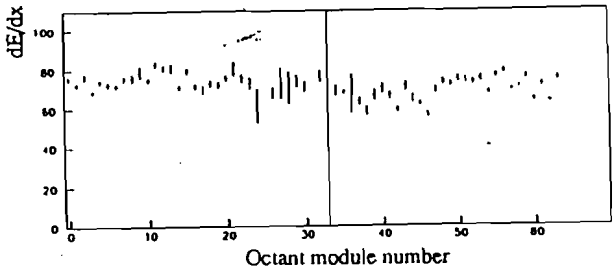

Figure D.9 VTPC module dependence

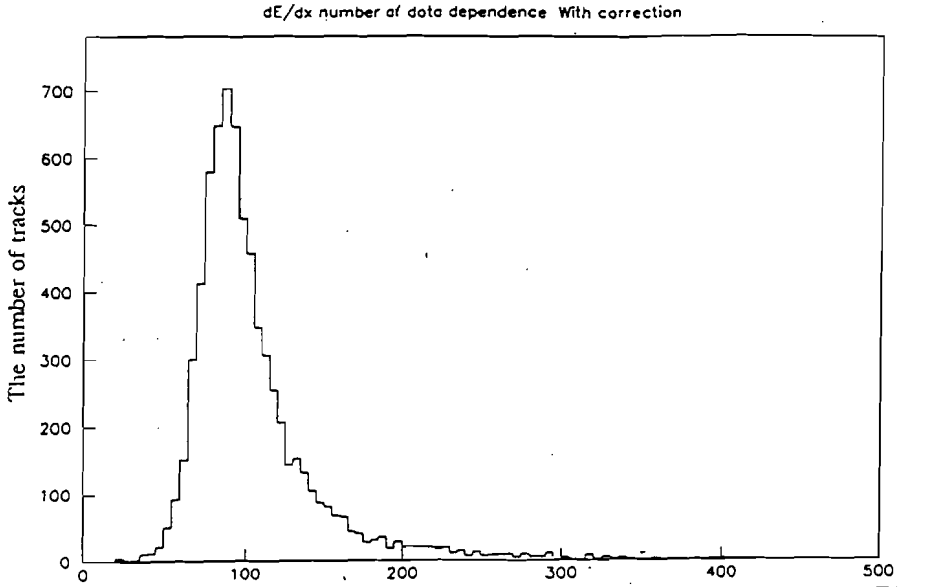

Figure D.11 Isolated track dE/dx distribution

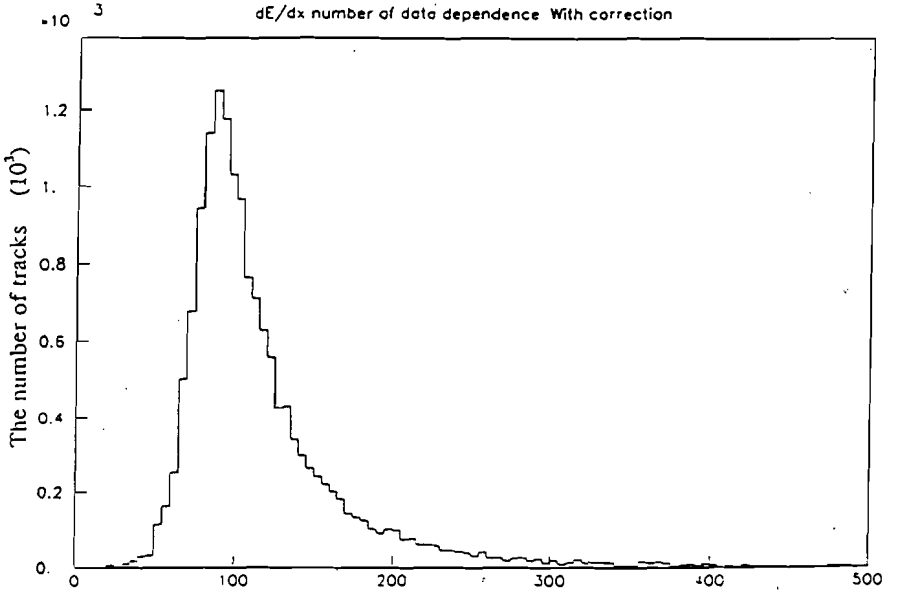

Figure D.12 Nonisolated track dE/dx distribution

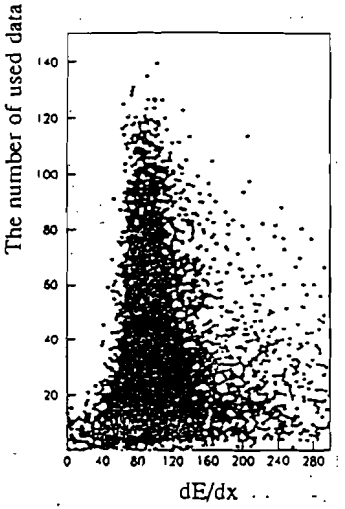

Figure D.13-A DE/dx distribution
the number of used time bins dependence

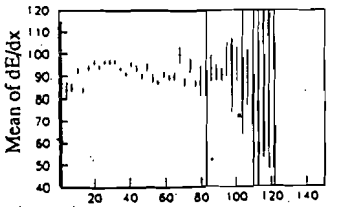

Figure D.13-B

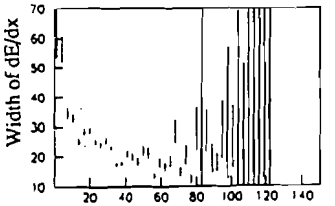

Figure D.13-C

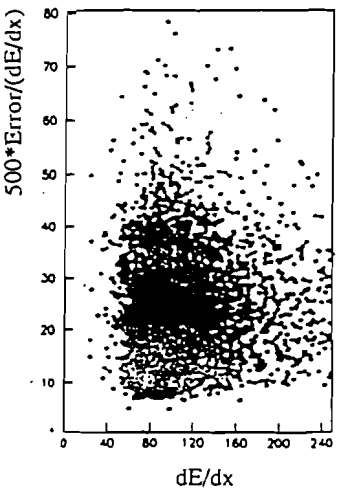

Figure D.14-A DE/dx distribution
Error dependence

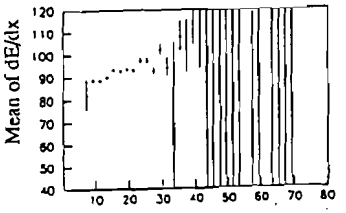

Figure D.14-B

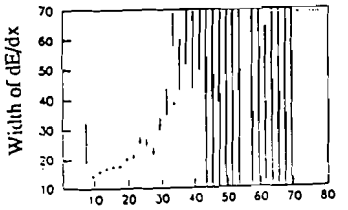

Figure D.14-C

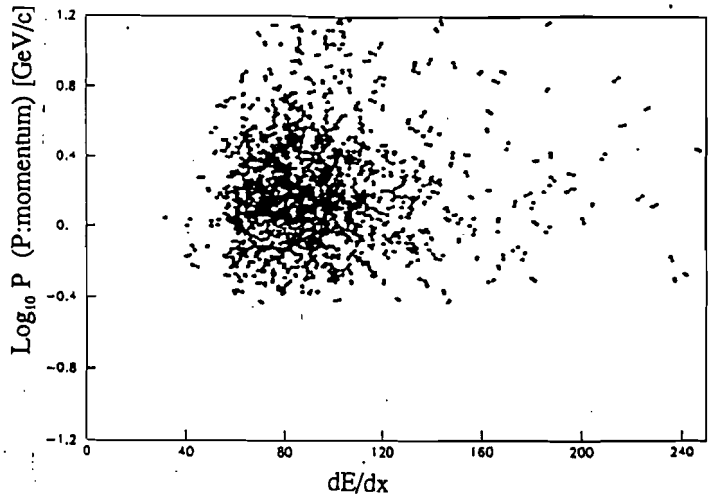

Figure D.15-A DE/dx momentum dependence (measured by CTC)

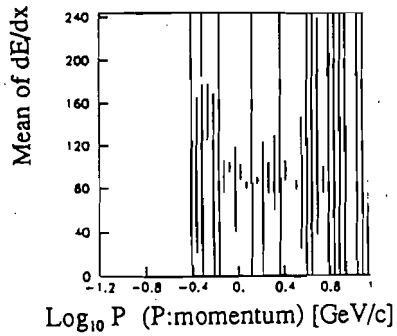

Figure D.15-B

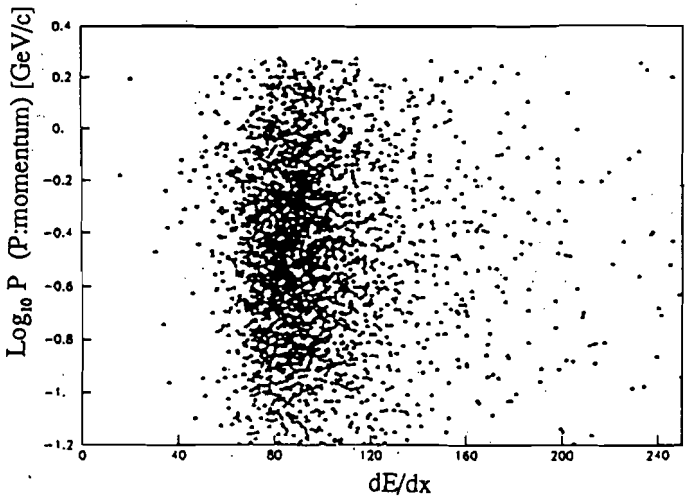

Figure D.16-A DE/dx momentum dependence (measured by VTPC pad)

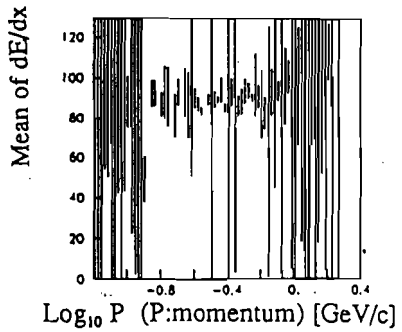

Figure D.16-B

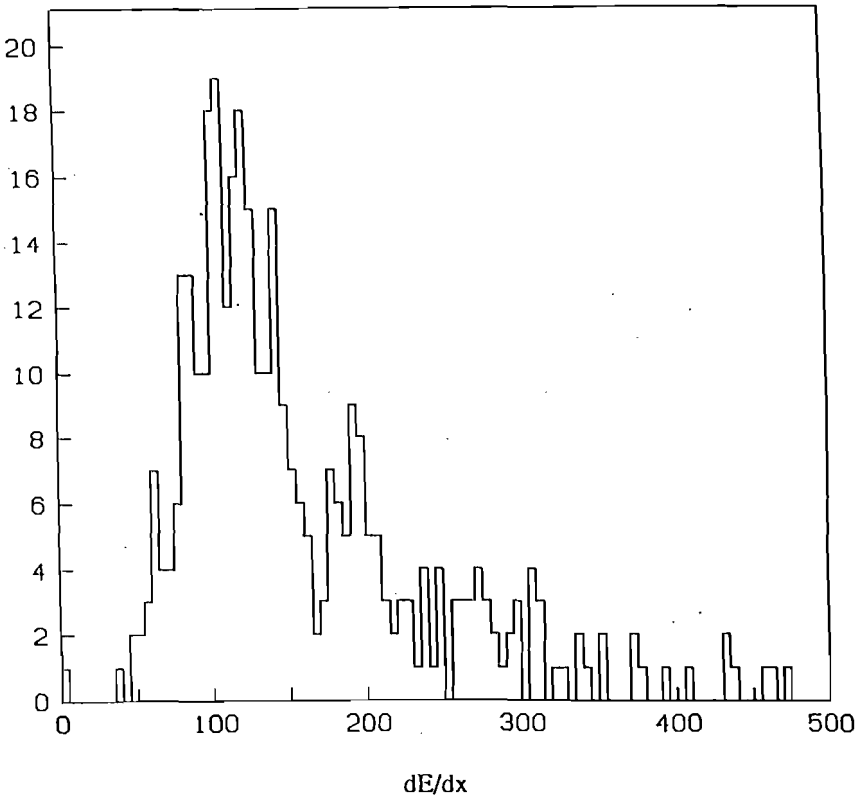

Figure D.18 Inclusive end plug electron dE/dx distribution

282

281

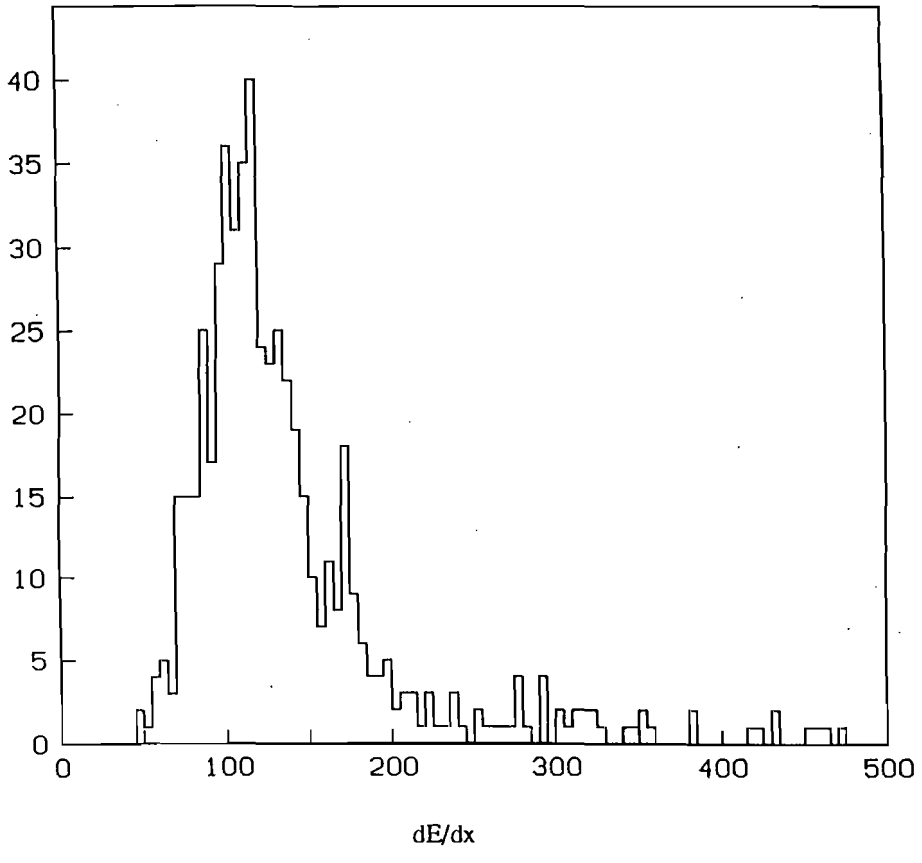

Figure D.17 W / Z the end plug electron dE/dx distribution

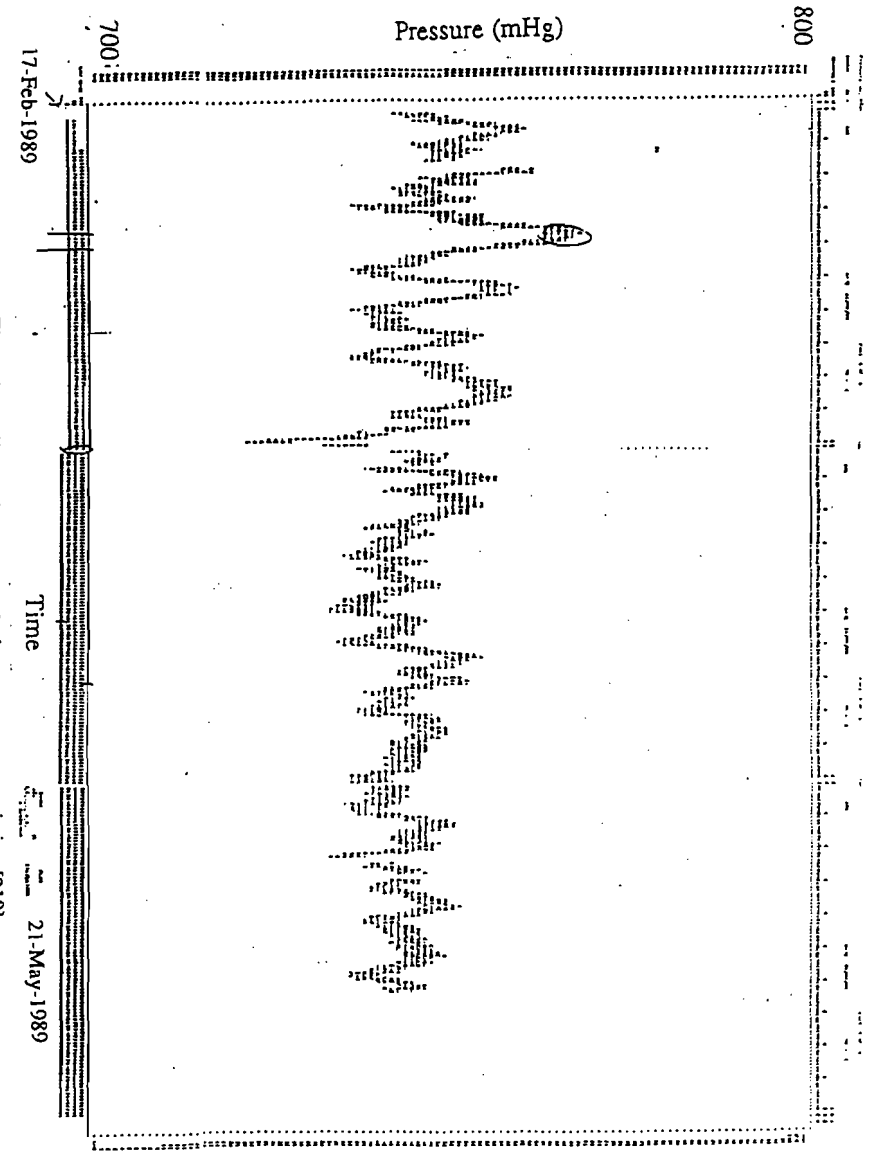

Figure D.19 The end plug gas calorimeter pressure variation [218]

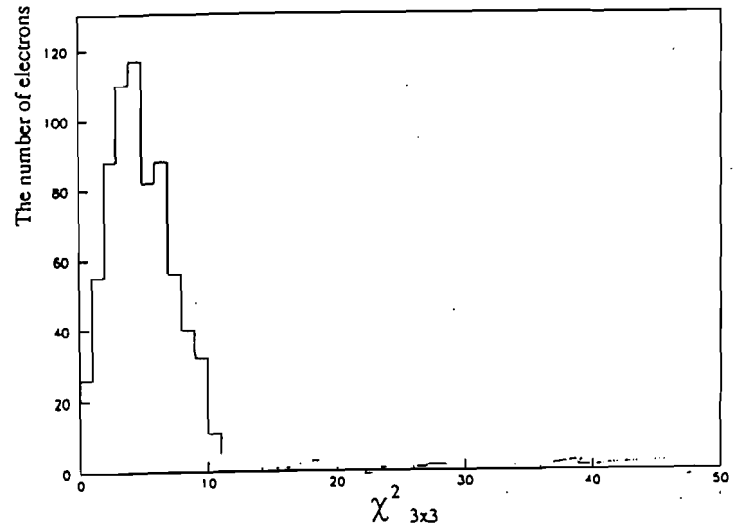

Figure D.20 χ^2_{3x3} distribution of the end plug W electrons

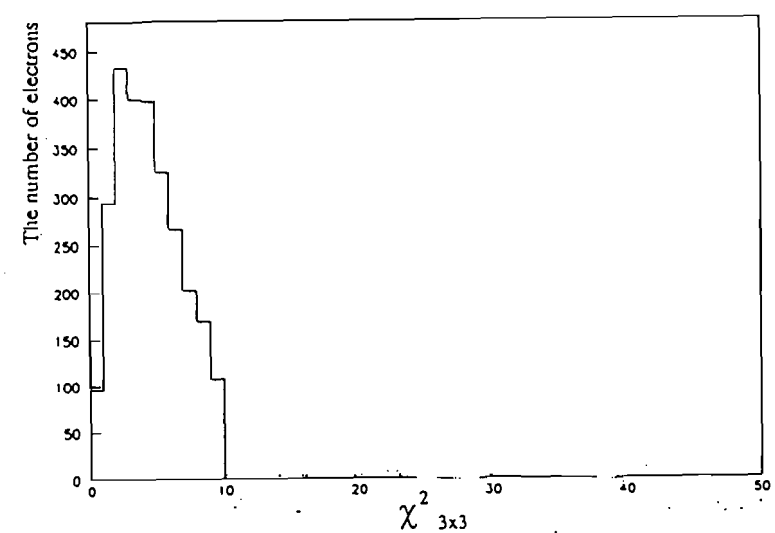

Figure D.21 χ^2_{3x3} distribution of the end plug inclusive electrons

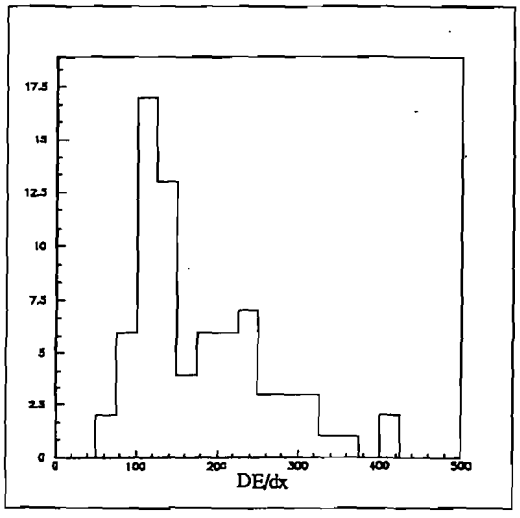

Figure D.22 Nonisolated electron dE/dx distribution (with pressure correction)

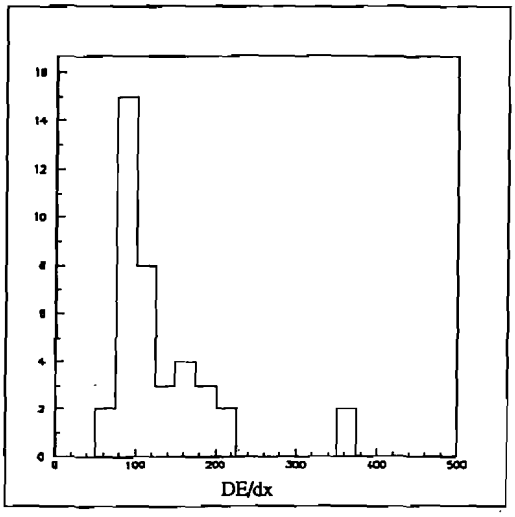

Figure D.23 Isolated electron dE/dx distribution (with pressure correction)